On the Thermodynamics of Planetary Impact Events

HARVARD UNIVERSITY
Graduate School of Arts and Sciences

DISSERTATION ACCEPTANCE CERTIFICATE

The undersigned, appointed by the

Department of Earth and Planetary Sciences

have examined a dissertation entitled
"On the Thermodynamics of Planetary Impact Events"

presented by Richard Gordon Kraus

candidate for the degree of Doctor of Philosophy and hereby certify that it is worthy of acceptance.

Signature _____

Typed name: Prof. Sarah T. Stewart-Mukhopadhyay

Signature _____

Typed name: Prof. Stein B. Jacobsen

Signature _____

Typed name: Prof. Jerry X. Mitrovica

Signature _____

Typed name: Dr. William J. Nellis

Signature _____

Typed name: Prof. Isaac Silvera

Date: May 3, 2013

On the Thermodynamics of Planetary Impact Events

A dissertation presented

by

Richard Gordon Kraus

to

The Department of Earth and Planetary Sciences

in partial fulfillment of the requirements

for the degree of

Doctor of Philosophy

in the subject of

Earth and Planetary Sciences

Harvard University

Cambridge, Massachusetts

May 2013

Dissertation Advisor: Professor Sarah T. Stewart Richard Gordon Kraus

On the Thermodynamics of Planetary Impact Events

Abstract

The history of planet formation and evolution is strongly tied to understanding the outcomes of a wide range of impact events, from slow accretionary events to hypervelocity events that melt and vaporize large fractions of the colliding bodies. To better understand impact processes, their effects on planetary evolution, and how to interpret geochemical data, we need to improve our knowledge of the behavior of materials over the entire range of conditions accessed by collisions. Here I present experimental results from gas gun, laser driven, and pulsed power facilities. Together these facilities can access the tremendously wide range of pressure and temperature conditions achieved in natural impact events.

This work focuses on the thermodynamics of impacts to better understand the phase transitions that most strongly affect the dynamics and chemical consequences of a collision. I show that the entropy generation during collisions is the most natural means of interpreting the thermodynamic processes that occur during an impact event. For materials with sufficient thermodynamic data at high pressures and temperatures, I present a method for obtaining the entropy generation during an impact. With the knowledge of the entropy, I present new shock-and-release techniques to investigate the liquid-vapor region of the phase diagram. I also show that for materials without sufficient data to calculate the entropy generation during an impact, one can use the shock-and-release techniques described here to determine the entropy in the high pressure shock state.

With better equation of state models that are constrained by our experimental data, our confidence in impact models improves dramatically. Using a high fidelity equation of state for H_2O

ice, I derive scaling laws for how much H_2O ice melts and vaporizes for impacts onto icy bodies. Recognizing that icy bodies are not pure ice, I have performed experiments to show how the impact energy partitions between the disparate phases. Finally, I discuss some of the uncertainties in using the laboratory experiments to directly interpret the effects of impacts in nature.

Contents

List of Figures

List of Tables

Acknowledgements

While I cannot acknowledge everyone, as there is a page limit, I would like to express my sincere gratitude to those who have supported my work throughout the years. I begin by thanking the members of my thesis committee: Jerry Mitrovica, Isaac Silvera, Stein Jacobsen, Rick O'Connell, and Bill Nellis.

My time at Harvard was made possible by support from the National Aeronautics and Space Administration, the Army Research Office, and the National Nuclear Security Administration High Energy Density Laboratory Plasmas Program. I would especially like to acknowledge the Department of Energy National Nuclear Security Administration Stewardship Science Graduate Fellowship, the Krell Institute for its administration, the Harvard James Mills Peirce Fellowship, and the Harvard Merit Fellowship.

I would like to express my sincerest gratitude to my advisor Sarah Stewart. During the past five years Sarah has taught me more about becoming a successful scientist than I could ever have hoped. She has allowed me to follow the research path, and oftentimes paths that interested me most, but also strongly encouraged me to finish every project I've started, which has proved productive. Sarah has encouraged me to think long term about science but has also been happy to chat about the minutest details of my experiments and models every time I dropped by her office. Sarah has also taught me a great deal about the science that occurs outside the lab and office, sending me to any meeting I wanted and teaching me about the inherent politics of a small scientific community. As

I reflect on everything I learned from her, and on the long hours working together over the years, there is something that stands out. From the beginning and everyday since, Sarah has always treated me as a collaborator, which has allowed me to build my scientific career on a foundation of confidence and humility. I consider myself lucky to have had Sarah as my graduate advisor, and I look forward to what are sure to be exciting collaborations in the future.

Damian Swift has been an advisor to me since I was an undergraduate intern at Los Alamos National Lab. I owe him my deepest thanks for introducing me to dynamic compression research, and for supporting my scientific career ever since. He is an excellent mentor and an even better friend–and for that I am truly grateful. I am looking forward to our future collaborations at Lawrence Livermore National Laboratory

I would like to thank my undergraduate advisor Aaron Covington for introducing me to the value and enjoyment of scientific research. I would also like to thank Tim Darling and Jeff Thompson for their support during my undergraduate research at the University of Nevada, Reno. I would also like to acknowledge Achim Seifter, an advisor at Los Alamos, who taught me a great deal about pyrometry, laboratory politics, and golf.

During my time at Harvard, I had the remarkable opportunity to work with many distinguished scientists. I would especially like to thank my collaborators at Lawrence Livermore National Laboratory, including Rip Collins, Damien Hicks, Jon Eggert, Ray Smith, Peter Celliers, Jim Hawreliak, Suzanne Ali, Bassem El-dasher, Bruce Remington, Brian Maddox, and Bob Cauble. At Los Alamos National Laboratory I would like to thank Cindy Bolme, Eric Loomis, Sheng Luo, and Andy Obst. I would like to thank my many collaborators at Sandia National Laboratory, including Seth Root, Marcus Knudson, Ray Lemke, Mike Desjarlais, Thomas Mattsson, Luke Shulenburger, Jean-Paul Davis, Chris Seagle, Dan Dolan, Dawn Flicker, and Mark Herrmann. I would also like to thank Jay Melosh for his support and our many interesting conversations about silica.

The large-scale experiments I have performed would not have been possible without the help of numerous laboratory technicians, including Charlie Meyer, Devon Dalton, the numerous target fab and Z facility technicians at Sandia, Walt Unites, Stephanie Uhlich, and the many technicians at the Jupiter Laser Facility at Livermore. I would also like to thank Markos Hankin, Lee Farina, and Greg Kennedy at the Shock Compression Laboratory here at Harvard.

The Earth and Planetary Science Department at Harvard is a close-knit, supportive community, and an excellent place to call home as a graduate student. I believe this is in large part because of the dedicated team that makes the place run and works hard to build that sense of community. I would like to thank Paul Kelley, Chenoweth Moffat, Maryorie Grande, Sarah Colgan, and the many other administrators and faculty coordinators in the department for their help and support. Thank you also for the free coffee, the mass quantities of which I consumed while writing this thesis could be considered as a separate scholarship.

I would like to thank my friends and colleagues at EPS for the many conversations and good times. Thank you Victor Tsai, John Crowley, Rita Parai, Phoebe Robinson, Nathan Arnold, Andy Rhines, Karin Louzada, Laurel Senft, Hilary Close, Glenn Sterenborg, Kate Dennis, Eric Morrow, Erik Chan, Carling Hay, Meredith Langstaff, Matt Newman (honorary G1), Jonathan Tucker, G1 (Simon Lock), Will Steinhardt, Patrick Kim, Ethan Butler, Dylan Spaulding, and everyone else. I also want to thank my longtime friends, whose support I counted on: thank you Dave, Trevor, Robert, Jessica, and Alyssa.

Finally, I would like to thank my family. Thank you Karen for your kindness and always upbeat attitude. I want to thank my fianceé Alise for her relentless love and support. And thank you mom and dad for always being there for me.

With this thesis, I would like to remember my late grandfather Ferd Deiters. His impressive work ethic, humility, and commitment to his family continue to be an inspiration.

Chapter 1

Introduction

"Equations of state are boring but important."
–Jie (Jackie) Li, University of Michigan

To understand planet formation, one must understand the entire range of impacts involved in their growth. The length and energy scales of the collisions range from the first condensed dust particles colliding at a few meters per second to the final stage of planet formation where Moon and Mars sized bodies collide at a few to a few tens of kilometers per second. It is this end stage of planet formation that generates the initial conditions for the thermal and chemical evolution of the surviving planets. This work focuses on the end stages of planet formation when the impact velocities are high and strong shock waves deposit large fractions of the kinetic energy as internal energy in the colliding bodies.

The final few giant impacts have dramatically shaped the terrestrial planets, as is hypothesized for the formation of our Moon (Benz et al., 1986; Canup and Asphaug, 2001; Cuk and Stewart, 2012; Hartmann and Davis, 1975) and the loss of Mercury's mantle (Benz et al., 2007; Benz et al., 1988). Giant impacts are also being observed in other solar systems (Lisse et al., 2009), as evidenced by warm debris disks generated from the vaporization of the colliding bodies. Our understanding of these planetary collisions is predominantly based upon numerical simulations of individual events.

Yet, our ability to quantitatively describe impacts of this scale is severely limited by our lack of knowledge of how planetary materials behave at the extreme conditions achieved during impacts at tens of kilometers per second. And although equation of state theory is advancing rapidly, we cannot yet predict the entire equation of state surface from first principles calculations. Experiments are needed to constrain the equation of state surface throughout the phase space of interest. For giant impacts, this requires considering temperatures of tens of thousand of degrees, pressures of up to a few times those at the center of the Earth, the low densities and temperatures of shock vaporized material, and all the states in between.

While there have been significant advances in experimental facilities and diagnostics used to probe matter at shock pressures of hundreds and even thousands GPa, the fundamental techniques have not changed significantly in the past 60 years. In this thesis I focus on the development of novel experimental techniques to constrain a region of the equation of state surface that has been neglected but is incredibly relevant to giant impacts during planet formation, the expanded states of matter. I discuss the use of these techniques to obtain important data for SiO_2 and Fe; end-member compositions of terrestrial bodies. In Chapters 2 and 3, I discuss the development of two novel techniques to measure the temperatures and densities on the liquid-vapor curves of a wide range of materials. In these chapters, I also emphasize the importance of understanding the entropy gain during shock compression as it is necessary for predicting phase changes during an impact event. In Chapter 2, I present results from a series of laser driven shock-and-release experiments, where my collaborators and I used post-shock temperatures from multi-Mbar shocks in SiO_2 to constrain the temperature along the liquid-vapor dome up to the critical point (Kraus et al., 2012a). In Chapter 3, I present results from a series of shock-and-release experiments at the Sandia Z machine to determine the density along the liquid-vapor dome of iron. As the density and entropy at the 1 bar boiling point of iron are well known, we are able to tie the entropy at

the boiling point to the entropy on the principal Hugoniot. This measure of the entropy on the Hugoniot also provides an accurate constraint on the criteria for vaporizing the cores of accreting planetesimals during the end stages of accretion.

The data taken in Chapters 2 and 3 of this thesis will be used to constrain new multi-phase equations of state for silica and iron. Once developed, these experimentally-constrained equation of state models are used in conjunction with shock physics hydrocodes to quantitatively describe the impact events. In Chapter 4, I present results from a series of impact simulations where I used an experimentally-constrained equation of state for H_2O ice to determine how much ice melts and vaporizes during cratering scale impact events (Kraus et al., 2011). The simulations and resulting scaling laws are significantly more accurate than previous work and have also uncovered a systematic error in the older, but widely cited melt scaling laws for H_2O ice (Pierazzo et al., 1997).

As celestial bodies are not always locally homogeneous in composition, it is necessary to understand the thermodynamics of impacts into mixtures. In Chapter 5, I discuss the results of the first shock and post-shock temperature measurements in an ice-rock mixture, performed at the Harvard Shock Compression Lab (Kraus et al., 2010). Using the results from this work, I present a model for how the energy deposited by the shock wave partitions into the components of the mixture, which is a function of the length scale of the mixture. This model can be combined with better equation of state models of the individual phases to accurately describe the outcomes of impacts into heterogeneous mixtures, such as undifferentiated icy bodies.

For microscopic mixtures, such as hydrated minerals, there is still great uncertainty into their response to shock compression. In Chapter 6, I evaluate the thermodynamic paths achieved in previous laboratory shock recovery experiments on hydrated minerals and discuss the difficulties in their interpretation. I also present the results of an experimental test on the sensitivity of our understanding of shock effects on hydrated minerals to the experimental design.

There is significant room for discovery in studying the thermodynamics of materials at extreme conditions. In the following chapters, I present descriptions of material behavior based on experimental data taken with novel experimental techniques. When used in shock physics hydrocodes, the models constrained by my data will significantly reduce the uncertainty of the thermal states achieved during impact events at all scales. As expressed in the quote by Jie Li, reducing the uncertainty is a tedious but important aspect of equation of state development. It is the commitment to developing useful models and the joy of discovering the importance of material properties that motivates this work.

Chapter 2

Shock Vaporization of Silica

The most energetic planetary collisions attain shock pressures that result in abundant melting and vaporization. Accurate predictions of the extent of melting and vaporization require knowledge of vast regions of the phase diagrams of the constituent materials. To reach the liquid–vapor phase boundary of silica, we conducted uniaxial shock-and-release experiments, where quartz was shocked to a state sufficient to initiate vaporization upon isentropic decompression (hundreds of GPa). The apparent temperature of the decompressing fluid was measured with a streaked optical pyrometer, and the bulk density was inferred by stagnation onto a standard window. To interpret the observed post-shock temperatures, we developed a model for the apparent temperature of a material isentropically decompressing through the liquid–vapor coexistence region. Using published thermodynamic data, we revised the liquid–vapor boundary for silica and calculated the entropy on the quartz Hugoniot. The silica post-shock temperature measurements, up to entropies beyond the critical point, are in excellent qualitative agreement with the predictions from the decompressing two–phase mixture model. Shock-and-release experiments provide an accurate measurement of the temperature on the phase boundary for entropies below the critical point, with increasing uncertainties near and above the critical point entropy. Our new criteria for shock-induced vapor-

An amended version of this Chapter was published with Sarah T. Stewart, Damian C. Swift, Cindy A. Bolme, Ray F. Smith, Sebastien Hamel, Benjamin D. Hamel, Dylan K. Spaulding, Damien G. Hicks, Jon H. Eggert, and Gilbert W. Collins in the Journal of Geophysical Research–Planets, Vol. 117, E09009, 2012.

ization of quartz are much lower than previous estimates, primarily because of the revised entropy on the Hugoniot. As the thermodynamics of other silicates are expected to be similar to quartz, vaporization is a significant process during high-velocity planetary collisions.

2.1 Introduction

During the end stage of planet formation, the nebular gas disperses and mutual encounter velocities increase via gravitational stirring from the largest bodies. N-body simulations of this stage find typical collision velocities between protoplanets of one to a few times the two-body escape velocity (Agnor et al., 1999). The kinetic energy of an impact is partially transferred to internal energy in the colliding bodies via passage of a strong shock wave. At the expected impact velocities of $\sim$10 to a few tens of km s^{-1} onto the growing planets, the internal energy increase is sufficient to melt and vaporize a large fraction of the colliding bodies. However, the predicted degree of melting and vaporization for a specific impact scenario has great uncertainty that primarily arises from poorly-constrained equations of state (EOS).

Accurate equations of state over a tremendous region of phase space are required to make predictions about the impact processes so prevalent during the formation of the solar system and its subsequent evolution. The last giant impact is invoked to explain the diverse characteristics of rocky and icy planets in the Solar System (e.g., Stewart and Leinhardt, 2012a), including the large core of Mercury (Benz et al., 2007; Benz et al., 1988), formation of Earth's moon (Canup and Asphaug, 2001), Pluto's moons (Canup, 2005), and Haumea's moons and family members (Leinhardt et al., 2010). In each case, the argument for a giant impact relies upon the details of the equations of state.

Although equation of state theory is advancing rapidly, the generation of accurate and complete equations of state from first principles is still not feasible for most geologic materials. Planetary

collisions are particularly challenging because of the need to understand both the extreme temperatures and high compression ratios achieved in the shocked states and the low densities and temperatures of shock-vaporized material. Experiments are required to constrain the equation of state throughout the phase space of interest.

Planar shock wave experiments, typically on gas guns, have been used to define the shock states for a wide range of materials, including many planet-forming rocks and minerals (Ahrens and Johnson, 1995a,b). The range of states that are accessible by laboratory shock wave experiments has increased dramatically, to thousands of GPa, with the development of pulsed lasers (e.g., Hicks et al., 2005) and electromagnetically launched flyer plates (e.g., Knudson and Desjarlais, 2009). The pressure, density, and internal energy increase can be accurately determined along the Hugoniot, the locus of shock states. For transparent materials, the shock temperature can also be determined by measuring the thermal emission from the shock front (Lyzenga and Ahrens, 1979; Miller et al., 2007).

The states achieved during decompression from the shocked states are much more difficult to investigate due to the technical limitations in reaching this region of phase space. In particular, accessing the equation of state surface near the liquid–vapor curve and up to the critical point for most relevant Earth materials is technically difficult as the temperatures (2,000 to 10,000 K) and pressures (up to a few GPa) cannot be obtained through quasi-static laser-heating techniques. Resistive-heating techniques have been used to isobarically heat samples to the temperature range of interest (Gathers et al., 1976); however, these techniques are only suitable for electrically conducting samples. Over the past 50 years, a significant number of shock-and-release experiments have been performed to probe the pressures, and in some cases the temperatures, along the liquid–vapor curve of the more volatile metals: lead (Ageev et al., 1988; Pyalling et al., 1998), tin (Bakanova et al., 1983; Ternovoi et al., 1998), bismuth (Kvitov et al., 1991), and cadmium (Bakanova et al.,

1983). In these experiments, the pressure at the intersection between the release isentrope and liquid–vapor curve was determined by measuring the shock generated in a downrange helium gas cell. Usually, the helium gas backing the metal was shocked to temperatures much higher than the release temperature in the metal, severely complicating the simultaneous study of the thermal emission from the metal.

Free-surface post-shock pyrometry measurements were performed on aluminum and cerium shocked to multi-Mbar pressures (Celliers and Ng, 1993; Reinhart et al., 2008); however, no other thermodynamic parameters were measured or associated with the apparent post-shock temperatures. Stewart et al. (2008) measured the shock and apparent free-surface post-shock temperatures for H_2O ice shocked into the fluid phase. Using a model for the entropy along the Hugoniot and assuming high emissivity, the post-shock states fell on the known liquid–vapor curve for water.

Recently, Kurosawa et al. (2010) used laser-launched flyers to shock diopside and quartz into a fluid state. Upon breakout of the decaying shock wave at the downrange free surface, a spectrograph coupled to an ICCD was used to observe late time emission lines from atomic and ionic species. Using a model for pressure broadening, the authors were able to estimate the temperature and pressure in the expanding vapor plume. However, the decaying-shock measurements did not constrain the liquid–vapor phase boundary for these materials.

In this work, we focus on silica, one of the most abundant minerals in the Earth's crust and an end-member composition of the mantle of rocky bodies. Throughout this work, quartz refers to the crystalline α-quartz phase of silica and fused quartz is explicitly noted. Variable definitions and annotations are defined in Table 2.1.

In §2.2, we discuss the thermodynamics of shock compression and release, with particular emphasis on understanding entropy. We calculate entropy at new reference states to determine the absolute entropy along the quartz principal Hugoniot, and the boiling point of silica is recalculated

using recent thermodynamic data for liquid silica. Then, we discuss the experimental techniques used in our new shock-and-release experiments that probe the temperature and density along the liquid–vapor curve up to the critical point (§2.3). In §2.4, we compare the results of our post-shock temperature measurements with a revised model for the liquid–vapor curve of silica. Next, we consider the time scales for phase decomposition during decompression (§2.5.1), which we find are short compared to the time scale of the experiments. To aid in interpretation of the experiments, we calculate the temperature and density profiles along release isentropes and as a function of distance in the expanding post-shock mixture (§2.5.2-2.5.3). Then, we develop a radiative transfer model to predict the apparent post-shock temperature of the two–phase mixture as a function of entropy (§2.5.4). The predicted post-shock temperatures and the measured post-shock temperatures are compared in §2.6.1. The agreement between the radiative transfer model and the experimental data indicates that the shock-and-release technique provides robust constraints on the liquid–vapor curve. Finally, we calculate the critical shock pressures for shock-induced vaporization (§2.6.2) and discuss the implications for planetary collisions (§2.6.3).

2.2 Reference Entropy States for Silica

The shock Hugoniot follows a complicated path through the EOS surface that depends on the equilibrium EOS, material strength, and kinetics related to phase transitions. Across the shock front mass, momentum, and energy are conserved, which allows one to exactly solve for the increase in internal energy, longitudinal stress, and density in the shocked state using the Rankine–Hugoniot equations (Rice et al., 1958a). Shock pressures above ∼110 GPa transform quartz to a fluid (Hicks et al., 2006; Lyzenga et al., 1983), where strength and kinetics of phase transformations have no effect on the path of the Hugoniot through the EOS surface. Figure 2.1 presents the pressure–temperature phase diagram of silica with the Hugoniot for quartz in the fluid region as has been

Table 2.1: Summary of primary variables and annotations.

Symbol	Definition
General Thermodynamic Variables and Constants	
R	Ideal gas constant
k_B	Boltzmann constant
E	Specific internal energy
H	Specific enthalpy
G	Specific Gibbs free energy
P	Pressure
S	Specific entropy
T	Temperature
V	Specific volume
ρ	Density
$U_{\rm s}$	Shock velocity
$u_{\rm p}$	Particle velocity
γ	Thermodynamic Grüneisen parameter
q	Exponent to volume dependence of Grüneisen parameter
$C_{\rm V}$	Isochoric heat capacity
$C_{\rm P}$	Isobaric heat capacity
$_{\rm CP}$	Subscript denoting critical point value
Absolute Entropy Calculation Variables (§2.2.1)	
$_{00}$	Subscript denoting reference state of stishovite at STP
$_{A}$	Subscript denoting intermediate state: stishovite on the principal isentrope at V_B
$_{B}$	Subscript denoting intermediate state: stishovite on the melting curve at 4500 K
$_{C}$	Subscript denoting intermediate state: fluid at intersection of fused quartz Hugoniot and melting curve
$_{D}$	Subscript denoting reference state of fluid silica at intersection of quartz Hugoniot and melting curve
$_{H,Qtz}$	Subscript denoting state along the quartz Hugoniot
$_{H,FQ}$	Subscript denoting state along the fused quartz Hugoniot
ΔS_{AB}	Entropy of isochorically heating stishovite from T_A to 4500 K
ΔS_{BC}	Entropy of melting stishovite at 4500 K
δS	Absolute uncertainty in the specific entropy
δT	Absolute uncertainty in the temperature
Stagnation Variables (§2.3.2)	
$P_{\rm s}$	Ablation pressure
$I_{\rm L}$	Drive laser intensity
$V_{\rm imp}$	Impact velocity of released silica onto LiF window
$\rho_{0,\rm F}$	Average density of decompressing fluid immediately prior to impact with LiF window
$P_{\rm LiF}$	Shock pressure induced in LiF window upon stagnation
$U_{\rm S,SF}$	Shock velocity in re-shocked silica fluid
$u_{\rm P,SF}$	Particle velocity in re-shocked silica fluid
$u_{\rm int}$	Velocity of interface between stagnating silica and LiF window
$C_{0,\rm SF}$	Intercept of $U_{\rm S,SF}$-$u_{\rm P,SF}$ relation
$s_{\rm SF}$	Slope of $U_{\rm S,SF}$-$u_{\rm P,SF}$ relation

Table 2.1: Summary of primary variables and annotations (continued).

Symbol	Definition
Phase Decomposition Variables (§2.5.1)	
τ_{spall}	Time scale for dynamic fragmentation to occur within the metastable fluid
ς	Surface tension
$\dot{\epsilon}$	Strain rate
c_{s}	Adiabatic sound speed
d_0	Fragmentation length scale
τ_{nucl}	Time scale for nucleation and growth to occur within the metastable fluid
Λ	Kinetic coefficient for nucleation
n	Number density of particles in volume V^*
V^*	Volume undergoing homogeneous nucleation
W	Work to form a critical size nucleus
ΔP	Pressure difference between metastable state and liquid–vapor curve
Post-Shock Temperature Buffering Variables (§2.5.2)	
S_m	Specific entropy of the liquid–vapor mixture
$T_{\mathrm{LV,m}}$	Temperature on liquid–vapor curve at specific entropy S_m
V_{avg}	Average specific volume of liquid–vapor mixture
χ_{vap}	Mass fraction of vapor
$\left(\frac{dP}{dT}\right)_{\mathrm{LV,T}}$	Slope of the liquid–vapor curve at temperature T
$_{\mathrm{liq}}$	Subscript denoting the liquid phase
$_{\mathrm{vap}}$	Subscript denoting the vapor phase
Post-Shock Density Profile Variables (§2.5.3)	
h	Lagrangian coordinate
x	Eulerian coordinate
ρ_i	Density along characteristic i
$c_{\mathrm{s,i}}$	Eulerian sound speed at density ρ_i
ρ_0	Initial density in Lagrangian coordinates
Radiative Transfer Model Variables (§2.5.4)	
T_{a}	Apparent post-shock temperature temperature
$Pr(x)$	Probability of a photon being absorbed at position x within a slice of thickness dx
α	Average absorption coefficient
L_{MFP}	Mean free path of a photon interacting with a liquid droplet
α_{vap}	Absorption coefficient of the vapor phase
D_0	Liquid droplet diameter
x_{fs}	Eulerian position of free surface of releasing fluid
$x(T_{\mathrm{a}})$	Eulerian position of the emitting region within the liquid–vapor mixture

previously measured by Hicks et al. (2006). The solid–solid and solid–melt phase boundaries are based upon experimental data (Akins and Ahrens, 2002a; Presnall, 1995, and references therein). The liquid–vapor curve is from the M-ANEOS model for silica by Melosh (2007).

M-ANEOS is an equation of state formulation that is widely used in the planetary science community for modeling impact events. M-ANEOS (Melosh, 2007) is an updated version of the ANEOS model (Thompson and Lausen, 1972) that allows for the correct degrees of freedom available to

molecular gases (vibrational, rotational, dissociation, ionization). In developing the M-ANEOS model for silica, Melosh (2007) constrained the liquid–vapor region by the thermodynamic data for the boiling point (Schick, 1960) and the triple point (Mysen and Kushiro, 1988). The silica M-ANEOS model is currently lacking in some areas: there is no melting transition and molecular dissociation is only included in the gas phase. Yet, with only one phase transition (quartz to stishovite), the M-ANEOS model generally reproduces the silica shock velocity–particle velocity relation, hereafter referred to as U_{s}–u_{p}, which ensures the internal energy gain along the Hugoniot is approximately correct. However, the temperatures along the M-ANEOS model Hugoniot are consistently much hotter than the Hicks et al. (2006) quartz shock temperature measurements, which were not available at the time of the model's development.

The irreversible work from shock compression can be dissipated as either temperature or entropy (the $-TS$ term in the free energy functions (e.g. Kittel and Kroemer, 1980)), where the balance between temperature and entropy depends upon the heat capacity. Hicks et al. (2006) found that the heat capacity in the fluid region on the quartz Hugoniot significantly exceeds the Dulong–Petit limit of $3k_B$ per atom, which is the assumed limit in the M-ANEOS model. As a result, more irreversible work is partitioned to entropy than predicted by the M-ANEOS model.

Although shock compression is irreversible, decompression from the shocked state is generally an isentropic process. Decompression will not be perfectly isentropic if the decompressing parcel of material becomes metastable upon going through a phase transition, has significant strength or viscosity, or conducts heat; however, these effects are generally negligible with respect to the entropy along the Hugoniot and can be neglected here. Consequently, for a parcel of material, the entropy in the decompressed state is effectively the same as the entropy in the shocked state. Using the $P-T$ phase diagram (Figure 2.1), one needs an accurate model isentrope to predict the final state(s) of a material after release from the shocked state. However, by using an entropy-

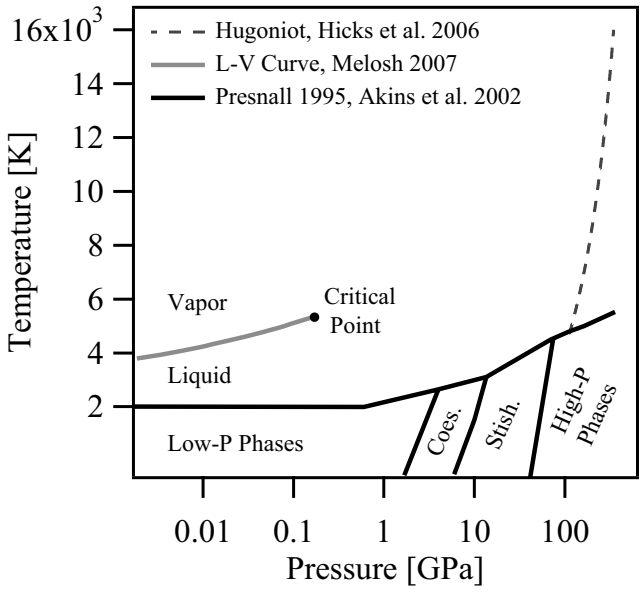

Figure 2.1: Partial phase diagram for silica. Material isentropically decompressing from the fluid region on the quartz Hugoniot (dashed line, Hicks et al., 2006) will intersect the liquid–vapor (L-V) phase boundary (gray line, Melosh, 2007). The triple point is 1920±50 K and ∼2 Pa (Mysen and Kushiro, 1988).

temperature ($S - T$) diagram, such as in Figure 2.2, one need only know the entropy along the Hugoniot and the entropies of the relevant phases at the final pressure in order to determine the final state(s). This realization is the basis for the "Entropy Method" (Ahrens and O'Keefe, 1972; Kieffer and Delany, 1979), which has been used in several studies to predict the amount of melting and vaporization that occurs during planetary impact events (e.g., Artemieva and Lunine, 2003; Kraus et al., 2011; Pierazzo et al., 1997; Stewart et al., 2008; Wünnemann et al., 2008). Next, we present new calculations for reference entropy states for silica.

2.2.1 Entropy on the Quartz Hugoniot

From the first law of thermodynamics, the change in entropy (dS) along any thermodynamic path is determined by the change in internal energy (dE) and specific volume (dV) at a given pressure (P) and temperature (T):

$$dS = \frac{dE}{T} + \frac{PdV}{T}. \tag{2.1}$$

Although the Hugoniot is not the thermodynamic path taken by a material during the shock compression process, it is a valid thermodynamic path through the equation of state surface. On the quartz Hugoniot, the pressure, volume, and internal energy are known up to 1600 GPa with high accuracy (e.g., a few percent) (Knudson and Desjarlais, 2009), and the shock temperature is measured to 800 GPa with an uncertainty of less than 8% (Hicks et al., 2006). The change in entropy along the Hugoniot may be obtained simply by integrating Equation 2.1; however, the shock temperatures in the solid phases are not sufficiently well-known to determine the absolute entropy by integrating from the standard state. Consequently, we used another thermodynamic path to determine the entropy at an alternate reference state: the point where the quartz Hugoniot enters the fluid region.

The path to the fluid reference state on the quartz Hugoniot (state D in Tables 2.1 and 2.2) was calculated starting with stishovite in the standard state (T_{00}=298 K, ρ_{00}=4.209 g cm^{-3} (Weidner et al., 1982), S_{00}=409 J kg^{-1} K^{-1} (Mao et al., 2001; Saxena, 1996)) via three intermediate states (A-C), where S_{00} is defined relative to the perfect crystal at T=0 K. Next, we present a calculation of the specific volume of the solid on the stishovite melting curve at the point crossed by the fused quartz Hugoniot.

The fused quartz Hugoniot leaves the stishovite melting curve at 70 GPa and 4500 K (Luo and Ahrens, 2004). The volume of stishovite at 70 GPa and $\sim$ 4100 K is 2.108(24) $\times$ 10^{-5} m^3 kg^{-1} (Akins and Ahrens, 2002a; Kraus et al., 2012b), which was calculated from the quartz Hugoniot in the stishovite phase (U_s=944(308)+1.99(0.10)u_p [m s^{-1}], covariance=-30.69, fit to data presented in Marsh (1980) and Trunin et al. (2001)). Then, a thermal correction was applied to determine

Table 2.2: Summary of thermodynamic states calculated to obtain the entropy at the intersection of the quartz Hugoniot and the melting curve.

State	Specific Volume [10^{-4} m^3 kg $^{-1}$]	Specific Entropy [J kg^{-1} K^{-1}]	Description
00	2.331	409 ± 20	Stishovite at STP
A	2.125 ± 0.027	409 ± 20	Stishovite on the principal isentrope at V_B (334 K)
B	2.125 ± 0.027	3567 ± 54	Stishovite on the melting curve at 4500 K
C	2.153 ± 0.048	3820 ± 160	Fluid SiO_2 at fused quartz Hugoniot and melting curve
D	1.983 ± 0.029	3820 ± 168	Fluid SiO_2 at quartz Hugoniot and melting curve

the specific volume of solid stishovite at 70 GPa and 4500 K: V_A=2.125(27)$\times 10^{-4}$ m^3 kg. We used a coefficient of thermal expansion of α=2×10^{-5} K^{-1}, which is extrapolated from the value calculated by Luo et al. (2002) at 120 GPa to 70 GPa by assuming the product of the coefficient of thermal expansion and isothermal compressibility (Panero et al., 2003) is a constant (Birch, 1952). For a discussion on the validity of this approximation see Anderson (1995).

The temperature on the stishovite principal isentrope at V_A was calculated via the thermodynamic relation,

$$T_A = T_{00} \exp\left[-\int_{V_{00}}^{V_A} \frac{\gamma}{V} dV \right], \tag{2.2}$$

where γ is the thermodynamic Grüneisen parameter. For the range of temperatures and volumes considered here, we assumed the Grüneisen parameter to be independent of temperature and follow an empirical function of volume,

$$\gamma = \gamma_0 \left(\frac{V}{V_{00}} \right)^q, \tag{2.3}$$

where γ_0 is the Grüneisen parameter at $V_{00} = 1/\rho_{00}$ and q is a fitting parameter. For stishovite, γ_0=1.35 (Watanabe, 1982) and $q = 2.6 \pm 0.2$ (Luo et al., 2002). Then, T_A=334±4 K at V_A.

Next, we determine the entropy change upon isochorically heating stishovite from T_A=334 K to

the melting curve, T_B=4500 K, using the experimentally-validated Kieffer model (Kieffer, 1979). For the thermal properties of silicates, the Kieffer model is preferred over the Debye model as it includes the anisotropy of elastic constants, the dispersion of acoustic waves toward Brillouin zone boundaries, and optical frequencies that are much greater than the predicted Debye frequency. We also corrected for the volume dependence of the mode frequencies (Kieffer, 1982) and, at high temperatures, for the anharmonicity of the vibrational modes (Gillet et al., 1990). As there is insufficient spectroscopic data to constrain the anharmonicity of the individual modes, we used a shock temperature measurement on fused quartz in the stishovite phase (Boslough, 1988; Lyzenga et al., 1983) to determine an average linear anharmonic correction at high temperatures. The overall effect of the anharmonic contribution is to increase the heat capacity of silica beyond the Dulong–Petit limit; for example, we find the heat capacity of stishovite at 70 GPa and 4500 K is $3.65(0.15)k_{\mathrm{B}}$ per atom. Details of the Kieffer model parameters and the anharmonic correction are presented in the online Auxiliary Materials. The entropy increase upon isochorically heating silica from the principal isentrope at T_A=334 K to the melting curve at T_B=4500 K is $\Delta \mathrm{S}_{AB}$=3158±50 J kg^{-1} K^{-1}.

The Clausius-Clapeyron relation was used to solve for the entropy of melting stishovite at 70 GPa and 4500 K. The slope of the melting curve is 10.8 K GPa^{-1} at 70 GPa (Luo and Ahrens, 2004). To determine the specific volume of liquid silica at 70 GPa and 4500 K, we compiled and fit the Hugoniot data for fused silica at pressures of 70 GPa to 1000 GPa (Brygoo et al., 2007; Lyzenga et al., 1983; Marsh, 1980),

$$U_{\mathrm{S}} = -295.7 + 2.139u_{\mathrm{p}} - 4.0117 \times 10^{-5} u_{\mathrm{p}}^2 \ [\mathrm{m\ s^{-1}}], \tag{2.4}$$

where the covariance matrix is

$$\begin{pmatrix} 402641 & -113.077 & 0.0052574 \\ -113.077 & 0.031936 & -1.49891 \times 10^{-6} \\ 0.0052574 & -1.49891 \times 10^{-6} & 7.26006 \times 10^{-11} \end{pmatrix}. \quad (2.5)$$

The volume of liquid silica on the fused quartz Hugoniot at 70 GPa is V_C=2.153(48)$\times 10^{-4}$ m^3 kg $^{-1}$, consequently the relative volume increase upon melting stishovite at 70 GPa and 4500 K is given by $(V_C - V_B)/V_B$=1.3%. From the Clausius-Clapeyron relation, the entropy of melting is then ΔS_{BC}=253 J kg^{-1} K^{-1}, which is within 15% of the empirical Rln(2) rule for the entropy of melting observed in many metals and silicates (Luo and Ahrens, 2004; Wallace, 2002). As the uncertainties in the volumes are on the order of the volume change of melting, formal error propagation would lead to what we consider to be an unreasonably large error in the entropy of melting. The systematics of melting constitute a constraint on the uncertainty that is not captured by formal error propagation. For the purpose of further error propagation, we assign an illustrative uncertainty in the entropy of melting stishovite at 4500 K to be 150 J kg^{-1} K^{-1}, which is very likely a conservative estimate given the previously mentioned systematics in the entropy of melting.

Next, we determine the point where the fluid isentrope from the base of the fluid region on the fused quartz Hugoniot (state C) intersects the quartz Hugoniot using Equation 2.2. The dominant source of uncertainty in the intersecting point is in the Grüneisen parameter of fluid silica. There are a number of sound velocity measurements in the fluid phase; using the Hugoniots for fused quartz (Eqn. 2.4) and quartz (Knudson and Desjarlais, 2009), we have reanalyzed and tabulated the corresponding Grüneisen parameters in Table S.4 of the Auxiliary Material. As there is a great deal of scatter in the Grüneisen parameters over such a small range of volumes, we used the weighted average, $\gamma = 0.7 \pm 0.3$. With the experimental average of the Grüneisen parameter, we found the isentrope from state C intersects the quartz Hugoniot at T_D=4790±140 K, which is

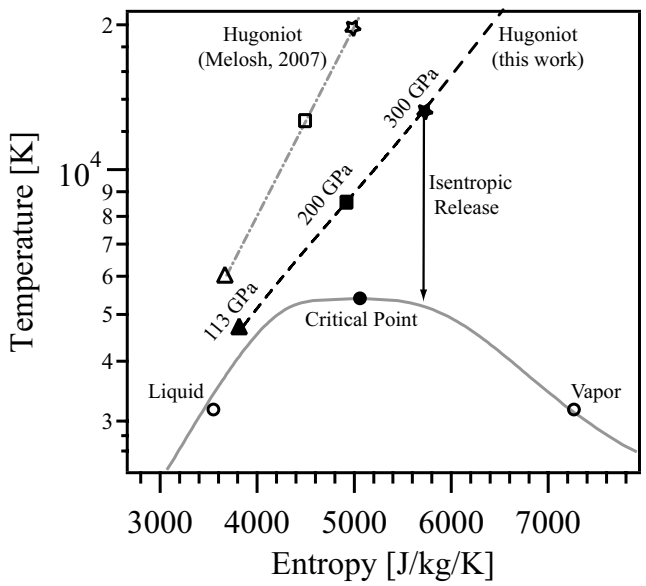

Figure 2.2: Entropies and temperatures on the silica liquid–vapor phase boundary and quartz shock Hugoniot. Revised entropies on the quartz Hugoniot from this work (dashed black line) are significantly higher than the M-ANEOS model Hugoniot (dot-dash gray line, Melosh, 2007). Symbols contrast shock pressures of 113 (where the Hugoniot enters the liquid field), 200, and 300 GPa on the two Hugoniots. Example release path from 300 GPa to the M-ANEOS liquid–vapor phase boundary (gray line, Melosh, 2007) denoted by vertical arrow. Filled circle is the M-ANEOS critical point; open circles are the revised entropies of the liquid and the vapor phases at the boiling point (3177 K at 10^5 Pa) from this work, where the symbol size represents the uncertainty in the liquid entropy.

very close to the melting temperature of 4800 K at 113 GPa (Luo et al., 2004). Hence, this fluid isentrope intersects at our desired reference state (D), the base of the fluid region on the quartz Hugoniot.

In summary, the entropy where the fused quartz Hugoniot leaves the melting curve, S_C, is the sum of the initial entropy of stishovite, the entropy upon heating stishovite from the isentrope to the melting curve, ΔS_{AB}, and the entropy of melting, ΔS_{BC}:

$$S_C = S_{00} + \Delta S_{AB} + \Delta S_{BC} = 3820 \pm 160 \text{ [J kg}^{-1} \text{ K}^{-1}] \tag{2.6}$$

With our estimate of the Grüneisen parameter, the entropy at the base of fluid region on the

quartz Hugoniot is the same as at the base of the fluid region on the fused quartz Hugoniot except with a slightly higher uncertainty: S_D=3820±168 J kg^{-1} K^{-1}. The entropy on the quartz Hugoniot in the fluid region, as presented in Figure 2.2, is the sum of reference state S_D and the entropy change along the Hugoniot, determined using Equation 2.1 and data from Knudson and Desjarlais (2009) and Hicks et al. (2006). The intermediate states calculated to determine the absolute entropy of the fluid region on the quartz Hugoniot are given in Table 2.2. The absolute entropy as a function of pressure along the quartz Hugoniot from 113 to 800 GPa is given by,

$$S_{H,Qtz} = 1793 + 22.40P - 0.0426P^2 + 4.319 \times 10^{-5}P^3 - 1.742 \times 10^{-8}P^4 \tag{2.7}$$

where P is the pressure along the Hugoniot in GPa, and $S_{H,Qtz}$ is the entropy along the quartz Hugoniot in J kg^{-1} K^{-1}. The absolute uncertainty in the entropy along the quartz Hugoniot is given by,

$$\delta_{S_{H,Qtz}} = 127.3 + 0.328P - 0.000193P^2. \tag{2.8}$$

The entropy on the fused quartz Hugoniot in the fluid region is the sum of reference state S_C and the entropy change along the fused quartz Hugoniot, determined using Equation 2.1 and data from Lyzenga et al. (1983) and Boslough (1988). The entropy as a function of pressure along the fused quartz Hugoniot from 70 to 110 GPa is given by,

$$S_{H,FQ} = 2294 + 26.82P - 0.0723P^2 \tag{2.9}$$

For this relatively small pressure range, the uncertainty in the entropy along the fused quartz Hugoniot is approximately equal to the uncertainty in the entropy at the base of the fused quartz

Hugoniot (160 J kg^{-1} K^{-1}).

Next, we present a calculation of the reference entropy states at ambient pressure.

2.2.2 Boiling Point Entropy of Silica

Although slightly arbitrary for all impacts except on Earth, the entropies of the liquid and vapor phases at the 10^5 Pa boiling point are often used to calculate the criteria for incipient and complete vaporization upon release from shock. As there are no direct measurements of the boiling point of silica at 10^5 Pa, the value must be calculated using thermodynamic data that is extrapolated from much lower temperatures. Previous calculations of the boiling point of silica used outdated thermodynamic data for the liquid phase; for example, the widely cited JANAF thermochemical tables (Chase, 1998) uses heat capacity data for silica liquid from Wietzel (1921).

Here, we calculated the boiling point for silica following a similar method to that of Schick (1960). In our analysis of chemical equilibrium, we included the reactions:

$$\mathrm{SiO_2^{(l)}} \rightleftharpoons \mathrm{SiO^{(g)}} + \frac{1}{2}\mathrm{O_2^{(g)}} \tag{2.10}$$

$$\frac{1}{2}\mathrm{O_2^{(g)}} \rightleftharpoons \mathrm{O^{(g)}} \tag{2.11}$$

$$\mathrm{SiO_2^{(l)}} \rightleftharpoons \mathrm{SiO_2^{(g)}}. \tag{2.12}$$

The energy cost for creating atomic silicon is too high for the partial pressure of silicon to effect the calculation of the boiling point, and the Si_2O_2 dimer is unstable at high temperatures (Schick, 1960). We used enthalpy data for liquid silica from Richet et al. (1982) and Tarasov et al. (1973), which extend up to 2400 K. Thermodynamic data for the vapor species were obtained from the JANAF thermochemical tables (Chase, 1998).

Table 2.3: Composition of silica vapor at the boiling point: 3177 K and 10^5 Pa. Uncertainties in the specific entropies, taken from Schick (1960), are estimates and are not experimentally determined.

Vapor Species	Partial Pressure [10^5 Pa]	Specific Entropy [J kg^{-1} K^{-1}]
SiO	0.587	6660 ± 9
O_2	0.253	8960 ± 8
O	0.080	13182 ± 12
SiO_2	0.080	6023 ± 33

The partial pressures of the vapor species considered in the reactions described in Equations A.27–A.29 sum to 10^5 Pa at T=3177±115 K. This boiling point is approximately 100 K higher than the analysis by Schick (1960) and only 20 K higher than the M-ANEOS result of 3157 K (Melosh, 2007) (shown in Figure 2.2). The physical reason for the higher boiling point is related to a higher average heat capacity and hence entropy in the liquid than previously thought, causing liquid silica to be more stable at higher temperatures. The temperature difference between this boiling point calculation and those calculations that used the JANAF thermochemical table (Chase, 1998) is not more pronounced is because the heat capacity data for liquid silica (Wietzel, 1921), cited in the JANAF table, is erroneously high. A discussion on the heat capacity of liquid silica is presented in the online Auxiliary Materials.

The partial pressures and specific entropies for the vapor species are given in Table 2.3. At 3177 K, the entropy of the vapor is 7254±8 J kg^{-1} K^{-1}, and the entropy of SiO_2 liquid is 3552±70 J kg^{-1} K^{-1}. Thus, the enthalpy of vaporization is 11770±950 kJ kg^{-1}. A detailed description of the boiling point calculation is presented in the online Auxiliary Materials.

With the new reference values for the entropy along the Hugoniot and the entropies of the liquid and vapor in the released state, the shock states are more accurately linked to final release states at 10^5 Pa (Figure 2.2). However, there are insufficient thermodynamic data to calculate the liquid–vapor boundary, using the free energy minimization described above, at pressures other than 10^5

Pa. Next, we present shock-and-release experiments to probe states along the liquid–vapor curve at pressures and temperatures up to the critical point.

2.3 Shock-and-Release Experiments

To reach the phase space near the liquid–vapor curve of silica, samples of c-cut α-quartz (initial density 2.65 g cm^{-1}) were shocked to a high–pressure fluid state. Once the shock wave reaches the downrange free surface, a zero pressure boundary condition, the shock wave is reflected as a centered rarefaction wave, which decompresses the fluid. The experiments were performed using the Janus laser at the Jupiter Laser Facility of Lawrence Livermore National Laboratory and utilized the line-imaging velocity interferometer systems for any reflector (VISAR, Barker and Hollenbach, 1972; Celliers et al., 1998) and the streaked optical pyrometer (SOP, Spaulding et al., 2007). Shock pressures and temperatures up to ∼300 GPa and ∼15,000 K were generated by direct laser ablation.

The Janus laser is a two-beam Nd:glass laser capable of delivering 350 Joules per beam at the frequency doubled wavelength of 527 nm for pulse lengths of 2 to 10 ns. The laser beams were focused onto the target and a random phase plate was used to create an ∼700 μm diameter spot. A randomizing phase plate maps any low-frequency spatial perturbations in the beam intensity into a uniform high-frequency speckle pattern. The intensity of the laser pulse was temporally shaped to generate a quasi-steady shock in the target. We refer the reader to Swift et al. (2004) for a general discussion of laser-driven shock compression.

The ablation surface of each quartz sample was coated with 100 nm of aluminum to protect downrange optical components from laser light, which was only necessary prior to the silica sample becoming opaque due to plasma generation at the ablation surface. The dimensions of the target, 80 to 120 μm thick and 3 mm diameter, were chosen to maximize the area under uniaxial strain and the thickness of the spall layer that formed when the rarefaction wave from the downrange

free surface interacted with the rarefaction wave created at the ablation surface. Hafnium oxide was used as an anti-reflective coating on the downrange free surface on most targets to decrease unwanted reflections in the VISAR diagnostic. However, post-shock temperature measurements were not made during experiments with anti-reflective coated samples so as to avoid any thermal contamination from the shocked coating material.

For shock pressures above the melting curve, the shock wave was partially reflecting to the VISAR laser wavelength (532 nm) (Hicks et al., 2006) and can be used as the reflecting surface for interferometric velocimetry. Two line-imaging VISAR's, configured with different velocity sensitivites, were used in each experiment; the uncertainties in the absolute magnitude of the shock velocity measurement were approximately 0.35 and 1.14 km s^{-1}, respectively. The VISAR signals were recorded on streak cameras with temporal resolution of $\sim$ 300 ps and total duration of 50 ns. An example line-VISAR image is shown in Figure 2.3. A timing fiducial was used to temporally synchronize the streak cameras.

The known Hugoniot of quartz (Knudson and Desjarlais, 2009) was used to determine the shock pressure from the measured shock velocity (in km s^{-1}):

$$U_s = 6.26\,(0.35) + 1.2\,(0.02)\,u_p - 2.56\,(0.15)\,u_p e^{-0.37(0.02)u_p}. \tag{2.13}$$

For experiments where the reflectivity at the free surface was on the order of the reflectivity of the shock front, a superposition of fringes was detected on the line-VISAR system. One set of fringes originated from the reflection off the moving shock front (the signal) and the other from the reflection off the stationary interface between quartz and vacuum (called a ghost fringe). The method for subtracting the ghost fringes is described in supplemental material of Celliers et al. (2010). In our analysis, we used the reflectivity and temperature of shocked quartz as a function

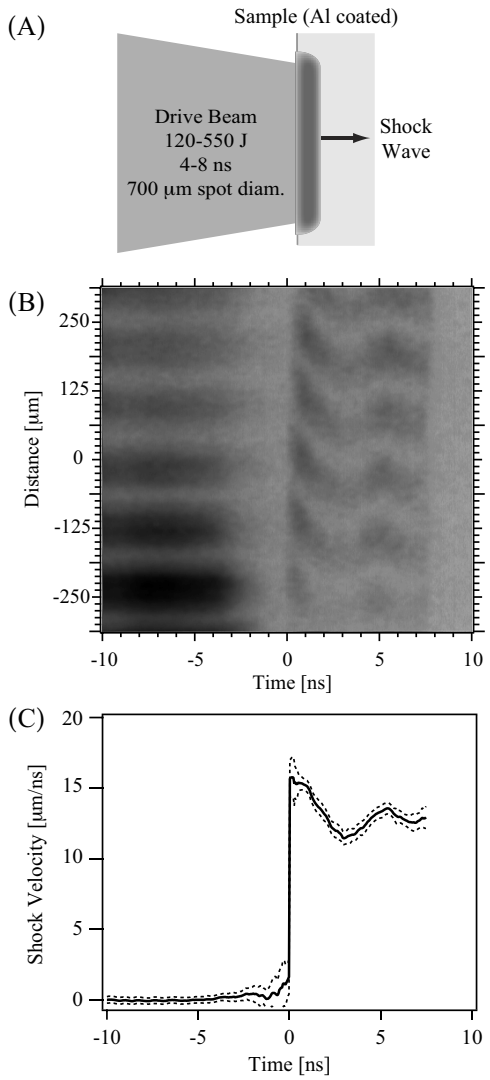

Figure 2.3: Overview of silica shock-and-release experiments. (A) Schematic of quasi-steady shock wave generation in quartz by a shaped laser pulse (not to scale). (B) Example line-VISAR streak camera image from experiment e100723s2. About 2 ns before the shock front becomes partially reflecting in the quartz sample (at time zero), the signal intensity decreases significantly due to a ∼Joule pre-pulse from the laser that ablates the 100-nm Al coating. VISAR fringes are lost upon shock breakout at the downrange free surface (7.5 ns). (C) Shock velocity determined from VISAR fringe shift in (B) with uncertainties given by the dotted lines.

of shock velocity. The shock front reflectivity measurements from Hicks et al. (2006) was revised in Celliers et al. (2010) (supplemental materials) to

$$R' = 0.006\,(0.0014) + 0.39\,(0.05)\left(\frac{U_s^{9.73(0.68)}}{U_s^{9.73(0.68)} + 16.2\,(0.2)^{9.73(0.68)}}\right), \tag{2.14}$$

which is valid for shock velocities from 10 to 32 km s^{-1}. The corresponding shock temperature (in K) $T_{H,Qtz}$ and temperature uncertainty $\delta T_{H,Qtz}$ along the quartz Hugoniot are given by

$$T_{H,Qtz} = -9350 + 2803U_s - 238U_s^2 + 10.62U_s^3, \tag{2.15}$$

$$\delta T_{H,Qtz} = -880 + 112U_s, \tag{2.16}$$

which are fits to the shock temperature measurements by Hicks et al. (2006) corrected for the revised reflectivity from Celliers et al. (2010) and are valid for shock velocities from 10 to 22 km s^{-1}.

2.3.1 Post-Shock Temperature Measurements

As quartz is transparent to visible radiation, thermal radiation emitted from the shock front was recorded as a function of time and space, along a line across the target, using the streaked optical pyrometer. Due to the expected low emission intensity in the post-shock state, the streaked optical pyrometer was spectrally integrated from 450 to ∼800 nm. As in previous pyrometry experiments (Spaulding, 2010; Spaulding et al., 2007), calibration of the SOP was made relative to the known shock temperature and reflectivity in quartz (Equations 2.14 and 2.15) (Celliers et al., 2010; Hicks et al., 2006). The uncertainty in the calibration is approximately 11% over the range of temperatures considered here; a complete description of the calibration technique is presented in the online Auxiliary Materials.

Upon breakout of the shock wave at the free surface, the radiating temperature of the sample should decrease almost instantaneously because of adiabatic cooling of the material. Transport of heat from the shocked material to the released material has been shown to keep released material from following a purely isentropic path in some experiments (Celliers and Ng, 1993). However, as the expected ionization state in the decompressed silica is low, thermal conduction was likely insignificant for the length scale (and hence time scale) of interest, we assumed isentropic decompression.

After shock breakout, the SOP signal intensity decays exponentially to a constant nonzero value with a time constant of $\sim$5 ns; example data are shown in Figure 2.4. The dominant source of the exponential, rather than stepwise, decay profile is due to convolution of the thermal emission in the shocked state by the camera-specific point spread function. To avoid contamination from the thermal emission in the shock state, we determined the post-shock thermal emission by averaging over a 10 ns period in the SOP intensity from at least 8 ns after shock breakout (the delay varied slightly depending on the intensity of the shock wave). The time period of 10 ns was chosen for consistency, and varying the period does not effect the measurement significantly as the post-shock thermal emission is approximately constant on these time scales. The reported uncertainties in the post-shock intensity were determined from both the spatial and slight temporal variation in thermal emission.

In calculating an apparent temperature of the post-shock state T_{a}, we made the approximation that the decompressed material radiated as a blackbody. We expect this approximation to be valid based upon two lines of reasoning. First, spectrally resolved post-shock thermal emission measurements on silica shocked up to 130 GPa are well fit by a blackbody function (Boslough, 1988). Similarly, in our experiments, we observed negligible reflected light from post-shock states with the VISAR diagnostic.

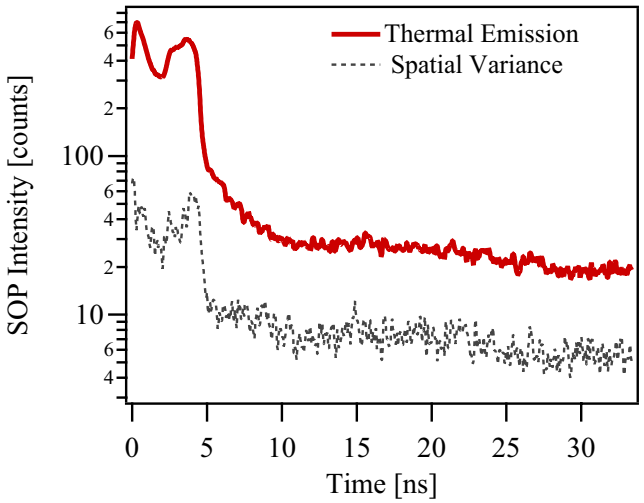

Figure 2.4: Example thermal emission profile from a silica shock-and-release experiment. The shock enters the sample at 0 ns and reaches the free surface at ∼5 ns. The streaked optical pyrometer intensity (red line) records a nearly constant post-shock thermal emission from 10 to 20 ns. The exponential decay in intensity from 5 to 10 ns, a result of the camera point spread function, is not included in the post-shock temperature measurement. The signal mean intensity and spatial variation are derived from a 100-μm line across the sample (experiment e100728s1).

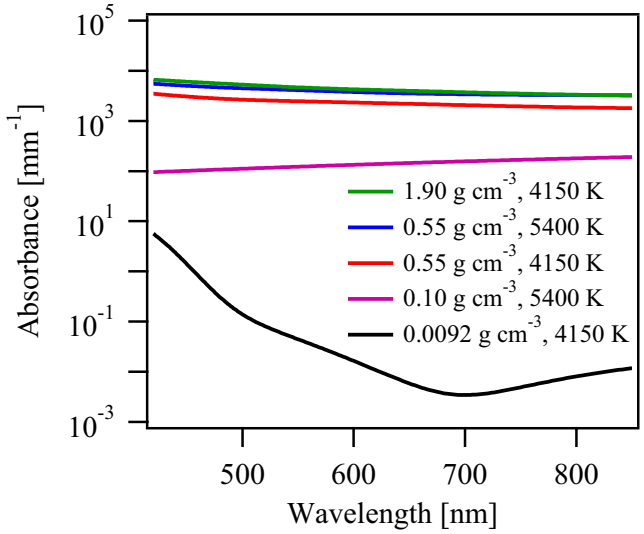

Figure 2.5: Absorption coefficients for SiO_2 liquid and vapor, calculated using the VASP FPMD–DFT code, for the wavelength range of the streaked optical pyrometer (450 to 800 nm).

Second, we calculated absorption coefficients in the visible range for SiO_2 liquid and vapor using first principles molecular dynamics (FPMD) simulations based on density functional theory (DFT) using the Vienna Ab initio Simulation Package (VASP) (Blochl, 1994). The results are shown in Figure 2.5, for a range of states around the critical point estimate from M-ANEOS of 5398 K and 0.549 g cm^{-3}. The calculated absorption coefficients for densities of 0.55 g cm^{-3} and greater are weakly dependent on wavelength and suggest an optical depth of less than about 0.5 μm. If phase separation occurred on the time scale of the experiment and the low-density vapor expanded ahead of the decompressed liquid, then the optical depth of the leading vapor would be negligible until a layer greater than about 200 μm formed. Below (§2.3.2), we discuss the results from a series of stagnation experiments that do not show significant fast-moving vapor ahead of the liquid. Thus, we infer that the vapor did not completely separate on the time scale of the experiments, and consequently, the decompressing vapor did not shield emission from the liquid–vapor interface. To first order, the problem can be simplified to emission from an opaque interface, where radiation is emitted from the interface between liquid and vapor. A more detailed analysis of the radiative transfer problem is presented in §2.5.4.

Post-shock SOP counts and calibrated apparent post-shock temperatures are presented in Table 2.4. Post-shock temperatures are associated with shock states based upon the shock velocity immediately prior to shock breakout at the free surface. For the lowest pressure experiment (e100728s4), the intensity of the free surface reflection was significantly greater than the shock wave VISAR signal, preventing a simultaneous shock velocity measurement. In this case, the shock state was determined from the shock temperature prior to breakout using the calibration developed from the higher-pressure experiments. Because the signal was expected to be low for this experiment, the gain on the SOP was increased from 30 to 40 and the calibration was adjusted accordingly.

Below, in §2.5, we discuss the kinetics of phase separation and the radiative transfer through

Table 2.4: Apparent post-shock temperature of silica from laser and gas-gun shock-and-release experiments. $I_{\rm cor}$ – streaked optical pyrometer signal corrected for non-zero reflectivity (see online Auxiliary Materials). The two uncertainties in the entropy are the random uncertainty in the shock pressure and the systematic uncertainty in the calculation of entropy along the Hugoniot, respectively. The gas-gun post-shock temperatures by Boslough (1988) are from quartz and fused quartz (FQ) shocked to the fluid region.

Experiment No.	$I_{\rm cor}$	T_a [K]	Shock Pressure [GPa]	Entropy‡ [J kg^{-1} K^{-1}]
e100728s1	23.6 ± 7	4961 ± 559	318 ± 18	$5798 \pm (117, 206)$
e100726s5	23.1 ± 6	4939 ± 540	307 ± 17	$5728 \pm (114, 206)$
e100726s2	20.5 ± 6	4823 ± 531	277 ± 14	$5525 \pm (104, 196)$
e100723s3	18.2 ± 6	4717 ± 527	244 ± 12	$5267 \pm (102, 191)$
e100722s4	13.8 ± 5	4470 ± 536	172 ± 10	$4584 \pm (119, 175)$
e100728s4	5.5 ± 3	3756 ± 519	136 ± 8	$4130 \pm (108, 169)$
Boslough, 1988†	–	4150 ± 20	126.6 ± 2.2	$4000 \pm (32, 168)$
Boslough, 1988	–	3890 ± 110	116.5 ± 2	$3848 \pm (32, 168)$
Boslough, 1988 (FQ)	–	3910 ± 50	73.3 ± 1.3	$3874 \pm (31, 160)$

the decompressing silica in more detail.

2.3.2 Stagnation Experiments and Post-Shock Density

To estimate the average density of the decompressing material, we performed a series of stagnation measurements on quartz shocked to pressures of about 200 and 340 GPa. Upon breakout of the shock wave at the free surface, the material uniaxially expanded across a gap of known distance and stagnated against an aluminized LiF window. The velocity at the interface between the stagnating silica and the LiF window was measured using the line-VISARs. These experiments were qualitatively similar to the gas-gun experiments by Asay and Trucano (1990), Chhabildas et al. (2006), and Alexander et al. (2010). The stagnation experiments complement the post-shock temperature experiments by probing the density gradient in the expanding material, which is important for interpreting the source of the thermal emission (see §2.5.4).

For each target, a spacer of known thickness (approximately 50, 100, and 200 μm) separated the downrange free surface of the quartz from a 1-mm thick LiF window. A schematic of the target design is presented in Figure 2.6. A 5-μm layer of aluminum coated the uprange LiF surface,

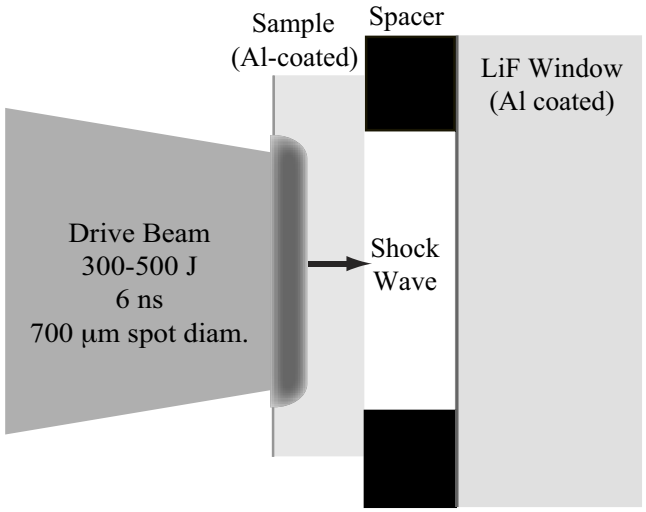

Figure 2.6: Schematic target design to infer bulk density after shock-and-release of silica (not to scale). A quasi-steady shock wave is generated by laser ablation of the aluminized sample. Upon shock breakout at the downrange free surface, the released material propagates across the gap and stagnates against an aluminized LiF window. The particle velocity in the LiF and time of impact were measured for three gap distances after 199 and 338 GPa shocks in the quartz sample.

forming both a reflecting interface for the VISARs and a thermal barrier as the transparency of LiF is strongly temperature dependent. Based upon two-dimensional hydrodynamic simulations using the CTH code (McGlaun et al., 1990), for these gap distances, the released silica maintains conditions of uniaxial strain over the duration of the stagnation measurement.

Because the aluminized LiF prevents direct observation of the shock in the quartz sample during the stagnation experiments, the shock pressures were determined by a separate series of experiments where the shock velocity was directly observed for varying laser pulse intensities. In combination with radiation hydrodynamics simulations using the Hyades code (Larsen and Lane, 2002), we derived a scaling law for the ablation pressure as a function of laser intensity for direct ablation of quartz with a 100-nm aluminum coating: $P_{\mathrm{s}}{=}5I_{\mathrm{L}}^{0.78}$, where the ablation pressure P_{s} is in GPa and the laser intensity I_{L} is in PW m^{-2}. The shock pressure of each stagnation experiment was derived from the measured laser intensities; each set of experiments should differ by less than 10%, which is similar to the magnitude of variation in the quasi-steady shock pressure during a single

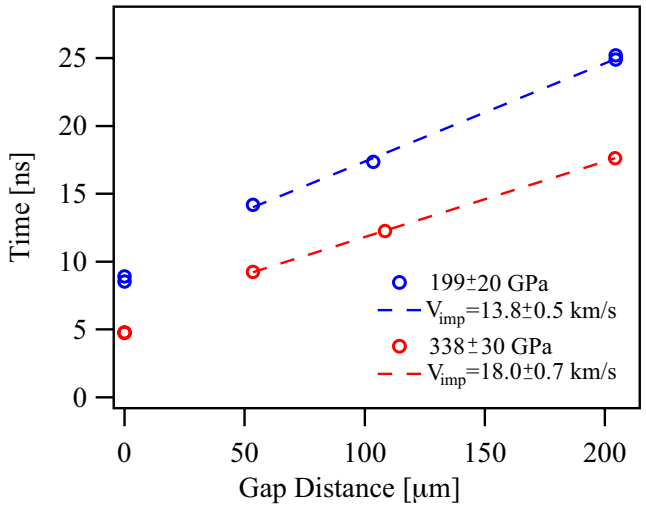

Figure 2.7: Velocity of decompressing silica derived from stagnation experiments. Times of impact onto LiF window, relative to the laser drive pulse, are corrected for the shock transit through the 5-μm Al coating. Uncertainties are on the order of the symbol size. The mean impact velocity of decompressing silica onto the LiF window, $V_{\rm imp}$, is determined from weighted linear least squares fits (dashed lines) through each set of transit data, neglecting time of shock breakout due to a systematic offset between measurement techniques. In the 338-GPa data set, two experiments were performed at the $\sim$200 μm gap distance.

experiment.

The average shock velocities experienced by the silica spall layer were $12.1\pm(0.35, 0.45)$ and $15.3\pm(0.20, 0.45)$ km s^{-1}, respectively. The corresponding shock pressures are $199\pm(14, 17)$ and $338\pm(10, 24)$ GPa, where the first uncertainty is the variation about the mean and the second term is the random uncertainty. Figure 2.7 presents the time at which the shock breaks out of the quartz sample and the time at which the decompressing silica impacts the LiF window for different gap thicknesses.

The mean impact velocity $V_{\rm imp}$ of the silica onto the LiF window was determined from a linear fit to the the transit time versus gap distance. The time of shock breakout was determined by the midpoint in the loss of reflectivity, whereas the time the stagnating silica impacts the LiF window was taken from the midpoint in the rise of the interface velocity corrected for the transit time through the aluminum coating. As there appears to be a systematic offset in the different time

measurements, the time of shock breakout was not included in the linear fit.

Example stagnation velocity profiles at the silica–LiF interface are presented in Figure 2.8. The VISAR fringe constant for the LiF window is 8.311 km s^{-1}, and the random uncertainty in the fringe position results in a particle velocity uncertainty of approximately 0.4 km s^{-1}. With increasing gap thickness, the rise time of the interface velocity increases because the density gradient decreases with expansion distance. The observed nanosecond precursor signal could represent vapor a few tens of microns ahead of the main density gradient, which would not be sufficient to absorb significant radiation from the liquid–vapor mixture.

To obtain the average density in the expanding silica from the interface velocity measurements, we analyzed the stagnation data in a manner similar to a reverse impact experiment. By assuming the density of the spalled silica layer is constant, the density of the spall layer just prior to impact can be determined using the impedance matching method,

$$\rho_{0,\mathrm{F}} = \frac{P_{\mathrm{LiF}}}{U_{\mathrm{S,SF}} u_{\mathrm{P,SF}}} \tag{2.17}$$

where $\rho_{0,\mathrm{F}}$ is the average density in the decompressing fluid immediately prior to impact, P_{LiF} is the shock pressure induced in the LiF window, $u_{\mathrm{P,SF}}$ is the particle velocity in the re-shocked silica fluid, and $U_{\mathrm{S,SF}}$ is the shock velocity in the re-shocked silica fluid. The shock pressure in the LiF was determined from the measured particle velocity and the known LiF Hugoniot (Ahrens and Johnson, 1995a). The particle velocity in the re-shocked silica fluid was equal to the impact velocity V_{imp} less the measured interface velocity u_{int}.

The shock velocity in the re-shocked silica fluid was not observed. As the Hugoniot of silicate fluids starting near the critical point is not known, we needed to make a prediction about the $U_{\mathrm{S,SF}}$–$u_{\mathrm{P,SF}}$ systematics of the decompressed silica fluid. There was not enough information to

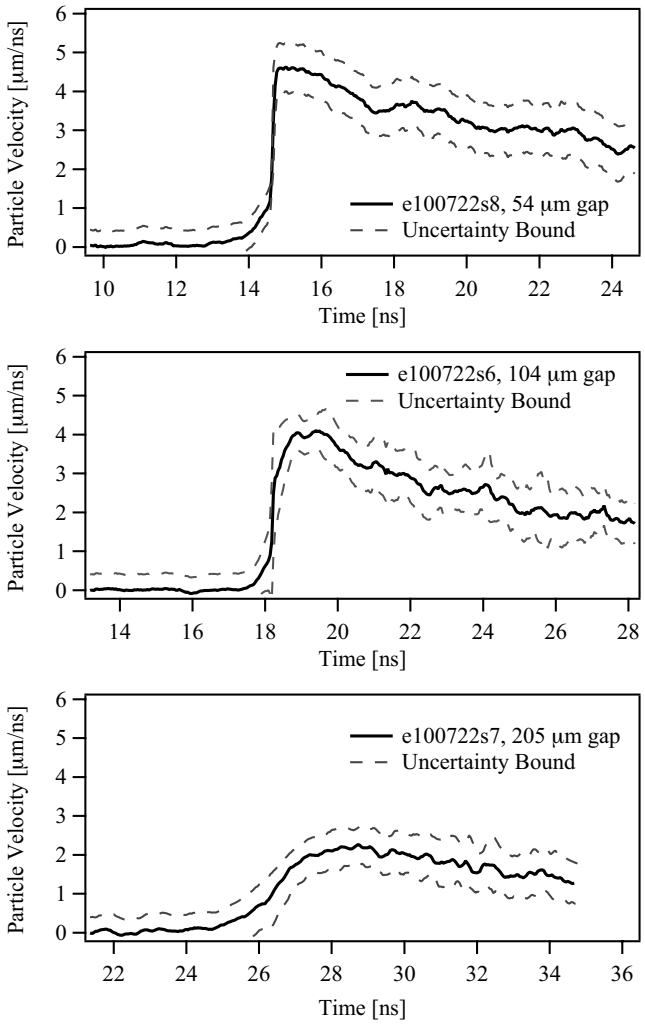

Figure 2.8: Particle velocity profiles in LiF window from shock-and-release stagnation experiments. The rise time of the particle velocity in the LiF window increases with increasing gap distance, reflecting the shallowing of the density gradient during the exapansion of the decompressing silica. Particle velocity data at the silica–LiF interface are from the 199-GPa shock-and-release stagnation experiment set (e100722s6-e100722s8).

estimate a Hugoniot for these decompressed fluid states based on thermodynamic measurements; consequently, we used model Hugoniots from the M-ANEOS equation of state for silica to estimate a bound on the shock velocity for a given particle velocity. For initial densities ranging from 0.007 to 1.3 g cm^{-3} and temperatures from 4000 to 6000 K, the shock velocity varies by only about 20%.

Using the M-ANEOS model Hugoniots, we fit the bulk sound speed, $C_{0,\mathrm{SF}}$, and slope of the $U_{\mathrm{S,SF}}$–$u_{\mathrm{P,SF}}$ relation, s_{SF}, with a linear function of the initial density (c.f., Anderson, 1997):

$$C_{0,\mathrm{SF}} = 0.45 + 1.2\rho_{0,\mathrm{F}} \tag{2.18}$$

$$s_{\mathrm{SF}} = 1.16 + 0.03\rho_{0,\mathrm{F}} \tag{2.19}$$

where density is in g cm^{-3} and $C_{0,\mathrm{SF}}$ is in km s^{-1}. We assigned an uncertainty in the shock velocity of 20%, which represents the envelope of model shock velocities, for a given particle velocity, for a fluid parcel of initially 25% to 75% vapor by mass.

Under the impedance matching assumption (Equation 2.17), the $U_{\mathrm{S,SF}}$-$u_{\mathrm{P,SF}}$ relation presented in Equations 2.18 and 2.19, and the LiF Hugoniot (Ahrens and Johnson, 1995a), we solved for the average density of the silica fluid immediately prior to impact, $\rho_{0,\mathrm{F}}$. The results are presented in Table 2.5. As expected, for higher initial entropies, the released state had a lower density. Note that significant vaporization was occurring on the time scale of a few nanoseconds as the average density decreased by a factor of 3 to 4.

The shock pressure in the LiF was determined assuming the measured particle velocity represents a Hugoniot state. Although this assumption is not strictly true for the experiments that show a ramp loading profile, the Hugoniot approximates an isentrope in pressure-volume and pressure-particle velocity space, within 7% in pressure, at the moderate pressures of the stagnation exper-

Table 2.5: Average post-shock densities of silica from shock-and-release stagnation experiments.

Experiment No.	Gap [μm]	$V_{\rm imp}$ [km s^{-1}]	$u_{\rm P,LIF}$ [km s^{-1}]	$P_{\rm LiF}$ [GPa]	$\rho_{0,\rm F}$ [g cm^{-3}]
		Release from 199 ± 22 GPa			
e100722s8	54	13.8 ± 0.5	4.6 ± 0.6	137 ± 16	1.16 ± 0.29
e100722s6	104	13.8 ± 0.5	4.0 ± 0.5	111 ± 12	0.86 ± 0.21
e100722s7	205	13.8 ± 0.5	2.2 ± 0.45	47 ± 8	0.28 ± 0.08
		Release from 338 ± 30 GPa			
e100727s5	54	18.0 ± 0.7	5.5 ± 0.5	182 ± 15	0.89 ± 0.20
e100727s3	109	18.0 ± 0.7	4.0 ± 0.55	111 ± 13	0.45 ± 0.11
e100727s4	204	18.0 ± 0.7	3.25 ± 0.45	136 ± 8	0.30 ± 0.07

iments. Also, there could be a systematic uncertainty in $\rho_{0,\rm F}$ related to the $U_{\rm S,SF}$–$u_{\rm P,SF}$ relation derived from M-ANEOS. However, the conclusion that significant vaporization occurred on the time scale of the experiment is robust.

More sensitive stagnation experiments are necessary to accurately probe the density gradient of a vaporizing fluid. Next, we compare the experimental results to the model liquid–vapor curve for silica.

2.4 Revised Liquid–Vapor Curve of Silica and Post-Shock Temperature Data

As the current M-ANEOS model liquid–vapor curve for silica does not lie within error bars of the boiling point entropy calculation from this work (Figure 2.2), we modified the M-ANEOS model parameters in the expanded region to fit the pressure, temperature, and entropy at the calculated boiling point (§2.2.2) and measured triple point (1920±50 K and ∼2 Pa) (Mysen and Kushiro, 1988).

The model liquid–vapor curve required only slight modifications to the M-ANEOS parameters in the expanded region to fit both the boiling point and triple point (Evap= 1.228×10^{11} erg g^{-1}, a_exp=1.6, Tdebye=660 K, Grun=0.77, C53=0 dynes cm^{-2}, C54=0). Note that these parameters should not be used in M-ANEOS to model the equation of state surface outside of the liquid-vapor dome. The model liquid–vapor curve is tabulated in the online Auxiliary Materials (Table S.5).

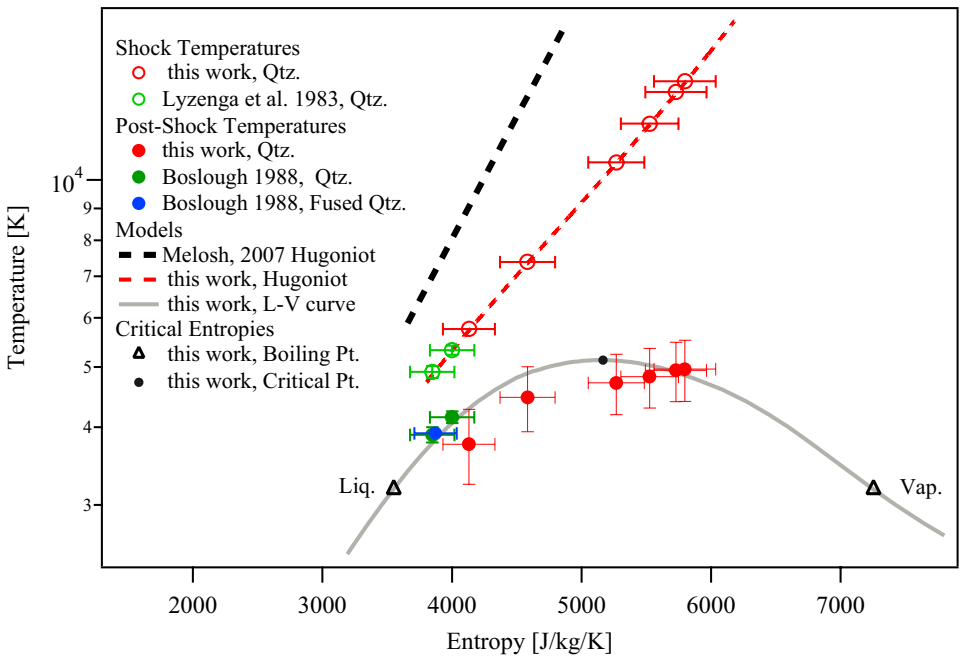

Figure 2.9: Post-shock temperatures (filled circles) for quartz (this work and Boslough, 1988)) and fused silica (Boslough, 1988) compared to revised model liquid–vapor phase boundary from this work. The Hugoniot states achieved in each shock-and-release experiment (open circles) are placed at the entropy and temperature coordinate corresponding to the measured shock velocity. Reported uncertainties in entropy reflect both uncertainties in the experimental shock pressure and the absolute entropy on the Hugoniot.

The critical point from our model occurs at $T_{\rm CP}$=5130 K, $\rho_{\rm CP}$=0.508 g cm^{-3}, $P_{\rm CP}$=0.13 GPa, and $S_{\rm CP}$=5150 J kg^{-1} K^{-1}.

In Figure 2.9, we present the new post-shock temperature data for silica (Table 2.4) in temperature–entropy space, assuming isentropic decompression from the Hugoniot state. Post-shock temperature measurements on quartz and fused silica from gas-gun experiments which achieved fluid shock states are also shown (Boslough, 1988; Lyzenga et al., 1983). The post-shock temperatures follow the new model liquid–vapor curve temperature up to states near the model critical point, where they begin to diverge slightly below the equilibrium liquid–vapor curve.

Boslough (1988) considered the possibility of the release isentropes from the shock states intersecting the liquid–vapor dome. However, without the stagnation measurements to show vaporiza-

tion was occurring on the time scale of the experiment, Boslough (1988) assumed the the fluid would supercool below the liquid–vapor phase boundary, as suggested in Zel'dovich and Raizer (1966). Consequently, Boslough (1988) used the post-shock temperatures to estimate post-shock densities and the fluid Grüneisen parameter. However, the form of the Grüneisen parameter assumed by Boslough (1988), which is usually correct for solids, is incorrect for fluids (e.g. Stixrude and Karki, 2005) and led to a significant overestimate of the post-shock densities ($\sim$3.76 g cm^{-3}).

Given the entropy in the shock states of Boslough (1988) and our model liquid–vapor curve, the post-shock density of the liquid should have been $\sim$2.00 g cm^{-3}, which is similar to the density of the liquid at the boiling point ($\sim$2.05 g cm^{-3}, Hudon et al. (2002)). For significantly higher entropies, such as in our stagnation experiments discussed in the previous section, the post-shock density would have been lower and would decrease rapidly with time due to a rapidly increasing volume fraction of expanding vapor. For example, for release from 200 GPa, the density of the liquid where the release isentrope intersects the liquid–vapor dome is 0.72 g cm^{-3}, which is comparable to the average density determined in the stagnation experiments at a gap distance of 100 microns, 0.86 g cm^{-3}, and significantly greater than the average density determined at a gap distance of 200 microns, 0.28 g cm^{-3}. Detailed comparisons between the average density determined in the stagnation experiments and the density of the liquid–vapor mixture were impractical due to the complicated experimental geometry; however the conclusion that bulk vaporization was occurring on the time scale of the experiment is robust.

Although the stagnation experiments were an integrated measurement of the momentum transfer between the silica and the LiF, post-shock temperature measurements were a significantly more local measurement. In the next section, we investigate the process of emission from a vaporizing fluid and assess how the apparent post–shock temperature should compare to the liquid–vapor curve.

2.5 Analysis of an Isentropically-Expanding Liquid–Vapor Mixture

Based on the relative absorbance of silica liquid and vapor, in §2.3.1 we argued that the post-shock thermal emission originated at the liquid–vapor interface. Here, we show that although the opacities of the liquid and vapor are uncertain, the dominant emitter was the silicate liquid and not the rapidly cooling low density vapor plume. To make this argument, we first estimate the dominant mechanism for phase decomposition. Then, we present the density and temperature profiles in the releasing fluid as a function of position. Finally, using the release profiles and estimates of the absorption coefficients, we performed a radiative transfer calculation to determine the emitting region in the released material.

2.5.1 Phase Decomposition

Phase decomposition is likely to occur by fragmentation, nucleation and growth, or spinodal decomposition. The dominant mechanism will depend on where the fluid release isentrope intersects the liquid–vapor dome and the relative time scales for each process (Povarnitsyn et al., 2008), where the fastest mechanism wins. Here, we explore the feasibility of each phase decomposition mechanism on the time scale observed in the stagnation experiments. Understanding the mechanisms for vaporization will aid in interpretation of the post-shock temperature measurements (Section 2.5.4) as well as the design of future shock-and-release experiments.

For a release isentrope that enters the liquid–vapor dome on the liquid side of the critical point (Figure 2.2), significant undercooling could allow the material to go into tension. If the tensile stress exceeds the spall strength of the liquid for sufficient time, the material will undergo fragmentation, also called cavitation. Grady (1988) derived a time scale for a liquid to undergo fragmentation if the the spall strength has been exceeded,

$$\tau_{\text{spall}} = \left(\frac{6\varsigma}{\rho \dot{\epsilon}^2 c_{\text{s}}^3} \right)^{1/3} \tag{2.20}$$

where ς is the surface tension, ρ is the density of the liquid, $\dot{\epsilon}$ is the strain rate, and c_{s} is the adiabatic sound speed. The surface tension decreases to zero at the critical point temperature T_{CP} in the form (Povarnitsyn et al., 2008),

$$\varsigma = \varsigma_0 \left(1 - \frac{T}{T_{\text{CP}}} \right)^{1.25}. \tag{2.21}$$

The coefficient ς_0 is calibrated using the surface tension of silica liquid at ~2000 K, $\varsigma = 0.3$ N m^{-1} (Boca et al., 2003).

In the shock-and-release experiments, the decompressing strain rate changed dramatically with distance from the free surface. For material within 10 μm of the free surface, the decompression strain rate can be approximated to an order of magnitude by assuming a constant decompression rate from the shocked density ~ 6 g cm^{-3} to a metastable liquid density ~ 1.5 g cm^{-3} in a time scale of a few nanoseconds, which leads to a strain rate of $\sim 4 \times 10^8$ s^{-1}. Assuming a sound speed of 1 km s^{-1} (consistent with the Hugoniot bulk sound speed), we found the time scale for cavitation to be 10 to 100 picoseconds for a range of temperatures below the critical point.

If the isentrope intersects the liquid–vapor dome near the critical point (Figure 2.2), the metastable liquid isentrope must undergo significant supercooling before it reaches a state of negative pressure. One can use the theory of homogeneous nucleation to model the nucleation of bubble droplets in the adiabatic decompression of fluids into the liquid–vapor dome (Povarnitsyn et al., 2008). The theory can also be used to predict the lag time, τ_{nucl}, between the fluid parcel becoming metastable and when nucleation and growth begins (Balluffi et al., 2005; Povarnitsyn et al., 2008), which is the most important factor in predicting the dominant mechanism for phase decomposition.

The lag time is given by

$$\tau_{\text{nucl}} = \frac{e^{\frac{W}{k_{\text{B}}T}}}{\Lambda n V^*}, \tag{2.22}$$

where $\Lambda \approx 10^{10}$ s^{-1} is the kinetic coefficient (Tkachenko et al., 2004), n is the number density of particles, V^* is the volume under consideration, $W = 16\pi\varsigma^3/\Delta P^2$ is the work required to form a critical size bubble, and ΔP is the difference between the pressure in the metastable state and the pressure on the liquid–vapor curve at the same temperature. Given the strain rates in these experiments, a reasonable volume element to consider is $(10\ \mu\text{m})^3$. The value for ΔP is dependent upon the time scale, but for the purposes of estimating the time scale for nucleation, we assumed $\Delta P = 0.01$ GPa and T=5000 K, which resulted in $\tau_{\text{nucl}} \approx 10$ ps, a time scale that would suggest nucleation of vapor droplets occurred well within the time frame of the experiments. This time scale is strongly dependent on the surface tension and ΔP. Consequently, the uncertainty in τ_{nucl} was poorly constrained as the surface tension is extrapolated well beyond the conditions of any experimental data and ΔP would depend strongly on the true release isentrope and the liquid–vapor curve.

Spinodal decomposition occurs when the free energy surface has negative curvature with respect to the extrinsic variable of interest (e.g., chemical composition or density). The early stage growth by spinodal decomposition in two-component chemical systems is relatively straightforward to treat analytically as one need only consider the equation of motion for the diffusion of atoms and mass conservation. However, to predict the dynamics of spinodal decomposition in density space, one need also consider the hydrodynamic equations of motion, which do not lend themselves to simple analytical solutions. Although few numerical studies have considered spinodal decomposition upon quenching into the liquid–vapor dome, recent two- and three-dimensional simulations for quenches

into the liquid–vapor dome of a van der Waal's fluid (Lamorgese and Mauri, 2009) provide useful constraints on the time scales for decomposition.

Lamorgese and Mauri (2009) find that spinodal decomposition process occurs in three stages. First, upon instantaneous quenching there is a time delay where no detectable phase separation takes place as the thermal density perturbations are not strong enough to overcome the surface tension in the fluid. The second stage is defined by a rapid phase separation to a state with liquid and vapor phases near the respective equilibrium densities. The third stage represents an asymptotic approach toward equilibrium where coarsening also takes place.

Most important to predicting whether phase separation occurs by nucleation and growth or spinodal decomposition is the time delay between quench and rapid phase separation. For the van der Waal's fluid, Lamorgese and Mauri (2009) find that the time delay depends extremely weakly on the surface tension, a useful result as the surface tension is poorly constrained for silicate fluids. As noted in Vladimirova et al. (1998), the time delay depends predominantly on the depth of the temperature quench with the intensity of thermal noise having a minimal effect on the time delay. Lamorgese and Mauri (2009) find that for a quench of 10% below the critical point temperature and a range of unstable densities, the time delay is on the order of 1 to 10 scaled time units. In their simulations, time is scaled by a macroscopic length scale divided by the sound speed in the medium. Consequently for a system size of $\sim$10 μm with a sound velocity of 0.1 to 1 μm ns^{-1}, the time delay before phase separation occurs in a 10% quench will be 10 to 1000 ns, significantly longer than the time scales expected for homogeneous nucleation at much smaller quenches.

Based on the relatively sparse data summarized above, we suggest that phase separation occurred by nucleation and growth rather than spinodal decomposition for the shock and release experiments presented here. However, future experiments are needed to determine the true kinetics and particle size distribution upon vaporization.

2.5.2 Post-Shock Temperature Buffering

The decrease in temperature with density during isentropic decompression from the shock state can be determined if the Grüneisen parameter of the fluid is known as a function of volume. However, upon the isentrope entering the liquid–vapor dome, it is no longer appropriate to integrate using the simple functional form of Equation 2.2 as the isentropic path is dominated by the relative mass of liquid and vapor. In effect, for an isentropically expanding mixture the temperature is buffered upon entering the liquid–vapor co-existence region. The equilibrium density–temperature path through the liquid–vapor dome can be determined if the entropy and specific volume of the liquid and vapor (S_{liq}, S_{vap}, V_{liq}, and V_{vap}) are known as a function of temperature. Upon entering the liquid–vapor dome, the entropy and volume of the mixture, S_m and V_{avg}, are given by

$$S_m = (1-\chi_{\text{vap}})\, S_{\text{liq}}(T) + \chi_{\text{vap}} S_{\text{vap}}(T), \tag{2.23}$$

$$V_{\text{avg}}(T) = (1-\chi_{\text{vap}})\, V_{\text{liq}}(T) + \chi_{\text{vap}} V_{\text{vap}}(T), \tag{2.24}$$

where χ_{vap} is the mass fraction of vapor. Using the Clausius-Clapeyron relation, Equations 2.23 and 2.24 can be combined into a more useful form,

$$V_{\text{avg}}(T) = V_{\text{liq}}(T) - \frac{S_m - S_{\text{liq}}(T)}{\left(\frac{dP}{dT}\right)_{\text{LV,T}}}, \tag{2.25}$$

where $\left(\frac{dP}{dT}\right)_{\text{LV,T}}$ is the slope of the liquid–vapor curve at temperature T.

Near the critical point, V_{liq} changes dramatically as a function of temperature; however, below about $0.95T_{\text{CP}}$ the volume of the liquid is relatively constant and negligible with respect to the volume of the vapor at the same temperature. For release isentropes that intersect the liquid–

vapor curve below about $0.95T_{\mathrm{CP}}$, the volume change in the liquid is small and consequently the entropy change in the liquid can be approximated assuming a temperature-independent isochoric heat capacity C_{V},

$$S_{\mathrm{liq}}\left(T\right) = S_m - C_V \ln\left(\frac{T}{T_{\mathrm{LV,m}}}\right), \tag{2.26}$$

where $T_{\mathrm{LV,m}}$ is the temperature where the isentrope entered the liquid–vapor dome. As most materials follow an Arrhenius law for the saturated vapor pressure as a function of temperature, the boiling point and triple point constrain the slope of the liquid–vapor curve,

$$\left(\frac{dP}{dT}\right)_{LV} = \frac{A_1}{T^2}\mathrm{e}^{(-A_2/T)}, \tag{2.27}$$

where A_1 and A_2 are constants, $5.58{\times}10^8$ Pa K and $5.85{\times}10^4$ K, respectively, for the liquid–vapor curve of silica from Melosh (2007).

Consequently, the average specific volume for the isentrope within the co-existence region has the simple functional form,

$$V_{\mathrm{avg}}\left(T\right) = V_{\mathrm{liq}}\left(T\right) + C_{\mathrm{V}}\frac{T^2 \ln\left(T_{\mathrm{LV,m}}/T\right)}{A_1 \mathrm{e}^{(-A_2/T)}}. \tag{2.28}$$

This analytic model is compared to M-ANEOS model isentropes in Figure 2.10. For isentropes that intersect the liquid–vapor curve near the critical point, the approximate solution in Equation 2.28 breaks down as the entropy change along the liquid side of the vapor curve is no longer dominated by the change in temperature but also by the significant decrease in volume upon cooling. However, even near the critical point, once the isentrope enters the liquid–vapor dome, the temperature decrease is only $\sim 10\%$ for over a 10-fold increase in volume.

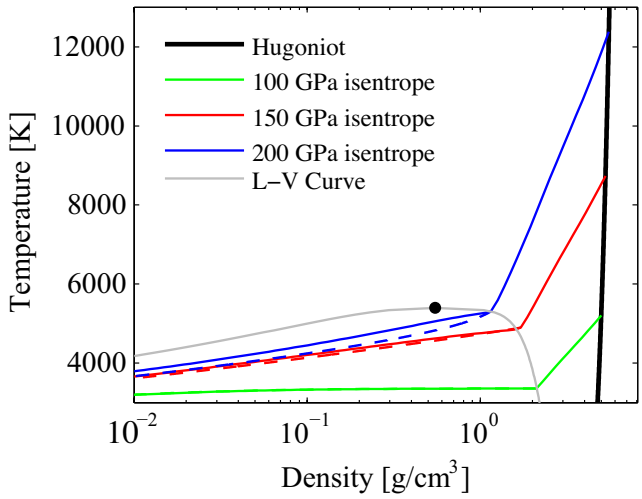

Figure 2.10: Example release isentropes through the liquid–vapor phase boundary (gray line, Melosh, 2007). Upon intersection of the isentrope with the liquid–vapor curve, the temperature of the expanding mixture is buffered by the phase change. The analytic model for the mixture (dashed colored lines, Equation 2.28) agrees well with isentropes from the M-ANEOS model for silica (Melosh, 2007) (solid colored lines). Note that the two models directly coincide for the 100-GPa isentrope.

The significant temperature buffering is caused by the statistical need to increase the entropy and thereby make vapor. For the post-shock temperature experiments described in Section 2.3.1, even though the leading edge of the fluid was decompressing rapidly, the temperature gradient in the vaporizing liquid–vapor mixture was small.

2.5.3 Post-Shock Density Profiles

To be able to calculate the radiative transfer through the expanding liquid–vapor mixture, in addition to the temperature profile, we need the density profile and information about the mixture geometry. Upon breakout of a steady one-dimensional shock at the free surface, a centered rarefaction wave propagates back into the silica sample. The compressibility of a liquid–vapor mixture is significantly lower than the pure liquid phase as most of the strain is taken up by the more compressible vapor phase. The discontinuity in compressibility as the material releases into the liquid–vapor dome results in a change in the slope of an isentrope in pressure–density space.

This compressibility discontinuity has significant implications for the density profile of a material undergoing isentropic decompression.

As an example, we calculated the rarefaction fan from a 200-GPa shock breaking out at a free surface using the method of characteristics (e.g. Zel'dovich and Raizer, 1966). The M-ANEOS model Hugoniot and release isentrope from 200-GPa are presented in pressure–density space in Figure 2.11A. The slope of a characteristic is given by

$$\left(\frac{dh}{dt}\right)_i = \frac{\rho_i c_{\mathrm{s,i}}}{\rho_0}, \tag{2.29}$$

where h is the Lagrangian coordinate, ρ_i is the material density along characteristic i, $c_{\mathrm{s,i}}$ is the Eulerian sound speed at density ρ_i, and ρ_0 is the density in the Lagrangian frame of reference. In Figure 2.11B, each characteristic is separated in density by 0.1 g cm^{-3}. The significant and abrupt decrease in sound velocity upon the isentrope entering the liquid–vapor dome leads to a separation of rarefaction waves. As a result, a plateau forms at the density where the isentrope intersects the liquid–vapor dome and increases in thickness with time.

We transformed the density profile in Lagrangian coordinates to Eulerian coordinates by considering conservation of mass,

$$\int_{x_0}^{x(\rho_i)} dx = \int_0^{h(\rho_i)} \frac{\rho_0}{\rho} dh \tag{2.30}$$

where x_0 is a constant of integration that will depend on the momentum transfer through the entire release path. The dependence of ρ on h was obtained from Equation 2.29. Equation 2.30 is valid for regions along the release isentrope where the Lagrangian sound speed increases monotonically with density. In regions where the Lagrangian sound speed decreases with density, a rarefaction shock wave will form, requiring the solution of the coupled conservation equations to

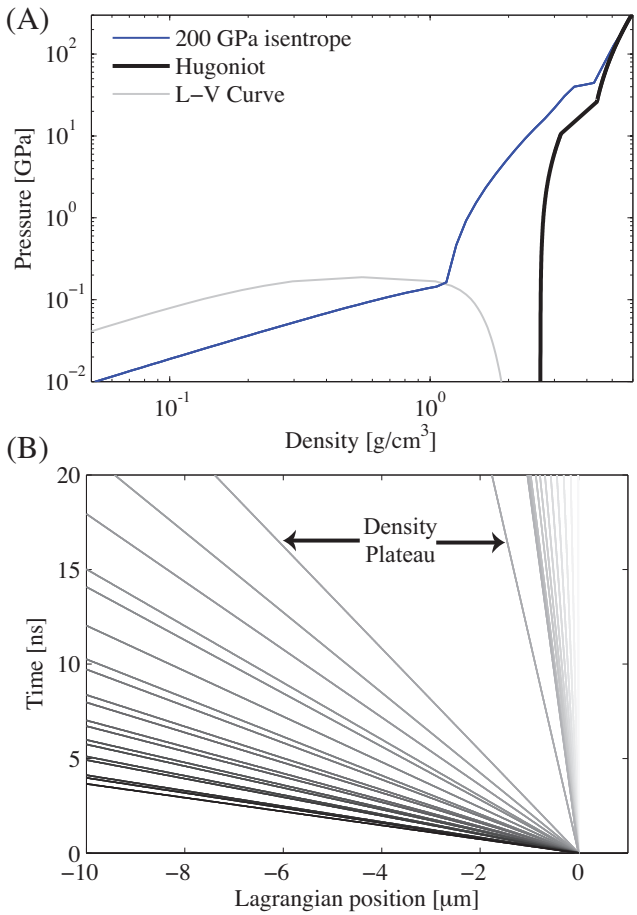

Figure 2.11: Analysis of the density profile in the decompressing silica using the method of characteristics. A. M-ANEOS model Hugoniot, liquid–vapor curve, and release isentrope beginning at 200 GPa on the Hugoniot (Melosh, 2007). The kinks in the Hugoniot and the release isentrope at 20 and 40 GPa, respectively, are the stishovite transition in the model. B. Rarefaction characteristics in Lagrangian coordinates upon breakout of a 200-GPa shock wave at the free surface (t=0 ns and h=0). Each characteristic is separated by 0.1 g cm^{-3} and the line opacity increases monotonically with density. Over time, a plateau develops at the density where the release isentrope enters the liquid–vapor curve.

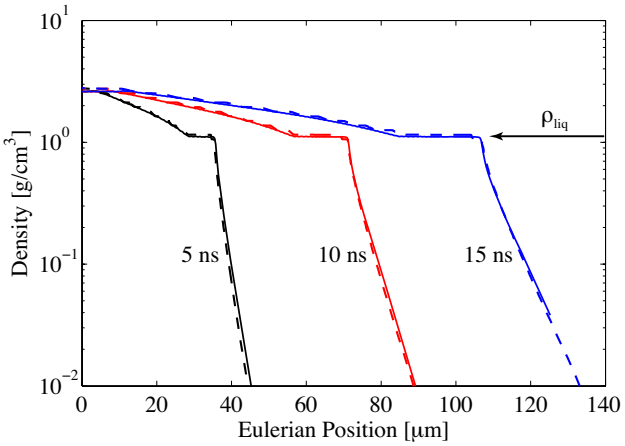

Figure 2.12: Calculated density profiles upon breakout of a 200-GPa shock wave in quartz at a free surface (initially at the origin). Solid lines – numerical simulations using M-ANEOS model in CTH code; dashed lines – density obtained by integrating Equation 2.30 up to the stishovite transition. A constant offset was added to the position of the analytic model as we do not consider characteristics above the stishovite transition in the M-ANEOS model. ρ_{liq} designates the density where the isentrope intersects the liquid side of the liquid–vapor dome.

predict the density profile. We then calculated the Eulerian density profile up to the stishovite transition, where the sound speed decreases with density on the M-ANEOS release isentrope, which is an artificial transition within the M-ANEOS model as it does not include a melting curve.

In Figure 2.12, the results of our analytic Eulerian density profiles are compared with density profiles obtained from adiabatic release calculations using the shock physics code CTH (McGlaun et al., 1990) and the M-ANEOS silica EOS. The density profiles obtained from integrating Equation 2.30 were offset in space to match the CTH profiles as we did not integrate over the characteristics beyond the stishovite transition. The general shape of the hydrocode and analytic calculations are in excellent agreement.

For isentropes that enter the silica liquid–vapor dome on the liquid side, the thickening plateau of material at the density of the phase boundary forms an optically-thick layer in the expanding mixture. Because the phase-boundary plateau is optically thick (Figure 2.5), thermal radiation from material at pressures above the liquid–vapor curve will not be observed after a period of

about 200 picoseconds. Consequently, only temperatures at or below the temperature where the isentrope enters on the liquid side of the liquid–vapor curve were observed in thermal emission after shock-and-release.

In contrast, for release isentropes that enter on the vapor side of the critical point, the phase-boundary plateau will be less pronounced and will eventually become nonexistent with increasing entropy. As a result, the observed thermal emission in such high pressure shock-and-release experiments would sample a larger range of temperatures than those at and below the liquid–vapor dome, and the interpretation of apparent temperatures would require a full radiative transfer calculation.

2.5.4 Radiative Transfer Model

We developed a simple radiative transfer model to aid interpretation of the post-shock temperature data. Due to the large uncertainties in the droplet size distribution, concentration, and optical scattering properties within the liquid–vapor mixture, the model does not include any particle scattering. We considered a more conservative, yet simple, assumption that any photon that interacts with a liquid droplet is absorbed.

Because of the high opacity of silica liquid, a high volume fraction of liquid droplets will be essentially opaque to any photons from uprange material. Consequently, even in experiments where a density plateau forms in the expanding mixture, the lower-density material ahead of the plateau may obscure thermal emission from material in the plateau. However, the difference between the temperature of the plateau and the temperature of a layer ahead of the plateau will be small due to the buffering by the phase boundary (§2.5.2).

To estimate the difference between the experimental apparent temperatures presented in Table 2.4 and the true temperature along the liquid–vapor boundary, we considered a radiative transfer model that conservatively assumes liquid droplets are opaque and constrained the absorption coeffi-

cient of the vapor phase from the FPMD-DFT simulations presented in Figure 2.5. The probability of a photon being absorbed within a slice of the two-phase liquid–vapor mixture of thickness dx is the sum of the probability of the photon interacting with a liquid droplet and being absorbed within the vapor phase,

$$Pr(x) = \alpha(x)dx = \frac{dx}{L_{\mathrm{MFP}}(x)} + \alpha_{\mathrm{vap}}(x)dx, \tag{2.31}$$

where $\alpha(x)$ is the average absorption coefficient at position x, L_{MFP} is the mean free path for a photon interacting with a liquid droplet, and α_{vap} is the absorption coefficient of the vapor phase. The mean free path for a particle interacting with liquid spheres of diameter D_0 and volume fraction $V_{\mathrm{liq}}/V_{\mathrm{avg}}$ is given by,

$$L_{\mathrm{MFP}} = \frac{D_0 V_{\mathrm{avg}}}{6V_{\mathrm{liq}}}. \tag{2.32}$$

We used the range of droplet sizes measured from the explosion of wire arrays (Sedoi et al., 1998; Tkachenko et al., 2004) (100 to 1000 nm) to constrain D_0.

The depth of emitting layers was found by calculating the thickness where the optical depth is unity,

$$\int_{x_{\mathrm{fs}}}^{x(T_{\mathrm{a}})} \alpha(x)dx = 1. \tag{2.33}$$

x_{fs} is the position of the vacuum interface and $x(T_{\mathrm{a}})$ is the position of the emitting region within the liquid–vapor mixture. To calculate $x(T_{\mathrm{a}})$ for a given entropy, we must know L_{MFP} and α_{vap} as a function of position, which requires a model for the absorption coefficient as a function of density and temperature and the pressure, density, and temperature states along the entire isentrope within

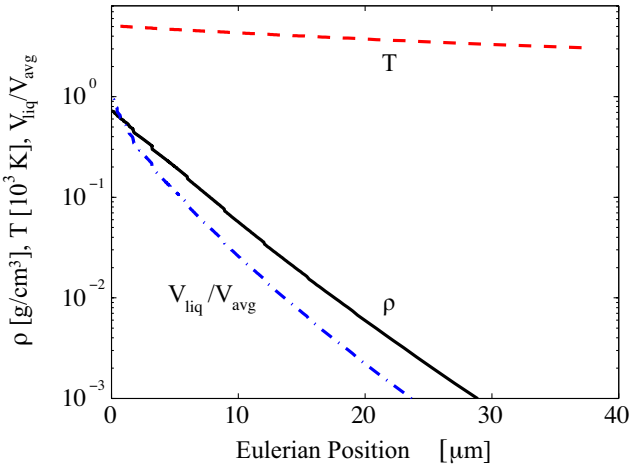

Figure 2.13: Spatial profile of the vaporizing silica at 10 ns after 200-GPa shock breakout at the free surface, corresponding to the typical time of post-shock temperature measurements. Average density, ρ, volume fraction of liquid, $V_{\rm liq}/V_{\rm avg}$, and temperature, T, calculated as a function of position along a release isentrope within our revised silica liquid–vapor dome at an entropy of 4890 J kg^{-1} K^{-1}. The absolute position is offset ($\sim$70 μm from the red curve in Figure 2.12) so that the state on the liquid–vapor curve occurs at the origin.

the liquid–vapor mixture.

Since this calculation was restricted to paths in the liquid–vapor co-existence region, we used our revised model liquid–vapor curve (§2.4) to determine the thermodynamic properties as a function of position and time within the expanding silica, following the same procedure as in §2.5.3. In Figure 2.13, we present the average density, the volume fraction of liquid, and the temperature as a function of position along a 4890 J kg^{-1} K^{-1} release isentrope (generated by a 200 GPa shock) at 10 ns after shock breakout. We considered the profile at 10 ns after shock breakout to be consistent with the time period observed for the experimental post-shock temperature data.

The 10-ns expansion profile was used to calculate $x(T_{\rm a})$, using Equation 2.33 and the density and temperature-dependent absorption coefficients of silica vapor. We used our FPMD-DFT simulations to constrain the absorption coefficient over a wide range of densities and temperatures by modeling the frequency-dependent opacity with the semiconductor Drude model (see online Auxiliary Materials). A radiometric measurement would record an apparent post-shock temperature,

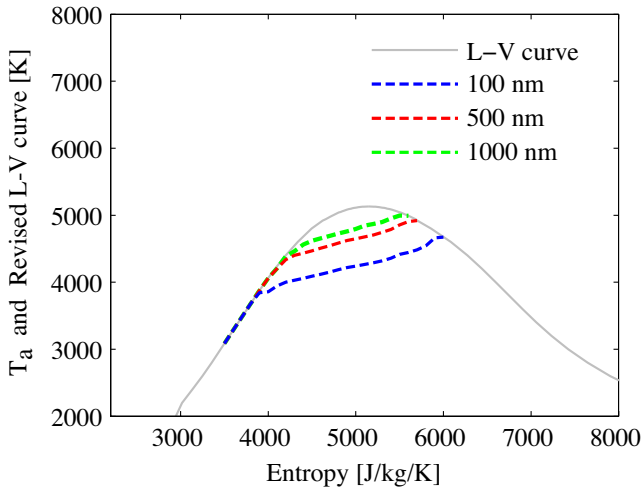

Figure 2.14: Predicted apparent post-shock temperatures (T_a) for silica shock-and-release experiments as a function of entropy and liquid droplet size (D_0=100 to 1000 nm). T_a was derived using our radiative transfer model (Equations 2.31–2.33) and our revised liquid–vapor curve for silica at 10 ns after shock breakout. Predicted values for T_a fall on the liquid–vapor curve up to ~4000 J kg^{-1} K^{-1} and intersect the liquid–vapor curve again on the vapor side at ~5500 J kg^{-1} K^{-1}, where higher-entropy shock-and-release experiments will record apparent temperatures above the liquid–vapor dome temperature.

T_a, corresponding to the temperature at $x(T_a)$, the location in the expanding mixture where the optical depth reaches unity.

In Figure 2.14, we present the predictions for the apparent post-shock temperature as a function of entropy in free-surface shock-and-release experiments on quartz. With increasing entropy, post-shock temperature measurements initially follow the liquid–vapor curve until reaching an entropy close to critical point, where the observed post-shock temperatures will start to diverge below the liquid–vapor curve. The divergence occurs when the materials leading the phase-boundary plateau become optically thick.

At an entropy state significantly greater than the critical point, the post-shock thermal emission will originate from materials above the liquid–vapor curve (Celliers and Ng, 1993). In this case, the sum of materials at densities on and below the liquid–vapor dome is not optically thick. The point at which apparent temperatures would rise above the liquid–vapor dome depends strongly on the

opacity of the fluid. Our model construction does not include the emission from states above the liquid–vapor curve; however, our model does calculate the point where the apparent temperature transitions from below to above the liquid–vapor dome.

2.6 Discussion

2.6.1 Shock-and-Release to the Liquid–Vapor Phase Boundary

Based on our analysis of an isentropically expanding liquid–vapor mixture, we find that post-shock temperature measurements are an excellent method for determining the temperature along the liquid–vapor curve at entropies below the critical point. The technique has increasing uncertainties as the entropy nears that of the critical point and above.

Even with the simplifications made in analyzing the structure of isentropically-expanding silica, the model for apparent temperature observations after shock-and-release (Figure 2.14) closely follows the data obtained in the experiments (Figure 2.9). At entropies lower than the critical point, the gas-gun and laser-driven shock data are on or near the model liquid–vapor curve. In these cases, the temperature in the released silica was buffered by the phase boundary and absorption by lower-density material was negligible. As the shock entropies increase toward the critical point entropy, the experimental apparent post-shock temperatures flatten in a manner similar to the model predictions. There was some absorption by material with densities below the phase boundary, but the temperature of this material was only slightly below the phase boundary. The experimental post-shock temperature data also appear to intersect the liquid–vapor curve on the vapor side of the critical point at a similar entropy as predicted by the radiative transfer model (about 5500 J kg^{-1} K^{-1}). Higher entropy shock-and-release experiments were not possible with the Janus laser. Our model suggests that such experiments would have recorded apparent post-shock temperatures above the liquid–vapor boundary.

The bulk density measurements in the stagnation experiments provide confirmation of release into a liquid–vapor mixture: the densities were well below the expected metastable liquid density and the rise time in the LiF window increased with time. However, the limitations in the experimental configuration did not allow for determination of a detailed density profile in the decompressing material. Future stagnation experiments could be used to measure the density where the release isentrope enters the liquid–vapor dome and to estimate the kinetics of vaporization and condensation.

Because of the abundance of thermodynamic data available for silica, we have been able to calculate a new liquid–vapor boundary and develop a model for post-shock temperatures independently of the data from our shock-and-release experiments. The model and data are self-consistent, which reinforces our confidence in both the physical model and the experimental technique.

Given the uncertainties in the experimental data and our radiative transfer model, we do not consider the data to be an indirect constraint on the mean droplet size in the decompressing silica. The mean droplet size is expected to change dramatically as a function of entropy within the liquid–vapor dome (Tkachenko et al., 2004) and consequently future experiments that directly measure the droplet size and the density structure in the expanding material would increase the accuracy of the radiative transfer model and allow for more detailed interpretation of apparent post-shock temperature measurements.

For the many materials where little data exists in phase space near the liquid–vapor boundary, shock-and-release experiments provide a means to obtain robust temperature measurements. The precision of post-shock temperature measurements can be improved in future work by including spectral resolution. Wavelength-dependent pyrometry is needed to be able to account for non-graybody emission. Higher temporal resolution would improve the radiative transfer calculations and allow for study of the absorption by the leading vapor. Future experimental configurations

that resolve the density structure in the expanding material may also provide robust density measurements by identifying the predicted phase-boundary plateau.

2.6.2 The Criteria for Shock-Induced Vaporization of Quartz

With our experimentally-validated model for the liquid–vapor curve of silica and new calculation of entropy on the Hugoniot, we determined the critical shock pressures required for incipient and complete vaporization upon decompression. Along the liquid–vapor curve, the temperature rises with ambient pressure; simultaneously, the entropies of the liquid and vapor converge with increasing ambient pressure (Figure 2.2). Therefore, the shock entropy required to initiate vaporization on release rises with ambient pressure while the shock entropy required for complete vaporization decreases.

For the example shown in Figure 2.2, a 300-GPa shock reaches an entropy of 5697±211 J kg^{-1} K^{-1}. Upon decompression to 10^5 Pa, by the lever rule, 58±6% of the silica is vaporized. In Table 2.6, we present the critical shock pressures, with 1-σ uncertainties, for incipient, 50%, and complete vaporization upon decompression to 10^5 Pa and the triple point ($\sim$ 2 Pa). For bodies with ambient pressures below the triple point, the decompressing silica will pass through the triple point and be buffered by the kinetics of freezing. Hence, the triple point serves as a useful reference point for shock-induced vaporization on airless bodies. The critical shock pressure for vaporization upon release to other ambient pressures may be determined by the entropy on the Hugoniot (Equation 2.7) and the entropies on the liquid–vapor curve, which are tabulated in the online Auxiliary Materials (Table S.5).

The critical shock pressure for complete vaporization of silica is about a factor of two lower than the M-ANEOS model prediction in Melosh (2007) and is approximately thirty percent less than a recent model by Kurosawa et al. (2012) that does not include the entropy of melting. As

Table 2.6: Criteria for shock-induced vaporization of 298 K α-quartz. Critical shock pressures and entropies for incipient (IV), 50%, and complete vaporization (CV) upon decompression to the triple point ($\sim$2 Pa) and 10^5 Pa ambient pressure.

Reference	$P_{ambient}$ [Pa]	S_{IV} [J kg^{-1} K^{-1}]	S_{CV} [J kg^{-1} K^{-1}]	P_{IV} [GPa]	$P_{50\%}$ [GPa]	P_{CV} [GPa]
This work	2	2890	9020	47 ± 2	342 ± 40	~ 3000
This work	1×10^5	3552	7254	75 ± 5	258 ± 25	715 ± 100
Melosh (2007)	1×10^5	3443	7240	95	380	1650

the M-ANEOS model liquid–vapor curve was near our revised model, the differences in critical shock pressures primarily reflect the lower entropy along the M-ANEOS model Hugoniot (Figure 2.2). The offset in entropy arises from a combination of factors, including the absence of a melting transition and the incorrect heat capacity in the fluid.

The heat capacity reflects the manner of dissipation of the internal energy gained from the shock wave. Rather than shock energy being dissipated as thermal energy, and ionization at the highest energies, more of the shock energy in silica is being dissipated as disorder. The source of the disorder in the supercritical fluid is not perfectly clear; Hicks et al. (2006) associate the higher heat capacity with dissociation and changes within the short range order in the molecular fluid. The contribution to the heat capacity from electrons is also likely greater than a thermally activated ionization model would predict as the concentration of free electrons increases dramatically upon melting, compression, and with increasing dissociation (Hicks et al., 2006; Laudernet et al., 2004). As the physical mechanism for the high heat capacity is likely to be applicable to all silicate liquids that start out as a bonded fluid, we expect the critical shock pressures for vaporizing all silicate liquids to decrease significantly from previous estimates that assumed the Dulong-Petit limit for the heat capacity of the fluid.

2.6.3 Implications for Planetary Impact Events

The pressure range under consideration, hundreds of GPa, is of particular importance to the end stage of terrestrial planet formation and subsequent impact cratering events. Peak shock pressures of about 100 GPa are achieved during impacts at velocities greater than ~ 8 km s^{-1}, comparable to the escape velocity of Earth-mass planets. Typical present-day impact velocities in the inner solar system range from about 5 to 40 km s^{-1} (Le Feuvre and Wieczorek, 2011). Silica is a major component in planetary crusts and an end-member for the compositional range in planetary mantles. Our work finds that vaporization of silica is an important process during planetary impact events.

A detailed analysis of the amount of vapor produced during planetary impacts is beyond the scope of this work. However, we estimated the magnitude of the effect of revising the critical shock pressure for vaporization. The pressure of a strong shock wave decays as one over the distance cubed from the impact point (Croft, 1982; Taylor, 1950). The volume of material shocked to or greater than a given pressure scales by distance to the same power. Consequently, our revision of the critical pressure for vaporization (lower by a factor of two) yields approximately a factor of two greater vapor production.

In the interior of planets, the temperatures and pressures are typically higher than the initial state of quartz studied here. For a higher initial temperature, as a first approximation, the entropy of heating may be added to the entropy on the 298 K Hugoniot. Second order differences in entropy, related to the different shock state attained when starting at a higher initial temperature and pressure, require a full equation of state model to calculate. A new multi-phase equation of state model of silica, that may be used in future hydrocode calculations of impact events, is currently under development (Kraus et al., 2012b).

Given our improved understanding of the physics of shock-induced vaporization of silicates,

it is very likely that previous studies have underestimated the amount of vapor produced during planetary impact events. Future simulations of planetary collisions using revised equation of state models that incorporate experimental constraints on the liquid–vapor coexistence region will more accurately reproduce the thermodynamics of planetary impact events.

2.7 Conclusions

For many materials, the liquid–vapor phase boundary is inaccessible via static experimental methods. In these cases, shock-and-release experiments are a robust technique to determine states on the phase boundary. In this work, we investigated shock-induced vaporization of silica experimentally and theoretically. We find that shock-and-release experiments provide an accurate measurement of the temperature on the phase boundary for entropies below the critical point, with increasing uncertainties near and above the critical point entropy. For entropies below the critical point, we predict the development of a plateau in the profile of the decompressing material at the liquid density.

In order to develop a theoretical model for the isentropic decompression of silica, we calculated reference entropy states using the most recent thermodynamic data. By performing an empirically constrained thermodynamic integration, we determined the absolute entropy at the point where the quartz and fused silica Hugoniots cross the melting curve. The entropy on the Hugoniots were determined using measured shock temperatures, pressures, and densities. The entropy on the quartz Hugoniot is significantly higher than the M-ANEOS model Hugoniot primarily because of the high heat capacity in the fluid. Using the M-ANEOS model construction for the expanded states, the liquid–vapor curve for quartz was refined to fit the entropies, densities, temperature, and pressure at the revised boiling point and triple point.

We calculated the temperature and density structure in isentropically decompressing silica. For

entropies below the critical point, the temperature along a release isentrope is strongly buffered at the point of intersection with the liquid–vapor curve. In addition, the change in sound speed upon entering the liquid side of the phase boundary leads to a plateau in the density profile at the state where the isentrope intersects the liquid–vapor curve. Then using a two-phase absorption model for silica, we predict the apparent temperature of the decompressing silica using a radiative transfer model.

The predicted post-shock temperatures are in excellent qualitative agreement with the experimental data (Table 2.4). Using the calculated entropies in the shock state, quartz post-shock temperature data initially follow the liquid–vapor phase boundary and diverge as the entropy approaches the critical point in a manner predicted by the radiative transfer model. The experimental data are self-consistent with the independently-derived liquid–vapor curve. The new model critical point for silica is $T_{\rm CP}$=5130 K, $\rho_{\rm CP}$=0.508 g cm^{-3}, $P_{\rm CP}$=0.13 GPa, and $S_{\rm CP}$=5150 J kg^{-1} K^{-1}.

Planetary impact events commonly generate the shock pressures required for vaporization upon decompression (100's GPa). The revised critical shock pressures for vaporization are lower than previously estimated, primarily due to the revised entropy on the quartz Hugoniot (Table 2.6). Based on the systematics of silicate fluids, we expect similar revision of the Hugoniot entropies of major mantle minerals. Hence, shock-induced vaporization is a significant process during the end stage of planet formation and subsequent impact cratering events.

Chapter 3

Vaporizing Planetesimal Cores and Entropy on the Iron Hugoniot

The degree of mixing and chemical equilibration between the iron cores of planetesimals and the mantle of the growing Earth has important consequences for understanding the end stages of planet formation. At the Sandia Z machine, we use a shock-and-release technique to determine the density on the liquid-vapor dome of iron, the entropy on the iron shock Hugoniot at ∼500 GPa, and the criteria for shock-induced vaporization of iron. We show that decompression from a $15^{+\mathbf{1.2}}_{-\mathbf{1.8}}$ km $\mathrm{s}^{-\mathbf{1}}$ impact will initiate vaporization of iron cores. Vaporization increases dispersal of planetesimal cores, enables more complete chemical equilibration with the mantle, and substantially reduces the highly siderophile element abundance on the Moon relative to Earth due to the expanding iron vapor exceeding the Moon's escape velocity.

This chapter is in preparation for submission with Seth Root, Raymond W. Lemke, Sarah T. Stewart, Stein B. Jacobsen, and Thomas R. Mattsson

The mechanics of mixing the iron-rich cores within planetesimals and planetary embryos into the growing Earth is central to understanding the process of core formation and the timescale for Earth's formation Kleine et al. (2009); Rubie et al. (2007). The uncertain timing of the end of the Earth's core formation, ranging from ∼30 to ∼100 Myr after the start of the Solar System Kleine et al. (2009), correlates with the unknown magnitude of metal-silicate chemical equilibration for impactors of different sizes and impact velocities. Complete equilibration via emulsification of iron in a mantle magma ocean requires mixing the cores to centimeter length scales Rubie et al. (2003). Numerical simulations of giant impacts generally find that the impactor's core penetrates through the mantle to the Earth's core Canup (2004); Cuk and Stewart (2012), and calculations of Rayleigh-Taylor instabilities and turbulent mixing do not achieve emulsification of iron cores larger than about 10 km Dahl and Stevenson (2010). Thus, previous studies suggest limited chemical equilibration of cores with the mantle.

Core formation removes highly siderophile elements (HSEs) from the mantle, but Earth's mantle contains orders of magnitude higher concentrations of HSEs than predicted by their metal-silicate partitioning coefficients Walker (2009). The concentrations and relative proportions of HSEs in the mantles of the Earth, Moon, and other planets are used to infer the accretion of chondritic planetesimals in a late veneer throughout the inner solar system Dale et al. (2012); Walker (2009). Perplexingly, the concentration of HSEs in the lunar mantle and crust is about one to two orders of magnitude smaller than expected if the Moon experienced the same population of late impactors as Earth Bottke et al. (2010); Schlichting et al. (2012); Walker (2009). To explain the low concentration of HSEs on the Moon, recent studies have proposed dynamical solutions, including the stochastic bombardment of a few large (∼ 1000 km) planetesimals Bottke et al. (2010) or enhanced gravitational focusing of slow, small (∼ 10 m) planetesimals onto the Earth Schlichting et al. (2012). However, N-body simulations of the end stages of terrestrial planet formation find

that the impact velocities of late accreting planetesimals are very large (1 to 4 times Earth's escape velocity) O'Brien et al. (2006); Raymond et al. (2009), and collisions between planetesimals are erosive Stewart and Leinhardt (2012b), leading to a size distribution of small bodies. To date, the role of shock-induced vaporization of iron cores during core formation and the addition of the late veneer has not been assessed, which is likely a result of the high value estimated for the shock pressure required to initiate vaporization, 887 GPa Pierazzo et al. (1997).

The shock pressure required for the onset of vaporization upon decompression is determined by comparing the entropy on the Hugoniot to the entropy of vaporization at ambient pressures Ahrens and O'Keefe (1972). In general, the entropy on the Hugoniot has been estimated by theoretical equation of state (EOS) models. However, the entropy on the Hugoniot may be determined more accurately by combining shock temperature measurements with thermodynamic data from lower pressures and temperatures Kraus et al. (2012a). While shock temperature measurements are relatively straightforward on transparent materials, the temperature of shocked opaque materials has been much more difficult to obtain. Consequently, experimentally-constrained thermodynamic integrations cannot be performed to determine the entropy along the Hugoniot of opaque solids such as iron, and the thermal EOS of opaque solids are generally poorly known.

Here, we developed an experimental technique to determine the entropy on the iron Hugoniot and derive the critical shock pressure for vaporization of iron. The entropy at a point on the iron Hugoniot was determined by finding the shock pressure where the release isentrope intersects the 1-bar boiling point on the liquid-vapor dome, where the entropy is experimentally constrained Chase (1998). The critical release isentrope was identified by measuring the density of iron at the state where the isentrope intersects the liquid branch of the liquid-vapor dome, see Kraus et al. (2012a) and Appendix B.

Sandia National Laboratory's Z machine M. E. Savage *et al.* (2007) was used to launch aluminum

flyer plates onto ∼200-μm thick samples of iron, generating a steady, planar shock wave with amplitudes between 487 and 632 GPa, significantly greater than what is achievable on a two-stage gas gun Brown et al. (2000) yet with similar accuracy. Upon the shock wave reaching the downrange free surface of the iron sample, a rarefaction wave propagates back into the sample, simultaneously accelerating and decompressing the iron along an isentropic path from the Hugoniot state to zero pressure. Due to the discontinuous change in sound velocity at the intersection of the isentrope with the liquid-vapor dome, the rarefaction wave splits into two separate waves, generating a region of material between the two waves that is inertially trapped on the liquid branch of the liquid-vapor dome. The decompressing iron expands uniaxially across a gap of known distance and impacts a standard window where the impact velocity of the inertially trapped liquid iron was determined by its transit time across the gap (multiple gap distances and two different standard windows were used). The density of the inertially-trapped liquid is determined by measuring the steady shock state generated in the window, as in a reverse impact experiment (see Kraus et al. (2012a) and Appendix B for experimental details and development of the technique).

In Figure 3.1, the measured density on the liquid branch of the liquid-vapor dome of iron is presented as a function of the shock pressure achieved in the iron sample and compared to the density of liquid iron at the 1-bar boiling point Beutl et al. (1994); Hixson et al. (1990). The intersection of the data and the boiling point density represents the shock pressure required for the release path to intersect the boiling point. Thus, we have experimentally linked the thermodynamic state at the 1-bar boiling point to the principal Hugoniot via the release isentrope. There are sufficient isobaric heat capacity measurements on solid and liquid iron at 1-bar to perform an experimentally-constrained thermodynamic integration from 0 K to the boiling point temperature, 3133±70 K, to calculate the entropy at the boiling point, 2240±60 J kg^{-1} K^{-1} Chase (1998). We find that the 1-bar boiling point entropy is achieved at 507(+65,-85) GPa on the iron principal

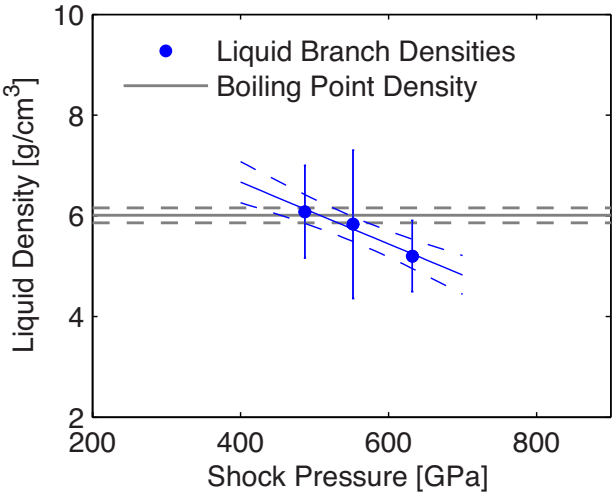

Figure 3.1: Iron density at the intersection of the release isentrope with the liquid branch of the liquid-vapor dome as a function of shock pressure (points) and the density of liquid iron at the 1-bar boiling point, see Beutl et al. (1994); Hixson et al. (1990) and Appendix B, (horizontal line) with 1σ confidence interval (dashed lines). The intersection between the release densities and the density at the boiling point determines the critical shock pressure to release to incipient vaporization.

Hugoniot. Hence, the critical shock pressure in iron required for the onset of vaporization upon decompression to 1-bar is 507(+65,-85) GPa.

Our experimentally-determined critical shock pressure for incipient vaporization of iron is significantly lower than a widely used theoretical estimate of 887 GPa Pierazzo et al. (1997). There are large differences between our result and the entropies on the most common theoretical Hugoniots used for planetary science and physics applications, shown in Figure 3.2. The entropy along the iron Hugoniot by Kerley (1993) is too high, which is consistent with the model's melting temperatures being lower than recent experiments Anzellini et al. (2013). The entropy on the ANEOS Hugoniot for iron Thompson and Lausen (1972) is too low and predicts a critical pressure for incipient vaporization that is too high, ∼635 GPa. These EOS models were developed without experimental constraints on the temperature or the entropy along the Hugoniot; our data will significantly improve future EOS models.

The entropy on the Hugoniot is a critical parameter for understanding shock-induced phase

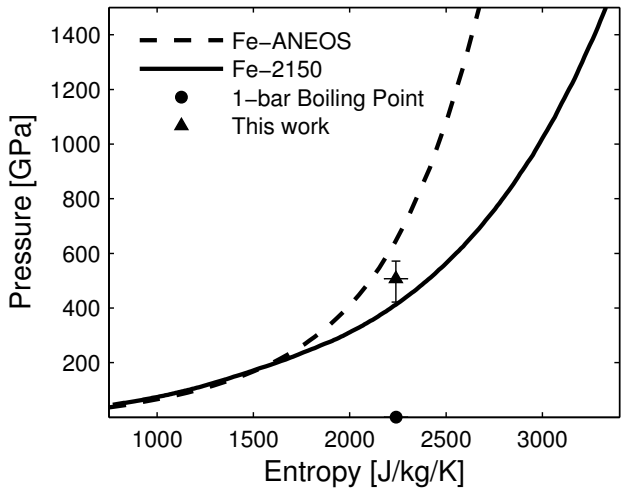

Figure 3.2: Comparison of the SESAME 2150 EOS for iron Kerley (1993), the ANEOS EOS for iron Thompson and Lausen (1972), and our data point for the entropy on the iron Hugoniot. Also shown is the entropy at the 1-bar boiling point Chase (1998).

changes during planetary impact events. With our data, we are able to accurately determine the critical impact velocity of a differentiated impactor that will lead to vaporization of the iron core upon decompression to 1-bar. Using the known Hugoniots for enstatite Spaulding et al. (2012), a proxy for the mantle, and iron (see Appendix B), we calculated the shock pressure and entropy in the impactor core assuming a planar impact approximation. Using the lever rule and the 1-bar entropies for incipient and complete vaporization, the percentage of vaporized iron core is determined as a function of the impact velocity of a differentiated impactor colliding with the proto-Earth mantle, shown in Figure 3.3A.

To place the critical impact velocities for vaporization in context, we compare our results to the distribution of planetesimal impact velocities onto bodies that are greater than 0.8 M_{Earth} from N-body simulations of terrestrial planet formation Raymond et al. (2009), which are representative of the impact velocities during the late veneer (Figure 3.3B). A significant fraction of these collisions achieve partial vaporization of an iron core. The large volume change associated with adiabatic expansion of iron vapor will accelerate core material away from the impact site. The expansion

velocities for iron vapor are large enough to gravitationally escape the Moon but not Earth (see Appendix B). Simulations of impacts by icy bodies onto the Moon find that partial vaporization is a critical factor in the escape of bulk impactor material from the Moon Artemieva and Shuvalov (2008). If the impactors were undifferentiated, then impact vaporization of the silicate/volatile matrix would drive dispersal of the iron metal Kraus et al. (2010, 2012a) at much lower impact velocities (e.g., shock-vaporization of SiO_2 begins at $\sim$7 km s^{-1} Kraus et al. (2012a)). Thus, we predict that shock-induced vaporization during a high-velocity late veneer leads to a lower concentration of HSEs being retained on the Moon compared to Earth and novel dynamical conditions are not required.

Core formation involves the accretion of both planetesimals and larger planetary embryos, which typically have lower impact velocities than planetesimals. For impactors that do not penetrate through the mantle (Figure 3B) and have impact velocities large enough to initiate vaporization, the adiabatic expansion of the partially vaporized iron core will enhance dispersal of iron over a large surface area of the Earth (see Appendix B). If a magma ocean were present or generated during the impact, then vapor-driven dispersal would increase the degree of chemical equilibration between impactor cores and Earth's mantle. Because impact velocities increase during planet formation, the degree of vapor enhanced equilibration increases with time.

During impact events at the end stages of planet formation, shock induced-vaporization of iron is an important process, contributing to metal-silicate equilibration during core formation and the difference in HSE abundance between the Earth and Moon. Detailed calculations of the magnitude of the expected difference in the HSEs retained on the Earth and Moon will require knowledge of the size and velocity distributions of late impacting planetesimals, which is presently poorly constrained due to the computational burden associated with the large number of bodies. In addition, new EOS models for use in hydrocode simulations are needed to be able to calculate vapor-driven escape of

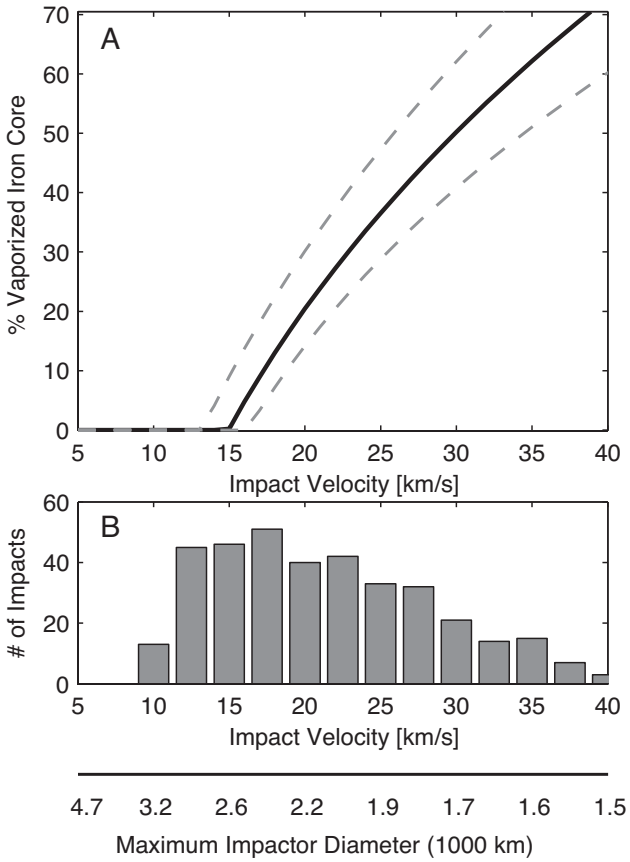

Figure 3.3: A. Vaporization fraction of iron cores as a function of impact velocity for 300 K initial temperature with 1σ confidence interval. For an initial temperature of 1500 K, the core begins to vaporize at 13 km s^{-1}. B. Histogram of impact velocities onto Earth-mass planets from N-body simulations of planet formation Raymond et al. (2009). Most impactors onto the Earth and Moon achieve partial vaporization of their cores. At each impact velocity, bodies larger than the estimated maximum impactor diameter may penetrate through Earth's mantle to the core (see Appendix B). Partial vaporization aids the dispersal of the cores of impactors smaller than this size limit.

impacting planetesimals.

The shock-and-release experiments described here traverse a wide range of states within the warm dense matter (WDM) region of phase space. WDM is exceptionally difficult to explore experimentally and complicated to model from first principles; yet, reliable descriptions of the WDM region are needed for accurate simulations of the most pressing problems in shock physics and planetary science. Our experimental techniques to measure the density on the liquid-vapor dome and the entropy on the Hugoniot provide an extremely sensitive test for the physics models employed in EOS development. These techniques are completely general, and we anticipate they will be used to probe the poorly understood regions of the EOS for a wide range of elements and compounds of key importance in physics, geophysics, and planetary science.

Chapter 4

Impact Induced Melting and Vaporization of H_2O Ice

Shock-induced melting and vaporization of H_2O ice during planetary impact events are widespread phenomena. Here, we investigate the mass of shock-produced liquid water remaining within impact craters for the wide range of impact conditions and target properties encountered in the solar system. Using the CTH shock physics code and the new 5-phase model equation of state for H_2O, we calculate the shock pressure field generated by an impact and fit scaling laws for melting and vaporization as a function of projectile mass, impact velocity, impact angle, initial temperature, and porosity. Melt production nearly scales with impact energy, and natural variations in impact parameters result in only a factor of two change in the predicted mass of melt. A fit to the π-scaling law for the transient cavity and transient-to-final crater diameter scaling are determined from recent simulations of the entire cratering process in ice. Combining melt production with π-scaling and the modified Maxwell Z-model for excavation, less than half of the melt is ejected during formation of the transient crater. For impact energies less than about 2×10^{20} Joules and impact velocities less than about 5 km s^{-1}, the remaining melt lines the final crater floor. However, for larger impact energies and higher impact velocities, the phenomenon of discontinuous excavation in H_2O ice concentrates the impact melt into a small plug in the center of the crater floor.

An amended version of this Chapter was published with Laurel E. Senft and Sarah T. Stewart in Icarus Vol. 214, 724-738, 2011.

4.1 Introduction

Impact craters are the most common geologic feature on planetary surfaces. Bolides impacting at typical velocities of a few to several 10's of km/s (Zahnle et al., 2003) achieve shock pressures capable of melting and vaporizing H_2O ice (Stewart et al., 2008). In some cases, impact-generated crater lakes may persist for geologically interesting timescales (Artemieva and Lunine, 2005; O'Brien et al., 2005; Thompson and Sagan, 1992). Giant impact events, which dominated the late stages of planetary accretion, may generate oceans of melt (Tonks and Melosh, 1993). Finally, an intense period of impact events could also lead to differentiation of a planet or satellite (e.g., Barr and Canup, 2010; Monteux et al., 2009; Tonks and Melosh, 1992; Tonks et al., 1993).

Impact events have also shaped planetary atmospheres. The production of vapor during accretionary impacts contributes shock-released volatiles to the growth of terrestrial atmospheres (e.g., Benlow and Meadows, 1977; Lange and Ahrens, 1982). However, when the mass of vaporized material becomes sufficiently large, rapid expansion may lead to partial loss of a pre-existing atmosphere (e.g., Ahrens, 1993; Melosh and Vickery, 1989; Shuvalov, 2009).

At present, it is difficult to predict the mass of melted and vaporized material associated with a particular size impact crater on ice-rich surfaces. Laboratory scale experiments do not produce significant amounts of melt, and unlike cratering on rocky planets, ground truth data does not exist for planetary scale craters in ice. Observations of crater melt sheets on the icy bodies of the outer solar system are limited (e.g., Schenk and Turtle, 2009) and complicated by the negative buoyancy of liquid water over ice.

Recent developments in shock physics models of the equation of state (EOS) and rheology of H_2O ice have led to simulations of full crater formation that reproduce much of the diversity of morphological features observed on icy bodies (Senft and Stewart, 2008, 2011). In particular, the

inclusion of high-pressure solid polymorphs in the EOS leads to an unusual phenomenon during crater formation in ice called discontinuous excavation (Senft and Stewart, 2011). Discontinuous excavation causes a concentration of impact melt in a small plug in the crater floor of similar dimensions to observed central pit features on the largest icy satellites.

In this work, we present calculations of shock-induced melting and vaporization of H_2O ice for the range of impact and target conditions found in the solar system. Our parameter space spans low velocity accretionary impacts to the highest velocity cometary impacts and considers the relatively warm solid ice of Earth to cold porous ice of Kuiper Belt objects. This work considers more impact and target parameters for impact induced melting and vaporization than included in previous studies. We also determine the fraction of shock-induced melt ejected from the crater using the modified Maxwell Z model (Croft, 1980; Maxwell, 1977). Then using crater size scaling relationships, the amount of melt produced during an impact event is related to the final crater size.

Section 4.2 provides a description of the numerical model, the equation of state, and the entropy method used to calculate the mass of material that was melted or vaporized. In section 4.3, the effects of impact angle, temperature, impactor composition, and porosity are presented, and two scaling equations are derived to predict the amount of melt and vapor produced for any impact condition. Section 4.4 discusses aspects of the calculations in more detail, compares the results to previous work, and addresses more complicated scenarios including icy mixtures. To estimate the mass of melt and vapor for a given size crater, section 4.5 presents scaling relationships for transient craters in ice, the mass of ejected melt during transient crater formation, and crater collapse.

4.1.1 The Shock Pressure Field from an Impact Event

When an impactor strikes a target, a strong shock wave propagates into the target and back into the impactor. The highest shock pressures are generated below the impact point in a nearly isobaric volume of target material called the isobaric core. The hemispherical shock front propagates into the target, decaying in amplitude with distance and depositing internal and kinetic energy. Above material-dependent critical shock pressures, the deposited internal energy is sufficient to melt or vaporize the target upon release to ambient pressure.

Croft (1982) developed a semi-analytic model for shock wave decay and found that the shock pressure P at a radial distance R is given by

$$P(R) = P_0 \left(\frac{R_{ic}}{R} \right)^n \tag{4.1}$$

where P_0 is the pressure at the radius R_{ic} of the isobaric core. The decay exponent n depends on both the material and impact velocity (Ahrens and O'Keefe, 1977; Pierazzo et al., 1997), and ranges from 1 to 3 for a wide range of nonporous materials.

The residual kinetic energy of the target after passage of the shock wave creates a divergent flow of material centered on the isobaric core, which leads to formation of the transient crater cavity (Croft, 1980; Maxwell, 1977). The excavated volume overlaps with the volume of most highly shocked material; hence, a significant fraction of melt is ejected from the crater. The melt that is not ejected lines the walls and floor of the transient crater. The shape of the transient crater is gravitationally unstable and must collapse to some degree. Smaller, simple craters undergo relatively little collapse. The walls of the transient crater slump, and a melt-rich breccia lines the bottom of the final bowl-shaped crater. The greater gravitational instability in larger transient craters leads to a more significant collapse and the formation of complex crater morphologies. The

spatial distribution of the melt sheet in complex craters depends on the final morphology (e.g., a central peak or peak-ring crater). For a more complete description of the dynamics of the impact cratering process see Melosh (1989).

4.1.2 Previous Work

Previous researchers have estimated the total amount of melt generated in an impact event by calculating the shock pressure decay field. We acknowledge the semi-analytic estimates for vaporization of water and melting of ice by Croft (1982, 1983). However, such semi-analytic approaches have been superceded by the use of a shock physics code coupled with an EOS model to calculate the pressure decay field in the target with much higher accuracy (e.g., Ahrens and O'Keefe, 1977; Artemieva and Lunine, 2003, 2005; Pierazzo and Melosh, 2000; Pierazzo et al., 1997). The mass of melt plus vapor is derived by calculating the volume of material that exceeded the critical shock pressure for melting. In particular, the comprehensive study by Pierazzo et al. (1997) calculated the volume of melt plus vapor produced for vertical impacts onto a wide range of materials. They found that most materials follow a single scaling law:

$$\log\left(\frac{V_m}{V_i}\right) = a + \frac{3}{2}\mu \log\left(\frac{U^2}{E_M}\right). \tag{4.2}$$

The form of Eq. 4.2 comes from an analytical analysis of melt volumes by Bjorkman and Holsapple (1987), where V_M is the volume of melt, V_i is the impactor volume, U is the impactor velocity, and E_M is the specific internal energy required to reach complete melting upon decompression from the shocked state on each material's principal Hugoniot. The nondimensional U^2/E_M is called the melt number. The values for the intercept, a, and the velocity exponent of the coupling parameter of Holsapple and Schmidt (1982), μ, were fitted to the combined simulation results for dunite, granite, aluminum, and iron to obtain $a = -0.80 \pm 0.14$ and $\mu = 0.709 \pm 0.041$ for $U^2/E_M > 30$ (Pierazzo

et al., 1997).

In Pierazzo et al. (1997), only H_2O ice deviated from Eq. 4.2, with about an order of magnitude greater melt volume. Artemieva and Lunine (2003, 2005) also calculated the volume of melt produced for impacts onto Titan using a revised water EOS (Turtle and Pierazzo, 2001) and found about an order of magnitude less melt than Pierazzo et al. (1997). However, a direct comparison of the two studies is imperfect as Pierazzo et al. (1997) considered vertical impacts onto nonporous ice and Artemieva and Lunine (2003, 2005) investigated impacts onto much colder ice with an 800-m porous surface layer. Barr and Citron (2011) studied impact melt production in a variety of materials including nonporous H_2O ice; they also found about an order of magnitude less melt compared to Pierazzo et al. (1997).

4.2 Methods

As discussed briefly in the introduction, calculating the amount of melt and vapor produced from an impact event is qualitatively very simple: i. determine the maximum shock pressure achieved as a function of initial position within the target and ii. compare the pressure field in the target to the critical shock pressures for melting and vaporization.

4.2.1 Numerical Model

The shock pressure field was calculated with the widely used Eulerian finite-volume shock physics code CTH (McGlaun et al., 1990). We considered impact velocities from 1-80 km s^{-1}, initial temperatures from 50-300 K, porosities of 0-60%, impactor compositions of a porous comet to a rocky asteroid, and impact angles from vertical to 30 degrees from the horizontal. To keep the melting and vaporization results general, gravity and thermal gradients were not included. The projectile diameter was 1 km in all simulations, and as it is the only length scale in the calculation,

the results can be scaled to other projectile sizes. The simulations were run until the shock wave decayed to pressures well below that required for melting (typically several seconds for the 1 km diameter projectile considered in this study). A separate set of full crater formation simulations was used to determine scaling laws for the transient crater diameter and crater collapse. A short description of the full crater formation simulations is provided in Section 4.5.1.

To complete the conservation equations, an equation of state provides the relation between density, energy, and pressure. A tabulated version of the ANEOS model by Melosh (2007) was used for the SiO_2 bolide. H_2O is modeled using the 5-phase EOS (Senft and Stewart, 2008), which includes ice Ih, ice VI, ice VII, liquid, and vapor. The 5-phase model EOS includes all phases identified on the ice shock Hugoniot (Stewart and Ahrens, 2005), although many more stable and metastable phases have been identified (primarily at low temperatures and high pressures) (Dunaeva and Antsyshkin, 2010; Petrenko and Whitworth, 1999). The model follows experimentally determined phase boundaries with the exception of an artifical boundary between ice Ih and ice VI. The model achieves excellent agreement with experimental Hugoniots for nonporous H_2O ice and liquid water (Senft and Stewart, 2008) and experimental shock and post-shock temperatures (Stewart et al., 2008). The 5-phase EOS is the first EOS used in shock-induced melting and vaporization calculations to include high-pressure solid polymorphs. The formation of high-pressure polymorphs is expected to modify the shock pressure decay exponent (Eq. 4.1) due to their higher shock impedance (density times sound speed) compared to liquid water and ice Ih.

Porous ice is also described by the 5-phase EOS using a $P-\alpha$ model with no strength (Herrmann, 1969), which is also known as a snow plow model. In the snow-plow model, the porous ice is assumed to compact to solid density immediately upon compression. The crush-up strength of laboratory porous ice is known to be small ($<\sim 0.25$ GPa Stewart and Ahrens, 2004), although natural porous ice is expected to have variable context-specific strength. Porous Hugoniots have higher shock

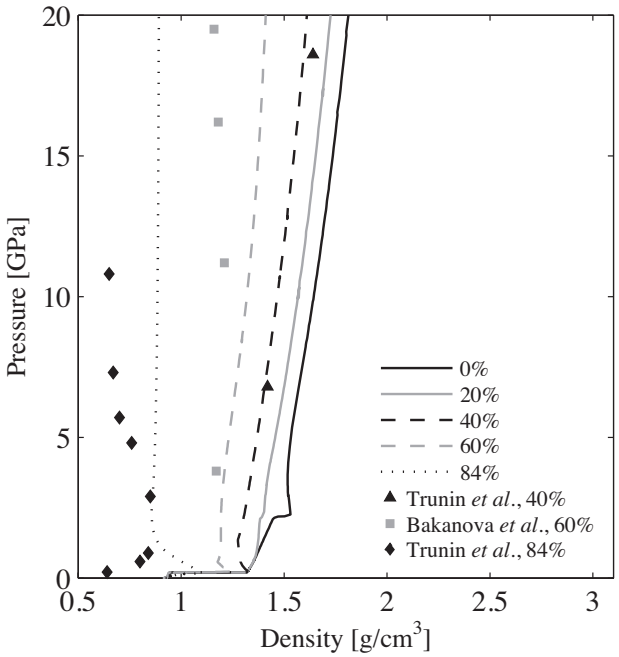

Figure 4.1: Comparison of 250 K porous Hugoniots derived from the 5-phase EOS for H_2O ice (lines) with experimental data for 40 and 84% porous ice (Trunin et al., 1999) and 60% porous ice (Bakanova et al., 1975) (points).

temperatures compared to the solid (at the same pressure) due to the extra work from the volume compression of the pores (Zel'dovich and Raizer, 1966). The accuracy of the 5-phase model EOS in predicting porous Hugoniots is shown in Figure 4.1. At intermediate porosities the model porous Hugoniots are in good agreement with the experimental data. At the highest porosity, the 5-phase EOS does not predict enough thermal pressure.

All calculations used to determine melt and vapor mass are hydrodynamic. CTH can also calculate deviatoric stresses if a constitutive equation is provided. However, the stresses considered in this study of melt and vapor mass are generally much greater than the Hugoniot elastic limit of ice (Stewart and Ahrens, 2005); consequently, the hydrodynamic approximation is adequate. We tested the hydrodynamic approximation by calculating the pressure field using the strength model for ice from Senft and Stewart (2008) for an impact onto solid ice at 50 K (the elastic strength is highest at low temperature). There was less than a 2% difference compared to the hydrodynamic

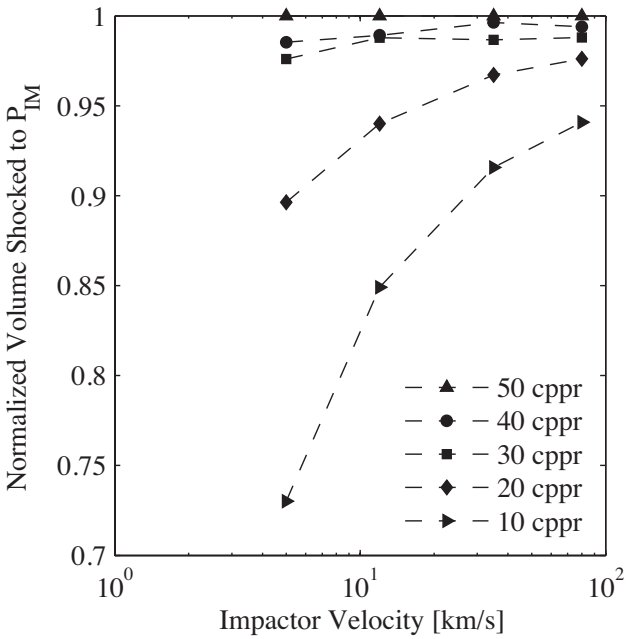

Figure 4.2: Comparison of the cumulative volume of target that is shocked to or above the pressure of initiating melting in ice at 150 K ice, P_{IM}. The volumes are normalized to the cumulative volume of target shocked above P_{IM} with a computational mesh of 50 cells per projectile radius (cppr).

pressure field.

To avoid uncertainties related to the cell size in the numerical integration scheme employed in CTH, a series of vertical impact simulations were performed at different computational mesh resolutions and impact velocities. In Figure 4.2, the volume of ice shocked to the critical pressure for incipient melting, 1.60 GPa for an initial temperature of 150 K (Stewart et al., 2008), is compared for mesh resolutions ranging from 10 computational cells per projectile radius (cppr) to 50 cppr. 40 cppr predicts volumes within 2% of 50 cppr for the wide range of impact velocities considered here, suggesting that 50 cppr is asymptotically approaching the theoretical limit for accuracy in the numerical model. One can also see from Figure 4.2 that any uncertainty derived from mesh resolution increases with lower impact velocities, which is discussed in more detail in Davison et al. (2010). To minimize computational time and maximize accuracy, a fixed resolution of 40 cppr is used for all the vertical impact simulations and 20 cppr for the three dimensional simulations. The

simulations did not use CTH's adaptive meshing capabilities.

In the two (three) dimensional simulations, a large rectangular (cuboid) grid of 10,000 Lagrangian tracers was used to record the pressure field of the shocked H_2O as a function of position and time within the icy target. The maximum pressure achieved at each tracer constitutes the peak shock pressure and the tracers are then combined to map the pressure decay field. The volume of material shocked to a critical pressure P^* was determined by adding up the separate volume elements represented by each tracer particle that reached a pressure equal to or greater than P^*. The cumulative volumes above P^* were calculated from 0.1 to 1000 GPa.

The uncertainty in the cumulative volume is partially dependent on the tracer resolution. The resolution in the large tracer grid was 160 m (680 m) between tracers in the two (three) dimensional simulations. A smaller but higher resolution grid of tracers was placed directly below the impact point to accurately track the decay near the quasi-isobaric core. The tracer resolution may seem significantly worse in the three dimensional simulations, however, because of the superimposed smaller grid at a resolution of 160 m between tracers, the three dimensional tracers have only a 3% higher uncertainty than the two dimensional grid. Tracer resolution tests were performed for the two dimensional simulations and suggest less than 5% uncertainty in the melt volumes is created by the current tracer configuration for impact velocities above 10 km s^{-1}. For impacts below 5 km s^{-1}, where the volume of ice melted and/or vaporized is on the order of the projectile volume, the uncertainty due to the tracer configuration could be up to 50%. However, to minimize the uncertainty, the maximum pressure field was linearly interpolated onto a finer grid of twice the resolution to decrease the uncertainty for impact velocities below 5 km s^{-1} to less than 25%.

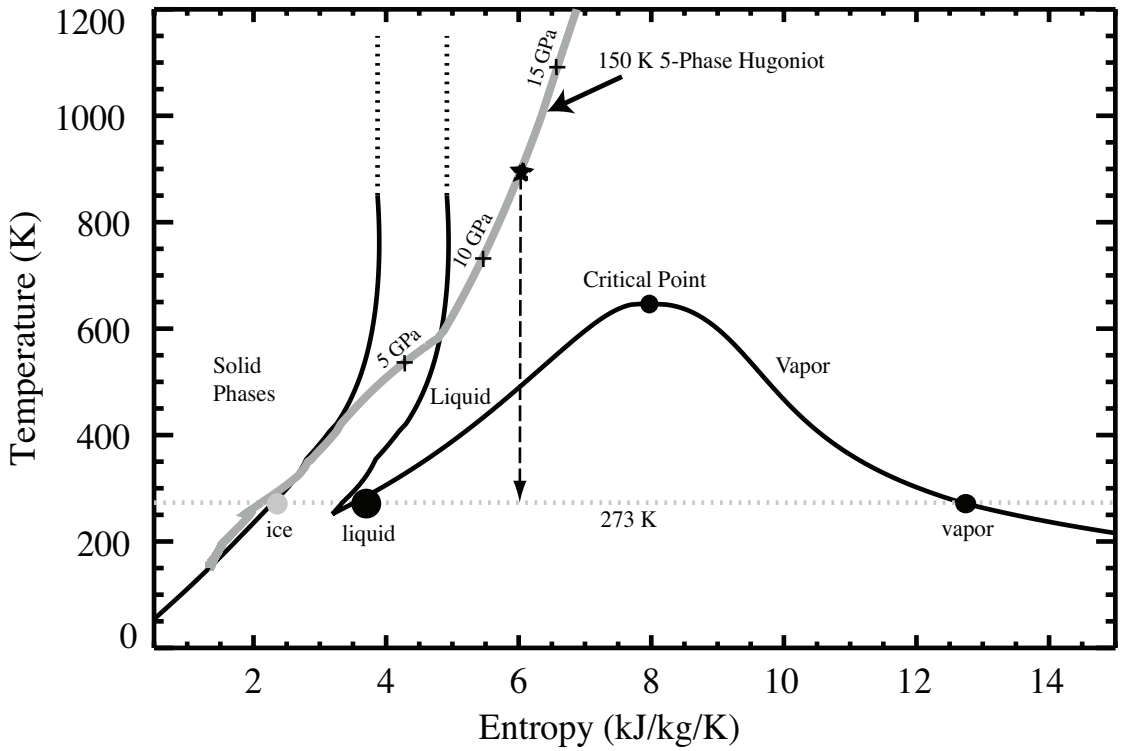

Figure 4.3: H_2O phase diagram in temperature-entropy space from the 5-phase model equation of state (EOS) (Senft and Stewart, 2008). The EOS includes ice Ih, ice VI, ice VII, liquid, and vapor. Example release from a point (star) on the shock Hugoniot (grey line) to the triple point; the relative mass of liquid and vapor is determined from the lever rule.

4.2.2 Critical Entropy Method

Shock waves compress a material to a line on the equation of state known as the Hugoniot. Decompression from the shocked state is adiabatic and, more specifically, isentropic. For a parcel of material, the entropy in the decompressed state is the same as the entropy in the shocked state (Figure 4.3). The cumulative volume greater than a given shock pressure P^* can thus be converted to the cumulative volume above a given entropy S^*. Ahrens and O'Keefe (1972) first used the change in entropy in the shock wave as a criterion for phase transitions on decompression to the final state. More recently, Pierazzo et al. (1997), Pierazzo and Melosh (2000), and Artemieva and Lunine (2003, 2005) used the entropy method to determine the critical pressure for complete melting upon decompression to one atmosphere of pressure.

For a given final entropy, the final phase on release from shock depends on the ambient pressure. Rather than one atmosphere, we use the triple point pressure of H_2O as the reference decompressed state (611 Pa). The triple point is a widely applicable reference state for many bodies in the solar system as decompression to ambient pressures lower than the triple point will pass through the triple point (c.f. Senft and Stewart, 2011). Using the triple point as the reference leads to calculation of the minimum mass of liquid water that would transiently exist before thermal equilibration with the planetary body's ambient pressure and temperature. For bodies with higher atmospheric pressures, e.g. 1 bar on Earth, the amount of melt could be ∼10-15% greater than what is presented here. The critical pressures for melting and vaporization upon release to the triple point pressure are presented in Table 4.1 for a range of temperatures and initial porosities. The critical pressures derived from the 5-phase EOS are also compared with critical pressures from several previously used model equations of state for H_2O. For material that reaches entropy states between incipient and complete melting and vaporization, the volumes of partial melt and vapor were determined using the lever arm rule as illustrated in Figure 4.3.

Table 4.1: Critical shock pressures (Stewart et al., 2008) for incipient melting (IM), complete melting (CM), incipient vaporization (IV), and complete vaporization (CV) as a function of initial target temperature and porosity (ϕ) for the 5-phase EOS (Senft and Stewart, 2008) compared to previous work. In this study, critical pressures for IM, CM, IV, and CV are determined for reaching critical entropies of 2.29, 3.51, 3.51, and 12.67 kJ/kg/K, respectively, which represents the entropies on the solid, liquid, and vapor phase boundaries at the triple point pressure of H_2O (611 Pa). Critical pressures for other equations of state are determined for release to 1 bar.

EOS	P_{IM} [GPa]	P_{CM} [GPa]	P_{IV} [GPa]	P_{CV} [GPa]	E_M [J/kg]
5-Phase, 50 K	2.1	3.96	3.96	70.4	8.42×10^5
5-Phase, 150 K	1.60	3.48	3.48	69.6	8.20×10^5
5-Phase, 250 K	0.49	2.69	2.69	66.9	8.05×10^5
5-Phase, 150 K,ϕ=0.2	0.78	2.20	2.20	46.20	7.85×10^5
5-Phase, 150 K, ϕ=0.4	0.48	1.23	1.23	28.36	7.20×10^5
5-Phase, 150 K, ϕ=0.6	0.24	0.62	0.62	15.39	6.60×10^5
Kieffer (1980)	3	10	–	–	-
Ahrens and O'Keefe (1985), 263 K	7.6	9.8	–	–	-
Tonks et al. (1993), ∼260 K	0.4	3	4.5	43	8×10^5
Turtle and Pierazzo (2001), 93 K	6	9.1	14.2	–	-

4.3 Results

4.3.1 Dependence on Impact Parameters

We follow the same general form of scaling law as developed by Bjorkman and Holsapple (1987), except the mass of material melted or vaporized and the mass of material vaporized, M_{M+V} and M_V, is scaled by the mass of the impactor M_i,

$$\log\left(\frac{M_{M+V}}{M_i}\right) = a + \frac{3}{2}\mu\log\left(\frac{U^2}{E_M}\right), \tag{4.3}$$

where the parameters a and μ are the same as Eq. 4.2 if the target and impactor are of the same density. Rather than presenting the volume of material that is melted or vaporized, we present the mass of material that is melted and vaporized for a number of reasons: 1) mass is conserved and hence the results are not ambiguous with respect to porosity, 2) the energy partitioned to the latent heat of melting and vaporization is straightforward to calculate, and 3) different impactor materials are easily treated, as the effect of a density contrast between target and impactor is included in scaling to the mass of the impactor (see Section 4.3.1).

In general, a and μ can be functions of all the variables that can be used to describe the impact event: impact velocity U, angle from horizontal θ, temperature T, porosity ϕ, and density contrast between impactor and target ρ_i/ρ_t. We investigate the functional form of $a = F\left(\theta, T, \phi, \rho_t, \rho_i\right)$ and $\mu = G\left(\theta, T, \phi, \rho_t, \rho_i\right)$ over the range of variable space that might be found in our solar system.

Because we consider projectiles of different compositions, the reported mass of melt does not include projectile material. Partial melt of the target is included.

Impact Angle

Without gravitational focusing the probability of an impact within an interval (θ, θ+dθ) is proportional to $\sin(\theta)\cos(\theta)\mathrm{d}\theta$ (Shoemaker, 1962). Consequently, the probability of a vertical impact is zero and 45 degrees is the most likely angle of impact. As seen by Pierazzo and Melosh (2000), the amount of impact melt decreases significantly with decreasing angle of impact. However, Pierazzo and Melosh (2000) looked at a complicated subsurface structure related to the Chixculub impact event at a single impact velocity (20 km s^{-1}); melt scaling in a homogeneous icy body may not scale in the same manner and may also depend on impact velocity. Artemieva and Lunine (2005) performed a number of simultions of oblique impacts onto a proxy for the surface of Titan; the upper 800 m of the target was porous, again complicating the scaling of the amount of melt to other situations.

The current study of oblique impacts into homogeneous H_2O ice surfaces covers a wide range of impact velocities and angles. As three dimensional runs are computationally expensive, only three impact velocities were considered (12, 25, and 65 km s^{-1}) with a starting target temperature of 150 K and no porosity. The impactor was a nonporous H_2O ice bolide. Figure 4.4 shows the maximum pressure contours for the three dimensional impact simulations. To determine the relative effect of an oblique impact, we normalize M_{M+V} for impacts at angle θ to M_{M+V} for a vertical impact (Figure 4.5). The mass of melt and vapor, normalized to the vertical impact, scales well to a power law of the sine of the angle of impact for all impact velocities,

$$\frac{M_{M+V}(\theta)}{M_{M+V}(90^\circ)} = \sin^n(\theta), \text{and} \tag{4.4}$$

$$\frac{M_V(\theta)}{M_V(90^\circ)} = \sin^m(\theta), \tag{4.5}$$

where $n = 0.7 \pm 0.07$ and $m = 0.6 \pm 0.08$; and there is a negligible dependence of the exponent of the

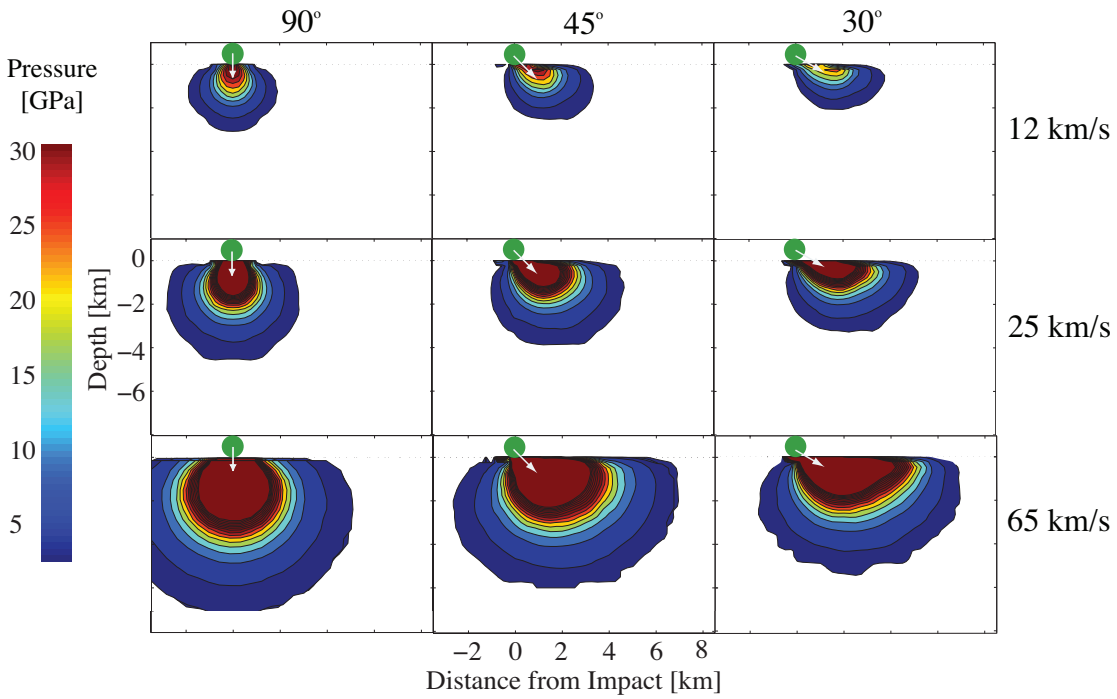

Figure 4.4: Cross section of a contour plot of maximum shock pressure as a function of position within the 150 K targets. Impacts occurred at 12, 25, and 65 km s^{-1} at angles of 90, 45, and 30 degrees from the horizontal. The largest contour line represents the region that has reached the entropy of incipient melting and within the smallest contour line the ice is completely vaporized.

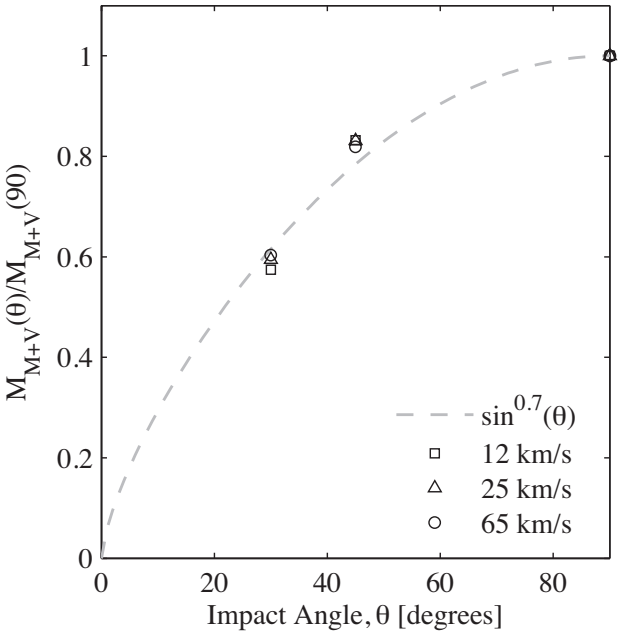

Figure 4.5: Scaled mass of material that has been melted and vaporized, as a function of impact velocity and impact angle. The mass of melt and vapor is normalized to that produced in a vertical impact. The effect of impact angle is independent of impact velocity.

coupling parameter μ on the impact angle. These results are in rough agreement with the power law fit for the melt volume data presented in Table III of Pierazzo and Melosh (2000). However, rather than presenting the $\sin^{0.8}(\theta)$ dependence for the melt volume in their simulations, Pierazzo and Melosh (2000) suggested one could treat oblique impacts as vertical impacts by artificially decreasing the size of the projectile to a vertical equivalent diameter D^{eq}_{proj}. We prefer to keep a direct dependence on impact angle for the scaling relationships as the projectile mass is used as the normalization factor.

Temperature Dependence

To test the relative effect of temperature on the amount of melt and vapor produced, initial ice temperatures were varied from what one might measure on the glaciers of Earth ($\sim$ 250 K) to the moons of Pluto ($\sim$ 50 K). The impactor for each simulation was an H_2O ice bolide at the same

temperature as the ice target (hereafter we refer to impacts with the bolide the same composition as the target as symmetric impacts). As the temperature of the target increases, the initial entropy increases, and hence the critical pressure required for melting and vaporization decreases. Figure 4.6 presents the normalized mass of H_2O that has been melted and vaporized, including partial melt and vaporization, as a function of melt number and temperature. Note that the melt energy E_M, derived from the 5-phase EOS, is a function of temperature; at 50, 150, and 250 K the melt energy, E_M, is 8.42, 8.20, and 8.05$\times 10^5$ J kg^{-1} respectively. However, for practical purposes one can use an average melt energy of 8.2$\times 10^5$ J kg^{-1} without loss of significant accuracy ($\sim$5% for 50 K ice). The melt energies used in this work are similar to that used by Pierazzo et al. (1997), E_M=8$\times 10^5$ J kg^{-1}, as determined by the ANEOS parameters from Tonks et al. (1993). To avoid using a melt energy E_M that depends on the model Hugoniot, Artemieva and Lunine (2005) suggested using the latent heat of fusion (3.33$\times 10^5$ J kg^{-1}) to scale the kinetic energy of the impactor. However, with this approach, different materials would not follow a single scaled power law as found with scaling by E_M. Hence, this study follows the work of Bjorkman and Holsapple (1987) and Pierazzo et al. (1997) and scales the kinetic energy of the impactor by the internal energy on the Hugoniot state required to reach complete melting upon decompression.

As expected, a slightly greater amount of melt and vapor is produced from surfaces with higher initial temperatures. Note that lower velocities deviate from the power law fits due to the non-negligible shock pressure required to get to the melting point (Stewart et al., 2008). A least squares fitting routine was performed for impact velocities of 8-80 km s^{-1} (melt number of ~ 80 to $\sim 8,000$). The intercept a is found to vary linearly with temperature while μ is approximately constant over the temperature range of 50 to 250 K:

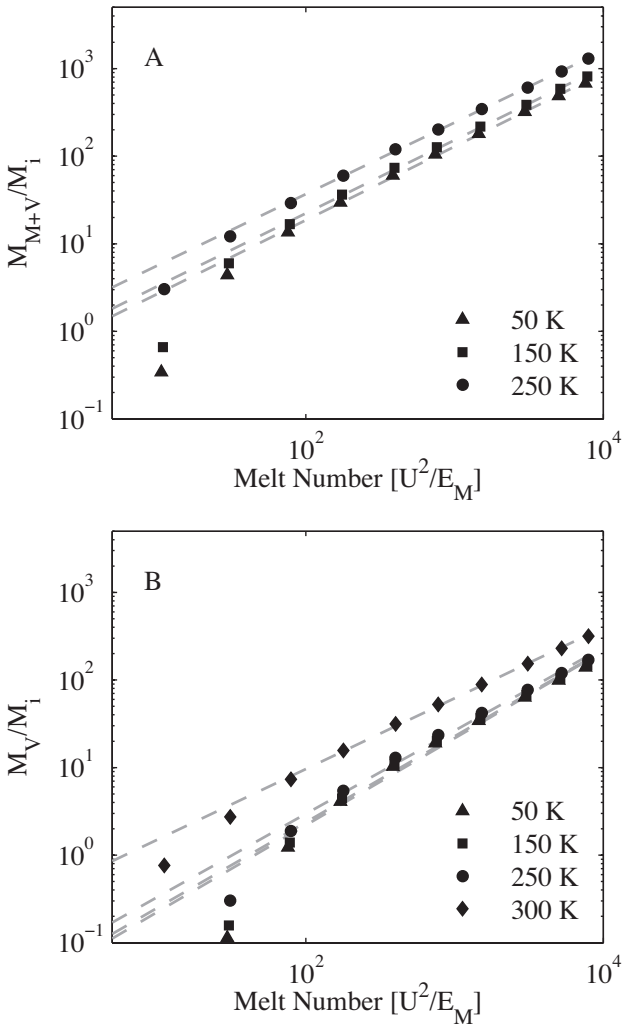

Figure 4.6: Scaled mass of H_2O ice that has been a) melted (including partial melt) and vaporized or b) vaporized upon release to the triple point pressure. Fits are valid from ∼8-80 km/s (melt number $>\sim 80$); however, the fits are extrapolated to lower velocities to show the relative error in using the fit. The normalized mass of melt does not include the impactor. In the 300 K target case, the vapor mass assumes release to 3540 Pa. As E_M is not defined for a liquid, the impact velocity for the 300 K target is scaled to the melt energy E_M for a 250 K target (8.05×10^5 J/kg)

$$a_{M+V}(T) = -0.53\,(0.1) + 0.0017\,(0.0006)\,T$$
$$\mu_{M+V} = 0.554\,(0.008)\,, \text{and} \tag{4.6}$$

$$a_V(T) = -1.71\,(0.24) + 0.0011\,(0.0001)\,T$$
$$\mu_V = 0.65\,(0.01)\,. \tag{4.7}$$

1-σ uncertainties in the fitted parameters are shown in parentheses.

We also considered a symmetric vertical impact onto a 300 K ocean at the pressure on the saturation vapor curve, 3540 Pa. The scaled mass of vapor upon release to 3540 Pa is fit by $a_V = -0.63(0.05)$ and $\mu_V = 0.54(0.01)$. In this case, the intercept a is significantly greater than Eq. 4.7 for ice extrapolated to an initial temperature of $T = 300$ K. The smaller value for a_V in ice is due to the extra energy required to overcome the latent heat of fusion.

Impactor Composition

Most solar system impactors are not the same composition as the target surface. Hence, we investigated the accuracy of scaling the mass of melt rather than the volume of melt in accounting for different impactor compositions. Previous work has shown scaling the mass of melt by the mass of the projectile would account for any density contrast between the impactor and target (Ahrens and O'Keefe, 1987; O'Keefe and Ahrens, 1977); however, the scaling has not been explicitly shown for icy bodies. To check the scaling laws for H_2O, the melt from the impact of a solid SiO_2 bolide and also a 20% porous H_2O ice bolide was calculated for a wide range of impact velocities. Velocities of the porous ice bolide were chosen to replicate the kinetic energy of the solid ice impactor at

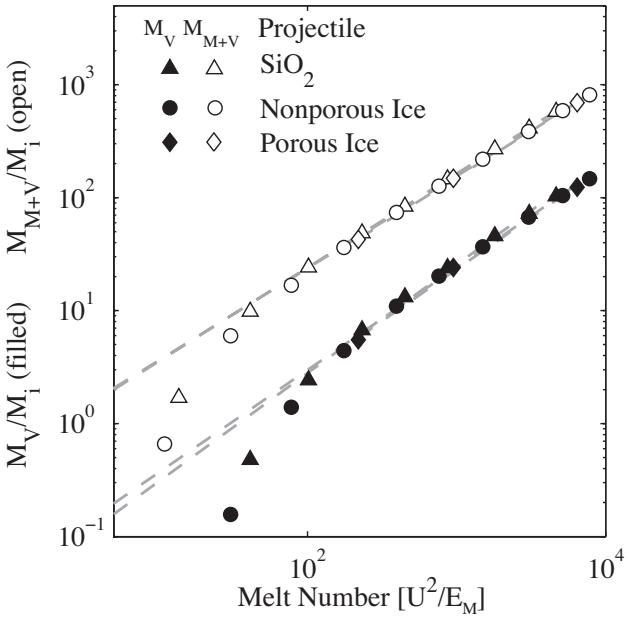

Figure 4.7: Scaled mass of H_2O ice that has been melted and vaporized (open symbols) or vaporized (filled symbols) for different projectile composition. Targets were 150 K nonporous H_2O ice; impactors were nonporous SiO_2 (triangles), nonporous 150 K H_2O (circles), and 20% porous 150 K H_2O (diamonds).

12, 25, and 65 km s^{-1}. In this series of simulations, the target was modeled as nonporous with a starting temperature of 150 K. As seen in Figure 4.7, the mass of melt and vapor, normalized to the projectile mass, follows the same scaling law, to within 6% of all fitted parameters, for a wide range of impactor densities. Consequently, scaling the mass of melt and vapor reduces the complexity of impact induced melting by removing a dependence on the density contrast between impactor and target.

Porosity

Many icy bodies in the solar system are likely to be porous throughout, e.g. comets, or have a porous surface layer. The effect of porosity on melting and vaporization has not been investigated previously for ice. We modeled vertical symmetric impacts at 12, 25, and 65 km s^{-1} into 150 K

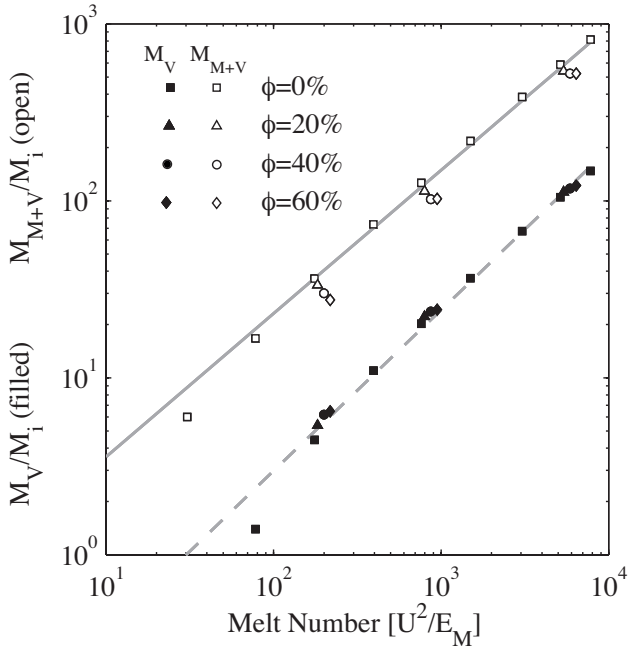

Figure 4.8: Scaled mass of H_2O ice that has been melted and vaporized (open symbols) or vaporized (closed symbols) as a function of melt number and initial porosity for vertical impacts onto 150 K targets. Best fit to the nonporous targets are shown in gray.

H_2O ice of 20, 40, and 60% porosity (Figure 4.8). Note that the melt energy, E_M, is a function of porosity (Table 4.1). For the same impact conditions, we find that up to 20% less mass of melt is produced for impacts into porous ice than solid ice. Interestingly, there is up to a 20% increase in the mass of vapor produced for impacts into porous bodies.

We find the parameter a, representing an absolute amount of melting and vaporization, is approximately linearly dependent on porosity ϕ,

$$a_{M+V}\left(\phi\right) = a_{M+V}^{\phi=0} - 0.46(0.02)\phi, \text{and} \tag{4.8}$$

$$a_{V}\left(\phi\right) = a_{V}^{\phi=0} + 0.27(0.23)\phi. \tag{4.9}$$

Unlike other impact variables investigated in this work, we found μ to be a function of porosity,

$$\mu_{M+V}\left(\phi, 150\right) = \mu_{M+V}\left(0, 150\right) + 0.07(0.01)\phi, \text{and} \tag{4.10}$$

$$\mu_{V}\left(\phi, 150\right) = \mu_{V}\left(0, 150\right) - 0.1(0.09)\phi. \tag{4.11}$$

The value of μ is expected to decrease with porosity, based on the semi-analytical analysis of shock wave decay in porous materials by Bjorkman and Holsapple (1987). The parameter μ_V behaves as expected. Although small in magnitude, the dependence of μ_{M+V} is opposite of that expected and may be due to the complicated decay profiles in the high-pressure polymorphs of H_2O ice. The dependence of μ and a on porosity is discussed below (Section 4.4.2).

4.3.2 General Scaling Laws for Impact Induced Melting and Vaporization

General scaling laws for melting and vaporization must encompass several parameters that may have subtle co-dependencies. We conducted a series of impact simulations where more than one parameter was varied (impact angle, target porosity, and impactor density). We found that the variables considered in this study may be considered independent of each other, as the mass of melt and vapor differed by only a few percent compared to the assumption of complete parameter independence.

By combining the dependencies of a and μ on temperature, impact angle, target porosity, and impactor composition, we provide two general equations for the total mass of melt and vapor (Eq. 4.12), or only vapor (Eq. 4.13), produced for impact conditions with $U >\sim 8$ km s^{-1} (a melt number of about 80):

$$\log\left[\frac{M_{M+V}}{M_i}\right] = -0.53 + 0.0017T + 0.7\log\left[\sin(\theta)\right] - 0.46\phi + \frac{3(0.554 + 0.07\phi)}{2}\log\left[\frac{U^2}{E_M(\phi)}\right] \tag{4.12}$$

$$\log\left[\frac{M_V}{M_i}\right] = -1.71 + 0.0011T + 0.6\log\left[\sin(\theta)\right] + 0.27\phi + \frac{3(0.65 - 0.1\phi)}{2}\log\left[\frac{U^2}{E_M(\phi)}\right] \tag{4.13}$$

Below $\sim$8 km s^{-1}, the melt and vapor production falls off dramatically due to the finite energy required to reach incipient melting. At $\sim$5 km s^{-1} the melting and vaporization volumes deviate below the scaling law by about a factor of two less melt and vapor; at $\sim$3 km s^{-1} the amount of melt and vapor is generally an order of magnitude less than that predicted by the scaling laws. Below 3 km s^{-1} less than half of the mass of the projectile is melted for all initial temperatures.

If one is only interested in the mass of melt produced upon impact into an icy body, then one can either subtract the amount of vapor produced, Eq. 4.13, from the amount of melt and vapor, Eq. 4.12, or simply use M_{M+V} as an approximation for the mass of melt produced. The mass of vapor is consistently two orders of magnitude less than the amount of melt produced.

In general, the mass of melt and vapor varies by less than a factor of two for impact angles between 30 and 90 degrees from vertical, temperatures from 50 to 250 K, and porosities from 0-60% for impact velocities greater than $\sim$8 km s^{-1}.

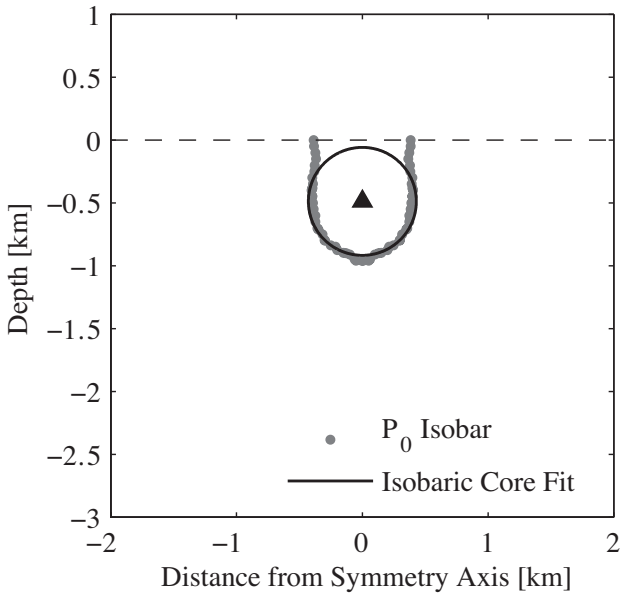

Figure 4.9: Example fit to an isobar of pressure P_0, the pressure at the perimeter of the isobaric core. One can see that a circle is a reasonable fit to the shape of the core below the surface. The depth of burial D_{ic} is the distance from the center of the circle (solid triangle) to the impact surface.

4.4 Discussion

4.4.1 Shock Wave Decay

Although we have covered a tremendous range of variable space in this study, it is still advantageous to be able to estimate the pressure field using analytical expressions, such as Eq. 4.1. Here, the radius R_0 and the depth of burial D_{ic} of the isobaric core are calculated for different impact velocities and porosities using the pressure decay field from a series of vertical symmetric impacts into 150 K H_2O ice. The pressure at the perimeter of the isobaric core, P_0 is derived from the intersection of the initially shallow power law in pressure vs. distance and the steeper power law at greater distances (e.g., Figure 4.11). The factor between the impedance match pressure and the perimeter pressure P_0 decreases as a power law from three at an impedance match pressure of 5 GPa to 1.4 at 1000 GPa (see Melosh (1989) or Ahrens (1987) for a description of the impedance matching technique).

We fit a circle to the P_0 isobar to optimize R_0 and D_{ic}, which are given in Figure 4.9. Within the uncertainties of the fits, the depth of penetration D_{ic} is insensitive to porosity. Following Pierazzo et al. (1997), the least squares fit to the depth of penetration for all impacts shown in Figure 4.10 is given by

$$\log\left[\frac{D_{ic}}{R_i}\right] = -0.17(0.03) + 0.09(0.02)\log\left[U\left(\text{km s}^{-1}\right)\right], \tag{4.14}$$

where R_i is the radius of the impactor. Note that the impactors considered in this section are of the same material as the target; a contrast in density between target and impactor can significantly change the depth of penetration and will not be considered here.

The radius of the isobaric core R_{ic} has a more significant dependence on porosity. To obtain a functional dependence of R_{ic} on porosity, we assume that velocity and porosity are independent. Then,

$$\log\left[\frac{R_{ic}}{R_i}\right] = 0.22(0.01) - 0.13(0.04)\phi - 0.18(0.01)\log\left[U\left(\text{km s}^{-1}\right)\right]. \tag{4.15}$$

One possible explanation for the decrease in R_{ic} with porosity is related to the larger relative crush-up of the impactor during the contact and compression stage. The shock wave sent back into the projectile during the contact and compression stage will crush the projectile to a nonporous state. As the size of the isobaric core depends on how quickly the decompression wave from the rear free surface of the projectile reaches the impactor-target interface; a highly porous projectile will decompress faster due to its relatively smaller non-porous diameter. Hence, the isobaric core will be smaller for more porous impactors.

Beyond the isobaric core, the divergent shock wave decays according to a power law in the radial distance R (Eq. 4.1). Shock wave decay in H_2O ice is significantly more complicated than

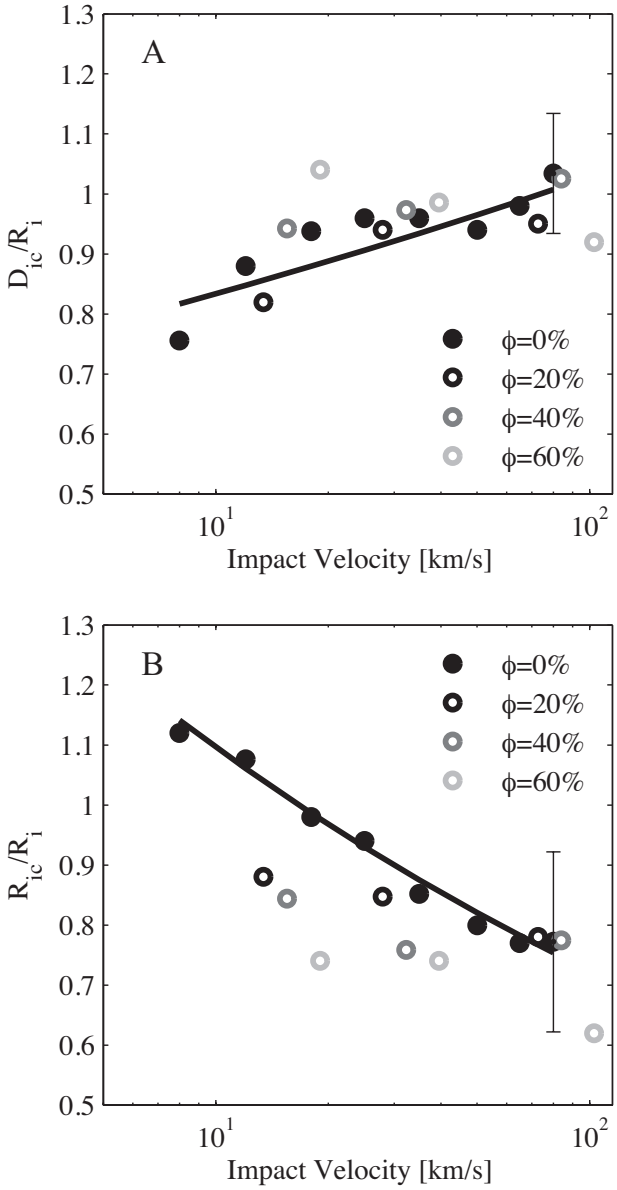

Figure 4.10: The depth of burial D_{ic} (A) and radius of the isobaric core R_{ic} (B), normalized to the radius of the impactor R_i. All data are plotted for impactors of the same density as the target material; a contrast in density between impactor and target can change the depth of burial dramatically. Representative error bars are shown on a nonporous data point; however, the uncertainties are similar for all data. Fits to the nonporous data are shown as solid lines.

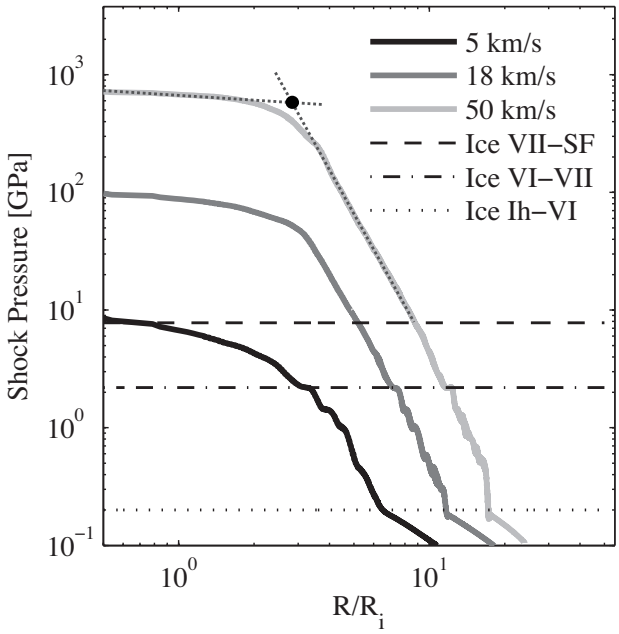

Figure 4.11: Comparison of shock wave decay profiles for impact velocities of 5-50 km s^{-1}. Decay profiles are scaled to the radius of the impactor R_i and are taken at an angle of 5 degrees from the vertical below the impact point. Critical shock pressures to reach the ice VII to superctical fluid (SF), ice VI to ice VII, and ice Ih to ice VI phase boundaries are shown. Fits to the pressure decay in the isobaric core and the supercritical fluid regime are shown for the 50 km s^{-1} impact; the pressure P_0 at the perimeter of the isobaric core is determined at the intersection of the two fits (dotted lines and points).

most materials. At sufficiently high shock pressures, the passage of the shock wave transforms an initially homogeneous ice Ih target into a hemispherically layered material composed of vapor, liquid, ice VII, ice VI, and ice Ih (see also Senft and Stewart, 2011). Noticable differences in the decay exponent are expected due to the impedance contrast between the high pressure polymorphs and the adjacent phases (fluid and ice Ih).

Figure 4.11 shows shock pressure decay curves for vertical impacts onto nonporous 150 K H_2O ice at three impact velocities. The decay profiles start at the impact point and follow a path into the target at an angle of five degrees from the vertical axis of symmetry. Also plotted in Figure 4.11 are the phase transition pressures between the supercritical fluid and ice VII, ice VII and ice VI, and ice VI and ice Ih on the 150 K Hugoniot. Notice the change in slope near these

phase transitions. To quantify the differences in each phase region, Figure 4.12 presents the decay exponents within the supercritical fluid region, n_{SF}, and within the high pressure polymorphs, n_{HP}. Note that the pressure of the phase transition depends on the principal Hugoniot; hence, there is a dependence on porosity. Ice Ih is shocked to a supercritical fluid above $\sim$ 8, 4, 2, and 0.6 GPa for 0%, 20%, 40%, and 60% porosity, respectively. At pressures below the fluid region down to $\sim$ 0.2 GPa (or the Hugoniot Elastic Limit, HEL, when strength is included), ice is shocked to a high-pressure polymorph. Below $\sim$ 0.2 GPa or the HEL, ice remains in the same phase when shocked. Temperature has a much smaller effect on the fluid transition pressure than porosity and hence the 150 K transition pressures are widely applicable. The HEL depends on temperature and peak shock stress; the values range between 0.2 and 0.4 GPa for weak shocks (Stewart and Ahrens, 2005). Notice that weak shocks in ice Ih decays with a similar slope for all impact velocities, $n = 1.47(0.07)$, consistent with the expected decay exponent of $n = 1.5$ for low pressure shock waves (Melosh, 1989).

The decay exponents in the supercritical fluid and the high pressure polymorphs increase significantly with porosity as well as impact velocity (Figure 4.12). To within the uncertainties of the data, the impact velocity and porosity are independent factors, and n_{SF} and n_{HP} can be expressed using a similar form as Ahrens and O'Keefe (1987) and Pierazzo et al. (1997):

$$n_{SF} = 2.9(0.1) + 1.0(0.25)\phi + 0.47(0.08)\log\left[U\left(\text{km s}^{-1}\right)\right] \text{ and} \tag{4.16}$$

$$n_{HP} = 4.0(0.2) + 2.7(0.5)\phi + 0.17(0.15)\log\left[U\left(\text{km s}^{-1}\right)\right]. \tag{4.17}$$

Note that the shock decay exponents in nonporous H_2O ice are much steeper than found for all other nonporous materials (Pierazzo et al., 1997). The steep shock decay is a reflection of the complexity of H_2O that arises from its exceptional polymorphism.

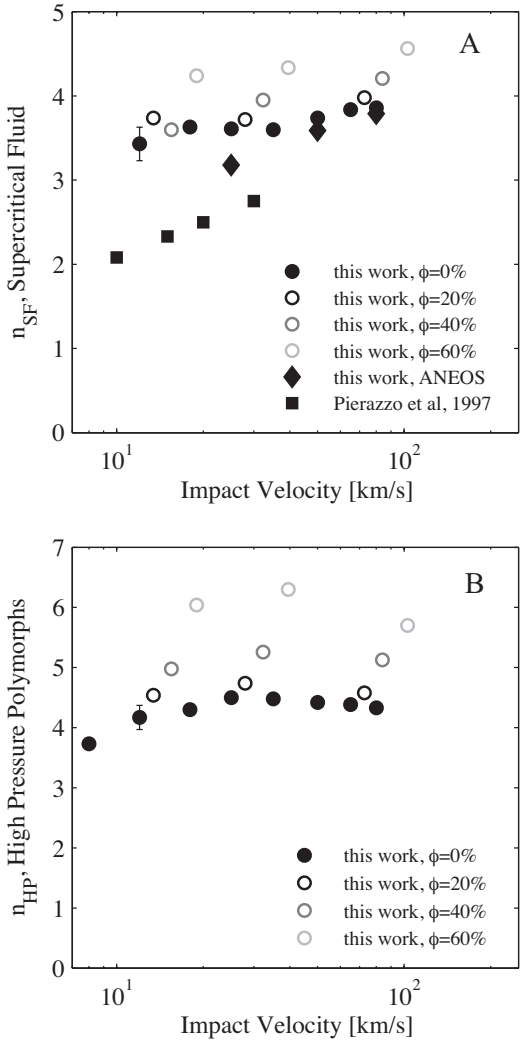

Figure 4.12: Pressure decay exponents of Eq. 4.1 plotted as a function of impact velocity for the supercritical fluid region (A) and high pressure polymorph region (B). The transition between supercritical fluid and high pressure polymorphs occurs at a different pressure for different initial porosity; at 0%, 20%, 40%, and 60% porosity the transition pressures are 7.8, 4, 1.4, and 0.6 GPa, respectively. A representative uncertainty for the decay profiles determined in this work is indicated by the filled circle with vertical error bars. The pressure decay exponents from two versions of the ANEOS model for H_2O ice are shown for comparison (Pierazzo et al., 1997; Turtle and Pierazzo, 2001). Note the significantly higher decay exponent in the high pressure polymorphs.

4.4.2 Melting and Vaporization in Porous Materials

The dependence of the melt and vaporization volume on impact angle, velocity, and target temperature was expected: at a shallow impact angle less energy is coupled deep into the target, at higher velocities there is more energy available to melt and vaporize, and at higher starting target temperatures less energy is required to melt or vaporize the ice. However, the reason for the decrease in melt mass with porosity is not immediately obvious. For porous materials the critical pressure required to melt and vaporize ice is significantly less due to the extra $P\mathrm{d}V$ work done in compacting the pore space (Table 4.1). Yet, the shock wave decays faster in a porous material as more of the mechanical shock wave energy is deposited as thermal energy in the target (Figure 4.12). The competing effects of faster decay but lower critical shock pressures with increasing porosity determines whether one would expect more or less melt/vapor from an impact into a porous body compared to a nonporous one. Our finding of lower melt mass with increasing porosity suggests that the effect of the faster decay dominates over the lower critical shock pressure for H_2O ice.

In contrast to the effect of porosity on melting in H_2O ice, Wünnemann et al. (2008) and Davison et al. (2010) found that more melt is produced from an impact onto a porous silicate. To confirm the difference between ice and silicates, we performed a series of impact simulations into 0, 20, and 40% porous dunite at 25 km s^{-1}. We used the same ANEOS for dunite from Benz and Cameron (1989). In agreement with Wünnemann et al. (2008), we find approximately a factor of two increase in melt mass for the porous over the nonporous silicate targets.

The difference is explained by consideration of the absolute values of the critical shock pressures required for melting and vaporization. For the range of natural impact velocities, shock-induced melting of silicates is primarily derived from the isobaric core. In contrast, more melt is derived from beyond the isobaric core in ice because the critical shock pressures are significantly lower than for silicates. As a result, the steeper decay of the shock wave in a porous ice target is the

dominating factor.

In support of our interpretation, a greater amount of vapor is produced for impacts into porous ice. At the higher shock pressures required to vaporize H_2O ice, the lowered critical shock pressure dominates over the effect of the faster decay with increasing porosity simply because most of the vaporization occurs in the isobaric core.

More generally, any factor that affects the size of the isobaric core will also influence the magnitude of the effects of porosity. For example, Davison et al. (2010) investigated impacts between comparably sized porous silicate bodies and found that the mass of shock-induced melt depended on both porosity and the mass ratio of the two bodies.

4.4.3 Melt Volumes of Ice: Comparison between Equations of State

Previous work by Pierazzo et al. (1997) determined scaling laws for the volume of H_2O ice that is completely melted during a vertical impact event using ANEOS parameters from Tonks et al. (1993). More recent work (Artemieva and Lunine, 2003, 2005; Barr and Citron, 2011) using revised ANEOS parameters from Turtle and Pierazzo (2001) calculated significantly lower melt volumes; however, the difference was interpreted to arise from the different initial target temperatures. The current simulations with the 5-phase EOS also calculate significantly less melt than in Pierazzo et al. (1997). However, our scaling laws are for release to the triple point and not one atmosphere of pressure.

To determine the absolute effect of the model EOS on the amount of melt produced during an impact event, we performed a number of duplicate simulations using the two different versions of ANEOS for H_2O. The results of the current work with the 5 phase EOS were reanalyzed to present the volume of H_2O ice that reaches the entropy of complete melting for a final release pressure of 1 bar. As seen in Figure 4.13, there is very little difference in the melt volume produced between the

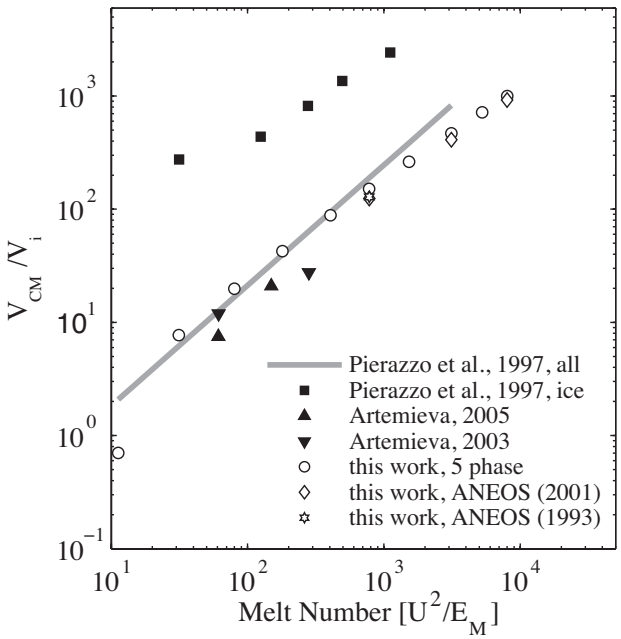

Figure 4.13: Comparison of scaled volume of ice reaching an entropy of 3.160 kJ/kg/K (completely melted at 1 bar) vs. scaled energy: Pierazzo et al. (1997) (filled squares), Artemieva and Lunine (2003, 2005) (filled triangles) for 93 K target temperature, 5-phase EOS (open circles). For direct comparison, we calculated melt volumes for two versions of ANEOS for H_2O (diamond - Turtle and Pierazzo (2001); star - Tonks et al. (1993)). The gray line is the melt scaling law fit to all materials except ice from Pierazzo et al. (1997).

two versions of ANEOS (Tonks et al., 1993; Turtle and Pierazzo, 2001), the 5-phase EOS (Senft and Stewart, 2008), and the scaled volume of melt for all non-ice materials determined in Pierazzo et al. (1997).

The comparable melt volumes are surprising as the critical pressures for melting are significantly higher with ANEOS compared to the 5-phase EOS, see Table 4.1. However, the pressure decay exponent n is significantly greater in the 5-phase EOS than with either version of ANEOS for the entire pressure range investigated. For comparison, the decay exponent for calculations using ANEOS are also shown in Figure 4.12A. The decay profiles are shallower with ANEOS because the high-pressure solid polymorphs are not included in the model. Here, we have an excellent example of two wrongs making a right. Although the critical pressures for melting are higher in the ANEOS

model, the shallower pressure decay profile produces nearly the same volume of melted material as the more accurate 5-phase EOS.

Note that other aspects of the ANEOS models for H_2O do not produce such fortuitous results. The model temperatures and phase boundaries are inaccurate (c.f. Stewart et al., 2008). And, because of the omission of high-pressure polymorphs, the phenomenon of discontinuous excavation is not produced in simulations of impact cratering using the ANEOS model.

As discussed in this work, Kraus and Stewart (2010), and Barr and Citron (2011), the scaling laws published in Pierazzo et al. (1997) overestimate the amount of melt by an order of magnitude. However, Barr and Citron (2011) conclude that the difference in initial temperature, ~ 50 K, could cause an order of magnitude difference in the volume of complete melt. This conclusion is incorrect and implies that small changes in temperature can have a dramatic effect on the critical pressure for complete melting and thus melt volume. This is not the case as demonstrated in Figure 4.6. The reason for the discrepancy between the melt volumes of H_2O ice determined in Pierazzo et al. (1997) and in subsequent work is unknown; it is not due to initial target temperature or the model EOS.

4.4.4 Complications due to Gravity, Thermal Gradients, and Compositional Mixtures

In order to make everything scaleable, the simulations presented here do not take into account surface gravity or any interior planetary structure. For small icy bodies (comets and small moons), the initial lithostatic pressure is a negligible perturbation to the shock pressure field. For larger bodies, the combination of a thermal gradient and self-gravity can be significant.

As shown in Section 4.3.1, variation in the initial temperature of ice produces at most a factor of 2 difference in the amount of melt. Hence, a thermal gradient in ice will make less than a factor of two difference in the total amount of melt and vapor created in an impact event. However, if the

thermal gradient leads to a subsurface ocean, the calculated volume of melt should be truncated at the base of the ice crust by considering the intersection of the pressure decay field with the ocean.

There are subtler second order effects with self-gravity. After shock compression of buried ice, the pressure upon release may be higher than the triple point, which will shift the critical pressures for melting. These effects are generally small in calculations of the total mass of melt from impact cratering events; however, details of the melt production and distribution around a final crater require full numerical simulations for giant impact events (e.g., where the curvature of the planet is important or the mass ratio between the bodies are comparable) or when breaching a subsurface ocean (see also Senft and Stewart, 2011).

As many bodies in the solar system are or were mixtures of ices, rock, and organic materials, mixed compositions should ideally be included within the scaling laws presented in Section 4.3.2. However, melting and vaporization in icy mixtures is extremely complicated (e.g., Ivanov and Pierazzo, 2011; Pierazzo et al., 2005; Stewart et al., 2004a). Only recently has it been understood how the initial shock wave partitions the internal energy between the components of a mixture of ice and quartz (Kraus et al., 2010). A general model for energy partitioning in arbitrary mixtures on the scale of planetary impact events requires more study.

Here we present a first order approximation of melting the ice component in an ice-rock mixture for a given impact event at velocity U. First, account for the higher initial shock pressure in the ice-rock mixture by calculating the mass-averaged Hugoniot. Hugoniot parameters for H_2O ice, quartz, and an example mixture Hugoniot are given in Table 4.2. The given parameters are for hypervelocity impacts that shock both components into supercritical fluid. Then, using impedance matching between the projectile Hugoniot and the mixture Hugoniot, calculate the peak shock pressure in the mixture at an impact velocity of U. Next, determine the equivalent impact velocity U^* that would give the same peak shock pressure in pure ice. Now simply use U^* with the scaling

relations presented in Section 4.3.2 to approximate the mass where ice would be melted and convert to volume. Finally, reduce the mass of melt by the volume fraction of ice.

Table 4.2: Initial density ρ_0, bulk sound speed c, and slope of D-u_p relation s for H_2O and α-quartz in the supercritical fluid regime. The linear D-u_p parameters given here are a fit to the nonlinear parameters given in Knudson and Desjarlais (2009). Also given are the Hugoniot parameters for an H_2O-SiO_2 mixture of 25% SiO_2 by mass. A more detailed discussion of calculating a mixture Hugoniot can be found in Meyers (1994).

Material	ρ_0 [g/cm^3]	c [km/s]	s	Reference
H_2O ice, SF	0.932	1.70	1.44	Stewart and Ahrens (2005)
α-quartz, SF	2.65	3.95	1.34	Knudson and Desjarlais (2009)
H_2O-SiO_2 mix, M_{SiO_2}=25%	1.11	2.26	1.42	Meyers (1994)

Quantitatively, assuming an impact of an ice-rock mixture into an ice-rock mixture target at velocity U, the maximum or impedance match pressure P_I in the mixture can be easily determined by the shock conservation of momentum equation,

$$P_I = \rho_{mix} D_{mix} u_{p,mix}, \tag{4.18}$$

where ρ_{mix} is the average density of the mixture, D_{mix} is the shock velocity in the mixture, and $u_{p,mix}$ is the particle velocity in the mixture. For an impact event where the impactor is the same materials as the target, a symmetric impact, the particle velocity in the target is half the impact velocity. As there is also a linear relationship between the shock wave velocity and particle velocity, Equation 4.18 can simplified to

$$P_I = \rho_{mix} \left(c_{mix} + s_{mix} \frac{U}{2} \right) \frac{U}{2}, \tag{4.19}$$

where c_{mix} is the mass average of the bulk sound speeds of the components, and s_{mix} is the mass average of the slopes of the linear shock velocity-particle velocity relation. The effective velocity for an impact into an ice-rock mixture can be determined by equating Eq. 4.19 with the impedance

match solution for a symmetric impact into pure ice at the effective velocity U^*.

$$U^* = \frac{-c_{ice}\rho_{ice} + \sqrt{c_{ice}^2\rho_{ice}^2 + 2c_{mix}\rho_{ice}\rho_{mix}s_{ice}U + \rho_{ice}\rho_{mix}s_{ice}s_{mix}U^2}}{\rho_{ice}s_{ice}} \tag{4.20}$$

To determine the mass of melted H_2O ice within the mixture, multiply M_{M+V}/M_i of Eq. 4.12 by the volume fraction of ice in the mixture, the density of ice ρ_{ice} and the volume of the impactor V_i.

The method outlined above should be used cautiously as there are two major assumptions in this approximation. It assumes first that both components attain the same shock pressure on their principal Hugoniots and, second, that the shock wave decays with the same exponents in the mixture as it does in H_2O ice. These assumptions are likely reasonable for mixtures that are less than about 50% vol rock. Above about 50% vol rock, it would be more accurate to use pressure decay curves for rock (e.g., from Pierazzo et al., 1997) to estimate the volume of mixture shocked above the critical melting pressures for ice (Table 4.1).

4.5 Application to Impact Cratering

Up to this point, we have only considered the shock pressure field and the process of melting and vaporization. Yet, not all of the melt remains within the transient crater and subsequently the final crater. To estimate the final mass of melt within a crater, we use π-scaling to determine the transient crater size, the modified Maxwell Z-model to predict the fraction of melt ejected from the crater, and crater collapse laws to estimate the final crater size. The crater size scaling relations are derived from recent numerical simulations (Senft and Stewart, 2011) of the full cratering process on Ganymede.

4.5.1 Full Crater Formation Simulations

The full crater formation simulations modeled vertical impacts of nonporous H_2O ice into a half-space of H_2O ice at 120 K and surface gravity of 1.43 m s^{-2} (surface gravity of Ganymede). Two sets of simulations were performed, one with an isothermal crust and another with a 20 K/km geothermal gradient. The mesh resolution was at least 20 cells per projectile radius. Simulations were performed using CTH with the same 5-phase model EOS for H_2O as previously described in Section 4.2.1. The quasi-static strength model of Collins et al. (2004) was used to describe the shear strength as a function of confining pressure and damage. The block model approximation (Melosh and Ivanov, 1999) of acoustic fluidization (Melosh, 1979) was used to transiently weaken the ice in order to obtain collapse of complex craters. A complete description of the full crater formation simulations can be found in Senft and Stewart (2011).

4.5.2 Transient Craters in Ice

In the gravity regime, the apparent transient crater diameter D_{at} (the diameter at the level of the pre-impact surface) is a function of the impactor radius R_i, impactor density ρ_i, gravity g, impact velocity U, and the density of the target ρ_t. As there are three physical dimensions (length, mass, time), the transient crater diameter is a function of two dimensionless ratios (π_2 and π_4) (c.f. Melosh, 1989). The non-dimensionalized diameter of the transient crater is given by

$$\pi_D = 0.62 \left(\frac{\rho_t}{\rho_i} \right)^{\frac{1}{3}} \frac{D_{at}}{R_i}. \tag{4.21}$$

Because of the finite energy required to melt ice, we are primarily interested in impact craters in the gravity-scaled regime, which is described by the inverse Froude number:

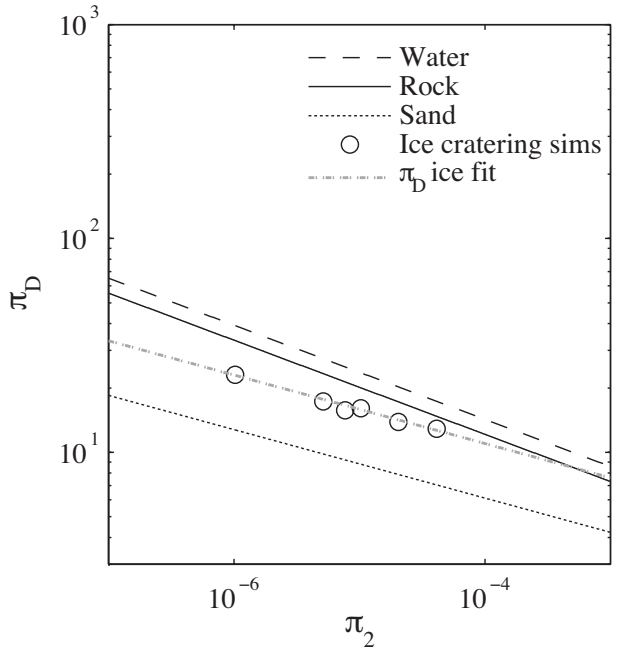

Figure 4.14: Comparison of π-scaling results for water, competent rock, and quartz sand (Melosh, 1989) with transient crater diameters determined from Senft and Stewart (2011) for full cratering simulations on Ganymede. The best fit coefficients for Eq. 4.24 are $C_D = 2.5 \pm 0.4$ and $\beta = 0.16 \pm 0.02$.

$$\pi_2 = \frac{3.22 g R_i}{U^2}. \tag{4.22}$$

Finally, π_4 is the ratio of target and projectile densities:

$$\pi_4 = \frac{\rho_t}{\rho_i}. \tag{4.23}$$

For impactors and targets of the same density, the empirical form for the relationship between π_D and π_2 is

$$\pi_D = C_D \pi_2^{-\beta}, \tag{4.24}$$

where C_D and β are parameters that must be determined by laboratory or numerical experiments.

Although it has been suggested that the transient crater in cold H_2O ice scales like rock in the gravity regime (Chapman and McKinnon, 1986; McKinnon and Parmentier, 1986; Turtle and Pierazzo, 2001), very little data in the gravity regime is available. We analyzed the transient crater diameters from the full crater formation simulations presented in Senft and Stewart (2011). The transient crater diameter is determined at the height of the pre-impact surface, when the ejecta curtain begins to kink as it detaches from the excavation flow. The calculated π-scaling for H_2O ice lies below that for competent rock and water (Figure 4.14). The best fit coefficients for 150 K ice are $C_D = 2.5 \pm 0.4$ and $\beta = 0.16 \pm 0.02$, which are intermediate between water and sand and below competent rock. Note that the fitted coefficients are for vertical impacts; the effect of impact angle can be taken into account by multiplying the impact velocity by the sine of the angle of impact (Chapman and McKinnon, 1986). Transient crater diameters were determined for both a 120 K isothermal crust and warm geothermal gradient of 20 K/km; however, there was less than a 10% difference in the transient crater diameters over the range of transient crater diameters investigated (D_{at}=1-40 km).

4.5.3 Crater Excavation and Ejection of Melt

Maxwell (1977) developed the streamline flow theory for transient crater formation from impacts or explosions. Croft (1980) improved on the Maxwell Z-model by recognizing that the center of the flow field will be buried beneath the surface, approximately at the center of the isobaric core. The material ejected from the crater lies above a critical streamline that truncates at the radius of the transient crater (Croft, 1980). In polar coordinates (r, ψ), with the origin at the center of the isobaric core, the critical streamline follows a path described by,

$$r = r_{exc} \left[1 - \cos(\psi)\right]^{\frac{1}{Z-2}} \tag{4.25}$$

where r is the radial distance away from the center of the isobaric core and ψ is the angle from the vertical with zero degrees pointing toward the center of the planet. Z is the model parameter that describes the curvature of the streamlines and hence angle of the ejected material at the surface; values between 2.5 and 3 are representative of most excavation flows (Croft, 1980; Stewart and Valiant, 2006). r_{exc} is the distance between the origin and the critical streamline at the burial depth D_{ic}. The streamline intersects the pre-impact surface at the radius of the transient cavity $R_{at} = D_{at}/2$. The critical streamline is given by

$$r_{exc} = \frac{R_{at}}{\frac{R_{at}}{r_{at}}\left[1 + \frac{D_{ic}}{r_{at}}\right]^{\frac{1}{Z-2}}}, \tag{4.26}$$

where r_{at}, the distance between the streamline origin and the apparent radius of the transient cavity, is defined by

$$r_{at} = \frac{R_{at}}{\cos\left[\tan^{-1}\frac{D_{ic}}{R_{at}}\right]}. \tag{4.27}$$

Since the pressure decay field is known, the location of the melt is also known. Then, it is straightforward to numerically determine the amount of melt above the streamline for excavation, Eq. 4.25. The melt above the streamline is ejected, and the fraction of melt left within the transient crater can then be determined.

We used a typical value of $Z = 2.7$ (Stewart and Valiant, 2006) to describe the flow field. To estimate the maximum uncertainty involved in using the Maxwell Z-model for oblique impacts, we varied Z between 2.5 and 3.4, end-member values for the flow field measured during oblique impact experiments at 1 km s^{-1} (Anderson et al., 2004). At the relatively low velocity of 1 km s^{-1}, the momentum driven component of the flow, which causes the excavation flow to deviate from the point source solution, will be greater than at higher velocities. Consequently, the uncertainty in

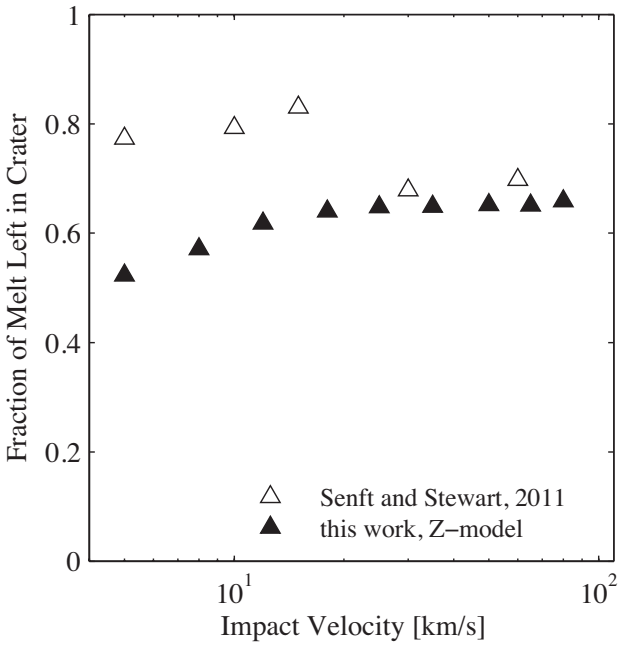

Figure 4.15: The fraction of melt left within a 20 km diameter transient crater is determined from ejecting melt from the transient crater based on Z-model flow. We estimate an uncertainty of ∼20% based on the experimentally determined variation in Z with azimuthal angle and ejection position for oblique impacts (Anderson et al., 2004). The Z-model results are compared with the fraction of melt left within the hot plug at the center of the final crater (Senft and Stewart, 2011).

the retained melt fraction as determined from variation in Z, $\sim$20%, can be considered as an upper limit.

The Maxwell Z-model is a simple analytic model that describes the axisymmetric portion of the flow field and cannot be used as a general theory to treat all regions of the flow field. For oblique impacts onto rocky bodies, the zone of melting is sufficiently close to the impact point, approximately three impactor radii away for a 20 km s^{-1} impact (Pierazzo et al., 1997), that the melt flow will not be axisymmetric and cannot be described by Z-model streamlines (Figure 3, Pierazzo and Melosh, 2000). However, the low critical shock melting pressures again differentiate ice from rock, for the zone of melting in water ice extends to $\sim$ 10 impactor radii away from the impact point for an 18 km s^{-1} impact (Figure 4.11). Following the π-scaling law presented in the previous section, a 1 km diameter body impacting at 18 km s^{-1} onto Europa produces a transient crater with radius $\sim$ 13 times that of the impactor radius. Consequently, the critical contour for incipient melting of ice is a large fraction of the radius of the transient crater.

Most observed craters are axisymmetric because the transient craters from which they collapsed were also axisymmetric. It thus follows that most of the excavation flow that formed the transient crater was dominated by axisymmetric flow, as evidenced by the hemispherical shape of the pressure contours below $\sim$10 GPa in Figure 4.4. If the melt originates near the radius of the transient crater, as it does in ice but not in rock, then a point source is a reasonable approximation for the shock wave that melts the ice and excavates the transient crater. Hence, in the case of cratering in ice, the mass of melt ejected from the crater may be estimated by the Z-model.

In Figure 4.15 (filled triangles), we present the results from the Maxwell Z-model for the fraction of incipient melt left within a 20 km diameter transient crater. Also in Figure 4.15 are results of retained melt fraction from full numerical simulations of impact cratering in ice (Senft and Stewart, 2011). The retained melt fraction is based on the mass of ice raised to 270 K within the final crater

at the end of the simulation and the total amount of incipient melt using Eq. 4.12. Note that the deviation between the simulations and the Z-model occurs at impact velocities that are optimal for hot plug formation via discontinuous excavation (Figure 11 in Senft and Stewart (2011)).

Based on the modified Maxwell Z-model results, between 1 and 200 km diameter transient craters, the fraction of melt left in the crater f varies between 50-80% for impact velocities above 8 km s^{-1} according to a simple power law in the diameter of the transient cavity D_{at},

$$f = 0.5 + 0.1\log\left(D_{at}\right) \tag{4.28}$$

where D_{at} is in kilometers.

4.5.4 Crater Collapse

To relate the mass of melt to a final crater size, we need an equation for the collapse of the transient crater. A volume conservation analysis by Holsapple (1993) suggests that the final crater rim radius R_f is a function of the transient crater rim radius R_t, an effective strength of the target Y, the density of the target ρ_t, and the acceleration of gravity at the surface g:

$$\frac{R_f}{R_t} = f\left(\frac{\rho_t g R_t}{Y}\right). \tag{4.29}$$

The strength of the body is difficult to ascertain *a priori*; however, the radius of a crater at the transition from simple to complex morphologies, R^*, can be determined from observations. Although not included in the work by Holsapple (1993), the final crater rim radius R_f is a factor κ greater than the R_t due to slumping of the rim wall. Then, as R^* is proportional to the effective strength of surface material, the final complex crater rim radius has a simple functional form of

$$\frac{R_f}{R_t} = \kappa \cdot F\left(\frac{R_f}{R^*}\right). \tag{4.30}$$

Based on a constant volume collapse model and empirical fits, Croft (1985) shows that the functional form of Eq. 4.30 is a power law. The rim radius of the transient crater R_t is related to the apparent radius R_{at} by a factor of 1.3 (Holsapple, 1993; Melosh, 1989). Then, a general relation between R_f and R_{at} is

$$\frac{R_f}{R_{at}} = 1.3\kappa\left(\frac{R_f}{R^*}\right)^{\eta}, \tag{4.31}$$

which can be solved for R_f to obtain,

$$\frac{R_f}{R_{at}} = (1.3\kappa)^{\frac{1}{1-\eta}}\left(\frac{R_{at}}{R^*}\right)^{\frac{\eta}{1-\eta}}. \tag{4.32}$$

The parameter η has not been determined for icy bodies; hence, we fit the impact cratering simulations on Ganymede (Senft and Stewart, 2011) for both the cold isothermal crust and warm geothermal gradient of 20 K/km. Figure 4.16 shows the relation between the transient crater apparent radius R_{at} to final crater rim radius R_f. A least-squares fit of Eq. 4.32 to the simulation results (for craters below 40 km diameter) gives $\kappa = 1.19 \pm 0.04$ and $\eta = 0.04 \pm 0.02$ (solid line). We used $R^* = 1$ km, as determined from the observed simple to complex crater on Ganymede (Schenk, 2002). Above 40 km diameter, the scaling law no longer applies to warm ice because the thermal gradient significantly weakens the ice and leads to greater collapse. We expect the fitted parameters in Eq. 4.32 to be similar on other cold icy bodies, with R^* adjusted inversely with gravity.

For comparison, the complex crater collapse law derived for rocky bodies by Holsapple (1993)

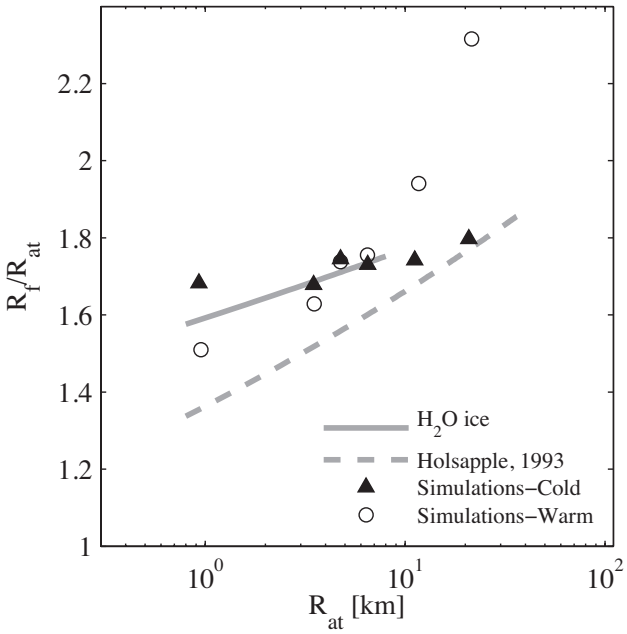

Figure 4.16: Comparison of the ratio of the final crater radius R_f to the transient crater apparent radius R_{at} from cratering simulations by Senft and Stewart (2011) for a 120 K isothermal crust (triangles) and a geothermal temperature gradient of 20 K/km (open circles). A least squares fit to Eq. 4.32 for craters less than 40 km final diameter is shown in the solid gray line; the scaling law for craters on rocky surfaces from Holsapple (1993) is shown for comparison (dashed line), with $\eta = 0.079$ and $\kappa = 1$.

predicts much less collapse just above the simple to complex transition and has a significantly different slope (dashed line in Figure 4.16)[i] It is well established that the final depth to diameter ratios for complex craters in ice are much less than in rock (e.g., Schenk, 2002) In addition, the slope of the depth-to-diameter vs. diameter are shallower in ice and fewer crater rimwall terraces are observed (Schenk, 1991, 2002). Hence, it is not a surprise that the crater collapse function is different between rock and ice.

For craters formed by impact energies less than about 2×10^{20} J and less than about 5 km s^{-1} (forming a ∼30 km diameter crater on Ganymede and Callisto), the melt lines the floor of the final cavity. For impacts with larger impact energies and impact velocities, the phenomenon of

[i]Note that the online crater scaling program by K. A. Holapple (v1.4, http://keith.aa.washington.edu/craterdata/scaling/index.htm) includes cold ice as a material but does not use the correct R^* for icy bodies. Hence, the program results are only valid in the strength regime.

discontinuous excavation concentrates the melt into a plug in the crater floor with a diameter of about 20% of the final rim diameter (Senft and Stewart, 2011).

4.5.5 Example Calculation: Melt within a 25 km Crater on Europa

Here, we estimate the amount of transient melt within a newly formed 25-km diameter crater on Europa. The two craters of similar size on Europa, Pwyll and Manannán, are transitional forms between central peak craters and multi-ring basins (Schenk and Turtle, 2009). These two craters have modified central structures and Manannán has observations of melt ponds and melt flow over the crater rim.

First, invert Eq. 4.32 to determine R_{at},

$$R_{at} = \frac{R_f^{1-\eta}(R^*)^{\eta}}{1.3\kappa}. \tag{4.33}$$

Next, solve for R_{at} using the fitted parameters $\kappa = 1.19 \pm 0.04$ and $\eta = 0.04 \pm 0.02$ and the simple-to-complex transition radius on Europa,

$$R^*_{\text{Europa}} = \frac{g_{\text{Ganymede}}}{g_{\text{Europa}}} \times R^*_{\text{Ganymede}} = 1100 \text{ m}. \tag{4.34}$$

The transient crater radius is about R_{at}=5300 m.

To determine the size of the impactor, we assume a nonporous H_2O ice projectile traveling at the mean impact velocity on Europa of 26,000 m s^{-1} (Zahnle et al., 2003) and the most probable angle of 45 degrees. Then, the π-scaling relation for H_2O ice from Section 4.5.2 gives the radius of the impactor, R_i,

$$R_i = \left[\frac{1.24}{C_D}\left(\frac{\rho_t}{\rho_i}\right)^{\frac{1}{3}}\left(\frac{3.22g}{(U\cos\theta)^2}\right)^{\beta} R_{at}\right]^{\frac{1}{1-\beta}} = 370 \text{ m}. \tag{4.35}$$

Given an average surface temperature on Europa of 110 K and assuming nonporous ice, the mass of melt produced from such an impact event is given by (Eq. 4.12)

$$\frac{M_{M+V}}{M_i} = (\sin\theta)^{0.7} \times 10^{-0.53+0.0017T-0.46\phi} \times \left[\frac{U^2}{E_M\,(\phi)}\right]^{\frac{3(0.554+0.07\phi)}{2}} \approx 94. \tag{4.36}$$

As determined by Eq. 4.28, at least 60% of the melt will remain in transient cavity. In summary, a 370-m radius nonporous ice projectile impacting the 110 K nonporous H_2O ice surface of Europa at the mean velocity (26 km s^{-1}) and 45 degree angle creates a 25-km diameter final crater with approximately 12 km^3 of melt lining the freshly made crater floor.

In a crater like Manannán, the transient melt pool would be about 10 m deep, which is consistent with observations of a limited melt pool for this crater size (Schenk and Turtle, 2009). Some of the melt will drain into fractures in the crater floor and the rest will freeze and sublimate.

4.6 Conclusions

Here we developed an accurate method to calculate the amount of melt and vapor produced for impacts into H_2O ice. A large number of hydrocode simulations were performed to investigate the effect of impactor composition, impact velocity, impact angle, initial temperature, and porosity on melting and vaporization. We found that natural variations in impact parameters resulted in up to a factor of two change in melt and vapor mass. We compared the results to numerical simulations of impact induced melting in H_2O ice performed by Pierazzo et al. (1997) and Artemieva and Lunine (2003, 2005) and found a discrepency in the work of Pierazzo et al. (1997) that is unrelated to the EOS or initial temperature.

Based on recent full crater formation simulations, we determined the first π-scaling parameters for transient crater formation in H_2O ice in the gravity regime. Contrary to previously thought,

transient crater scaling in ice is not the same as rock and falls between quartz sand and water. The modified Z-model was then used to predict the fraction of melt left within the transient crater; the fraction varies from 50-80% of the total melt produced for 1-200 km transient craters. For impact energies below 2×10^{20} Joules and impact velocities less than 5 km s^{-1}, the melt will line the floor of the entire crater. At higher energies the melt concentrates at the center of the crater due to the phenomena of discontinuous excavation (Senft and Stewart, 2011). We also determined transient to final crater scaling laws for complex craters and find that there is significantly greater collapse in H_2O ice than rock.

To conclude the paper, we present an example calculation for how to determine the amount of melt that initially lined the floor of a 25-km diameter crater on Europa.

Chapter 5

Thermodynamics of Impacts into Heterogeneous Mixtures

Melting of H_2O ice during planetary impact events is a widespread phenomenon. On planetary surfaces, ice is often mixed with other materials; yet, at present, the partitioning of energy between the components of a shocked mixture is still an open question in the shock physics community. Knowledge of how much energy is partitioned into the ice component is necessary to predict and interpret a wide range of processes, including shock-induced melting and chemistry. In this work, we construct a conceptual framework for the thermodynamic pathways of the components in a shocked hydrodynamic mixture by defining three broad regimes based on the characteristic length scale of the mixture compared to the thickness of the shock front: (1) small length scale mixtures where pressure and temperature equilibrate immediately behind the shock front; (2) intermediate length scales where pressure but not thermal equilibration is achieved behind the shock front; and (3) long length scales where pressure equilibration requires multiple shock wave reflections. We conduct shock wave experiments, reaching pressures from 8 to 23 GPa, in an H_2O ice–SiO_2 quartz mixture in the intermediate length scale regime. In each experiment, all the parameters required to address the question of energy partitioning were determined: the shock velocity in the mixture, the shock front thickness, and the shock and post-shock temperatures of the H_2O component. The

An amended version of this Chapter was published with Sarah T. Stewart, Achim Seifter, and Andrew W. Obst in Earth and Planetary Science Letters, Vol. 289, 162-170, 2010.

measured pressure is in agreement with the bulk compressibility of the mixture. The shock and post-shock temperatures of the H_2O component indicate that the ice was shocked close to the principal Hugoniot. Therefore, in the intermediate length scale regime, the partitioning of shock energy is defined initially by the Hugoniots of the components at the equilibrated pressure. We discuss energy partitioning in mixtures over the wide range of length and time scales encountered during planetary impact events and identify the current challenges in calculating the volume of melted ice. In some cases, the criteria for shock-induced melting of ice in a mixture are the same as for pure ice.

5.1 Introduction

Shock-induced melting of H_2O ice during impact cratering events is an important planetary phenomenon. As relatively low shock pressures are required to melt ice (Stewart et al., 2008), large volumes of melt may be produced during impact events. Depending on the size of the event, the liquid water may persist for time scales relevant for prebiotic chemistry (e.g., Artemieva and Lunine, 2003; Furukawa et al., 2009). Hence, impact craters may have played a key role in the development of habitable environments (Cockell and Bland, 2005). The generation of liquid water during impact events has been inferred from the distinct morphologies of craters on Mars (e.g., Carr et al., 1977) and the Galilean icy satellites (Senft and Stewart, 2011). On Mars, cumulative impact events may have significantly redistributed water contained in near-surface reservoirs (e.g., Stewart et al., 2004b) and, early in the planet's history, large impacts may have created transiently clement global climatic conditions (Segura et al., 2008, 2002). The amount of liquid water produced by shock melting pure ice during an impact event has been revisited using numerical simulations (Kraus et al., 2011) that include a revised ice shock Hugoniot (Senft and Stewart, 2008; Stewart and Ahrens, 2005) and new criteria for shock-induced melting (Stewart et al., 2008).

However, on planetary surfaces, H_2O ice is commonly mixed with other materials. For example, ice is mixed with silicates and other refractory materials on the surfaces of Earth, Mars, some icy satellites, and dwarf planets. H_2O ice may also be mixed with other, more volatile ices in bodies in the outer solar system, such as some icy satellites, comets and their parent bodies. Numerical studies of collisions onto such bodies have modeled material mixtures using two different approaches: (1) the mixture is treated as a single material using an averaged equation of state (e.g., Pierazzo et al., 2005) and (2) each component is modeled with individual equations of state and the energy partitioning between components is calculated (e.g., Stewart et al., 2004b). The former has the advantage of being numerically stable and the disadvantages of significantly simplifying the thermodynamics of icy mixtures and preventing phase separation. The latter approach allows for phase separation and retains the thermodynamic properties of individual phases but may not properly model their interaction (e.g., hydration). A major uncertainty in the latter approach is the user-applied assumption on how the energy is partitioned between phases. For example, one may assume that the constituent materials are always in pressure equilibrium (allowing for different temperatures) or that the energy is partitioned proportionally to the compressibility of each material (allowing for different pressures and temperatures). For H_2O ice, the various assumptions for energy partitioning between phases has a significant effect on the calculated volumes of impact-generated melt. Hence, shock compression experiments are required to determine the correct treatment of icy mixtures.

The response of a mixture to a shock wave, including the partition of energy, will depend upon the characteristic length scale in the mixture compared to the shock front thickness. As natural settings have a wide range of length scales and the thickness of an impact-generated shock front increases significantly as the amplitude of the shock wave decreases (e.g., Melosh, 2003), we need to understand how to describe the thermodynamics of shock waves in mixtures of all length scales.

We propose three principal regimes of interest that divide the thermodynamics of shock wave propagation in a hydrodynamic mixture: (1) the length scales are sufficiently small that pressure and temperature equilibrate immediately behind the shock front; (2) the length scales are such that pressure equilibrates immediately behind the shock front but thermal equilibration requires more time; and (3) the length scales are sufficiently large that the shock wave must reflect multiple times to reach the equilibrium shock pressure between the components.

Propagation of waves in the largest and smallest length scale regimes are well understood. In an icy mixture at the largest length scales, the thermodynamic path in the H_2O component would be similar to a quasi-isentropic "ring-up" experiment (e.g., Ogilvie and Duvall, 1983). In a standard ring-up experiment, a layer of lower impedance material is sandwiched between two layers of a higher impedance material; when a shock is driven through one of the higher impedance layers, multiple shock wave reflections within the low impedance material bring it into pressure equilibrium. For the smallest length scales, Duvall and Taylor (1971) derived the thermodynamic properties of a two-component mixture in which pressure and temperature equilibrium is achieved behind the shock front. The difference between quasi-isentropic loading (via multiple shock waves) and single shock loading (along a single Rayleigh line) is presented in pressure-volume space in Figure 5.1. The increase in internal energy (the $P\mathrm{d}V$ work) is much less under quasi-isentropic loading compared to a single shock. Therefore, the onset of shock-induced melting of a particular component depends sensitively on the loading path, which is, in turn, dependent on the length scales.

In this work, we focus on understanding the energy partitioning within a mixture in the intermediate length scale regime. Previous experiments have demonstrated that a steady shock wave can propagate in the intermediate length scale regime in many different materials (e.g., Holmes and Tsou, 1972; Larson et al., 1973; Zhuang et al., 2003). Consequently, the Rankine-Hugoniot

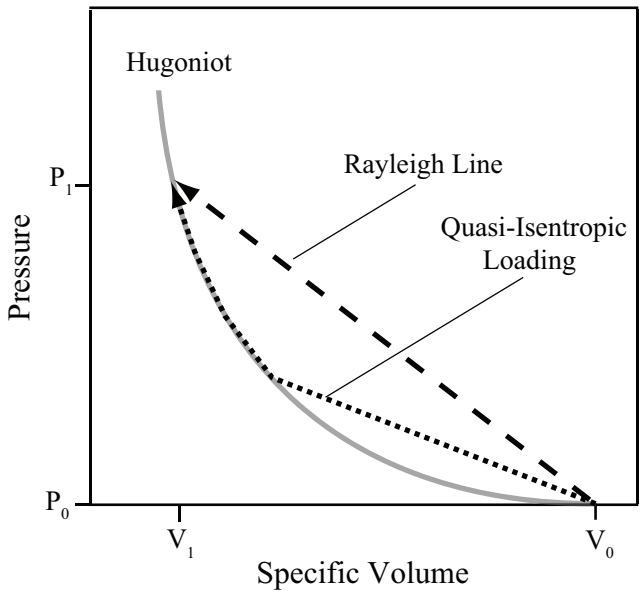

Figure 5.1: Schematic of different thermodynamic paths to the same final shock pressure and volume (P_1, V_1) via (1) a single shock wave or (2) multiple shock waves. An ideal single shock wave loads the material along a Rayleigh line, which is the straight line connecting the initial state (P_0, V_0) with the shocked state. If loaded to (P_1, V_1) by means of multiple shock waves, the material is said to follow a quasi-isentropic path. The increase in internal energy is the area under the thermodynamic path.

conservation equations for mass, momentum, and energy (c.f., Rice et al., 1958b) apply to the bulk mixture, and the total internal energy increase is defined. However, the partitioning of energy between the individual phases is not well understood. Duvall and Taylor (1971) comment that pressure and temperature equilibration is difficult to achieve in a real (rather than ideal) composite because of the much longer time required to reach thermal equilibrium compared to stress equilibrium. Barker (1971) and Munson and Schuler (1971) suggested that the soft component of the mixture will undergo quasi-isentropic loading. In a study considering a wide range of energy partitioning ratios, Krueger and Vreeland (1991) conclude that energy partitioning cannot be determined using measurements of macroscopic shock parameters (shock velocity, particle velocity, pressure, and density) because the amplitude of the difference in the thermal pressure from each component is within the uncertainties of the experiment.

If the temperature of the components of a mixture were measured, then the partitioning of shock energy could be derived. In practice, this is difficult. However, for mixtures of ice and rock, ice is usually more compressible than the rock. In general, a more compressible material will reach a higher shock temperature compared to a harder material shocked to the same pressure. Hence, the observed radiance from a shocked ice-rock mixture should be dominated by the ice component.

In this study, we consider an H_2O (ice Ih) and SiO_2 (α-quartz) mixture composed of a particle size that we expect to fall into the intermediate length scale regime. H_2O and SiO_2 are materials of tremendous geologic importance; hence, both are well studied under shock compression (Akins and Ahrens, 2002b; Luo et al., 2003a; Stewart and Ahrens, 2005). The shock and post-shock temperature of pure H_2O ice has been determined experimentally (Stewart et al., 2008). Based on calculations of shock temperature (Wackerle, 1962) and post-shock temperature measurements (Raikes and Ahrens, 1979b) for SiO_2, the emission from the SiO_2 component is expected to be much less than from the H_2O component in a mixture.

Here, we present the results from the first shock and post-shock temperature measurements on a H_2O–SiO_2 mixture. Our results are used to make inferences regarding the energy partitioning for the components within intermediate length scale mixtures. We then discuss the implications for calculating the volume of impact-induced melting in the H_2O component of an icy planetary body.

5.2 Experimental Method

Semi-transparent samples were prepared from a 60:40 volumetric mixture of degassed distilled H_2O ice and high purity quartz sand (Mill Creek, OK, No. 1 Dry, U.S. Silica Co.). This volumetric ratio was chosen to minimize porosity in the sample while retaining a significant quartz fraction. The constituent materials were sifted to a particle size of 125 to 250 μm, mechanically mixed, and cold pressed in an evacuated ($\sim$ 1 Pa) piston-die assembly into $\sim 3.0 \times 30.3$ mm discs in a 263 K cold room. The bulk density of the samples was ρ_0=1.65 ± 0.03 g cm^{-3}. The ice particles were brought to near the melting point during compression to about 5 tons. The flowing ice/liquid filled the pore space, and upon decompression the sample solidified. The porosity is assumed to be $1.0 \pm 0.5\%$ based on mass balance in similarly prepared samples. In one experiment (18.5 GPa), the sample had a different volumetric ratio of H_2O to SiO_2 (40:60).

The experimental configuration, shown in Figure 5.2, was similar to previous simultaneous pyrometry and velocity interferometry experiments on pure H_2O ice (Stewart et al., 2008). The sample was mechanically affixed to an Al-2024 driver plate and encased in a $<$ 1 microtorr vacuum chamber with a downrange CaF_2 window. The target assembly was cooled with liquid nitrogen to 108 ± 12 K in order to prevent sublimation of the ice component under vacuum. The downrange free surface velocity was measured using interferometric velocimetry (VISAR, Barker and Hollenbach, 1972). Emitted radiation was collected downrange and split between two silicon photodiodes (centered at 650 and 810 nm) and a four-wavelength infrared pyrometer (centered at 1.8, 2.3, 3.5,

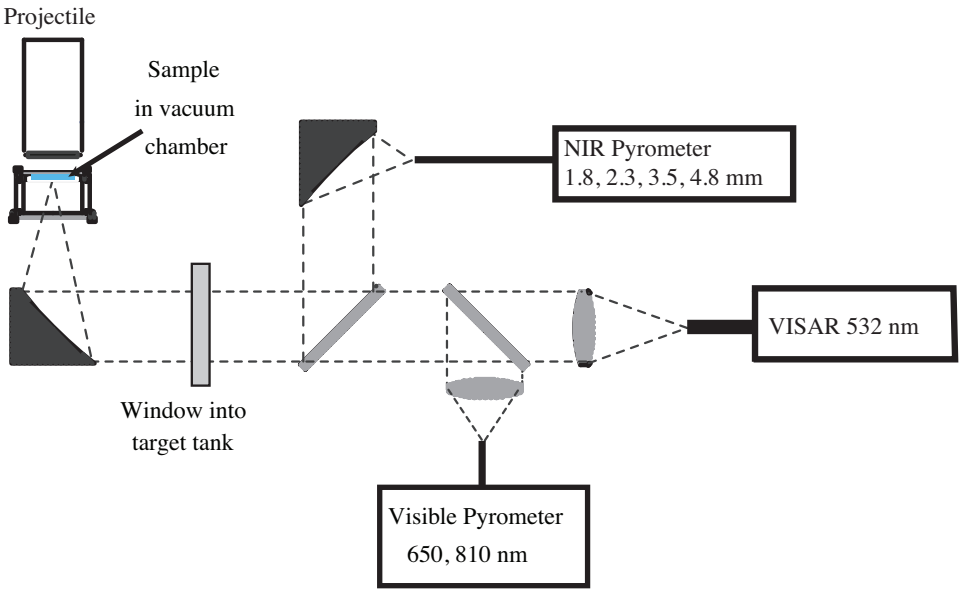

Figure 5.2: Plan view of experimental schematic for simultaneous pyrometry and VISAR measurements on the Harvard 40-mm single stage gun.

and 4.8 μm) developed by Boboridis et al. (2003) at Los Alamos National Laboratory. The infrared pyrometer is sensitive to radiance at temperatures as low as 300 K with a time resolution of 17 ns. The silicon diodes have a time resolution of 3 ns. The typical error in spectral radiance is 2% at each wavelength.

Planar shock wave experiments were performed by impacting the driver with stainless steel flyer plates accelerated to velocities between 1.2 and 2.7 km s^{-1} using the 40-mm single stage powder gun in the Harvard Shock Compression Laboratory. Projectile velocities were measured immediately prior to impact using three cross-barrel laser diodes. Shock pressures of 7.9 to 22.7 GPa were induced in the sample, which are well above the Hugoniot elastic limits of both ice and quartz.

The experiments are summarized in Table 5.1. Shock pressures were calculated by the impedance match solution of the release isentrope from the driver and Rayleigh line in the sample (the initial density times the observed shock velocity in the sample). The quoted 1σ error in the shock pressure is based on formal error propagation. Note that the shock pressures are close to those predicted

with a mixture Hugoniot derived from a mass average of the pure H_2O and SiO_2 Hugoniots (Meyers, 1994). Other parameters for the impedance match solution and additional experimental details are provided in the supplemental online materials.

Table 5.1: Summary of shock temperature experiments in an ice-quartz mixture. Uncertainties are 1σ.

Shock Pressure [GPa]	Impact Velocity [m/s]	Mixture Density [g/cm^3]	Sample Thickness [mm]	T_0 [K]	Shock Velocity [m/s]
7.9 ± 0.5	1192 ± 7	1.66 ± 0.05	3.09	119	4020 ± 120
12.9 ± 1.1	1725 ± 15	1.67 ± 0.05	2.59	114	4679 ± 259
16.2 ± 1.3	2030 ± 6	1.66 ± 0.04	2.61	109	5102 ± 256
18.5 ± 2.5	2110 ± 30	1.88 ± 0.04	3.05	153	4700 ± 1000
22.7 ± 1.6	2712 ± 7	1.61 ± 0.04	3.34	92	5560 ± 230

5.3 Data Analysis

Here we present a three-step method to derive the shock temperature of the H_2O component in the H_2O-SiO_2 mixture from the spectral radiance data. First, in Section 5.3.1, we determine the radiation emitted from the shocked layer in a transparent or semi-transparent material. Next, in Section 5.3.1, we introduce a novel method to separate the radiation emitted from the H_2O component from the total radiation from the shocked layer. Then, in Section 5.3.1, we address the effect of shock compressed air, stored in the pore spaces, and fit the individual radiance contributions from air and H_2O. Finally, we describe the post-shock temperature analyses in Section 5.3.2.

Our analysis relies on the assumptions of a steady wave front and immediate pressure equilibration behind the shock front. Steady shock waves have previously been measured in ice-sand mixtures (Larson et al., 1973). Pressure equilibration is assumed to be achieved based on flat top wave profiles in intermediate length scale mixtures (e.g., Dolgoborodov et al., 1992; Larson et al., 1973).

5.3.1 Shock Temperature Analysis

Spectral Radiance from the Shocked Layer

As the sample is semi-transparent in the visible and the near-IR wavelengths (0.65, 0.81, 1.8, and 2.3 μm), a method of analysis described by Boslough (1985) and Luo and Ahrens (2004) was used to determine the spectral radiance emitted from the shocked layer, $\epsilon^s L_2$. The spectral radiance observed at the pyrometer, L_0, is fit by

$$L_0 = L_1 e^{-a^s D^s} e^{-a^u D^u} + \epsilon^s L_2 e^{-a^u D^u} \tag{5.1}$$

at each wavelength. L_1 is the spectral radiance emitted at the driver-sample interface, a^u and a^s are the wavelength-dependent unshocked and shocked absorption coefficients, D^u and D^s are the thicknesses of the unshocked and shocked material, and ϵ^s, the emissivity of the shocked layer, is given by $1 - e^{-a^s D^s}$. Throughout this work, superscripts differentiate between shocked 's' and unshocked 'u' material parameters. The fit is performed as a function of time, t, where $D^u = D - U_s t$, $D^s = (U_s - u_p)t$, D is the initial thickness of the sample, U_s is the shock wave velocity (determined from the spectral radiance versus time data, see Figure 5.3), and u_p is the particle velocity behind the shock front. Reflectivity is neglected in the analysis based on the low reflectance coefficients determined by the Fresnel Equation.

Representative spectral radiance data are shown in Figure 5.3. As Boslough (1985) suggests, the peak in radiance at the start of the data record is likely due to a small amount of air at the interface between the driver and the sample. The radiation from the interface is attenuated as the thickness of strongly absorbing shocked material increases with shock wave propagation. Then, the observed radiation from the shocked layer increases with time as the thickness of unshocked material ahead of the shock front decreases. Spectral radiance data and fits for the other experiments are provided

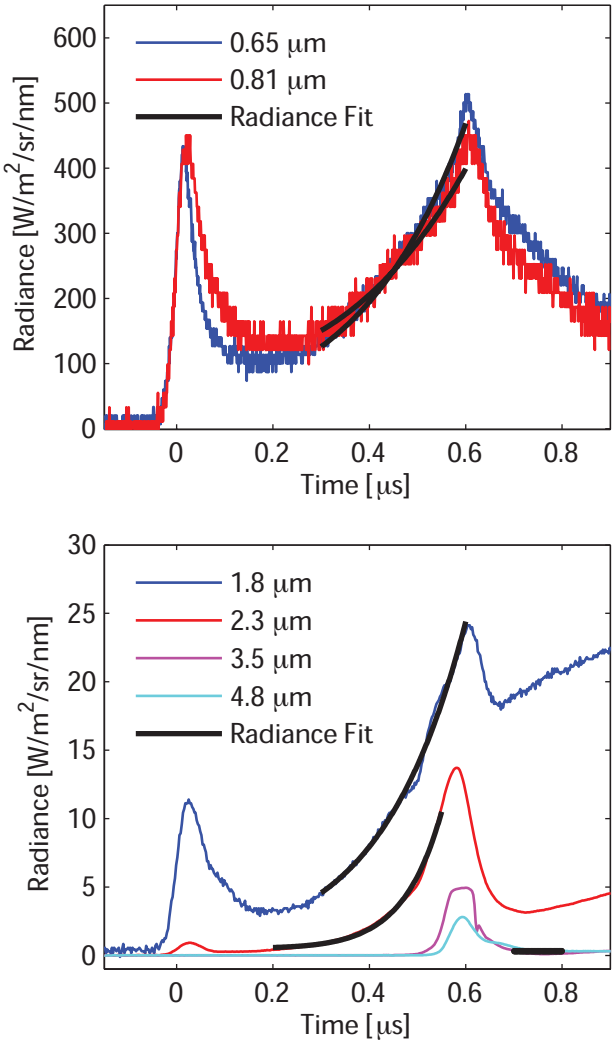

Figure 5.3: Spectral radiance emitted from a mixture of H_2O and SiO_2 subjected to a 22.7 GPa planar shock wave. For 0.65, 0.81, 1.8, and 2.3 μm, black lines are fits using Equation 5.1. For 3.5 and 4.8 μm, black lines denote time interval used to determine post-shock temperatures.

in the supplemental materials.

For a single-component sample, ϵ^s is the emissivity of the shocked layer and L_2 is the blackbody radiation from the shocked layer. L_2 can then be used to determine the apparent temperature, T_{ap}, of the shocked layer using Planck's Law. T_{ap} is an idealized temperature assuming a perfect blackbody source. The fitted values in Equation 5.1 and T_{ap} for each wavelength are provided in Table 5.2. For the 7.9, 12.9, and 16.2 GPa experiments, typical errors in T_{ap} are about 100 K in the shorter wavelengths and 15 K in the two longer wavelength channels. For the 22.7 GPa experiment, the error in the short wavelength channels are about 30 K, and the error in the longer wavelength channels are about 20 K. For the 18.5 GPa experiment, the radiance from the shock front was not derived as the detectors were saturated.

Spectral Radiance from the H_2O Component

Although it has been shown experimentally that pressure equilibrates almost immediately after passage of the shock front for mixtures of similar volume ratio, particle size, and shock front thickness (e.g., Dolgoborodov et al., 1992), thermal equilibrium will not be reached immediately. We estimate the time scale for thermal equilibration by conduction (as radiative transport can be neglected). Using coefficients of thermal diffusivity and conductivity for H_2O (Abramson et al., 2001) and SiO_2 (Kieffer et al., 1976) at pressures and temperatures near those in our experiment, we have numerically solved the one-dimensional thermal diffusion equation. For the time scale of our experiments (< 1 μs), the diffusion length scale in the ice is ~ 2 μm in the H_2O and ~ 6 μm in the SiO_2 (see supplemental material). Considering that the average particle size is ~ 180 μm, inter-granular thermal equilibrium is not obtained in the time scale of the experiment.

Seifter and Obst (2007) developed a method to separate the radiation from materials with equal emissivities but different temperatures using spectral radiance data. We have extended their

Table 5.2: Apparent shock temperatures, T_{ap}, and fitted parameters are determined using Equation 5.1 at 0.65, 0.81, 1.8, and 2.3 μm. Post-shock radiances and apparent post-shock temperatures are determined at 3.5 and 4.8 μm (section 5.3.2). T_H denotes an intermediate temperature inferred for H_2O after separation from the SiO_2 component (Sections 5.3.1 and 5.3.2).

Pressure [GPa]	Wavelength [μm]	a_s [m^{-1}]	a_u [m^{-1}]	L_1 [$W/m^2/sr/m$]	$\epsilon^s L_2$ [$W/m^2/sr/m$]	T_{ap} [K]	T_H [K]
7.9	0.65	1060	971	2.45×10^{11}	4.80×10^{10}	2220	2221
	0.81	1063	672	1.25×10^{11}	4.87×10^{10}	2006	2007
	1.80	3290	960	1.50×10^{10}	2.16×10^{9}	1003	1009
	2.30	3915	1632	1.89×10^{10}	8.49×10^{8}	813	824
post shock	*3.50*	–	–	–	*6.28×10^{6}*	*391*	*393*
	4.80	–	–	–	*4.87×10^{6}*	*326*	*332*
12.9	0.65	4020	270	4.99×10^{11}	1.35×10^{11}	2476	2479
	0.81	2797	10	5.82×10^{11}	1.79×10^{11}	2351	2353
	1.80	3295	341	6.87×10^{10}	9.2×10^{9}	1224	1232
	2.30	5137	2604	6.28×10^{9}	4.02×10^{9}	1021	1029
post shock	*3.50*	–	–	–	*1.06×10^{8}*	*536*	*539*
	4.80	–	–	–	*1.41×10^{8}*	*517*	*528*
16.2	0.65	3090	229	8.63×10^{11}	1.66×10^{11}	2536	2538
	0.81	2279	62	6.88×10^{11}	1.77×10^{11}	2348	2350
	1.80	3860	630	2.15×10^{11}	9.30×10^{9}	1227	1229
	2.30	9153	1933	9.90×10^{11}	4.38×10^{9}	1035	1044
post shock	*3.50*	–	–	–	*3.34×10^{8}*	*631*	*631*
	4.80	–	–	–	*3.07×10^{8}*	*597*	*611*
post shock	*3.50*	–	–	–	*3.86×10^{8}*	*644*	*650*
(18.5)	*4.80*	–	–	–	*4.84×10^{8}*	*657*	*679*
22.7	0.65	8830	701	4.79×10^{12}	4.70×10^{11}	2879	2881
	0.81	6467	591	4.38×10^{12}	4.00×10^{11}	2632	2634
	1.80	8070	1010	4.20×10^{11}	2.45×10^{10}	1441	1450
	2.30	4460	2230	1.05×10^{12}	1.92×10^{10}	1373	1379
post shock	*3.50*	–	–	–	*4.01×10^{8}*	*648*	*652*
	4.80	–	–	–	*2.92×10^{8}*	*591*	*605*

method to determine the temperature of a hot material surrounded by a significantly colder material with different emissivity.

We begin by considering the spectral radiance from the shocked layer, $\epsilon^s L_2$ (determined in the previous section), to be an ideal superposition of radiance from the H_2O and SiO_2 components:

$$\epsilon^s L_2 = \alpha_H^R \epsilon_H^s L_H + \alpha_S^R \epsilon_S^s L_S. \tag{5.2}$$

For each material, subscripted 'H' for H_2O and 'S' for SiO_2, α^R is the radiative area fraction from the shocked layer, and ϵ^s is the emissivity in the shocked state. We can simplify this equation by

comparing the spectral radiance from the shocked SiO_2, using theoretical estimates from Wackerle (1962) and Kleeman and Ahrens (1973), to the total radiance from the shocked layer. The calculated radiance from the SiO_2 is negligible: $< 1\%$ at each wavelength and smaller than the precision of the calibration. Therefore, within error, the spectral radiance from the H_2O component in the shocked layer, L_H, is given by

$$L_H = \frac{\epsilon^s L_2}{\alpha_H^R \epsilon_H^s}. \tag{5.3}$$

The physical area fraction, denoted by superscript 'P', of H_2O in the shocked layer is estimated by the initial area fraction, as material in a planar impact undergoes uniaxial strain. However, the radiative area fraction of H_2O in the shocked layer depends on the opacity of the shocked SiO_2. For example, if shocked SiO_2 has a very low absorption coefficient, the radiative area fraction of the H_2O will be approximately one, as radiation emitted from H_2O grains directly behind SiO_2 grains will be transmitted. From a one dimensional radiative absorption analysis (see supplemental materials), the difference between the physical area fraction, α_H^P, and the radiative area fraction, α_H^R, of H_2O in the shocked layer is given by

$$\alpha_H^R = \alpha_H^P + \alpha_S^P e^{-a_S^s d_S^s}, \tag{5.4}$$

where, for shocked SiO_2, a_S^s is the absorption coefficient and d_S^s is the average length of a grain.

From the one-dimensional radiative absorption analysis, we also find that the emissivity of the shocked H_2O is slightly dependent on the SiO_2 absorption,

$$\epsilon_H^s = \left(1 - e^{-a_H^s D_H^s} e^{-a_S^s D_S^s}\right) \frac{\left(1 - e^{-a_H^s d_H^s}\right)}{\left(1 - e^{-a_H^s d_H^s} e^{-a_S^s d_S^s}\right)}, \tag{5.5}$$

where D_H^s and D_S^s are the summed linear thicknesses of the shocked H_2O and SiO_2 components in

the sample, respectively. One may notice that D_H^s and D_S^s increase as the shock wave propagates through the sample, and consequently the emissivity of the H_2O would be a function of time, complicating the interpretation of Equation 5.3. However, for the fits performed with a time-dependent emissivity, we find that the emissivity of the shock front is not well constrained. Hence, the emissivity must be a very weak function of time. The inferred time independence requires the absorption coefficients be sufficiently high such that $\left(1 - e^{-a_H^s D_H^s} e^{-a_S^s D_S^s}\right) \approx 1$ for all the experiments.

The infrared absorption coefficients of H_2O at the pressures and temperatures reached in our experiments are not well constrained; however, based on shock temperature experiments (Stewart et al., 2008), absorption coefficients for H_2O significantly increase with increasing pressure and temperature. In determining the uncertainty on L_H associated with ϵ_H^s, we set a lower bound on the near-IR absorption coefficients of H_2O at the low temperature, ambient pressure values for ice, 909 and 1770 m^{-1} at 1.8 and 2.3 μm, respectively (Warren, 1984). The exact magnitude of the upper bound is not important as the exponential terms in Equation 5.5 associated with H_2O quickly go to zero.

For SiO_2, the absorption coefficients, while in the α-quartz phase, are constrained to within a factor of two of the ambient pressure and temperature values, ~ 1.0 m^{-1} at 0.65, 0.81, 1.8, and 2.3 μm (Drummond, 1936). The tight constraint is based on visible pyrometry measurements on fused quartz, where a negligible increase in the absorption coefficients was found under shock pressures up to about 30 GPa (Kondo and Ahrens, 1983). Note that the dramatic increase in absorption coefficients at shock pressures above 30 GPa was likely due to the structural phase transition to stishovite. According to Zhugin and Krupnikov (1987), the shock-induced phase transition from α-quartz to stishovite does not begin until 23 GPa. For this reason, we assume the α-quartz grains in our samples do not undergo a phase transition during our experiments. The possibility of a change in SiO_2 absorption in the highest pressure experiment is discussed below.

With these assumptions for the absorption coefficients in H_2O and SiO_2, the results from Equations 5.4 and 5.5 are used in Equation 5.3 to determine the spectral radiance from the shocked H_2O component, L_H, under the assumption of an ideal two-component system. Then, the ideal radiance temperatures of the shocked H_2O component, T_H, are derived from L_H using Planck's law at 0.65, 0.81, 1.8, and 2.3 μm. The results are presented in Table 5.2. Note that the ideal H_2O radiance temperatures are very close to the apparent temperatures, T_{ap}, the ideal blackbody temperature from the combined spectral radiance of all the components in the shocked layer. In the case of an H_2O–SiO_2 mixture, the presence of SiO_2 has a negligible effect on the radiative area fraction and emissivity of H_2O in the shocked layer, which are both close to 1. Hence, we consider the formal errors on T_H to be the same as quoted above for T_{ap}.

Effect of Initial Porosity

The ideal radiance temperature of the H_2O component, T_H, is highest at the shortest wavelength and monotonically decreases with increasing wavelength (Table 5.2). This systematic variation was first observed in post-shock temperature measurements on metals (Seifter and Swift, 2008) and has been explained by the presence of small area fractions of material radiating at significantly higher temperatures, known as "hotspots" (Seifter and Obst, 2007).

The ice-quartz samples have an estimated porosity of 1%. The amount of air trapped in pore spaces was minimized by starting with bubble-free ice and pressing the mixture under vacuum; however, even a small amount of shock compressed air reaches much higher temperatures than shocked ice. The magnitude of the radiance from shocked air cannot be predicted due to the unknown mass of air in the pores.

Following the analysis of Seifter and Obst (2007), we fit T_H as a function of wavelength (from

0.65 to 2.3 μm) with a two-component model representing the H_2O and hotspots of air,

$$T_H = \frac{c_2}{\lambda \ln\left[\left(\frac{1-\alpha_{\text{air}}}{e^{c_2/\lambda T_{\text{H}_2\text{O}}}-1} + \frac{\alpha_{\text{air}}}{e^{c_2/\lambda T_{\text{air}}}-1}\right)^{-1} + 1\right]}, \tag{5.6}$$

where $c_2 = hc/k \approx 1.439 \times 10^{-2}$ m K is the second radiation constant, h is Planck's constant, c is the speed of light, and k is Boltzmann's constant. α_{air} is the area fraction of shocked air, T_{air} is the temperature of the shocked air, and $T_{\text{H}_2\text{O}}$ is the true temperature of the shocked H_2O. The three model variables, α_{air}, T_{air}, and $T_{\text{H}_2\text{O}}$, are constrained by four wavelengths using a least squares fit weighted by the uncertainties at each wavelength. The fits for each experiment are presented in Figure 5.4 and Table 5.3. The two-component model is an excellent match to the values for T_H at each wavelength. The tabulated uncertainties are the formal uncertainties on the weighted two-component fit. Note that the area fraction of trapped air is comparable to the estimated porosity in the samples.

Table 5.3: Shock and post-shock temperatures for H_2O. Shock state from 2-component analysis, where temperature of shocked air (T_{air}), area fraction of shocked air (α_{air}), and shock temperature of H_2O ($T_{\text{H}_2\text{O}}$) are fit using Equation 5.6. Post-shock temperatures are the average of the H_2O radiance temperatures at 3.5 and 4.8 μm. Uncertainties are 1σ.

Shock	Shock State			Post-shock State
Pressure [GPa]	α_{air}	T_{air} [K]	$T_{\text{H}_2\text{O}}$ [K]	T_{H_2O} [K]
7.9	0.001 ± 0.0003	7700 ± 1400	630 ± 140	*360 ± 40*
12.9	0.005 ± 0.002	6500 ± 1100	760 ± 200	*530 ± 10*
16.2	0.004 ± 0.0009	7200 ± 800	850 ± 70	*620 ± 20*
18.5	–	–	–	*660 ± 20*
22.7	0.009 ± 0.003	7700 ± 900	1220 ± 50	*630 ± 30*

5.3.2 Post-Shock Temperature Analysis

Up to this point, we have not discussed the radiance measurements at 3.5 and 4.8 μm because H_2O is completely opaque at these wavelengths (Warren, 1984). The opacity of H_2O at these wavelengths makes the spectral radiance data suitable for deriving post-shock temperatures as radiation from

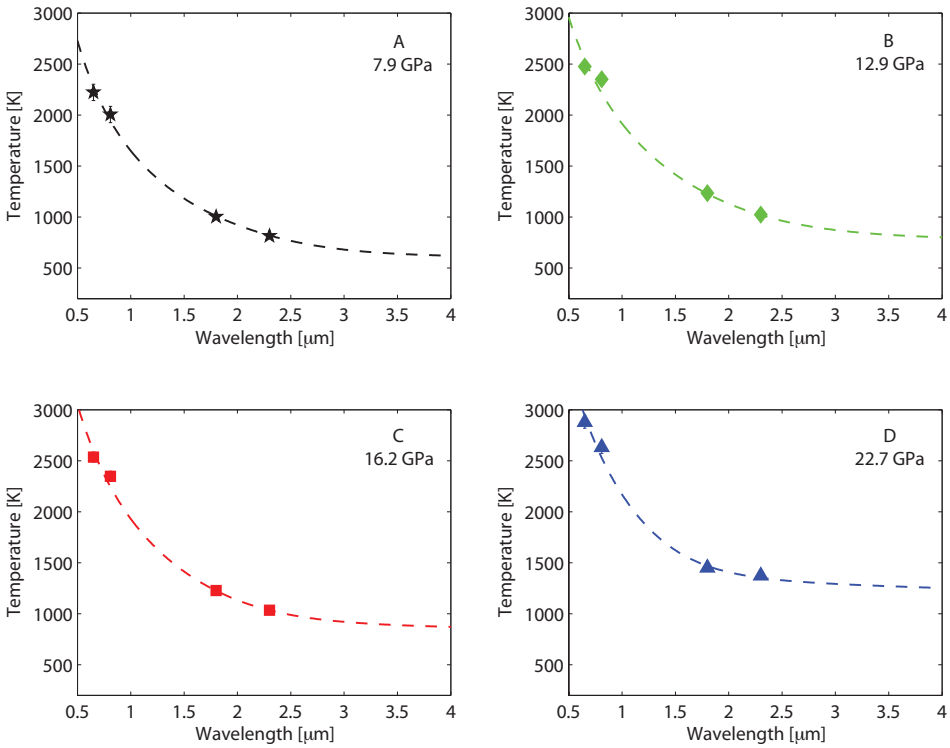

Figure 5.4: Two-component (shocked H_2O and shocked air) fits to T_H as a function of wavelength using Equation 5.6.

shocked material will not contaminate the light emitted from the material released from the shock state by wave reflection at the downrange free surface.

The spectral radiance of the released material, L_0, at 3.5 and 4.8 μm is obtained by taking an average of the radiance data for a short time interval after the shock front has reached the free surface (Figure 5.3). As in Section 5.3.1, we compare the radiance from shock released quartz (Raikes and Ahrens, 1979b) with the post-shock radiance data from the ice-quartz mixture. The radiance contribution from the shock released SiO_2 is negligible at both 3.5 and 4.8 μm. Consequently, we can again simplify our analysis of the post-shock spectral radiance to

$$L_H = \frac{L_0}{\alpha_H^R \epsilon_H} \ , \tag{5.7}$$

where L_H is the radiance from the H_2O, α_H^R is the radiative area fraction of the H_2O, and $\epsilon_H \approx 1$ as H_2O is known to be sufficiently opaque at 3.5 and 4.8 μm (Warren, 1984). The reflectivity of free surface of the sample is negligible (Downing and Williams, 1975), according to the Fresnel Equation.

As in the shock temperature analysis, α_H^R is determined by Equation 5.4, where we can again approximate the physical area fractions with their unshocked area fraction. This assumption is reasonable as release is uniaxial for the short period of measurement. At 3.5 and 4.8 μm, the absorption coefficients in SiO_2 are significantly lower than in H_2O: 33 and 950 m^{-1}, respectively (Drummond, 1936). The post-shock radiance temperature of the H_2O component of the mixture is derived from the post-shock radiance, obtained with Equation 5.7, using Planck's law. The results are tabulated as T_H in Table 5.2. The radiance temperature difference between the two wavelengths is small (10 to 60 K); therefore, we infer that the post-shock radiance is negligibly contaminated by released hotspots at the free surface. Hence, we report the true post-shock temperature in H_2O,

$T^{\text{post}}_{\text{H}_2\text{O}}$ in Table 5.3, by the average of the radiance temperatures T_H of H_2O at 3.5 and 4.8 μm. The tabulated uncertainty is from the two-wavelength average.

5.4 Results

In this section, we summarize the shock and post-shock temperature measurements in the context of what is known about the phase diagram and shock response of H_2O. Then, we present information about the shock front thickness from the measurements of free surface velocity. We conclude the section with a discussion of uncertainties.

5.4.1 Shock Temperatures

The H_2O component in the initially $\sim$100 K ice-quartz mixture reaches temperatures between 630 and 1220 K when shocked to pressures between 7.9 and 22.7 GPa (Table 5.3). The shock temperatures of the H_2O component are plotted in Figure 5.5 with a model 100 K principal Hugoniot, quasi-isentrope and principal isentrope. The Hugoniot and isentrope were derived from the 5-Phase H_2O model equation of state (EOS), which is described in detail in the appendix of Senft and Stewart (2008). The quasi-isentrope was constructed by considering a ring-up configuration of H_2O-ice between SiO_2; for a given equilibrium pressure between the two components, the quasi-isentrope temperature is given by the 5-Phase H_2O EOS temperature at the first pressure step.

As shown in Figure 5.5, the shock temperatures in the H_2O component are clearly much higher than the principal isentrope and the quasi-isentrope. The data points are in agreement with the 5-Phase EOS 100 K principal Hugoniot. The lowest pressure point is in perfect agreement with an experiment in pure H_2O ice: 673 K at 8.2 GPa (Stewart et al., 2008). The shock temperature of the H_2O component at 12.9 GPa (760 ± 200 K) is less than found in pure H_2O shocked to a similar pressure (about 1000 K), but the two agree within 2σ error. The two highest pressure data points

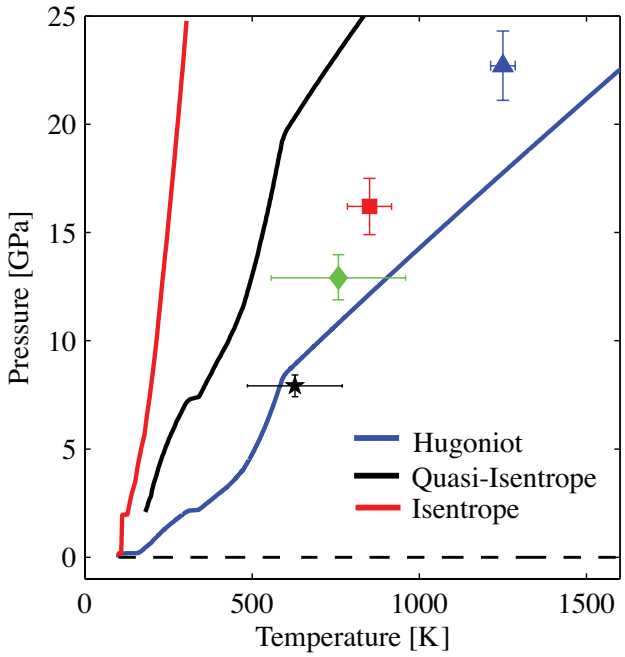

Figure 5.5: Shock temperatures in the H_2O component of the mixture (T_{H_2O}, Table 5.3). Shock states are compared to the model 100 K H_2O ice Hugoniot, quasi-isentrope, and principal isentrope derived from the 5-Phase H_2O EOS (Senft and Stewart, 2008) (blue, black, and red curves, respectively).

are colder than the 5-Phase EOS 100 K principal Hugoniot predicts; however, note that there is no shock temperature data in this pressure regime on pure H_2O ice.

5.4.2 Post-Shock Temperatures

The post-shock temperatures in the H_2O component range between 360 and 660 K (Table 5.3) upon release from shock pressures between 7.9 and 22.7 GPa. Such high temperatures are not expected for full release to ambient pressure. Post-shock temperature measurements by Stewart et al. (2008) revealed that pure H_2O shocked to supercritical fluid initially releases to the saturation vapor curve because full decompression cannot occur until volume expansion allows for production of low-density vapor. On the time scale of the experiments presented here, full decompression is not achieved.

The release to the saturation vapor curve is intuitively presented in temperature-entropy ($T-S$) space because unloading from the shock state is isentropic and follows a vertical line downward. In Figure 5.6, the shock and post-shock temperatures of the H_2O component (filled and open symbols, respectively) are plotted versus the entropy on the principal Hugoniot derived from the 5-Phase H_2O model. The measured post-shock temperatures are in excellent agreement with the saturation vapor temperature at the assumed principal Hugoniot entropy. The temperature and entropy on the saturation vapor curve are very well established (e.g., Wagner and Pruss, 2002). Hence, the post-shock temperatures strongly constrain the entropy attained in the shock state. The entropy indicates that the H_2O component reached a state close to the principal Hugoniot at the pressure defined by the bulk impedance of the mixture.

5.4.3 Free Surface Particle Velocities

The thickness of the shock front can be constrained by the rise time of the shock breakout at the downrange free surface. VISAR measurements of the free surface velocity are presented in

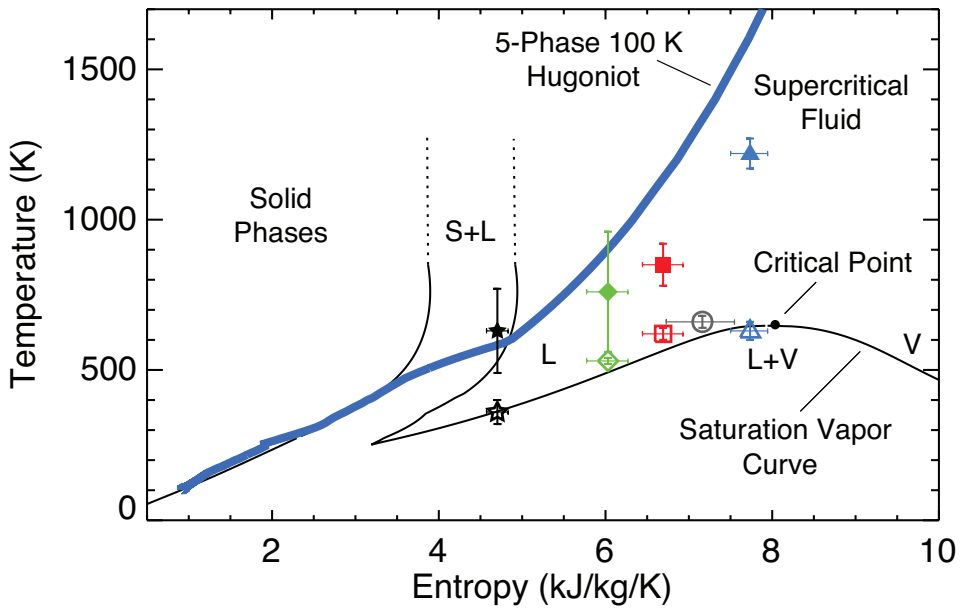

Figure 5.6: Simplified temperature-entropy phase diagram for H_2O, with phase boundaries (thin black lines) and the 5-Phase model 100 K Hugoniot (thick blue line). Shock and post shock temperatures in H_2O ice are plotted using the entropy attained by single shock loading to the 5-Phase model Hugoniot (closed and open symbols, respectively).

Figure 5.7 for the 7.9 and 22.7 GPa experiments. Using the shock velocity determined from the radiance measurements (Table 5.1), the rise times indicate shock front thicknesses of about 220 and 60 μm for the lowest and highest pressure experiments, respectively. As the thickness of the shock front is comparable to or larger than the grain size in the H_2O–SiO_2 mixture, the shock wave is unable to reflect and/or interact multiple times with a single grain before the final shock pressure is achieved. Thus, according to the general classifications presented in the introduction, these experiments fall into the intermediate length scale regime.

5.4.4 Uncertainties

The tabulated uncertainties for the shock temperature of the H_2O component are formal errors based on the least squares fit using the two-component model (Table 5.3). Note that high radiance temperatures due to trapped air were also observed in the visible in the shock experiments on pure

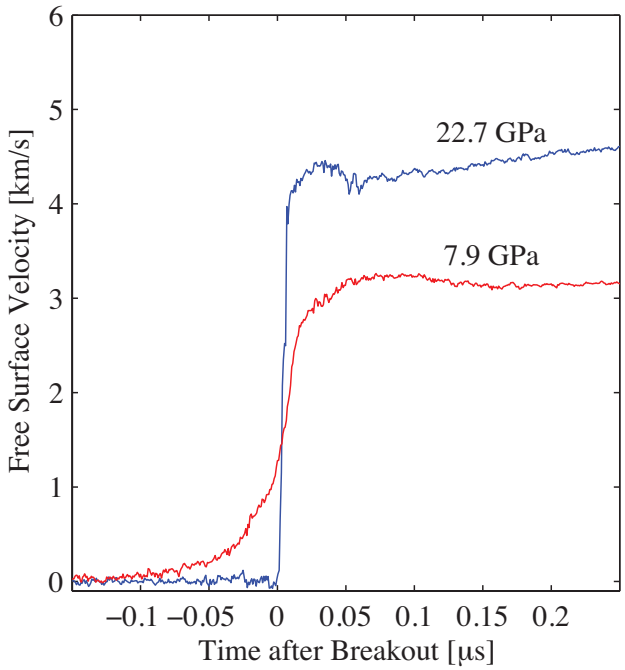

Figure 5.7: Free surface particle velocities from the 7.9 and 22.7 GPa experiments measured by velocity interferometry (VISAR). Time axis is adjusted to align shock breakout to the midpoint of the rise in particle velocities.

H_2O ice; however, the relative contribution to the radiance at 1.8 μm and 2.3 μm was significantly less in the pure H_2O experiments because of the differences in sample preparation.

The high radiance in the visible also raises the possibility of nonthermal emission. For example, shock-induced luminescence has been observed in α-quartz at shorter wavelengths than used in this study (Schmitt and Ahrens, 1989). If nonthermal emission contaminated the two shortest wavelengths used here, then the contribution from hotspots (air) to the total radiance would decrease and the true shock temperatures of the H_2O component would increase to contribute a larger fraction of the radiance observed at the two longer wavelengths. However, the goodness of fit between the measurements and the two-component model coupled with the fact that the fitted area fraction of hotspots is comparable to the porosity in the samples leads us to favor trapped air over nonthermal emission. Some amount of trapped air is expected, and it is unlikely that a

nonthermal process mimics air in pore spaces so well.

Another source of uncertainty in the shock temperature of the H_2O component is the assumption of transparency of the SiO_2 component over the range of pressures and temperatures reached in these experiments. Between 0.65 and 2.3 μm, the absorption in SiO_2 is orders of magnitude less than in H_2O under ambient conditions. In the visible, low opacity under shock compression is confirmed by experiments on fused quartz (Kondo and Ahrens, 1983), and we assume that low opacity is also preserved under shock at 1.8 and 2.3 μm. The greatest uncertainty in the opacity of shocked SiO_2 occurs in the highest pressure experiment where there is the possibility of a phase change to stishovite. In this experiment, if the SiO_2 component were opaque, then the shock temperature of the H_2O component would have to be about 300 K higher to yield the same total radiance. In general, uncertainties in the opacity of SiO_2 and the presence of nonthermal emission lead to a possible underestimate in the true shock temperature of H_2O.

The tabulated uncertainties in the post-shock temperature of the H_2O component assume no contamination from hotspots at the free surface. If there were a small high temperature component, then the H_2O release temperatures would be slightly lower and closer to the radiance temperature at 4.5 μm (a difference of < 60 K). The uncertainty in the nonthermal radiation in the shocked SiO_2 has no effect on uncertainty of the post-shock temperatures because of the high opacity of H_2O at the two longest wavelengths. If the assumed radiative area fraction of H_2O were less (e.g., equal to the physical area fraction by an increase in the opacity of SiO_2), then the post-shock temperature of the H_2O component would have to be higher by at most 50 K to achieve the same total radiance. Hence, the post-shock temperatures are extremely robust.

5.5 Discussion

5.5.1 Energy Partitioning in Mixtures

In each H_2O–SiO_2 mixture experiment, all of the parameters required to address the question of energy partitioning were determined. We simultaneously measured the (1) shock velocity in the mixture, (2) the shock front thickness, (3) the shock temperature of the H_2O component, and (4) the post-shock temperature of the H_2O component. The shock pressure of the mixture was derived from the shock velocity and impedance match with the aluminum driver. Because of the low compressibility and low emissivity of α-quartz, the radiation from the shocked SiO_2 was negligible. As a result, the radiance from the shock front was dominated by the H_2O component and trace amounts of air. The wavelength-dependent radiance temperatures from the shock front are very well described by a two-component mixture of shocked H_2O and shocked air. The shock temperatures of the H_2O component are in agreement with the 5-Phase model principal Hugoniot at the shock pressure of the mixture. Upon release to the saturation vapor curve, the post-shock temperatures of the H_2O component are strong evidence for single shock compression of the H_2O.

Our results indicate that in the intermediate length scale regime, each component is shocked to a state close to its principal Hugoniot at the shock pressure determined by the bulk impedance of the mixture. Thus, the energy partitioning immediately behind the shock front is simply approximated by the individual Hugoniots of the components in the mixture.

We interpret the observed energy partitioning in a mixture in the context of the three general regimes described in the introduction. In the small length scale regime, the characteristic length scale of the mixture must be small enough such that the thermal equilibration time is comparable to the rise time of the shock front. Consequently, the energy partitioning is determined by full thermodynamic equilibrium between the components. In the intermediate length scale regime, the

shock front thickness is comparable to the length scale of the mixture, and the thermal equilibration time is longer than the rise time. The components are loaded simultaneously to the shock pressure determined by the bulk impedance of the mixture; and the initial energy partitioning is determined by the principal Hugoniots of the components. In the large length scale regime, the characteristic length scale of the mixture is much larger than the shock front thickness. Hence, the shock front is able to reflect at the component boundaries. Pressure equilibration between the components is achieved by a ring-up loading path, and the energy partitioning is determined by the impedance mismatch between the components.

5.5.2 Melting Ice during Planetary Impact Events

Based on the mixture regimes presented above, we now have a framework for calculating the thermodynamic pathways for planetary impacts onto icy mixtures. Here, we focused on the importance of the length scale of the mixture and the rise time of the shock front. In order to calculate melting upon release from the shock state, one also needs to know the total duration of the shock.

For intermediate length scales, the components of a mixture may be out of thermal equilibrium immediately behind the shock front. However, the duration of the shock pulse will determine how much heat and entropy is lost from the H_2O, via conduction, before release from the shock state. The unloading pathway is isentropic; hence, the entropy of the unloaded H_2O component in an intermediate mixture will depend on the extent of thermal equilibration.

The criteria for shock-induced melting can be considered in terms of a critical entropy that is needed for melting upon release to ambient pressure (Ahrens and O'Keefe, 1972). The criteria can also be thought of as a critical shock pressure required to increase the entropy to the critical value. However, if any entropy is lost via thermal conduction prior to release, the critical shock pressure for melting on release will increase. For pure H_2O ice, the criteria for shock-induced melting and

vaporization is well established (Stewart et al., 2008). If shock release occurs before significant thermal conduction between the components, then the critical shock pressures for melting ice in a mixture is simply the same as for pure ice. However, in cases of significant thermal conduction, the entropy at the time of release must be estimated to determine the higher critical shock pressure required for melting on release.

Therefore, determining the criteria for shock-induced melting requires knowledge of the length scale of the mixture and the duration of the shock pulse. In general, these quantities are not well known in planetary situations. Based on shock wave profiles measured from explosive experiments, the thickness of the shock front at low amplitudes is large (up to 100s of meters) and potentially resolvable in numerical simulations (Melosh, 2003). At present, detailed modeling of the initial unequilibrated state and subsequent thermal equilibration in a mixture is not a feature in hydrocodes used for planetary impact events. Hence, hydrocode results will have to be interpreted based on assumptions of mixing lengths and time scales to derive the volumes of melt in a mixture.

This work has demonstrated that in some cases, the volumes of melting in a mixture may be calculated using the criteria for pure H_2O. Details of the volume of melting under different length and time scales is the subject of future work. Future work will also consider the effects of varying the mixture ratio and the role of strength in the matrix of the mixture.

5.6 Conclusions

In this work, we address the question of energy partitioning during shock compression of a hydrodynamic material mixture. We construct a conceptual framework to delineate between the different general thermodynamic regimes that are denoted by the ratio of the length scale of the mixture to the thickness of the shock front.

Specifically, we focus on shock-induced melting of H_2O ice in an ice-quartz mixture at intermedi-

ate length scales. We performed shock and post-shock temperature experiments and simultaneously determined the shock pressure and shock front thickness. The results indicate that the H_2O ice component was shocked to the principal Hugoniot in the regime where the shock front is comparable to the length scale of the mixture. Hence, the energy partitioning immediately behind the shock front in the intermediate length scale regime is determined by the Hugoniots of the components. In some planetary situations and in these laboratory experiments, release from the shock state occurs before significant heat is lost to the SiO_2 via conduction. In these situations, the critical shock pressures required to melt ice are the same as for pure ice.

In some cases, the length scale of the mixture and the duration of the shock pulse allow for significant thermal conduction between the components before isentropic release to ambient pressures. In these cases, the shock pressures required to melt ice in a mixture will be higher than in pure ice. At present, numerical simulations of impacts onto icy mixtures are not able to capture the complexity of the problem, and educated assessments of length and time scales are needed to infer the amount of melting. This work illustrates the richness and challenges that underlie the deceptively simple question: How much ice melts in a planetary impact event?

Chapter 6

Uncertainties in the Shock Devolatilization of Hydrated Minerals: A Nontronite Case Study

Controlled recovery of hydrated minerals subjected to planar shock loading is challenging because of the large difference in shock impedance between the natural samples and the engineering materials used as the recovery capsules. Significant differences in recovery capsule design confound straightforward interpretation of existing data on shock modification of hydrated minerals. We present results from new experiments on nontronite (a smectite clay observed on Mars) and identify major issues in the interpretation of recovered samples. Most previous work assumes that the first shock pressure step in a ring-up configuration is the most important factor in the interpretation of shock modification. By comparing experiments with similar first shock steps but different final shock states, this work demonstrates the need for a deeper understanding of the thermodynamics of ring-up experiments in order to be able to interpret the results in terms of an equivalent single shock loading pressure for planetary applications. In this work we also show that venting of the samples does not matter significantly at low pressures, but at high shock pressures, vented capsules are essential in order to characterize the degree of devolatilization upon shock release. We have developed a recovery method and validation test that allows us to address the major issues and

This chapter is in preparation for submission with Sarah T. Stewart, Matthew G. Newman, Ralph E. Milliken, and Nicholas J. Tosca.

technical tradeoffs with shock recovery experiments on volatile materials.

6.1 Introduction

Recent detailed observations of hydrated minerals on Mars has rejuvenated interest in understanding the effects of shock processing on major phyllosilicate phases. Understanding the distribution of hydrated minerals in space and time will ultimately constrain paleo-surface conditions, providing insight into the evolution of the Martian climate. Phyllosilicates are confined largely to Noachian age terrains (e.g., Bibring et al., 2006; Ehlmann et al., 2013) and thus formed contemporaneously with a period of intense impact cratering. As a result, phyllosilicates may carry an overprint of crustal impact modification. Such pervasive shock processing may have significantly modified or destroyed some phyllosilicates through mechanical and/or thermal processes, which would in turn modify their spectral signatures. Detailed interpretation of the origin(s) and modification of phyllosilicate deposits requires an understanding of the effects of shock modification of the specific phases observed on Mars. Iron-magnesium smectites (nontronite or saponite) are the most common clays identified on Mars, followed by aluminum-rich phases (montmorillonite or kaolinite), chlorite, and serpentine (Ehlmann et al., 2013). In this work, we conduct shock recovery experiments on nontronite and address key technical issues related to interpreting shock-induced modification of hydrated minerals.

Despite previous experimental attempts aimed at understanding shock-induced structural and spectroscopic changes of phyllosilicates, the data are sparse and difficult to interpret. Part of the difficulty in interpreting the experimental results stems from the significant differences between laboratory shock conditions and planetary impact events and differences between laboratory experimental designs. The differences between the laboratory and nature include the duration of shock

loading, step-wise (or ring-up) vs. single-shock loading paths in pressure-volume-temperature space, and confined vs. unconfined conditions upon decompression from the shock state. In this work, we examine the importance of the latter two issues by comparing the shock-modification of nontronite subjected to different loading paths and under both confined and unconfined decompression.

In standard shock-recovery studies, samples are recovered in metal containers that are designed to produce a nearly uniform shock loading history over the entire sample and to confine the sample upon decompression (e.g., Bourne and Gray III, 2005). Because hydrated minerals have lower densities and sound speeds compared to steel, the shock wave reverberates in the sample, leading to a step-wise loading path to the peak shock pressure. A step-wise loading path attains much lower entropy and lower shock temperature compared to single shock loading to the same peak shock pressure. Because most of the entropy is gained in the first shock state, some studies interpret shock-induced modifications in terms of the pressure in the first shock state (e.g., Tyburczy et al., 1990) or in terms of the total $\int PdV$ work (Bowden et al., 2000; DeCarli et al., 2002; Prescher et al., 2011) for comparison to single shock states in natural impact events. However, other studies interpret their results in terms of the peak shock pressure without reporting the loading path. The difficulties of interpreting the results in terms of the peak shock stress has been sufficiently discussed by DeCarli et al. (2002). However, the validity of interpreting shock modification in terms of the first shock step or the total energy deposited has not been demonstrated.

In many studies of volatile-bearing phases, above a material-dependent threshold shock pressure, the capsules burst due to expansion of gases upon decompression (e.g., Skala et al., 2002; Weldon et al., 1982; Zhang and Sekine, 2007), often preventing successful recovery of the sample. Ivanov et al. (2002) calculated the equilibrium isentropic decompression path of carbonate and found that devolatilization requires expansion to multiple orders of magnitude times the original volume. In recognition of the need for volume expasion to study devolatilization, various capsule designs have

incorporated vent holes from the sample. In most cases, these vents close during the passage of the shock through the recovery container (Ivanov et al., 2002). Unfortunately, the incorporation of vent holes in the recovery capsule has the undesirable side effect of introducing heterogeneous shock loading of the sample. The need for volume expansion upon release is thus a serious technical issue in shock-devolatilization studies.

Previous work has found that shock processing can change the near- and mid-infrared spectra of nontronite and other phyllosilicates (Boslough et al., 1980; Gavin et al., 2013; Sharp et al., 2012): e.g. the 3 μm O-H stretch and Si-O vibration bands at approximately 9 and 20 μm. In general, the O-H stretch feature is diminished and the Si-O vibrational bands are completely removed and replaced by a less distinct glassy spectrum as the shock pressure increases. These spectral changes with increasing pressure were interpreted to be a result of the (1) loss of water; (2) collapse of the interlayer structure in smectites; and (3) at the highest pressures, shock-induced amorphization.

In this work, we discuss some of the differences between laboratory recovery experiments on clays and impact cratering. We present new shock recovery experiments on nontronite using a novel capsule design to allow for volume expansion while maintaining a simple loading history in the sample. The recovery experiments were designed to illustrate the importance of the recovery fixture itself on the results of the experiment. To better understand the states reached during the recovery experiments, we present measurements of the principal Hugoniot for the nontronite clay used in this study. Finally, we caution against simple interpretations of shock recovery experiments and make suggestions for future experimental designs that would reduce the difficulty in comparing natural impacts to laboratory experiments.

6.1.1 Previous Shock Modification Studies on Nontronite

Boslough and colleagues conducted two impact shock recovery experiments on nontronite that reached peak pressures of about 18 and 30 GPa (Boslough et al., 1980; Weldon et al., 1982). The samples were placed in a steel recovery chamber with downrange steel plates backing the sample followed by an enclosed expansion volume. The nontronite samples, from Riverside, CA, were powdered and pressed to a density of 2.7 g cm^{-3}. They found that the basal layer collapsed from 14.9 to 11.7 angstroms and that some of the bound OH was lost in the 30 GPa experiment. In their experimental configuration, the downrange expansion volume led to a second shock loading of the sample upon striking the downrange wall of the recovery chamber. The effects of the second loading event were not considered in the analysis. In a subsequent study, Boslough et al. (1986) conducted a series of explosively-driven shock recovery experiments (13 to 48 GPa peak pressures) on 37 to 62% porous nontronite in unvented copper fixtures to measure magnetic properties, XRD, and Mössbauer spectroscopy. These experiments suffered from severe heterogeneity in the shock pressure across the sample. In two cases, their capsules ruptured and the results were different than for the enclosed samples, but the details of the differences was not discussed.

More recently, Gavin et al. (2013) collected a wide range of spectroscopic data on shock recovered clays, including nontronite. Their experiments utilized a sealed recovery capsule and non-planar impact conditions: a 4×1 mm steel flyer on a 7×4.5-mm polycarbonate sabot impacting a 100×20-mm recovery capsule with a centered 6×5-mm sample located 5 mm from the impact plane (all dimensions are cylindrical diameter×thickness). The samples were pressed powders with unreported densities. The relative dimensions of the projectile and capsule led to highly heterogeneous shock pressure histories in the samples that were estimated by modeling the laboratory experiments using an estimated Hugoniot for the sample. In nontronite, samples subjected to estimated peak pressures of 5.4-17.5 GPa and average shock pressures of 0.9-1.6 GPa did not exhibit any significant changes

in the near-infrared spectra but did have changes in the mid-infrared. Gavin et al. (2013) also note that the recovered samples exhibit a greater degree of modification than samples studied during heating-only experiments (Gavin and Chevrier, 2010), where the predicted post-shock temperature from the shock experiments are significantly less than the heating experiments. However, these experiments are extremely difficult to interpret because of the combined problems of heterogeneous, nonplanar shock loading, uncertainty in the capsule venting, and unknown Hugoniot of the sample.

Sharp et al. (2012) conducted a series of controlled planar shock recovery experiments on clays in a stainless steel recovery cell. They recovered samples of nontronite that achieved peak pressures ranging from about 10 to 40 GPa. They observe increasing modification to the visible and infrared reflectance spectrum with increasing peak shock pressure (Friedlander et al., 2012) and a broadening of the peaks in the X-ray diffraction spectrum leading to amorphization during the experiment that achieved a ∼40 GPa peak shock state. It is not clear whether or not the recovered samples were allowed to freely expand during decompression.

6.2 Shock Experiments on Nontronite

We conducted shock Hugoniot measurements and shock recovery experiments on the Harvard 40-mm single stage gun (Stewart, 2004). The nontronite samples were the American Petroleum Institute Clay Mineral Standards H-33a and H-33b from the Lockwood Siding road cut, Manito, WA.

In most shock recovery experiments on clays, the effects of the shock are presented as a function of peak shock pressure within the recovery cell (e.g. Gavin et al., 2013; Sharp et al., 2012). The decision to present the recovery data against peak shock pressure is often necessitated by the uncertainty in the Hugoniot of the clay sample, and hence, uncertainty in the first shock step in the shock reverberation. In this work, we measured the Hugoniot of the nontronite clay used in our

shock recovery experiments to be able to determine the shock loading path in the metal recovery cells.

6.2.1 Hugoniot Measurements

The nontronite samples were powdered, sieved to less than 65 μm, and pressed to an average density of 2.14±0.06 g cm^{-3}. Impact velocities from 1.3 to 2.6 km s^{-1} with aluminum or steel flyers generated shock pressures from 2.5 to 23 GPa in the nontronite clay. In experiments 80 and 82, shock velocities were measured by transit times between multiple embedded magnetic particle velocity gauges (Dremin and Adadurov, 1964; Dremin and Shvedov, 1964; Petersen et al., 1970; Sheffield et al., 2006). In experiments 85-93, shock velocities were determined by using the relative transit time between two samples of different thickness. A multi-beam velocity interferometer system for any reflector (VISAR) (Barker and Hollenbach, 1972) or piezoelectric pins were used to determine the time that the shock wave reached the free surface. Piezoelectric pins were also applied to the driver plate to determine the tilt of the flyer at impact, which was then used to correct the transit times where appropriate. We impedance matched the shocked nontronite sample to the polycarbonate driver (experiments 80 and 82) or the stainless steel driver (experiments 85-93) assuming that the release path of the driver is described by the reflected Hugoniot, which is an accurate approximation for the relatively low pressures achieved in this study.

To impedance match to the polycarbonate drivers, we combined the Hugoniot datasets of Millett and Bourne (2006) with those of Marsh (1980) and fit the U_s-u_p data below a particle velocity of 1 km s^{-1} with a linear function. Above 1 km s^{-1}, the data deviate significantly from the low pressure linear fit. To impedance match polycarbonate to higher pressures, one should use a higher order polynomial fit to account for the change in slope. Below a particle velocity of 1 km s^{-1}, the

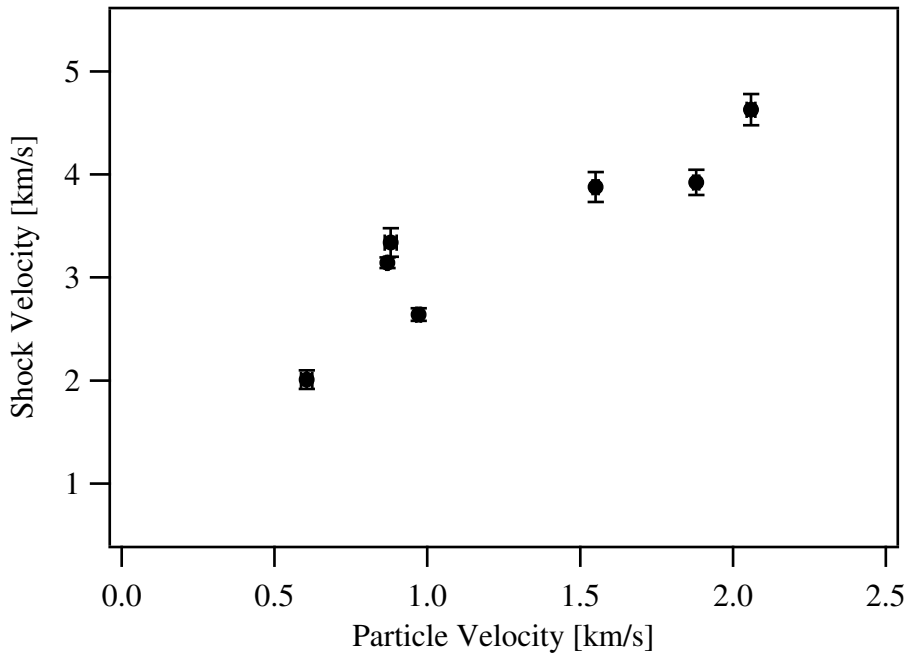

Figure 6.1: Principal Hugoniot of nontronite pressed powder with an average initial density of 2.14±0.06 g cm^{-3}.

polycarbonate Hugoniot is well fit by

$$U_s = 2.00(0.11) + 2.09(16)u_p, \tag{6.1}$$

where the correlation coefficient between the intercept and slope is -0.93498, the velocities are in km s^{-1}, and the initial density is $\rho_0 = 1.196$ g cm^{-3}. To impedance match to the stainless steel driver, we used the Hugoniot for SS-304 from Duffy and Ahrens (1997).

The Hugoniot data for nontronite are presented in Table 6.1 and in Figure 6.1. Over this particle velocity range, the linear fit is

$$U_s = 1.62(9) + 1.37(8)u_p, \tag{6.2}$$

where the correlation coefficient between the intercept and slope is -0.9368. In Figure 6.1, note the

large range of shock velocities near particle velocities of ∼0.9 km s^{-1}. The scatter is not a result of a systematic difference in the shock velocity measurement techniques as both the embedded magnetic gauge method and the multi-sample transit time method produced a relatively high and low shock velocity point in this region of the Hugoniot. The reason for this feature on the Hugoniot is not known.

Table 6.1: Summary of Nontronite Hugoniot data.

Experiment	ρ_0 [g cm^{-3}]	V$_{imp}$ [km s^{-1}]	U$_s$ [km s^{-1}]	u$_p$ [km s^{-1}]	P [GPa]	ρ_1 [g cm^{-3}]
80	2.03 ± 0.08	1.229 ± 0.015	2.01 ± 0.09	0.60 ± 0.02	2.47 ± 0.16	2.90 ± 0.26
82	2.20 ± 0.02	2.078 ± 0.013	3.34 ± 0.14	0.88 ± 0.02	6.45 ± 0.32	2.98 ± 0.21
85	2.15 ± 0.02	2.268 ± 0.005	3.92 ± 0.12	1.88 ± 0.01	15.83 ± 0.52	4.13 ± 0.28
86	2.16 ± 0.02	2.551 ± 0.008	4.63 ± 0.15	2.06 ± 0.01	20.60 ± 0.70	3.89 ± 0.26
89	2.14 ± 0.02	1.116 ± 0.009	2.64 ± 0.06	0.97 ± 0.01	5.48 ± 0.01	3.38 ± 0.14
90	2.14 ± 0.03	1.024 ± 0.050	3.15 ± 0.05	0.87 ± 0.00	5.85 ± 0.13	2.96 ± 0.09
93	2.17 ± 0.02	1.881 ± 0.006	3.88 ± 0.14	1.55 ± 0.01	13.10 ± 0.50	3.62 ± 0.27

In general, the intercept of the U_s-u_p fit is the bulk sound velocity in the material. In this work we measured the longitudinal and transverse sound velocity of the nontronite samples at a density of 2.14±0.02 g cm^{-3} and find the longitudinal, shear, and bulk sound velocities to be 1.47(2), 0.99(5), and 0.93(8) km s^{-1}, respectively. The measured bulk sound velocity is significantly lower than the intercept of the U_s-u_p curve. A difference between the measured bulk sound speed and intercept of the U_s-u_p curve is not unexpected for porous or heterogeneous materials due to the crush-up of pore space and modified grain-grain interactions.

While there are significant residuals, our U_s-u_p data for nontronite are nearly identical to the Hugoniot for a 'green deep-lying clay' with low water content studied by Al'tshuler and Pavlovskii (1971): $U_s = 1.6 + 1.47u_p$. While the clay studied by Al'tshuler and Pavlovskii (1971) is not positively identified as nontronite, the description, density ($\rho_0 = 2.15$ g cm^{-3}), and similar Hugoniot lends confidence to the Hugoniot measurements obtained in this study.

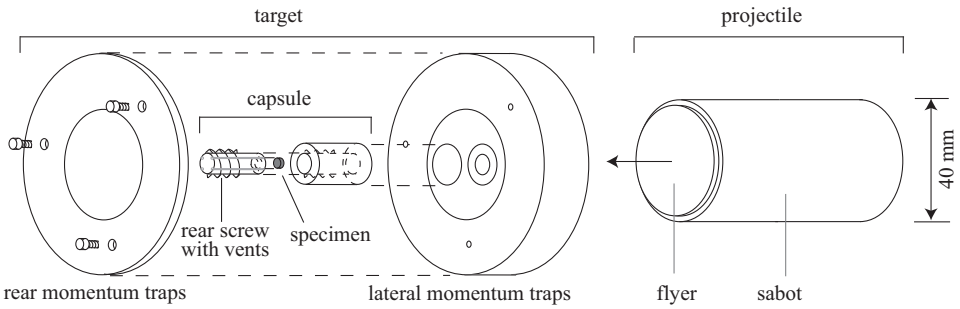

Figure 6.2: Schematic of a typical target configuration for a shock recovery experiment where two off-axis specimens are shocked simultaneously, modified with permission from Louzada et al. (2007). The disc-shaped specimens are positioned 1.5 mm from the impact surface. Samples are off-axis to avoid stress concentrations on the center line. Lateral and rear momentum traps prevent pressure excursions after the primary shock wave. In a subset of these experiments, the sample capsule was vented by 4 grooves down the entire length of the rear screw holding the specimen in place. However, these grooves closed during the experiments, limiting the possible venting.

6.3 Shock Recovery Experiments

Two specimens of nontronite were shocked simultaneously in recovery capsules made of either stainless steel (SS-304) or aluminum (Al-2024). The recovery capsule design, shown in Figure 6.2, includes both lateral and rear momentum traps to minimize late time reflections of the shock wave from the free surfaces of the recovery capsule.

The nontronite samples were powdered, sieved to less than 65 μm, baked at 95°C to remove adsorbed water, and pressed to a density of 2.30±0.05 and 2.32±0.08 g cm^{-3} in 8×2 mm discs within the steel and aluminum recovery cells, respectively. The recovery samples could be pressed to higher density than the Hugoniot samples because of their smaller diameter. This pressed density of 2.31 g cm^{-3} is within 2% of the crystal density of nontronite. At the relatively low pressures considered here, the mechanical (P, V, U_s, u_p) variables on the Hugoniot are not strongly affected by the $\sim$ 9% porosity in the nontronite samples used for the Hugoniot measurements; however, the temperature and entropy along the Hugoniot is sensitive to the starting porosity. Consequently, we attempted to reach the reach the crystal density in the nontronite samples used in the recovery

experiments to reduce complications related to initial porosity.

We designed the impact velocity for the aluminum and steel recovery fixture so that the first step shock pressure, and hence peak temperature, would be approximately equal. However, the peak shock pressure is higher in the steel capsule. The stainless steel recovery fixture was impacted at 1.211±0.005 km s^{-1} by a steel flyer. Using the Hugoniot for stainless steel (Duffy and Ahrens, 1997) and our measured Hugoniot for nontronite, we find the first step shock pressure in the nontronite to be 7.1±0.2 GPa and the peak shock stress after ring-up in the steel to be 26.1±0.2 GPa. The aluminum recovery fixture was impacted at 1.293±0.006 km s^{-1} by an aluminum flyer. Using the Hugoniot for aluminum (Al-2024) (fit presented in Duffy and Ahrens, 1997) and our measured Hugoniot for nontronite, we find the first step shock pressure in the nontronite to be 6.1±0.2 GPa and the peak shock stress after ring-up in the aluminum to be 11.2±0.1 GPa.

Using the CTH shock physics code (McGlaun et al., 1990), we modeled the pressure history within the center of the nontronite samples, shown in Figure 6.3. To model the nontronite, we used a Mie-Grüneisen equation of state (Asay and Shahinpoor, 1993) derived from the Hugoniot measurements and an assumed value for the Grüneisen parameter of 1.2, which is consistent with K_0'=4 (Vocadlo et al., 2000). For the stainless steel recovery cell, we use the Sesame 4272 tabular equation of state, and for the aluminum recovery cell, we used the Sesame 3700 equation of state. Both tables accurately represent the Hugoniot and re-shock states within the pressure range investigated. One can see that the first step shock pressures achieved were very close in magnitude, within 15% of each other, while the peak shock stress in the steel recovery cell was greater than in the aluminum by more than a factor of two. If the post-shock devolatilization of nontronite is solely driven by the entropic contribution to the free energy, then we would expect these recovery experiments to show qualitatively similar results, as has been assumed in previous work (e.g., Tyburczy et al., 1990).

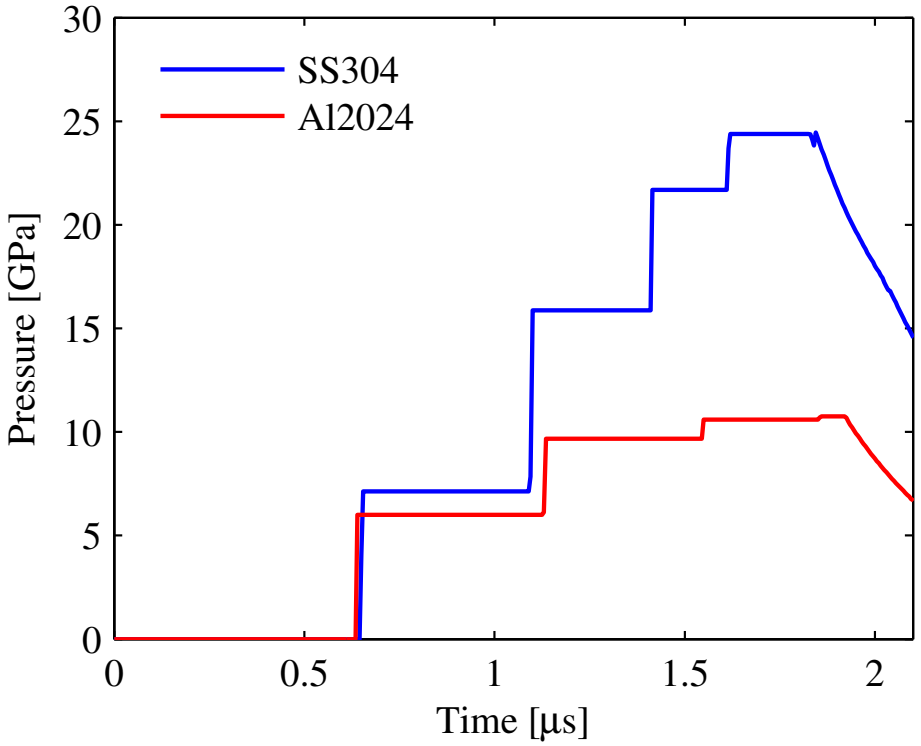

Figure 6.3: Model pressure histories within the center of the nontronite samples for recovery experiments using the steel (SS304) and aluminum (Al2024) recovery cells. The shock pressure in the sample is released by the rarefaction wave from the rear of the flyer plate.

6.3.1 Venting the Sample

Another difference that has been thought to be important in some studies (Skala et al., 2002) is whether the sample is allowed to release into vacuum, hereafter called vented, or if it is contained within the recovery fixture over the entire release path to ambient pressure and temperature, hereafter unvented. The unvented samples may not follow an isentropic release path as the recovery cell may conduct heat across the sample-recovery cell interface during the decompression process, thereby changing the entropy of the sample and the thermodynamic drive for devolatilization. For the timescale of the experiment, $\sim$1 μs, and a reasonable thermal diffusivity of a rock, $\sim 10^{-7}$ m^2 s^{-1}, the thermal diffusion length scale during the decompression process is of order one micron, which suggests a negligible mass of nontronite will be effected by thermal conduction from the steel or aluminum recovery cell during the decompression process. Boslough et al. (1980) considered the possibility that the post-shock temperature of the recovery cell was sufficient to devolatilize the sample prior to the experimenter removing the nontronite from the cell, over a time scale of 10's of minutes. However, as was concluded by Boslough et al. (1980), the post-shock temperature of the aluminum and steel recovery cells would be approximately 130 and 200 °C (Raikes and Ahrens, 1979a), respectively, which is insufficient to devolatilize bound water from nontronite (Frost et al., 2002).

To test the effect of venting on devolatilization, we reduced the thickness of one of the nontronite samples in the aluminum recovery cell to 1 mm and increased the thickness of the corresponding aluminum capsule face, from 1.5 to 2.5 mm, which decreased the plastic strain caused by the differential compression of the nontronite and the recovery cells. Vent holes were also placed in the rear of the steel recovery cell, Figure 6.2, however, it was found that the holes completely closed during the experiment.

6.4 Analysis of Recovered Samples

6.4.1 Infrared Reflectance Spectroscopy

A Thermo Nicolet 6700 FTIR spectrometer in reflectance mode was used to study the IR-active vibrational spectrum of the shocked and un-shocked nontronite clay. In Figure 6.4 the near-infrared reflectance spectra of the recovered samples are compared with an unshocked sample. The nontronite absorption bands at 1.43, 1.91, 2.28 and 2.76 microns are marked by the dot-dash vertical black lines. The band at 1.43 microns is caused by both structural OH and molecular H_2O and the band at 1.91 microns is related to interlayer molecular H_2O (Gavin et al., 2013). The bands at 2.28 and 2.76 microns are related to the Fe-OH bond. One can see the complete loss of the aforementioned absorption bands in the nontronite sample recovered from the steel recovery cell, whereas very little modification occurs to the nontronite samples recovered from the aluminum recovery cell. In Figure 6.5 the mid-infrared reflectance spectra of the recovered samples are compared with the unshocked sample. Interestingly, the 6.2 micron feature related to H_2O bending is observed in all samples, however, this could be related to water adsorbed onto the clay after recovery from the experiment.

6.4.2 X-ray Diffraction

A Scintag XDS2000 fixed sample position powder diffractometer was used to obtain the x-ray diffraction spectrum from the shocked and unshocked nontronite samples. The x-ray spectrum was obtained over a 2θ range of 2 to 40 degrees with a step size of 0.02 degrees and at a wavelength of 1.54 angstroms. In Figure 6.6 the x-ray diffraction spectra of shocked and un-shocked nontronite are compared. The complete loss of scattered intensity from the basal layer, at 2θ=6.45 degrees, and the broad peak at higher scattering angles from the sample recovered from the steel cell suggests amorphization of the nontronite sample. As this is a recovery experiment without temporal resolution, it is not clear whether amorphization occurred during the compression or decompres-

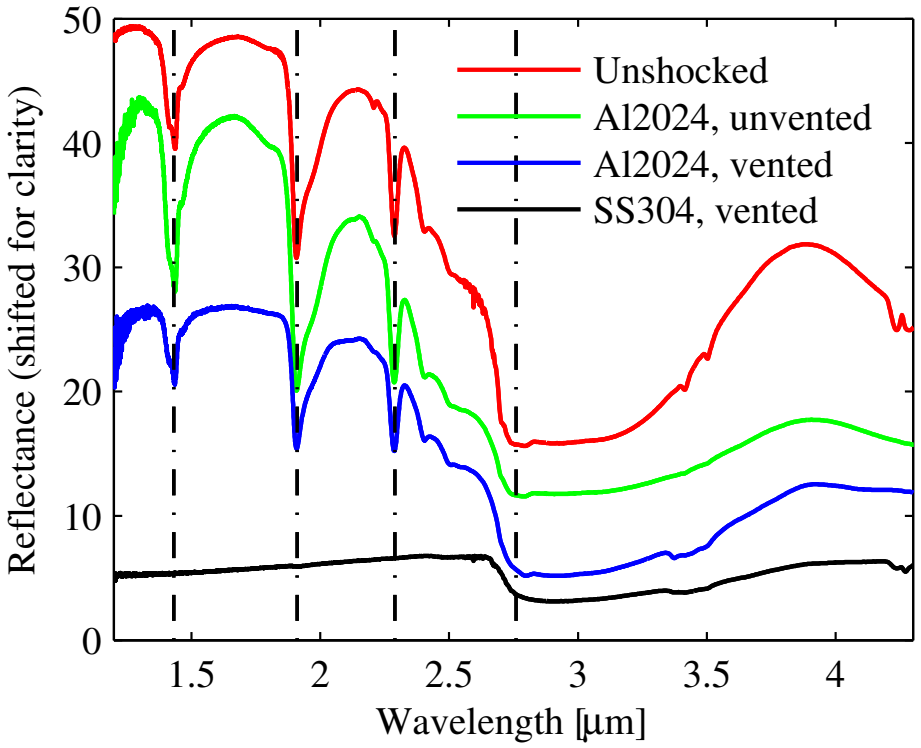

Figure 6.4: Near-infrared reflectance spectra of shocked and un-shocked nontronite. The spectra are offset vertically for clarity.

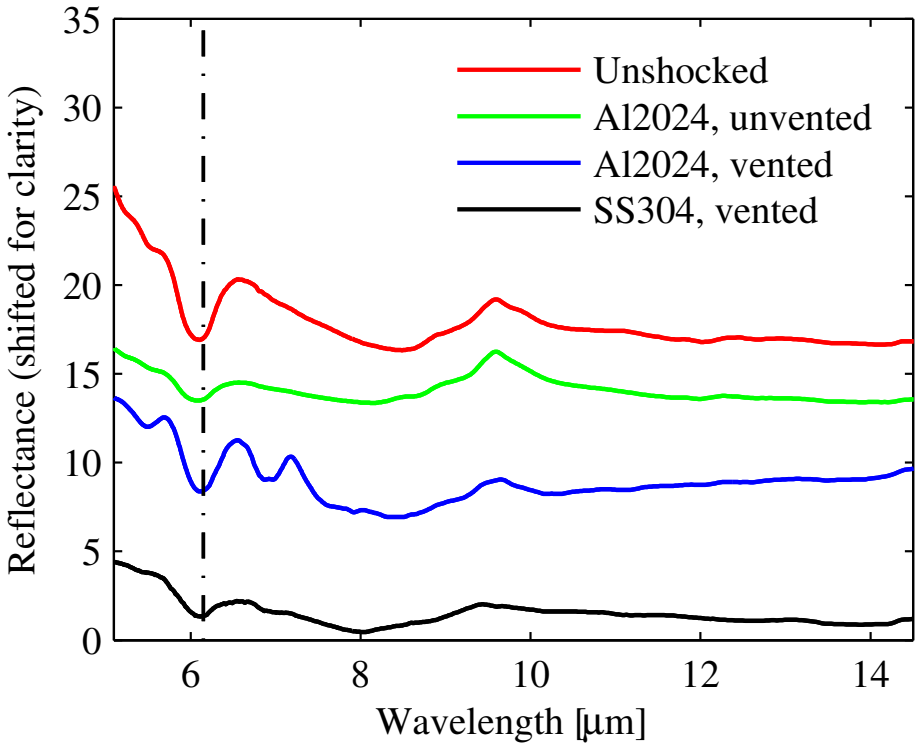

Figure 6.5: Mid-infrared reflectance spectra of shocked and un-shocked nontronite. The spectra are offset vertically for clarity.

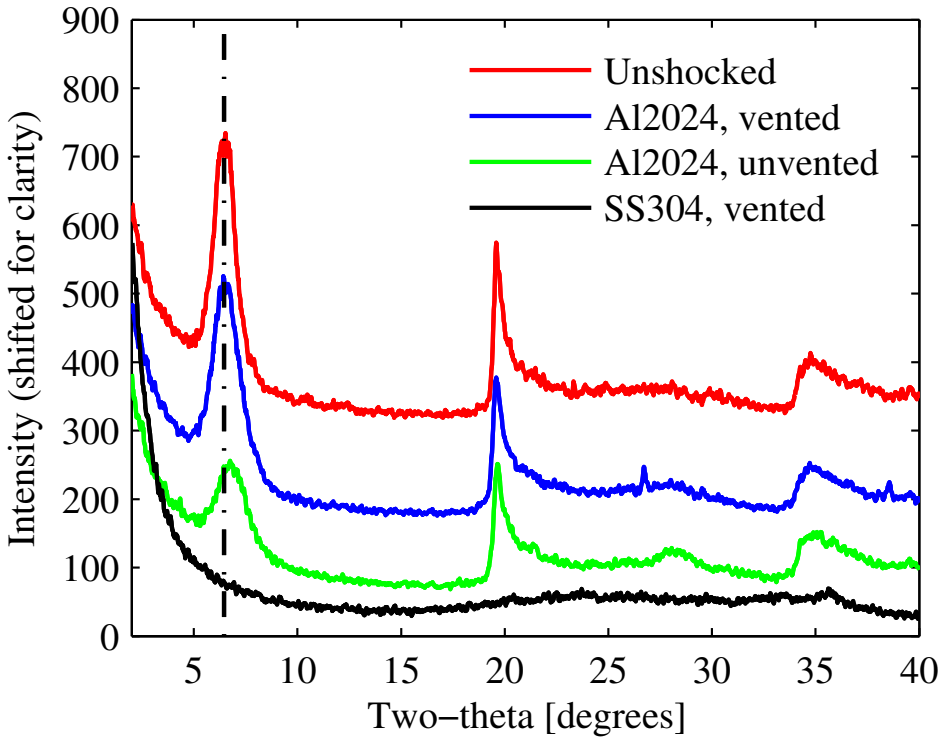

Figure 6.6: X-ray diffraction spectra of shocked and un-shocked nontronite. The spectra are offset vertically for clarity.

sion path; however, it is clear that the x-ray diffraction spectra is significantly different from the nontronite sample recovered from the aluminum cell. For the nontronite sample recovered from the aluminum recovery cell that vented to the chamber during the experiment (blue line in Figure 6.6), there appears to be no difference between the shocked and unshocked x-ray diffraction spectra.

6.4.3 Effect of Venting

At an impact velocity of 1.293±0.006 km s^{-1}, we were successful in recovering unvented nontronite from the aluminum capsule with the thicker face and also vented nontronite from the capsule with the thinner face that failed during compression. One can see in the infrared reflectance spectroscopy, Figures 6.4 & 6.5, that there is very little difference in the molecular and bound water signal. Unexpectedly, there is a slight decrease in the basal layer d-spacing in the unvented sample,

while there appears to be no modification to the basal layer in the unvented sample, Figure 6.6. The samples were prepared in an identical manner and consequently a significant difference in the pre-impact mechanical properties would not be expected.

While we were not able to recover an unvented sample from the highest pressure experiment in the steel recovery cell, we can compare our result with the results of Boslough et al. (1980) who were able to recover an unvented sample of nontronite in a stainless steel cell that was impacted at 1.36 km/s, yielding a peak shock stress of 30.0 GPa. Because of the significantly higher starting density of their nontronite samples, 2.7 g cm^{-3}, which is suggestive of a mineral mixture, we avoid using our measured Hugoniot to compare the first step shock pressure in the Boslough et al. (1980) recovery experiments.

While the peak shock stress in the work by Boslough et al. (1980) is slightly higher than that of our experiment, 26.1 GPa, we find starkly different results. Boslough et al. (1980) observe a decrease in the basal layer d-spacing from 14.9 to 11.7 angstroms and that only some of the bound OH was lost, whereas we observe a complete loss in the basal layer peak and an overall x-ray diffraction spectrum that is suggestive of amorphization. We also observe complete loss of the absorption bands in the near infrared reflectance spectrum related to bound OH. These results suggest that venting is an important variable in the interpretation of recovered clay minerals at high peak stresses, which is in contrast to the lower stress experiment in the aluminum recovery cell where venting does not seem to be important to the interpretation of the shock recovery experiment.

It is possible that the nontronite sample recovered from 30 GPa in the experiment by Boslough et al. (1980) was significantly laterally released, and hence did not achieve the peak impedance matching pressure in the steel. However, the experiment under consideration used a small sample of nontronite, 16 mg, and is unlikely to have seen the same degree of lateral release as the experiments conducted with much thicker samples. Future experiments will be required to unambiguously

determine the effect of venting on the interpretation of these shock recovery experiments.

6.5 Discussion

6.5.1 Natural Impacts and Laboratory Experiments

The thermodynamic path taken by a clay sample recovered from a laboratory experiment is significantly different than what would be achieved during a natural impact event (DeCarli et al., 2002). In the laboratory, one can see in Figure 6.3 that the pressure increases by a series of steps, with the step height depending on the recovery cell material. The pressure history achieved by a clay sample during a natural impact would be much simpler, a single strong shock wave followed by adiabatic decompression to ambient pressure.

Ignoring the thermal differences created by the path differences, the compressive response of a material can depend on the specific loading path due to the inherent rate dependence of plastic deformation (e.g. Root and Asay, 2010). For nontronite, the path difference between a ring-up and single shock loading could lead to modified criteria for amorphization during compression.

The largest difference in material response between a ring-up, or reverberation, and single-shock loading to the same stress is in the thermal state of the material. Because of the the lesser amount of work done in compressing the sample to the same pressure, see Figure 1 in Kraus et al. (2010), the temperature will be significantly lower during a ring-up experiment. It is also not entirely accurate to say that the first-step shock in the ring-up is solely responsible for the temperature and entropy increase. For the pressure states considered in the recovery experiments performed here, Figure 6.7 presents the relative temperature increase upon ring-up in a steel and aluminum recovery cell. One can see that the second-step shock temperature increase is greater than 30% of the first step in the steel, while the maximum shock temperature is over 140% of the first-step shock temperature. This is in contrast to a ring-up in an aluminum recovery cell where the second-step

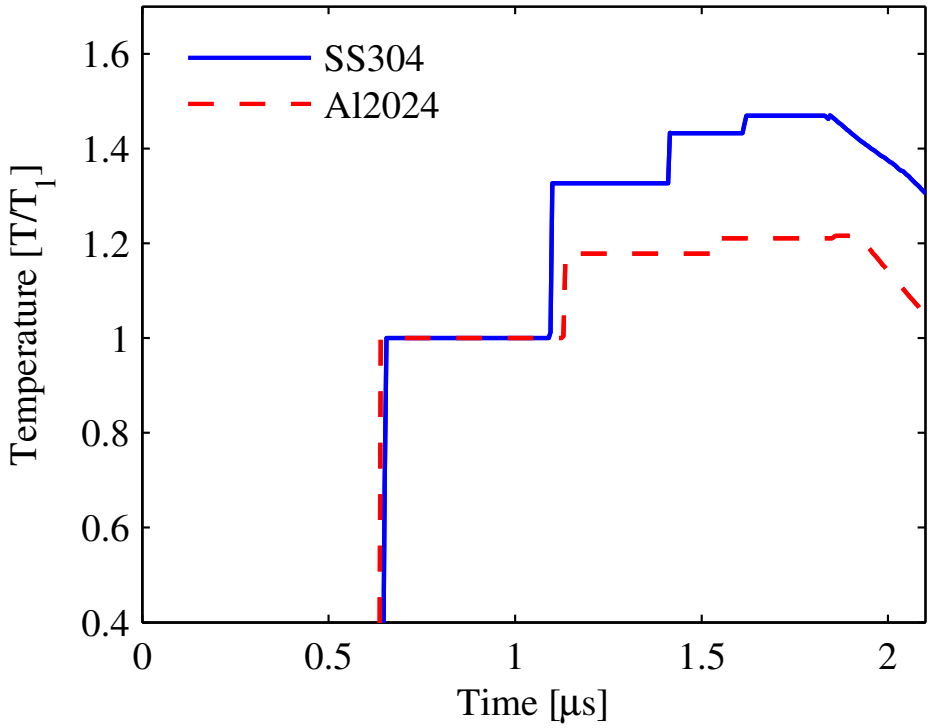

Figure 6.7: Model temperature histories within the center of the nontronite samples for the recovery experiment using the steel (SS304) and aluminum (Al2024) recovery cells. The temperature histories are normalized to the first step shock temperature, showing the significantly greater second-shock temperature jump in the steel recovery cell than in the aluminum recovery cell. Absolute temperatures are not plotted because of the uncertainty in the heat capacity. Shock and post-shock temperature measurements are needed.

shock temperature increase is just under 20% of the first step shock temperature increase, with only a few percent increase in temperature to the peak stress state. For comparison, the shock temperature increase upon single shock loading to the peak stress state in the steel (26.1 GPa) and aluminum (11.1 GPa), as in a natural impact event, would be ∼4.5 and ∼2 times greater than the first-step ring-up temperature increase and ∼3.2 and ∼1.6 times greater than the maximum temperature increase achieved in the ring-up experiments, respectively. Consequently, the thermal state achieved during a ring-up experiment depends sensitively on the type of recovery cell, for a given peak stress. And in general, ring-up experiments at high shock stresses do a very poor job of simulating the thermal state achieved during a natural impact event.

6.5.2 Recommendations for Future Clay Recovery Experiments

As there are currently no shock or post-shock temperature measurements on nontronite, it is difficult to interpret the absolute thermal history during the ring-up experiment; this is why we have presented the model temperatures as ratios, which are relatively insensitive to the absolute value of the heat capacity. Until such temperature measurements become available, it will be important to experimentally simulate the loading path achieved in a natural impact event in order to be confident that the laboratory experiments mimic nature, while acknowledging the timescale differences between the laboratory and natural events (DeCarli et al., 2002).

The closest impedance matched structural material to the clay used in this study is polychlorotrifluoroethylene, with trade name Kel-F. Kel-F is a high density thermoplastic with a well characterized Hugoniot up to 80 GPa (Marsh, 1980),

$$U_s = 2.03 + 1.64u_p, \tag{6.3}$$

where the velocities are in km s^{-1} and the initial density is $\rho_0 = 2.122$ g cm^{-3}. Nontronite contained

in a recovery cell made from Kel-F that is impacted at 2.7 km s^{-1} would reach a first-step shock pressure 11.4 GPa, which is ∼94% of the peak ring-up stress, and a temperature that increases by only a few percent after the first-step shock. However, with a low impedance recovery cell one cannot reach the same peak stresses as with a higher impedance recovery cell, such as steel, and one must also be sure to remove the recovered nontronite clay rapidly from the recovery cell, as the post-shock temperature in the Kel-F recovery cell could be sufficient to devolatilize the clay.

6.6 Conclusion

Here we measured the principal Hugoniot of nontronite, a smectite clay, over a stress range of 2 to 23 GPa. While there is significant scatter in the individual Hugoniot points, the best fit Hugoniot is in excellent agreement with a green clay measured by Al'tshuler and Pavlovskii (1971).

The measured Hugoniot of nontronite was used to interpret the loading history of two shock recovery experiments. One of the experiments used a stainless steel recovery system and the other an aluminum recovery system. The impact velocities were chosen so that the first step shock pressures were similar, however they would have a significantly different peak shock stress. We successfully recovered samples of nontronite shocked to a peak stress of 26.1 GPa in the steel and 11.2 GPa in the aluminum, with first step shock pressures of 7.1 and 6.1 GPa, respectively. Based on near and mid-infrared reflectance spectroscopy and x-ray diffraction, we found significantly different results between the samples recovered in the steel and aluminum recovery cells, which suggests that one cannot solely use the first step shock pressure to interpret these types of shock recovery experiments. This statement is especially true for steel and other high impedance recovery cells; because of the large difference in impedance between the nontronite and steel recovery cell, the second step shock increases the temperature, and hence entropy, of the nontronite by a significant fraction of the peak ring-up state. Consequently, for shock recovery experiments that depend on

the thermal and not just the mechanical state achieved, it is extremely important to both know the pressure history in the sample and mitigate the effects of secondary wave reflections by impedance matching the sample to the recovery cell.

The effect of venting on the devolatilization of nontronite was tested in both recovery experiments. For the aluminum recovery system, one of the nontronite samples vented to the chamber during the experiment and the other was contained for the duration of the experiment. Very little difference was found between the vented and the unvented sample for the specific stress history achieved in the aluminum recovery cell. At significantly higher peak stresses, the vented nontronite sample recovered in these experiments could be compared to the unvented sample recovered in the work of Boslough et al. (1980). A significant difference was found, with the vented sample appearing to amorphize and lose all signatures of being a clay mineral and the unvented sample showing only some loss of interlayer and bound water. However, because of the uncertain loading history in the unvented sample recovered by Boslough et al. (1980), more work is needed to determine the significance of venting at high peak stresses.

Given the state of our understanding of how nontronite behaves during shock compression experiments, any inferences made about the pre-impact state of phyllosilicates on Mars will have significant and unquantified uncertainties.

Chapter 7

Conclusions and future work

Shock waves are a tool that can be used to study the behavior of materials over tremendous regions of phase space, arguably more so than any other field in materials research. This breadth also allows for an increase in the depth of our understanding, for the equation of state surface is stitched together by the laws of thermodynamics, making measurements in disparate regions of phase space useful to one another.

In Chapters 2 and 3 we have tried to exploit this aspect of dynamic materials property research to gain an understanding of materials that would not be possible without this breadth of accessible phase space. In Chapter 2, we discuss a shock-and-release technique to measure the temperature on the liquid-vapor dome. We used this technique, combined with the large amount of data on silica at high pressure, to learn about the poorly constrained liquid-vapor dome of silica. In Chapter 3, we discuss the development of a novel shock-and-release technique to measure the density on the liquid-vapor dome. With this technique we can use the known properties of iron on the liquid-vapor dome to learn about the thermal properties of iron at high pressure. And while this type of research is important to our fundamental understanding of the behavior of materials, this work is directly applicable to the end stages of planet formation, where nature mimics the thermodynamic paths taken in the lab (or is it the other way around?).

From the experimentally constrained thermodynamic integration of the entropy along the quartz Hugoniot in Chapter 2, we are able to definitively say that more silicate vapor will be produced in giant impacts than previous models would suggest. With vapor being a greater fraction of the ejecta, the post-impact flow fields will be modified with unquantified uncertainty until an equation of state is developed that is constrained by the entropy on the Hugoniot and the liquid-vapor dome presented in Chapter 2.

For opaque solids, such as iron, one cannot perform an experimentally constrained thermodynamic integration to obtain the entropy, as there are no accurate shock temperature measurements. In Chapter 3, we describe a shock-and-release technique to determine the entropy on the iron Hugoniot at ∼500 GPa, or more exactly we determine the pressure required to isentropically release to the 1 bar boiling point, which has a known entropy. This measure is then also a direct measure of the critical shock pressure to vaporize iron. We show that for the late stages of Earth's accretion, vaporization of the core of accreting planetesimals will be a significant process that can more efficiently disperse the core material over the surface of the proto-Earth. Vaporization of the planetesimal cores can also help to explain the difference in abundance of the highly siderophile elements between the Earth and the Moon, as adiabatic expansion of the vaporizing core material will lead to greater loss of material from the Moon due to its lower gravity. The exact details of planetesimal core disruption on the Earth and loss of core material from the Moon will require direct numerical simulations of numerous individual impact events, again necessitating improved equation of state models for the iron cores and silicate mantles. However, the data presented in Chapter 3 can be used as an accurate constraint on a critical aspect of the equation of state for planetary applications, the entropy generation during shock compression.

For more volatile transparent minerals such as H_2O ice, the phase space relevant to impact induced vaporization can be accessed using a light gas gun (Stewart and Ahrens, 2005). An accurate

experimentally constrained equation of state model has previously been developed for H_2O ice (Senft and Stewart, 2008). In Chapter 4, we use the multiphase equation of state model for H_2O in hydrocode simulations to accurately determine the amount of melting and vaporization that occurs for impact events onto icy bodies. We also use results from previous hydrocode simulations of impact crater collapse (Senft and Stewart, 2011) to determine how much melt should be left within a crater on icy bodies. These results are relevant to a wide-range of impact conditions on the icy bodies of our solar system. An area of future work should include considering the effect of different ice compositions and mixtures on vaporization and melting during collisions on icy bodies.

A major uncertainty in the area of shock propagation in mixtures was the question of how the shock wave energy partitions to the multiple phases present. In Chapter 5, we use shock and post-shock temperature measurements on ice-rock mixtures to suggest that the energy partitions to the low density phase as if it had been shocked along a Rayleigh-line to the bulk pressure in the mixture. This result is relevant to the differentiation of icy bodies in the solar system, as impact heating has been considered as a mechanism for separating the high density rock phase from the icy mantles. In particular, this result would suggest that the mechanism Barr and Canup (2010) used to describe the source of the dichotomy in differentiation between Ganymede and Callisto is wrong. For equivalent impactor parameters, impacts into the undifferentiated ice-rock mixtures would clear a significantly larger volume of rock than is assumed for pure ice, which would cause Callisto to undergo significant differentiation. As there is a difference in the differentiated state of Ganymede and Callisto, this subject should be revisted using the model for how energy is deposited into ice-rock mixtures, such as the one described in Chapter 5 and in Kraus et al. (2010).

For more intimate mixtures than those described in Chapter 5, the model for how to treat shock propagation and energy partitioning no longer applies. In Chapter 6 we considered the problem of devolatilization and shock modification of hydrated minerals. This problem has received a

particularly large amount of attention because of the hydrated minerals on Mars and the desire to understand early Martian history by inverting the effects of 4 billion years of impact bombardment on the surface. Most work on the subject has attempted to perform shock recovery experiments in order to directly relate what is observed on Mars to the impact conditions in the laboratory. However, as noted in DeCarli et al. (2002), this comparison cannot be easily made due to the differences in timescale and loading paths in the laboratory and nature. In Chapter 6, we developed a test of the common interpretation of using the first step shock pressure in a ring-up configuration as a guide to comparing to natural events. We show that this interpretation is not adequate for high density recovery systems, such as steel. We also experimentally show that one must consider the need for a devolatilizing mineral to expand to large volumes, making solid enclosures of recovery cells more complicated. The best way to avoid these difficulties will be to develop a chemical equilibrium model for shock induced devolatilization and modification of hydrated minerals; however, this will require shock temperature measurements to constrain the thermal properties and development of a reaction model, such as those used for reacting explosives, to describe the time dependence of the devolatilization process.

Work on equations of state will never be done, more data can always be taken and the models can always be improved. To some people, equations of state are boring, but they are important to understanding the world around us. The question that needs to be asked is, "are the equations of state that I am using good enough for the question that I am trying to answer?" To answer this question, future work in the field should include uncertainty quantification in the equation of state models themselves, so that the analytic uncertainties determined from the experiments, can be propagated through to the final, oftentimes integrated, result.

Appendix A

Additional calculations for Chapter 2

A.1 Heat capacity of stishovite

To treat the anisotropy of crystals and accurately model the dispersion relation near the Brillouin zone boundary, Kieffer (1979) proposed a vibrational density of states for the acoustic modes in a crystal of the form,

$$g(\omega)d\omega = \sum_{t=1}^{3} \frac{3N_{\mathrm{A}}\left(2/\pi\right)^{3}\left[\sin^{-1}\left(\omega/\omega_{\mathrm{t}}\right)\right]^{2}}{Z\left(\omega_{\mathrm{t}}^{2}-\omega^{2}\right)^{1/2}}d\omega, \tag{A.1}$$

$$\omega_{\mathrm{t}} = v_{\mathrm{i}}K_{\max}\left(2/\pi\right), \tag{A.2}$$

where ω_{t} is the maximum frequency for each of the three acoustic modes at the zone boundary, $K_{\max}$ is the radius of the Brillouin zone, v_{i} is the sound velocity for each acoustic wave (longitudinal and shear waves), Z is the number of molecules in the unit cell (2 for stishovite), and N_A is Avogadro's number. The size of the Brillouin zone is given by,

$$K_{\max} = 2\pi\left(\frac{3N_{\mathrm{A}}}{4\pi ZV\mu}\right)^{1/3}, \tag{A.3}$$

where V is the specific volume and $\mu = 0.06008$ kg mol^{-1} of molecules.

Table A.1: Summary of variables and annotations used in the Auxiliary Materials.

Symbol	Definition
General Variables	
P	Pressure
V	Specific volume
E	Internal energy
T	Temperature
S	Entropy
H	Enthalpy
ω	Angular frequency
$h, \hbar$	Planck constant, reduced Planck constant
c	Speed of light
k_B	Boltzmann constant
N_A	Avogadro's number
R	Gas constant
$_\mathrm{H}$	Subscript denoting state on the Hugoniot
$_{00}$	Subscript denoting initial state on the Hugoniot
$_\mathrm{S}$	Subscript denoting state on an isentrope
Heat capacity of stishovite (§SA.1)	
$g(\omega)$	Vibrational density of states
ω_t	Maximum frequency of acoustic vibrational modes at zone boundaries
K_max	Radius of the Brillouin zone
Z	Number of SiO_2 molecules in unit cell
μ	Molar mass
g_0	Frequency continuum of optic modes
v_i	Sound velocity of each acoustic mode
n_m	Number of atoms per molecule
q_E	Proportion of optic modes stored in Einstein oscillators
$\omega_\mathrm{l}, \omega_\mathrm{u}$	Lower and upper frequency bounds to continuum of optic modes
ω_E	Frequency of Einstein oscillators
C_V	Isochoric heat capacity
Λ, κ, ξ	Density of state functions for acoustic, optical, and Einstein phonon modes, respectively
x	$\hbar\omega/k_\mathrm{B}T$
γ_i	Mode Grüneisen parameter for acoustic mode i
V_0	Specific volume of stishovite at ambient pressure
$v_{0,\mathrm{i}}$	Ambient pressure sound velocity of acoustic mode i
a_i	Linear anharmonicity parameter
α_T	Coefficient of thermal expansion
K	Adiabatic bulk modulus
Q	Partition function for a system of harmonic oscillators
E_i^h	Internal energy of harmonic oscillator i
$C_{V\,i}^h$	Contribution to the isochoric specific heat from harmonic oscillator i
E_tr	Specific energy of transformation from low to high pressure phase

The remaining vibrational degrees of freedom are treated as a continuum of optic modes, g_0, or individual Einstein oscillators, g_E. The vibrational density of states within the frequency range of

Table A.1: Summary of variables and annotations used in the Auxiliary Materials (continued).

Symbol	Definition
Revised boiling point for SiO_2 (§SA.2)	
$^{(g)}$	Superscript denoting gas phase
$^{(l)}$	Superscript denoting liquid phase
C_P	Isobaric heat capacity
$K_{\mathrm{Eq.i}}$	Equilibrium constant for reaction i
$\Delta^f H$	Heat of formation
N	Number of moles
G	Gibbs free energy
Streaked optical pyrometer (SOP) calibration (§SA.3)	
L	Radiance
ϵ	Emissivity
λ	Wavelength
R'	Frequency-dependent optical reflectivity
T_0, A	Calibration coefficients (Equation A.53)
I_{cor}	Reflectivity-corrected SOP intensity
Absorbance of silica fluid (§SA.4)	
σ	Frequency-dependent conductivity
n_{e}	Free electron concentration
e_{c}	Charge of an electron
τ_{e}	Electron relaxation time
ϵ_0	Permittivity of free space
m_{eff}	Effective electron mass
R_0	Interatomic distance
u_{e}	Mean electron velocity
E_{g}	Band gap energy
A_0, A_1, A_2	Constants for linearized E_{g} (Equation A.61)
T_n, ρ_n	Normalization constants (Equation A.64)
B_0, B_1, B_2	Fitting parameters (Equation A.64)
$\alpha(\omega)$	Frequency-dependent absorption coefficient
$n_1(\omega)$	Real part of the frequency-dependent index of refraction
σ_1	Real part of frequency-dependent conductivity
α_{vap}	Absorption coefficient along the release isentrope
α_{RM}	Rosseland mean absorption coefficient
κ_λ	Spectral response of the Streaked Optical Pyrometer
L_λ	Planck function

the optic modes, $\omega_{\mathrm{l}} < \omega < \omega_{\mathrm{u}}$, and at the frequency of Einstein oscillators, ω_{E}, are given by,

$$g_0 = \frac{3N_{\mathrm{A}}n_{\mathrm{m}}\left[1-(1/s)-q_{\mathrm{E}}\right]}{\omega_{\mathrm{u}}-\omega_{\mathrm{l}}}, \tag{A.4}$$

$$g_{\mathrm{E}} = 3q_{\mathrm{E}}N_{\mathrm{A}}n_{\mathrm{m}}\delta\left(\omega-\omega_{\mathrm{E}}\right), \tag{A.5}$$

where n_{m} is the number of atoms per molecule, q_{E} is the proportion of optic modes stored in Einstein oscillators at frequency ω_{E}, and δ is the delta function.

The isochoric heat capacity, C_V, is determined by summing three functions that integrate over the density of states in the acoustic Λ, optical κ, and Einstein phonon modes ξ:

$$\Lambda\left(x_i\right) = \left(\frac{2}{\pi}\right)^3 \int_0^{x_i} \frac{\left[\sin^{-1}\left(x/x_i\right)\right]^2 x^2 e^x}{\left(x_i^2 - x^2\right)^{1/2} \left(e^x - 1\right)^2} dx, \tag{A.6}$$

$$\kappa \begin{pmatrix} x_{\mathrm{u}} \\ \\ x_{\mathrm{l}} \end{pmatrix} = \int_{x_{\mathrm{l}}}^{x_{\mathrm{u}}} \frac{x^2 e^x}{\left(x_{\mathrm{u}}^2 - x_{\mathrm{l}}^2\right)^{1/2} \left(e^x - 1\right)^2} dx, \tag{A.7}$$

$$\xi\left(x_E\right) = \frac{x_E^2 e^{x_E}}{\left(e^{x_E} - 1\right)^2}, \text{ and then} \tag{A.8}$$

$$C_V = \frac{3N_{\mathrm{A}}k_{\mathrm{B}}}{n_{\mathrm{m}}Z} \sum_{i=1}^{3} \Lambda\left(x_i\right) + 3N_{\mathrm{A}}k_{\mathrm{B}} \left(1 - \frac{3}{3n_{\mathrm{m}}Z} - q_{\mathrm{E}}\right) \kappa \begin{pmatrix} x_{\mathrm{u}} \\ \\ x_{\mathrm{l}} \end{pmatrix} + 3N_{\mathrm{A}}k_{\mathrm{B}}q_{\mathrm{E}}\xi\left(x_E\right), \tag{A.9}$$

where $x = \hbar\omega/k_{\mathrm{B}}T$.

To determine the isochoric heat capacity in the compressed state, Kieffer (1979) suggests integrating the definition of the mode Grüneisen parameter,

$$\gamma_{\mathrm{optic}} = -\frac{\partial \ln(\omega)}{\partial \ln(V)}, \tag{A.10}$$

to determine the change in frequency with volume of the optical modes. The wave velocity, v_{i}, for each acoustic mode is assumed to change according to (Kieffer, 1982),

$$v_{\mathrm{i}} = v_{0,\mathrm{i}} \left[1 - \left(\frac{V}{V_0} - 1\right)\left(\gamma_i - \frac{1}{3}\right)\right] \tag{A.11}$$

where V_0 is the volume of stishovite at ambient pressure, $v_{0,\mathrm{i}}$ is the ambient pressure sound velocity of acoustic mode i, and γ_i is the mode Grüneisen parameter of acoustic mode i. Then, the cutoff

frequencies for each acoustic branch of the phonon spectrum can be calculated using Equations A.2 and A.3.

Next, we summarize the method discussed by Gillet et al. (1990), and references therein, to determine the effect of anharmonic potentials on the heat capacity. A mode anharmonic parameter a_i can be used to describe the anharmonicity of a vibrational mode of frequency ω_i,

$$a_i = \left(\frac{\partial \ln \omega_i}{\partial T}\right)_V . \tag{A.12}$$

The mode parameter, a_i, describes the change in frequency of a certain mode as a function of temperature at constant volume. As most experimental measurements are not performed at constant volume, but at constant pressure or temperature, it can be shown that

$$a_i = \alpha_T \left(\gamma_{iT} - \gamma_{iP}\right) \tag{A.13}$$

with

$$\gamma_{iT} = K \left(\frac{\partial \ln \omega_i}{\partial P}\right)_T , \tag{A.14}$$

$$\gamma_{iP} = -\frac{1}{\alpha_T} \left(\frac{\partial \ln \omega_i}{\partial T}\right)_P , \tag{A.15}$$

where α_T is the coefficient of thermal expansion and K is the bulk modulus.

To determine the effect of the anharmonicity parameter on the heat capacity of a material, we start with the internal energy, E, of a system of harmonic oscillators. The oscillator energy changes with temperature as

$$E(T) = k_{\mathrm{B}} T^2 \left(\frac{\partial \ln Q}{\partial T}\right)_V . \tag{A.16}$$

Here Q is the partition function for a system of harmonic oscillators,

$$Q = \prod \frac{1}{1 - \exp\left(-\hbar\omega_i / k_{\mathrm{B}} T\right)}, \tag{A.17}$$

where the product is over all available vibrational modes of the system, ω_i.

Inserting Equation A.17 into Equation A.16, one obtains

$$E(T) = \sum E_i^h \left(1 - a_i T\right), \tag{A.18}$$

where E_i^h is the internal energy of harmonic oscillator i. The heat capacity at constant volume is then,

$$C_V = \sum \left[C_{Vi}^h \left(1 - a_i T\right) - a_i E_i^h \right], \tag{A.19}$$

where a_i is assumed to be independent of temperature. At high temperatures, E_i^h is approximately $C_{Vi}^h T$, where C_{Vi}^h is the isochoric heat capacity contribution from harmonic oscillator i. Consequently, Equation A.19 can be further simplified to

$$C_V = \sum C_{Vi}^h \left(1 - 2a_i T\right). \tag{A.20}$$

The anharmonicity parameter, a_i, has been measured for a few optical modes of stishovite (Gillet et al., 1990). However, as noted in Gillet et al. (1990), there is significant uncertainty in using the average of the anharmonicity parameters for the three measured vibrational modes. To constrain the anharmonicity parameter, we compare the measured shock temperature in the stishovite phase with a thermodynamic model for the shock temperature where the only unconstrained parameter is a_i.

For materials that undergo a high-pressure phase transition, shock temperatures are calculated

using the method from Lyzenga and Ahrens (1980). The internal energy increase of a material subjected to shock compression is determined by the Rankine-Hugoniot equation,

$$\Delta E = \frac{1}{2}\left(P_{\mathrm{H}} - P_{00}\right)\left(V_{00} - V_{\mathrm{H}}\right) \tag{A.21}$$

where subscript $_{00}$ denotes the pressure and volume of the starting phase. As the shocked state is in equilibrium, the calculation of internal energy is path independent. For a material shocked from a low-pressure phase to a high-pressure phase, such as fused quartz to stishovite, the internal energy increase upon going from the initial state (P_{00}, V_{00}) to the shock state (P_{H}, V_{H}) is obtained by summing the energy of transition from the low pressure to the high pressure phase E_{tr} (Table A.2) at P_{00}, the work done in compressing the the high-pressure phase isentropically from the initial volume V_0 to the volume in the shocked state V_{H}, and the energy of heating the material from the isentrope to the Hugoniot state:

$$\Delta E = E_{\mathrm{tr}} + \int_{V_0}^{V_{\mathrm{H}}} P_{\mathrm{S}} dV + \int_{T_{\mathrm{S}}}^{T_{\mathrm{H}}} C_V dT. \tag{A.22}$$

T_{S} is the temperature on the isentrope at volume V_{H}, and T_{H} is the temperature on the Hugoniot at volume V_{H}. We use a third-order Birch-Murnaghan EOS with parameters from Panero et al. (2003) to calculate pressure on the isentrope, $P_{\mathrm{S}}(V)$.

In spite of the large number of shock wave experiments performed on silica polymorphs, there are few accurate shock temperature measurements on silica that are confidently within the stishovite phase. Here we focus on the shock temperature measurement by Lyzenga et al. (1983) on silica glass shocked to stishovite (later corrected by Boslough, 1988). At a shock pressure of 58.9±1 GPa, the shock temperature is 4960±100 K (where V_{H}=2.17(3)$\times 10^{-4}$ m^3 kg^{-1} (Ahrens and Johnson, 1995a)).

Table A.2: Published enthalpies of transition for quartz to stishovite and fused quartz to stishovite. The primary sources of the thermodynamic data are: (a) Robie and Waldbaum (1968), (b) Robie et al. (1978), (c) Navrotsky (1995) and Richet and Bottinga (1986) (d) Saxena et al. (1993), (e) our recommended value used in calculating the stishovite Hugoniot, transition enthalpy from fused quartz to stishovite determined using enthalpy data for fused quartz from Richet et al. (1982) (heat of formation of quartz at 298 K is 910.700 kJ mol^{-1}, heat of formation of fused quartz at 298 K is 901.554 kJ mol^{-1}, at 0.06008 kg mol^{-1}, ΔH (quartz to fused quartz)=0.152 MJ kg^{-1}).

Source	ΔH [MJ kg^{-1}] quartz to stishovite	ΔH [MJ kg^{-1}] fused quartz to stishovite
Panero et al. (2003)[a]	0.89	0.70
Lyzenga et al. (1983)[b]	0.822	0.697
Akins and Ahrens (2002a)[c]	0.86	0.70
Luo et al. (2003b)[d]	0.7772	–
Akaogi et al. (1995)[e]	0.6162	0.464

Table A.3: Standard density Kieffer model parameters for stishovite.

Parameter	Value	Source
V_0 [m^3 kg^{-1}]	2.331×10^{-4}	Weidner et al. (1982)
v_1 [m s^{-1}]	5050	Gillet et al. (1990)
v_2 [m s^{-1}]	6190	Gillet et al. (1990)
v_3 [m s^{-1}]	11000	Gillet et al. (1990)
ω_l [cm^{-1}]	230	Gillet et al. (1990)
ω_u [cm^{-1}]	1020	Gillet et al. (1990)
q_E	0	Gillet et al. (1990)
γ_{optic}	0.95	Kieffer (1982)
γ_1	0.59	Kieffer (1982)
γ_2	0.59	Kieffer (1982)
γ_3	2.35	Kieffer (1982)
a_i [K^{-1}]	-3.1(6)$\times 10^{-5}$	this work

To match the measured shock temperature with the heat capacity model presented above (Equation A.19) requires an average anharmonicity parameter of a_i=-3.1(6)$\times 10^{-5}$ K^{-1}, which is slightly above the three measured anharmonicity parameters for individual optical modes of stishovite (Gillet et al., 1990). The other parameters used in the Kieffer model calculation are given in Table A.3.

Using a_i=-3.1(6)$\times 10^{-5}$ K^{-1}, the isochoric heat capacity of stishovite at a temperature of 4500 K is 3.65(0.15)k_B per atom, significantly above the Dulong-Petit limit. Note that we are forcing the phonon contribution to account for the entire temperature dependence of the entropy; however,

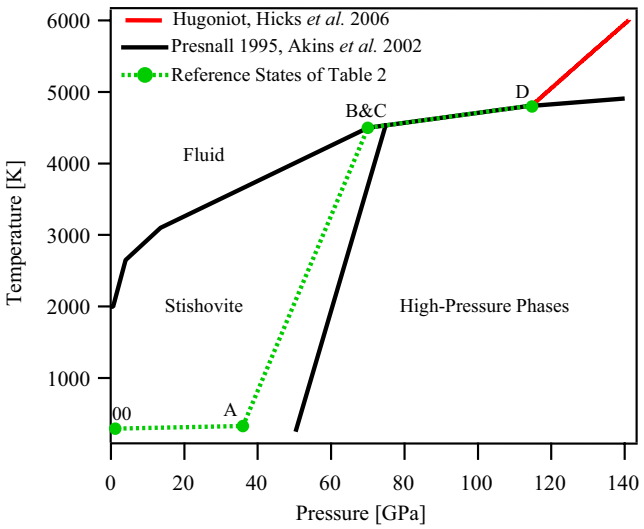

Figure A.1: Reference entropy states of Table 2 plotted on a pressure-temperature phase diagram of silica. The stability region of stishovite is expanded beyond that of the equilibrium phase diagram to represent the zero pressure reference state used in the main text.

at these high temperatures, it is not unlikely that transitions between electronic energy levels or defect generation may contribute to the heat capacity at high temperatures.

A.2 Revised boiling point for SiO_2

A.2.1 Heat capacity of liquid silica at 1 bar

The entropy change along an isobar is found by integrating the heat capacity at constant pressure, C_P, from $T = 0$ K, where the entropy is zero from the third law of thermodynamics, to the temperature of interest T^*,

$$S = \int_0^{T^*} \frac{C_P}{T} dT, \tag{A.23}$$

where C_P is defined below (Equation A.24).

In the recent literature, there are two primary sources of data for C_P of silica liquid at 1 bar. The well-known JANAF thermodynamic tables are widely cited (Chase, 1998); however, the heat capacity data above 1700 K are only estimates based upon extrapolation to lower temperature data

by Wietzel (1921) and agreement with liquid heat capacities of various silicates. The second widely-cited source of heat capacity data for liquid silica is from Richet et al. (1982). Where the enthalpy of silica glass was measured through the glass transition at ≈1600 K, for a fast cooling rate, up to 1776 K. The heat capacity data of Richet et al. (1982) are the most accurate measurements on silica liquid in the literature with error estimates of ∼0.3%. Note, however, that 1776 K is still below the equilibrium melting temperature of cristoballite, ∼1995 K. Using DFT-MD methods, Karki et al. (2007) found the isochoric heat capacity of liquid silica at 3000 K to be significantly higher than the measurements of Richet et al. (1982). de Koker et al. (2008) re-analyzed the DFT-MD data of Karki et al. (2007) in a thermodynamically consistent manner and found the heat capacity to increase quasi-linearly from 3000 up to 6000 K; however, without any simulations below 3000 K, it is difficult to determine the source of the difference between the experimental data and the theoretical calculations. Recently, Ottonello et al. (2010) calculated the heat capacity of liquid silica up to 3000 K and found their calculated C_P to agree with heat capacity measurements of Richet et al. (1982). de Koker (private communication) suggests the difference could be in the numerical models, the DFT-MD methods include depolymerization of the SiO_2 structure and the electronic contribution to the heat capacity, which would both cause an increase in the calculated heat capacity. However, it should be noted that DFT methods may underestimate the band gap and consequently overestimate the electronic contribution to the heat capacity.

Interestingly, there is more enthalpy data above 1800 K, from 1400 to 2400 K (Tarasov et al., 1973), that has been neglected in the literature due to scatter in the data. However, as the data is over a much larger temperature range than that of Richet et al. (1982), the enthalpy data were fit to a second order polynomial to obtain a temperature dependence to the isobaric heat capacity. Even with the reasonably high uncertainties in enthalpy, $0.8 - 1.3\%$, the combined data of Richet et al. (1982) and Tarasov et al. (1973) provide experimental constraints on the enthalpy and hence

heat capacity over a wider temperature range than previously considered.

The best fit to the combined enthalpy data of Richet et al. (1982) and Tarasov et al. (1973) from 1600 to 2400 K is as follows,

$$C_P \text{ [J mol}^{-1}\text{K}^{-1}] = 80.1(1.8) + 0.0079(58)\,(T - 1600) \tag{A.24}$$

where temperature is in Kelvin and the covariance between the uncertainty in the intercept and the slope is -0.00465. Although the increase in heat capacity with temperature is relatively uncertain, it is significant. Since the band gap for SiO_2 is 8.9 eV (Laughlin, 1980), we expect the electronic contribution to the heat capacity to be small in the temperature range from 2000 to 3000 K.

A.2.2 Entropy of liquid silica at 1 bar

Upon integration of all available thermodynamic data, Richet et al. (1982) calculated the absolute entropy of amorphous silica at the observed glass transition temperature of their experiments, S=154.757 J mol^{-1} K^{-1} at 1600 K. As the transition between glass and liquid is second order, there is no entropy discontinuity, and the heat capacity can be integrated across the glass transition temperature. Hence, above 1600 K, we use the isobaric heat capacity (Equation A.24) to determine the entropy of liquid silica for temperatures above 1600 K:

$$\begin{aligned} S(T > 1600\text{K}) &= 154.0(3.0) + 80.1(1.8)\ln\left(\frac{T}{1600}\right) \\ &\quad +0.0078(58)\left[(T - 1600) - 1600\ln\left(\frac{T}{1600}\right)\right]. \end{aligned} \tag{A.25}$$

We also calculated the enthalpy of liquid silica above 1600 K using the tabulated value from Richet et al. (1982) at 1600 K and the isobaric heat capacity (Equation A.24), noting that the

covariance between the uncertainty in the linear term and the quadratic term is -0.00465:

$$\begin{aligned} H(T > 1600\text{K}) - H(298\text{ K}) &= 87849 + 80.1(1.8)\,(T - 1600) \\ &\quad + \frac{0.0079(58)}{2}\,(T - 1600)^2\,. \end{aligned} \tag{A.26}$$

A.2.3 Equilibrium vaporization of silica

We include the following reactions to calculate equilibrium between liquid and vapor:

$$\mathrm{SiO_2^{(}}l\mathrm{)} \rightleftharpoons \mathrm{SiO^{(}}g\mathrm{)} + \frac{1}{2}\mathrm{O_2^{(}}g\mathrm{)}, \tag{A.27}$$

$$\frac{1}{2}\mathrm{O_2^{(}}g\mathrm{)} \rightleftharpoons \mathrm{O^{(}}g\mathrm{)}, \tag{A.28}$$

$$\mathrm{SiO_2^{(}}l\mathrm{)} \rightleftharpoons \mathrm{SiO_2^{(}}g\mathrm{)}. \tag{A.29}$$

Equilibrium between the reactions described in Equations A.27 and A.28 must be solved simultaneously with the constraint that the partial pressures of the product gases from reactions A.27 to A.29 must sum to 1 bar at the vaporization temperature. The equilibrium constants for reactions A.27 and A.28 are defined as follows,

$$K_{\text{A.27}} = \frac{P_{\mathrm{SiO}} P_{\mathrm{O_2}}^{1/2}}{a_{\mathrm{SiO_2}}} \tag{A.30}$$

$$K_{\text{A.28}} = \frac{P_{\mathrm{O}}}{P_{\mathrm{O_2}}^{1/2}} \tag{A.31}$$

$$K_{\text{A.29}} = \frac{P_{\mathrm{SiO_2}}}{a_{\mathrm{SiO_2}}} \tag{A.32}$$

where $a_{\mathrm{SiO_2}}$ is the activity of SiO_2 in the liquid phase. As in Schick (1960), we now make the assumption that the liquid is a pure compound and hence the activity of the pure phase is $a_{\mathrm{SiO_2}}$=1.

To calculate the equilibrium partial pressures within reactions A.27 and A.28, we assume a

closed system. Thus, the number of moles, N, of molecular oxygen in the system can be related to the number of moles of SiO and atomic oxygen by

$$N_{\mathrm{O_2}} = \frac{1}{2} N_{\mathrm{SiO}} - \frac{1}{2} N_{\mathrm{O}}. \tag{A.33}$$

As 1 bar and a few thousand Kelvin is not close to the critical point for any of the species considered above, the ideal gas law is valid. Then, the relation between the partial pressures of the species is

$$P_{\mathrm{O_2}} = \frac{1}{2} P_{\mathrm{SiO}} - \frac{1}{2} P_{\mathrm{O}} \tag{A.34}$$

Equations A.30 to A.34 can be solved with knowledge of the equilibration constants or, more specifically, the difference in Gibbs free energy of reactions A.27 to A.29.

The Gibbs free energy of a reaction, ΔG_{rxn}, is most accurately determined from the heat of reaction less the entropy difference between the products and reactants, $\Delta H_{\mathrm{rxn}} - T\Delta S_{\mathrm{rxn}}$. The heat of formation of $\mathrm{SiO_2^{(\mathit{l})}}$, $\Delta^f H_{\mathrm{SiO_2^{(\mathit{l})}}}$, was calculated at 2000 K by Richet et al. (1982). As this calculation required only a small extrapolation of experimental calorimetry data, we expect the uncertainty to be similar to the uncertainty in the heat content data, $\sim 0.5\%$. There is a scarcity of information regarding the heat of formation of SiO gas; consequently, we consider the analysis by Schick (1960) of the heat of formation of SiO vapor at 2000 K to be reasonable. At $T = 2000$ K, the heats of formation are

$$\Delta^f H_{\mathrm{SiO_2^{(l)}}}\ (2000\ \mathrm{K}) \quad = \quad -934862 \pm 4674 \ \ \mathrm{J\ mol^{-1}}, \tag{A.35}$$

$$\Delta^f H_{\mathrm{SiO^{(g)}}}\ (2000\ \mathrm{K}) \quad = \quad -151190 \pm 5289 \ \ \mathrm{J\ mol^{-1}}. \tag{A.36}$$

The enthalpy change of reaction A.27 at temperatures greater than 2000 K is then

$$\begin{aligned}\Delta H_{\text{A.27}}(T) &= \Delta^f H_{\text{SiO}^{(g)}}(2000\text{ K}) \\ &\quad + [H_{\text{SiO}^{(g)}}(T) - H_{\text{SiO}^{(g)}}(2000\text{ K})] \\ &\quad + \frac{1}{2}\left[H_{\text{O}_2^{(g)}}(T) - H_{\text{O}_2^{(g)}}(2000\text{ K})\right] \\ &\quad - \Delta^f H_{\text{SiO}_2^{(l)}}(2000\text{ K}) \\ &\quad - \left[H_{\text{SiO}_2^{(l)}}(T) - H_{\text{SiO}_2^{(l)}}(2000\text{ K})\right]. \end{aligned} \tag{A.37}$$

The enthalpy of SiO_2 liquid above 2000 K is given in Equation A.26. The enthalpy of O_2, tabulated in the JANAF thermochemical tables (Chase, 1998), was fit to a polynomial, which accurately describes the enthalpy of molecular oxygen as a function of temperature for T>2000 K:

$$H_{\text{O}_2^{(g)}}(T) - H_{\text{O}_2^{(g)}}(2000\text{ K}) = -63925 + 33.918T + 0.0009777T^2 \tag{A.38}$$

As uncertainties are not presented in the JANAF thermodynamic tables, we assume the same level of uncertainty in the enthalpy difference as presented in the analysis of Schick (1960), $\sim 1\%$.

The heat capacity of SiO vapor has not been measured. We assume the heat capacity follows the heat capacity of an ideal diatomic molecule at high temperatures, i.e. $C_P = \frac{9}{2}R$. Schick (1960) performed a more rigorous assessment of the enthalpy and entropy based on spectroscopic data; however, their rigorous derivation again suggests $C_P = \frac{9}{2}R$.

The entropy of reaction is just the difference in standard entropy at temperature T between products and reactants:

$$\Delta S_{\text{A.27}}(T) = S_{\text{SiO}}(T) + \frac{1}{2}S_{\text{O}_2}(T) - S_{\text{SiO}_2}(T). \tag{A.39}$$

The entropy of SiO_2 liquid is given in Equation A.25. The entropy of O_2 is obtained from the JANAF thermochemical table (Chase, 1998), where we fit the polynomial,

$$\begin{aligned} S_{\mathrm{O}_2^{(g)}}(T) &= 211.5 + 0.0405T - 7.0794 \times 10^{-6}T^2 \\ &\quad +5.617 \times 10^{-10}T^3. \end{aligned} \tag{A.40}$$

We defer to the calculation of the entropy of SiO gas by Schick (1960), where

$$S_{\mathrm{SiO}^{(g)}}(T) = 276.31 + \int_{2000}^{T} \frac{C_P}{T} dT, \tag{A.41}$$

and assume $C_P = \frac{9}{2}R$ over the temperature range of interest.

The enthalpy change of reaction A.28 at temperatures above 2000 K is

$$\begin{aligned} \Delta H_{\mathrm{A.28}}(T) &= \Delta^f H_{\mathrm{O}^{(g)}}(2000\ \mathrm{K}) \\ &\quad + [H_{\mathrm{O}^{(g)}}(T) - H_{\mathrm{O}^{(g)}}(2000\ \mathrm{K})] \\ &\quad -\frac{1}{2}\left[H_{\mathrm{O}_2^{(g)}}(T) - H_{\mathrm{O}_2^{(g)}}(2000\ \mathrm{K})\right]. \end{aligned} \tag{A.42}$$

The enthalpy and entropy of monatomic oxygen are tabulated in the JANAF thermodynamic tables and have been fit to a polynomial,

$$H_{\mathrm{O}^{(g)}}(T) - H_{\mathrm{O}^{(g)}}(2000\ \mathrm{K}) = -41188 + 20.404T + 9.4859 \times 10^{-5}T^2 \tag{A.43}$$

$$\begin{aligned} S_{\mathrm{O}^{(g)}}(T) &= 168.04 + 0.024223T - 4.5631 \times 10^{-6}T^2 \\ &\quad +3.7315 \times 10^{-10}T^3 \end{aligned} \tag{A.44}$$

and the heat of formation of monatomic oxygen at 2000 K is 255,299 J mol^{-1}.

The enthalpy change of reaction A.29 at temperatures above 2000 K is

$$\begin{aligned}
\Delta H_{\text{A.29}}(T) &= \Delta^f H_{\text{SiO}_2^{(g)}}(2000\text{ K}) \\
&\quad + \left[H_{\text{SiO}_2^{(g)}}(T) - H_{\text{SiO}_2^{(g)}}(2000\text{ K})\right] \qquad \text{(A.45)} \\
&\quad -\Delta^f H_{\text{SiO}_2^{(l)}}(2000\text{ K}) \\
&\quad - \left[H_{\text{SiO}_2^{(l)}}(T) - H_{\text{SiO}_2^{(l)}}(2000\text{ K})\right]. \qquad \text{(A.46)}
\end{aligned}$$

The enthalpy and entropy of SiO_2 gas, tabulated in the JANAF thermodynamic tables, were fitted with polynomials:

$$\begin{aligned}
H_{\text{SiO}_2^{(g)}}(T) - H_{\text{SiO}_2^{(g)}}(2000\text{ K}) &= -121630 + 60.327T + 24.4\times10^{-5}T^2 \qquad \text{(A.47)} \\
S_{\text{SiO}_2^{(g)}}(T) &= 237.13 + 0.069519T - 12.757\times10^{-6}T^2 \\
&\quad +10.178\times10^{-10}T^3 \qquad \text{(A.48)}
\end{aligned}$$

and the heat of formation of SiO_2 gas at 2000 K is -361,747 J mol^{-1}.

Using the thermodynamic data detailed above, the Gibbs free energy of the reactions described in Equations A.27 to A.29 were fit with linear functions in temperature,

$$\begin{aligned}
\Delta G_{\text{A.27}} &= 7.684\times10^5 - 231.7T, \qquad \text{(A.49)} \\
\Delta G_{\text{A.28}} &= 2.442\times10^5 - 61.57T, \qquad \text{(A.50)} \\
\Delta G_{\text{A.29}} &= 5.539\times10^5 - 153.3T, \qquad \text{(A.51)}
\end{aligned}$$

where the free energy is in J mol^{-1} and temperature is in Kelvin. We find that the partial pressures of the vapor species in Equations A.27 to A.29 sum to 1 bar at 3177 K.

Table A.4: Experimental values for Grüneisen parameter in silica fluid. The sound velocity measurements were reanalyzed using the Hugoniots for (a) fused quartz: Equation 4 in the main text and (b) quartz: Knudson and Desjarlais (2009).

Source	Volume [10^{-4} m^3 kg^{-1}]	γ
Hicks et al. (2006)	$\leq\sim 1.7$	~ 0.6
Trunin (1994, 1998)	~ 2	0.6 ± 0.1
Lyzenga et al. (1983)[a]	2.127	0.75 ± 0.3
McQueen (1992)[a]	2.11	1.2
McQueen (1992)[b]	1.90	0.4

Due to the large, previously unknown, uncertainty in the heat capacity of SiO_2 liquid, the uncertainty in $\Delta G_{\mathrm{A.27}}$ presented in Schick (1960) needs to be increased. As the uncertainty in the enthalpy and entropy are strongly correlated by the uncertainty in the heat capacity of the materials, to first order it is reasonable to approximate the uncertainty in the free energy of reaction with the uncertainty in the enthalpy of reaction. Using values for the uncertainty in the enthalpy of formation and heating of SiO gas and O_2 gas given in Schick (1960), the enthalpy of formation of SiO_2 liquid given in Richet et al. (1982), and the enthalpy of heating SiO_2 liquid determined here, we find the enthalpy of reaction A.27 is uncertain to within $\sim$29,000 J mol^{-1} at 3000 K. Consequently, the boiling point will be uncertain to $\pm$115 K.

A.3 Streaked optical pyrometer calibration

The spectral radiance emitted from a surface at temperature T is described by Planck's law,

$$L(\lambda, T) = \epsilon \frac{2hc^2}{\lambda^5} \frac{1}{e^{hc/\lambda k_{\mathrm{B}} T} - 1}, \tag{A.52}$$

where ϵ is the emissivity, λ is the wavelength of light, and T is the temperature of the radiating surface. From Kirchoff's law for an opaque surface, ϵ=(1-R'), where R' is the frequency-dependent the reflectivity. Here we make the assumption that R' is frequency independent over the range of

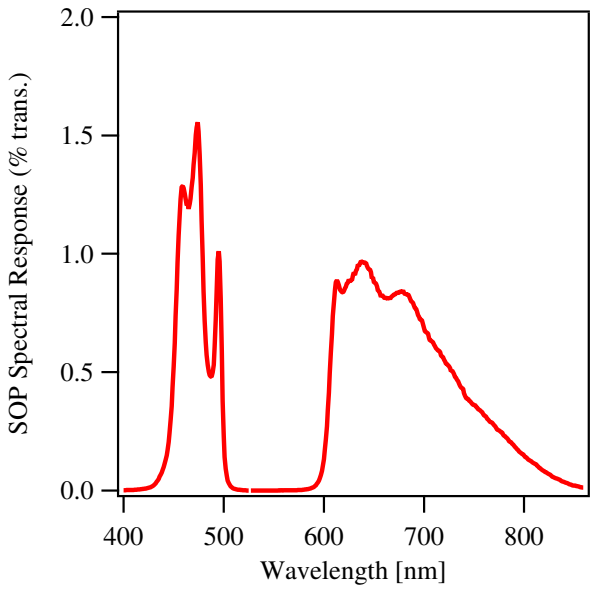

Figure A.2: Spectral response of the streaked optical pyrometer used in post-shock temperature measurements at the Janus laser. The gap in transmission from 500 to 600 nm was created by multiple notch filters used to block light from the drive laser (527 nm) and the VISAR probe laser (532 nm).

interest. Based on previous measurements of spectrally resolved and absolutely calibrated detectors (Lyzenga et al., 1983), our assumption of gray-body emission is reasonable. For a pyrometer that collects light over a small wavelength band, Planck's law can be inverted into a form more suitable for apparent temperature measurements,

$$T_{\mathrm{a}} = \frac{T_0}{\ln\left(1 + \frac{A}{I_{\mathrm{cor}}}\right)}, \tag{A.53}$$

where T_0 and A are coefficients determined from calibration of the pyrometer and I_{cor} is the pyrometer signal corrected for a non-zero reflectivity (Celliers et al., 2010).

In Figure A.2, the spectral response of the Janus Streaked Optical Pyrometer (SOP) is given as a function of wavelength (which includes transmission through the optical components and wavelength dependence of the Hamamatsu C7700 streak camera detector efficiency). Quartz shock

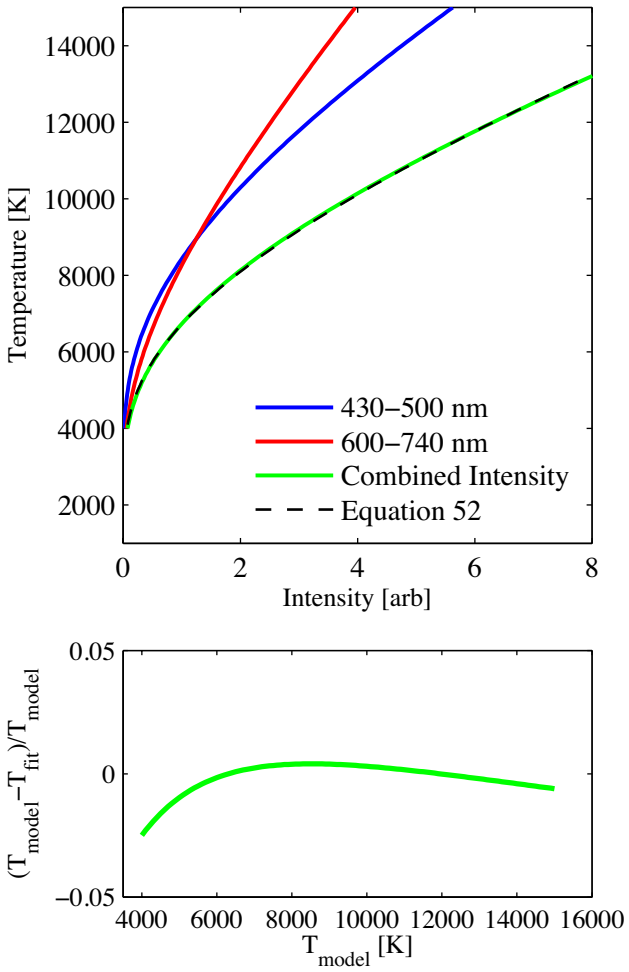

Figure A.3: Top: Model streaked optical pyrometer intensity as a function of temperature for emission bands from 430–500 nm (blue), 600–740 nm (red), and the combined emission spectrum (green). Equation A.53 is fit to the combined spectrum (dashed black line). Bottom: Relative difference between the model temperature and the temperature derived from Equation A.53. The error is less than 2% for the range of temperatures considered here.

temperatures were absolutely calibrated using the SOP at the Omega laser, which has a sensitivity spectrum similar to Figure A.2. However, the spectrum is split into two channels at Omega, and consequently, it is reasonable to treat the emission from each channel as though it occurs over a small wavelength range (Miller et al., 2007). At Janus, radiation from the entire spectrum (Figure A.2) is combined into one channel; hence, a delta function approximation for the emitting frequency does not seem appropriate.

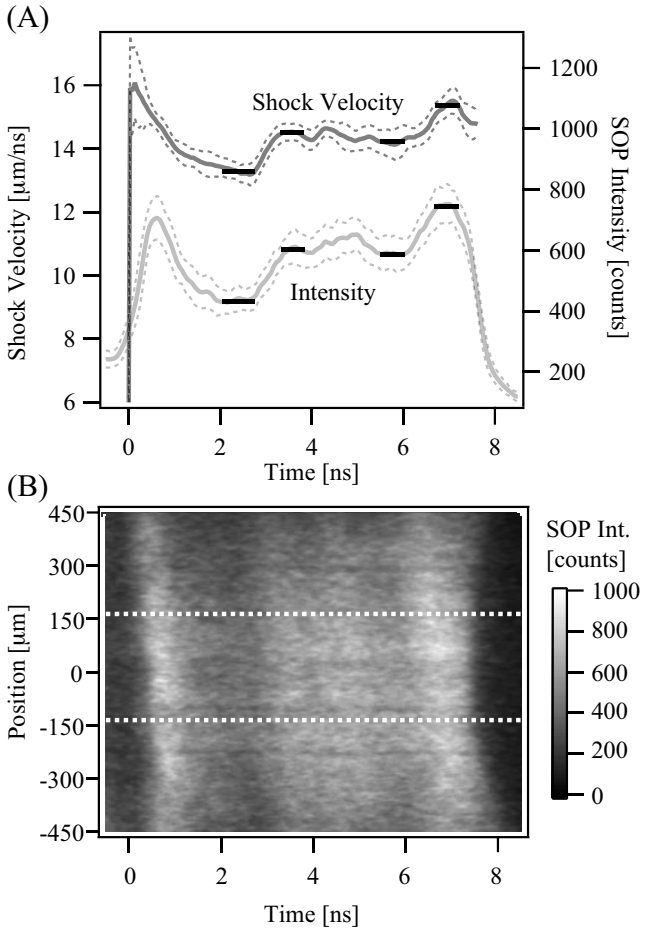

Figure A.4: (A) Shock velocity and corrected streaked optical pyrometer (SOP) intensity I_{cor} from shot e100726s4. The dark grey line (dashed) represents the shock velocity (uncertainty), light grey line (dashed) represents the corrected thermal emission (uncertainties) measured by the SOP for the same experiment. Dark horizontal bars represent regions of time where we are confident the shock velocity corresponds to the respective SOP intensity (i.e., where the structure in the profiles are obviously corresponding). (B) SOP image from shot e100726s4, dashed white lines represent region of space over which the corrected SOP intensity was taken. Uncertainties from part (A) of this figure are determined from the scatter in the SOP intensity at a given time. For the given laser spot size and target thickness, lateral release waves do not reach the area of interest.

However, upon simulating the combined thermal emission with the SOP response (Figure A.3), we find the error in using Equation A.53 to be less than 2% over the temperature range of interest here. At temperatures greater than 20,000 K, the error in using Equation A.53 can increase beyond 5% and should be accounted for in data analysis of high-temperature shock wave experiments.

We fit the SOP calibration coefficients T_0 and A to shock velocity–I_{cor} data from six different

experiments (with no intermediate modifications to the SOP or collecting optics). The structure in the thermal emission from quasi-steady shock waves is similar to the structure in the shock velocity measurements. Paired intensity and shock velocity data were selected at locations with correlated structure for the calibration, as shown in Figure A.4. The paired shock velocity and intensity data were taken at least 2 ns after the shock wave enters the quartz to avoid any possible pre-heating related to hard x-ray deposition within the quartz sample. The intensity of the thermal emission is corrected for the reflectivity of the shock front using the reflectivity of quartz as a function of shock velocity (Celliers et al., 2010). For targets that did not have an anti-reflective coating on the down-range free surface, a second correction for the reflectivity of an interface between disparate indices of refraction was done using the Fresnel equation (1.547 for c-axis quartz). The calibration uses the shock velocity–temperature calibration from Hicks et al. (2006) with the corrected reflectivity from Celliers et al. (2010). The fit to Equation A.53 is shown in Figure A.5. The least-squares fitted coefficients are $A = 3140(760)$ [counts] and $T_0 = 24300(2350)$ [K] with a covariance of 1.745×10^6.

For the lowest-pressure experiment (e100727s1 in Figure A.5), the SOP intensity data were not determined from the companion shock wave velocities because of the lack of reflectivity in the shock front. Instead, the intensity is calibrated by the superheating signature in quartz. As superheating temperatures are rate dependent (Luo et al., 2003c), we calibrate using the temperature measurements of Hicks et al. (2006) rather than the more accurate gas-gun measurements by Lyzenga et al. (1983).

Upon formal propagation of errors, the uncertainty in the post-shock temperature measurements is $\sim 11\%$, which is a combination of both the uncertainty in the fit presented in Figure A.5 and the 8% uncertainty in calibration of the quartz standard by Hicks et al. (2006). The uncertainty in our calibration fit is due to random noise and spatial variability in the SOP ($> 5\%$) and the random error in shock velocity measurement ($2\% - 4\%$). The uncertainty in the reflectivity correction to

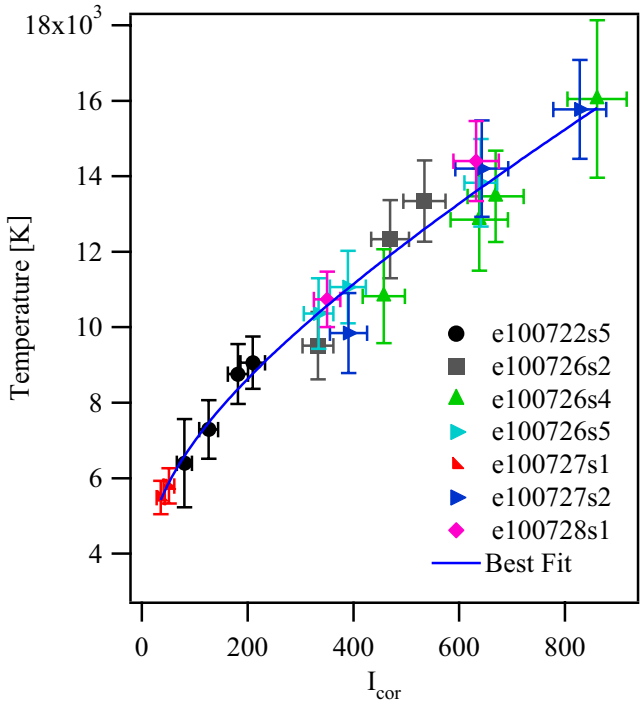

Figure A.5: Streaked optical pyrometer calibration. Data from individual experiments (symbols) are fit to Equation A.53. The least-squares fitted coefficients are $A = 3140(760)$ [counts] and $T_0 = 24300(2350)$ [K] with a covariance of 1.745×10^6.

$I_{\rm cor}$ is small due to the low reflectivity at these pressures.

A.4 Absorbance of silica fluid

We used first-principle MD simulations to generate samples of thermally perturbed positions for a model of fluid silica with 96 atoms under temperature and pressures relevant to planetary impacts. In FPMD, the forces governing the dynamics are evaluated using Density Functional Theory (DFT) (Hohenberg and Kohn, 1964), which is in principle an exact representation of the many-body Schrödinger equation and in practice is only limited by the approximation of the exchange-correlation functional. The FPMD simulations were performed using the Vienna ab initio Simulation Package (VASP) (Kresse and Hafner, 1993). We used the Perdew-Burke-Ernzerhof (PBE) (Perdew et al., 1996) level of approximation to the exchange correlation functional with projector-augmented wave (PAW) (Blochl, 1994) pseudopotentials to account for the core electrons. We used Born-Oppenheimer MD (BOMD) within the NVT-ensemble (with a Nose-Hoover thermostat with a frequency of 13.2 THz and a 1.0 fs ionic time step). For the MD, the Brillouin zone was sampled at the Γ-point and the plane-wave cutoff was set to 1200 eV. The electron occupancy are set according to a Fermi-Dirac distribution function ($T_e = T_{ions}$). For the optical properties post-processing calculations, the sample configurations are drawn from a 5 ps trajectory (after equilibration). We used 30 well spaced configurations, a lower plane-wave cutoff of 900 eV, a smearing of 0.03 eV for the spectra and enough unoccupied bands to cover all excitations within a 80 eV window. For each configuration drawn from the trajectories, we used the Gamma point electronic density from the MD to evaluate the set of Kohn-Sham orbitals at the $(\frac{1}{4}, \frac{1}{4}, \frac{1}{4})$ k-point (again using Fermi broadening at the ionic temperature). Based on these orbitals, we use the Kubo-Greenwood formula to estimate the real component of the frequency dependent conductivity, $\sigma_1(\omega)$ (e.g. Holst et al., 2008;

Mattsson and Desjarlais, 2006).

$$\begin{aligned}\sigma(\omega) &= \frac{2\pi e^2\hbar^2}{3m^2\omega\Omega}\sum_{\mathbf{k}} W(\mathbf{k})\sum_{j=1}^{N}\sum_{i=1}^{N}\sum_{\alpha=1}^{3}[F(\epsilon_{i,\mathbf{k}}) - F(\epsilon_{j,\mathbf{k}})] \\ &\quad \times|\langle\Psi_{j,\mathbf{k}}|\nabla_\alpha|\Psi_{i,\mathbf{k}}\rangle|^2\delta(\epsilon_{i,\mathbf{k}} - \epsilon_{j,\mathbf{k}} - \hbar\omega), \end{aligned} \tag{A.54}$$

where e and m are the electron charge and mass, Ω the cell volume, α denotes the x, y and z directions and $F(\epsilon_{i,\mathbf{k}})$ is the occupation number of the "i"th eigenvalue at the "k" k-point. Note that for the present work, only one k-point is used. The DC conductivity is obtained as the zero frequency limit of $\sigma_1(\omega)$ averaged over the different configurations while the imaginary component of the conductivity is obtained using the Kramers-Kronig transform.

$$\sigma_2(\omega) = -\frac{2}{\pi}M\int_0^\infty \frac{\sigma(\nu)\omega}{(\nu^2-\omega^2)}d\nu \tag{A.55}$$

where M denotes the principal value of the integral. Using the complex conductivity, we can get the complex dielectric function, the index of refraction, and the coefficient of extinction:

$$\epsilon_1(\omega) = 1 - \frac{4\pi}{\omega}\sigma_2(\omega) \quad ; \quad \epsilon_2(\omega) = \frac{4\pi}{\omega}\sigma(\omega) \tag{A.56}$$

$$\epsilon(\omega) = \epsilon_1(\omega) + i\epsilon_2(\omega) = [n(\omega) + ik(\omega)]^2 \tag{A.57}$$

$$R(\omega) = \frac{[1-n(\omega)]^2 + k^2(\omega)}{[1+n(\omega)]^2 + k^2(\omega)} \tag{A.58}$$

To get an estimate of the opacity of the vapor, we ran a short MD simulation using 4 SiO molecules and 2 O_2 molecules in a large volume to capture a sample of bond vibrations. The density was 0.0092 g/cc. Here, a plane-wave cutoff of 500 eV was used. Configurations from this short MD were used to get the conductivity with enough unoccupied bands to cover all excitations within a 11 eV window.

The FPMD-DFT opacity calculations are thought to be reasonably accurate for silicate fluids based on their previous success in predicting optical properties of supercritical fluids (Clérouin et al., 2005; Laudernet et al., 2004). Given the computational expense in calculating the opacity at a single (ρ,T) point, creating a opacity table from DFT calculations that is sufficiently populated for accurate interpolation is not yet feasible.

Hence, we use a semiconductor type Drude model to determine how the opacity scales as a function of density and temperature. The Drude model has been shown to adequately describe the increase in reflectivity along the supercritical fluid Hugoniot of LiF, Al_2O_3, H_2O, and He (Celliers et al., 2004, 2010; Hicks et al., 2003). We use the FPMD-DFT calculations to constrain the parameters in the Drude model.

The Drude model for the conductivity is given as,

$$\sigma(\omega) = \frac{n_e e_c^2 \tau_e}{2\epsilon_0 m_{eff}(1 - i\omega\tau_e)}, \tag{A.59}$$

where n_e is the free electron concentration, e_c is the charge on the electron, τ_e is the electron relaxation time, m_{eff} is the effective mass of the electron, which is approximately the mass of an electron, and ω is the angular frequency. For disordered materials the electron relaxation time τ_e is close to the Ioffe-Regel limit (Ioffe and Regel, 1960), at which the scattering length is close to the interatomic distance R_0. The relaxation time is then $\tau_e = R_0/u_e$, where u_e is the mean electron velocity, which is approximately proportional to $T^{1/2}$; consequently $\tau_e = A_0\rho^{1/3}T^{-1/2}$, where A_0 is a constant. The free electron concentration n_e in the semiconductor model is described by the carrier concentration of an intrinsic semiconductor (Kittel and Kroemer, 1980), which for thermal

energies lower than the gap energy scales approximately as

$$n_{\mathrm{e}} = n_0 T^{3/2} \exp\left(-\frac{E_{\mathrm{g}}(\rho, T)}{2k_{\mathrm{B}}T}\right), \tag{A.60}$$

where E_{g} is the gap energy and n_0 is a constant. The gap energy has been found to be linearly dependent on density and temperature for a number of materials (Celliers et al., 2004, 2010; Hicks et al., 2003), and consequently, we assume the form below for SiO_2 in the expanded regime,

$$E_g = A_1 + A_2\rho + A_3 T, \tag{A.61}$$

where A_1, A_2, and A_3 are constants.

The frequency-dependent absorption coefficient $\alpha(\omega)$ is given by (Clérouin et al., 2005)

$$\alpha(\omega) = \frac{4\pi\sigma_1(\omega)}{n_1(\omega)c}, \tag{A.62}$$

where c is the speed of light and $n_1(\omega)$ is the real part of the index of refraction. As $n_1(\omega)$ has a relatively weak dependence on temperature and density, we consider it a constant.

Substituting the previously mentioned scalings for τ_{e}, n_{e}, and the real part of the conductivity $\sigma'(\omega)$, one finds

$$\alpha(\omega) = \frac{4\pi}{n_1 c}\frac{e_c^2}{2m_e\epsilon_0}\frac{A_0\rho^{1/3}T^{-1/2}}{(1+\omega^2\tau_{\mathrm{e}})} n_0 T^{3/2} e^{-\frac{A_1+A_2\rho+A_3T}{k_B T}}. \tag{A.63}$$

As the electron relaxation time τ_{e}, is greater than ω when the mean electron velocity is comparable to the Fermi velocity of metals, we assume $\omega^2\tau_{\mathrm{e}}^2 \ll 1$. Note that this assumption also removes any frequency dependence of the absorbance. Collecting terms that are independent of of temperature and density, and normalizing the temperature and density terms by arbitrary constants T_n and ρ_n,

we find the absorption coefficient scales as,

$$\alpha_{\text{vap}} = B_0 \left(\frac{\rho}{\rho_n}\right)^{1/3} \left(\frac{T}{T_n}\right) \mathrm{e}^{-B_1 \frac{T_n}{T}} \mathrm{e}^{-B_2 \frac{\rho T_n}{\rho_n T}}, \tag{A.64}$$

where B_1 and B_2 are dimensionless fitting parameters and B_0 scales the absolute absorbance and has units of absorbance.

To compare with the FPMD-DFT calculations of frequency dependent absorbance, we calculate a Rosseland mean absorption coefficient α_{RM} for each DFT point,

$$\frac{1}{\alpha_{RM}} = \frac{\int_0^\infty \frac{\kappa_\lambda}{\alpha(\lambda)} \frac{\partial L_\lambda}{\partial T} d\lambda}{\int_0^\infty \kappa_\lambda \frac{\partial L_\lambda}{\partial T} d\lambda} \tag{A.65}$$

where the weighting function κ_λ describes the spectral response of the SOP and L_λ is the Planck function. The mean absorption coefficient ranges from 0.008 mm^{-1} for the silicate vapor at ~ 9 kg m^{-1} and 4150 K up to 4400 mm^{-1} for the silicate liquid at 1900 kg m^{-1} and 4150 K.

To constrain B_0, B_1, and B_2, we fit Equation A.64 to the mean absorption coefficients calculated using Equation A.65. Using $\rho_n = 1900$ kg m^{-1} and $T_n = 4150$ K, we find $B_0 = 6.0 \times 10^{14}$ [mm^{-1}], $B_1 = 37$, $B_2 = -11.6$. The fit is shown in Figure A.6.

Spectroscopic measurements of post-shock thermal emission from samples of diopside shocked into the high pressure fluid phase suggest that the vapor phase could be partially ionized (e.g. Kurosawa et al., 2012). However, in their measurements the shock state in the diopside was not measured and so it is not clear that the measurements are in a comparable region of the phase diagram.

Ionization is not taken into account in our radiative transfer model because the ionization energies for silicon and oxygen are sufficiently high to expect negligible vaporization at the measured temperatures in these experiments. More work is needed to determine the quantitative effect of

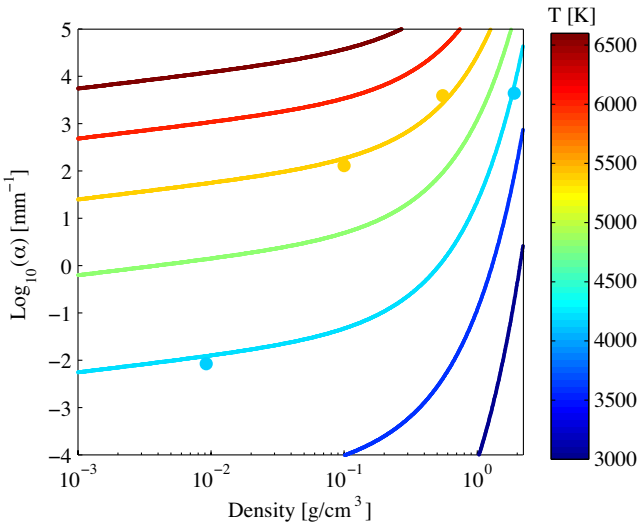

Figure A.6: Comparison of DFT-MD absorbance calculations for silica over a range of temperatures and densities (filled circles), with fitted absorbance model (lines, Equation A.64) based on semiconducting Drude model.

ionization on the thermodynamics of shock induced vaporization.

Appendix B

Additional calculations for Chapter 3

B.1 Experimental Technique

The concept behind measuring the density on the liquid-vapor dome is that of a reverse-impact experiment, where the sample of interest is launched at a target with a well-known equation of state, see Figure B.1. By measuring the shock state generated in the target, in our case a transparent window, one can determine the properties of the impacting sample of interest, in our case liquid iron. The theoretical development for measurement of density on the liquid branch of the liquid-vapor dome via shock-and-release experiments can be found in Kraus et al. (2012a). The shock-and-release experiments to measure the density on the liquid-vapor dome of iron were performed on the Z machine at Sandia National Laboratory Knudson and Desjarlais (2009); M. E. Savage *et al.* (2007); Matzen (1997).

An overview of the experimental configuration is presented in Fig. B.2. Due to the large spatial scale of the aluminum flyer plates on the Z machine (∼50 mm high by 30 mm wide by 1.2 mm thick), multiple downrange windows could be used as targets simultaneously at gap distances of ∼200 and ∼400 μm from the free surface of the ∼200 μm thick iron samples. All lateral dimensions were sufficient to avoid lateral release waves over the duration of the experiment, as determined by detailed simulations using the CTH shock physics code McGlaun et al. (1990).

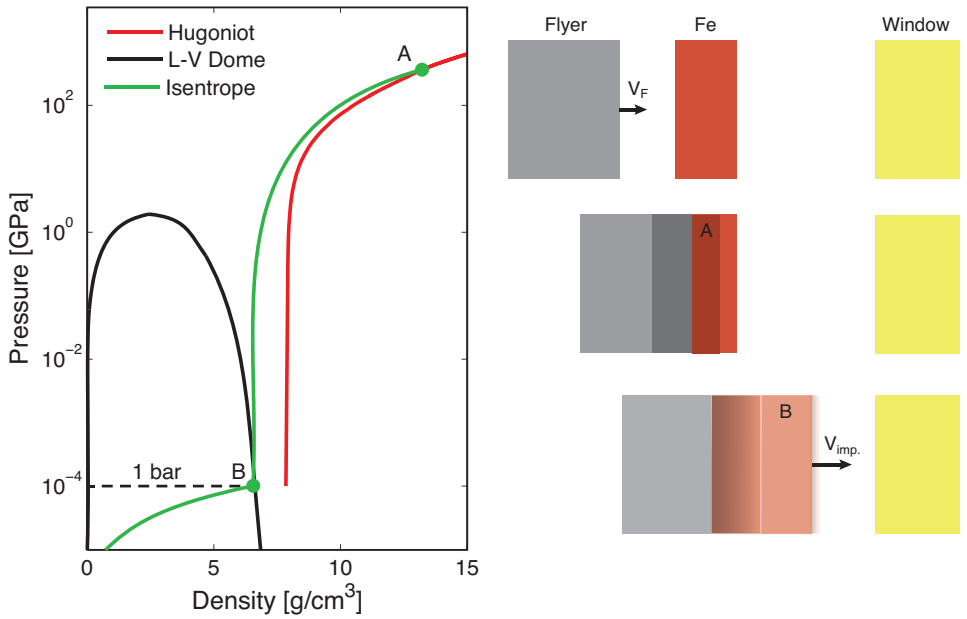

Figure B.1: Left: Schematic phase diagram for iron with annotations of the thermodynamic states reached during the planar shock-and-release experiments on iron. Top-right: the Al flyer plate impacts the iron sample at velocity V_F. Middle-right: the impact generates a planar shock wave in the iron sample, behind the shock wave the iron sample is at state (A) on the Hugoniot. Bottom-right: the decompressing iron accelerates across the gap towards the window at velocity V_{imp}. Because of the discontinuous change in sound velocity as the release isentrope intersects the liquid-vapor dome at state (B), the decompression wave splits and inertially traps a region of material at state (B), which then impacts the window and generates a strong steady shock wave.

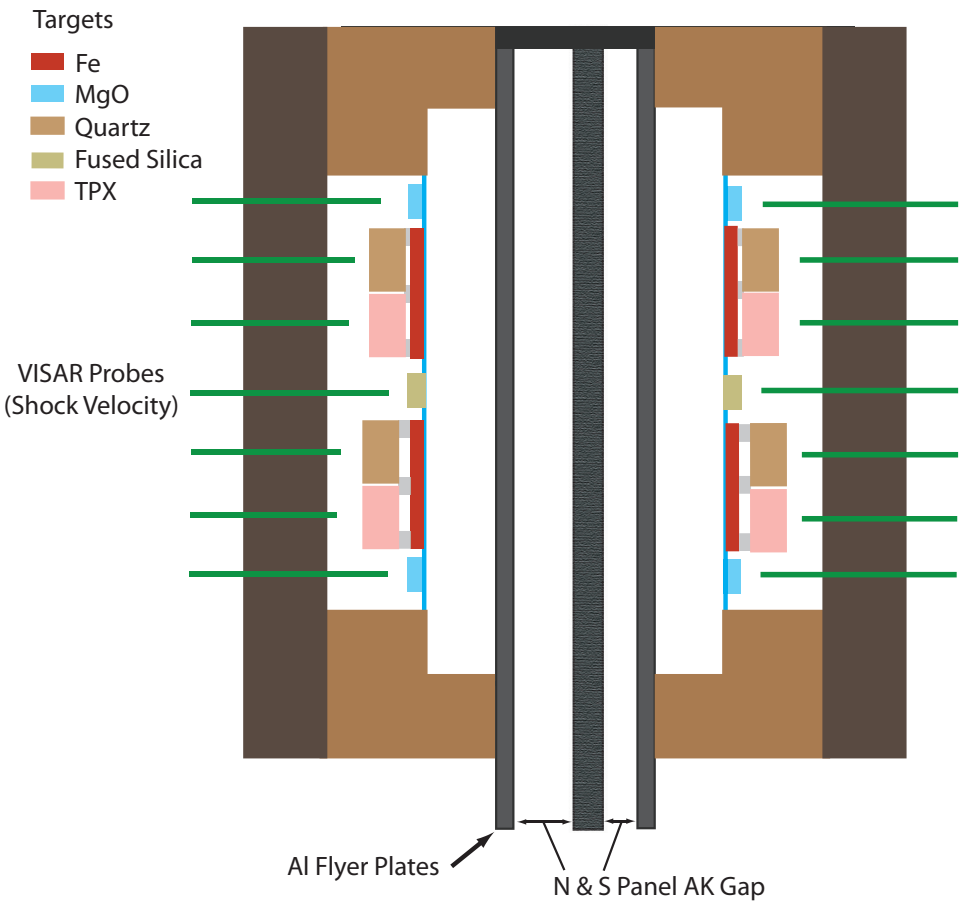

Figure B.2: Schematic experimental configuration for planar shock-and-release experiments on iron (side view of a cut through the center line). Al flyer plates induce a planar shock in iron samples (red). Flyer velocity and tilt are measured through the MgO and fused silica windows. When the shock reaches the downrange free surface, the iron decompresses and expands across a gap, impacting a standard window. Gap thicknesses are tuned to maximize the thickness of iron inertially trapped on the liquid branch of the liquid-vapor dome. VISAR measurements of the steady shock state generated in the standard windows (quartz and TPX) are used to derive the density of the iron on the liquid branch of the liquid-vapor dome, Equation B.1. For clarity the figure is not to scale, see dimensions in text.

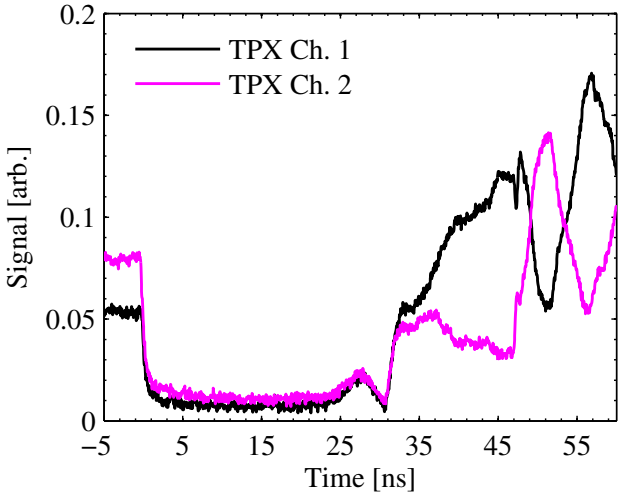

Figure B.3: Raw VISAR signal from a probe centered on an iron sample, an ∼400 μm gap, and a TPX window. The time axis has been shifted so that time zero occurs when the shock wave breaks out of the free surface of the iron sample.

Downrange windows/targets were either z-cut α-quartz, a well characterized impedance matching standard Knudson and Desjarlais (2009) or polymethylpentene (TPX, Mitsui Chemicals, grade DX845), which is a low density thermoplastic that has recently been thoroughly characterized as an impedance matching standard at Sandia. At shock pressures greater than ∼1 Mbar, both quartz and TPX become sufficiently conductive that the shock front becomes reflective to optical light, allowing the VISAR diagnostic Barker and Hollenbach (1972) to measure the shock velocity directly.

Figure B.3 presents a time history of two VISAR channels used to measure the shock velocity in the window for iron stagnating against a TPX window at an ∼400 μm gap. Prior to any contrast in the VISAR signal, starting at ∼33 ns, one can see the rise of reflectivity at ∼31 ns, and the increase of incoherent light from the vapor stagnating against the window, starting at ∼23 ns. Figure B.4 presents a time history of the shock velocity through TPX windows at gap distances of ∼200 μm and ∼400 μm. The constant shock velocity initially generated in the window verifies that material of constant density impacted the TPX window.

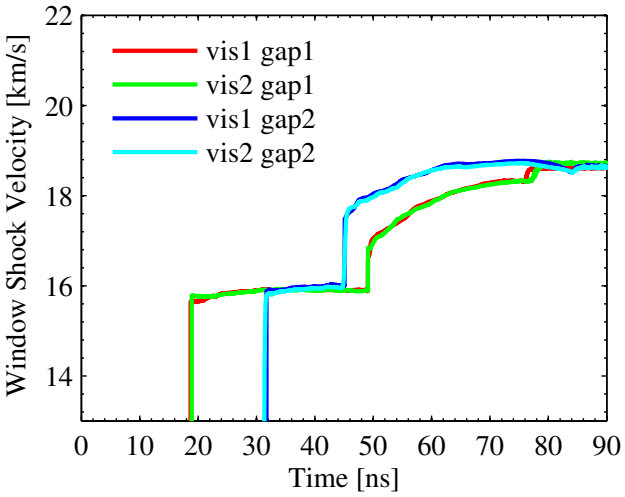

Figure B.4: Measured shock velocity through the TPX windows at gap distances of ∼200 and 400 μm. The initial steady shock velocity is a result of material of constant density impacting the window. The shock velocity increase at late times is the arrival of a reflected wave from the iron sample.

With the measured shock velocity in the window, the shock pressure and particle velocity in the window, P_{wnd} and u_{wnd}, respectively, are obtained from the known Hugoniot of the window material (Section B.1.2). The impact velocity, V_{imp}, of the iron liquid with the window is determined from the transit time across the gaps of known distance. A second order correction at the few percent level is required for the transit time to account for the time it takes for the shock wave to overtake the low pressure ramp wave generated from the stagnating vapor ahead of the iron liquid. A description of this correction is provided in Section B.1.3.

The shock impedance of the iron liquid, Z_{liq}, is determined by using the requirement for continuity of pressure and particle velocity at the interface between the iron liquid and the window, $Z_{liq}u_{liq}$=P_{wnd} and $u_{liq} = V_{imp} - u_{wnd}$, respectively. The shock impedance is the product of the shock velocity through the iron liquid, $U_{s,liq}$, and the initial density of the iron liquid, ρ_{lv}, which is the density on the liquid branch of the liquid-vapor dome. And while the shock velocity through the iron liquid is not directly measured on the experiments at the Z-machine, a review of the liter-

ature has shown that to zeroth order the high-pressure shock velocity-particle velocity relationship is insensitive to material properties Nellis (2006), where most fluids have a linear relationship between the shock velocity and the particle velocity. The shock velocity particle velocity relation is most sensitive to the initial density, where the coefficients can be reliably parameterized as a linear function of initial density Anderson (1997); Kraus et al. (2012a). There are a significant number of measurements of the porous Hugoniot of iron covering the range of initial liquid iron densities considered here, allowing for an experimental constraint on the density dependence of the porous iron Hugoniot (Section B.1.4). And as the re-shocked iron is not at the same initial internal energy state as the porous material, we use the Mie-Grüneisen equation of state derived in Section B.1.4 to accurately determine the effect of the higher initial internal energy on the re-shocked Hugoniot of the iron liquid inertially trapped on the liquid-vapor dome (Section B.1.5).

The density on the liquid branch of the liquid-vapor dome, state B in Figure B.1, is then measured as a function of the initial shock state in the iron, state A in Figure B.1, and is given by,

$$\rho_{lv} = \frac{P_{wnd}}{U_{s,liq} u_{liq}}, \tag{B.1}$$

where $U_{s,liq}$ is the shock velocity in the liquid iron generated upon impact with the window. The initial shock state in the iron, state A in Figure B.1, is obtained by impedance matching the iron Hugoniot to the aluminum flyer, see Section B.1.6.

B.1.1 Summary of Uncertainty Contributions

The dominant contribution to the uncertainty in ρ_{lv} is the uncertainty in the re-shocked iron particle velocity, u_{liq}, as it enters directly into Equation B.1 for ρ_{lv} and is also the independent variable in the equation for the shock velocity through the iron liquid, $U_{s,liq}$, Equation B.6. The relative uncertainty in u_{liq} is ∼10-30 %, see Table B.2, and because of the additional dependence of $U_{s,liq}$

on u_{liq}, the uncertainty in ρ_{lv} is overwhelmingly dominated by the uncertainty in u_{liq}.

The dominant contribution to the uncertainty in u_{liq} is the uncorrected liquid impact velocity, $V_{imp,uncorr}$, with a 5-7% experimental uncertainty. The correction to the impact velocity, described in Section B.1.3, is sufficiently small that even the large random uncertainties in the correction parameters do not increase the uncertainty in $V_{imp,corr}$ over $V_{imp,uncorr}$ by more than a few percent.

The second largest contribution to the uncertainty in ρ_{lv} is the uncertainty in the model $U_{s,liq}$ for a given u_{liq}, which we determine to be 7%. The model uncertainty in $U_{s,liq}$ is the sum of the envelope of the residuals in the model porous Hugoniots, ∼4% (Figure B.5), and the effect of the conservative estimate of a 30% uncertainty in the internal energy of liquid iron at the boiling point on the iron shock velocity, ∼2 to 4% (Figure B.6). Realistically, the uncertainty in the internal energy of liquid iron at the boiling point is much less, on the order of the uncertainty in the heat capacity ∼5 to 10%, however, we have chosen this value to illustrate the insensitivity of the liquid iron Hugoniot to an elevated internal energy state.

The final contribution to the uncertainty in ρ_{lv} is the relative uncertainty of shock pressure in the window as a function of the measured shock velocity, which for quartz and TPX is on the order of 1%.

B.1.2 Window Response

The Hugoniot of α-quartz has been measured to very high accuracy over the entire pressure range under consideration Knudson and Desjarlais (2009). The particle velocity in the window in the steady shock state was determined from a quadratic fit to the Hugoniot data presented in Knudson and Desjarlais (2009).

The Hugoniot of TPX has also been measured at the Sandia Z machine at the shock states

considered here. The best fit Hugoniot is

$$U_s = 2.64(6) + 1.313(3)u_p. \tag{B.2}$$

Using the Hugoniots for quartz and TPX, we use the steady shock velocities in the windows, Table B.1, to obtain the pressure, P_{wnd} and particle velocity, $u_{p,wnd}$, which are presented in Table B.2.

Table B.1: Stagnation Data

$P_{0,Fe}$ [GPa]	$u_{0,Fe}$ [km s^{-1}]	$V_{imp,uncorr}$ [km s^{-1}]	$V_{imp,corr}$ [km s^{-1}]	$U_{s,Qtz}$ [km s^{-1}]	$U_{s,TPX}$ [km s^{-1}]
632 ± 9	6.08 ± 0.05	13.42 ± 0.57	13.54 ± 0.57	14.85 ± 0.02	15.92 ± 0.03
552 ± 8	5.60 ± 0.05	11.67 ± 0.91	11.99 ± 0.93	13.93 ± 0.08	14.73 ± 0.05
487 ± 5	5.18 ± 0.03	10.90 ± 0.46	11.17 ± 0.48	13.30 ± 0.04	14.10 ± 0.07

$P_{0,Fe}$ – Initial shock pressure in Fe; $u_{0,Fe}$ – Initial shock particle velocity in Fe;$V_{imp,uncorr}$ – Uncorrected liquid Fe impact velocity; $V_{imp,corr}$ – Corrected liquid Fe impact velocity; $U_{s,Qtz}$ – Shock velocity in quartz window; $U_{s,TPX}$ – Shock velocity in TPX window.

Table B.2: Window shock states

$P_{0,Fe}$ [GPa]	P_{Qtz} [km s^{-1}]	$u_{p,Qtz}$ [km s^{-1}]	$u_{liq,Fe-Qtz.}$ [km s^{-1}]	P_{TPX} [km s^{-1}]	$u_{p,TPX}$ [km s^{-1}]	$u_{liq,Fe-TPX}$ [km s^{-1}]
632 ± 9	318 ± 3	8.07 ± 0.02	5.47 ± 0.57	134 ± 2	10.09 ± 0.03	3.45 ± 0.57
552 ± 8	278 ± 4	7.44 ± 0.06	4.55 ± 0.93	113 ± 2	9.18 ± 0.04	2.81 ± 0.93
487 ± 5	247 ± 5	7.01 ± 0.03	4.16 ± 0.48	102 ± 2	8.70 ± 0.06	2.47 ± 0.48

$P_{0,Fe}$ – Initial shock in Fe; P_{Qtz} – Shock pressure in the Qtz window; $u_{p,Qtz}$ – Particle velocity in the Qtz window; $u_{liq,Fe-Qtz}$ – Re-shock particle velocity in the iron liquid upon stagnation against the Qtz; P_{TPX} – Shock pressure in the TPX window; $u_{p,TPX}$ – Particle velocity in the TPX window; $u_{liq,Fe-TPX}$ – Re-shock particle velocity in the iron liquid upon stagnation against the TPX.

B.1.3 Transit Time Correction to the Impact Velocity of Liquid Iron

Upon stagnation of the vaporizing liquid iron against the downrange window of quartz or TPX, a reflecting shock rapidly forms in the window. The velocity of the shock wave is measured using the VISAR diagnostic Barker and Hollenbach (1972). Starting at the downrange free surface of the window, the position of the shock wave in the window can be integrated backwards in time to determine the position of the shock wave when it becomes reflecting. For the impact conditions in

the experiments presented here, the shock wave is found to have propagated through a few tens of microns of window for the reflecting shock to be observed due to the stagnation of the small amount of liquid-vapor mixture ahead of the liquid iron. The stagnating liquid-vapor mixture generates an opaque ramp-compression wave and so obscures the strong shock that is generated at the impact of the liquid-density plateau. The shock becomes reflecting, and hence measurable by the VISAR diagnostic, when the strong shock overtakes the opaque ramp-wave. The velocity of the shock wave through the ramp compressed material and the position of the shock wave when it becomes reflecting can be used to determine the time at which the liquid iron impacts the window, relative to the time the shock wave becomes reflecting.

We performed detailed numerical simulations of these shock-and-release experiments using CTH McGlaun et al. (1990). The iron samples were modeled using the ANEOS model Thompson and Lausen (1972). The quartz window was modeled using the SESAME 7360 model Kerley (1993) and the TPX window was modeled using a user defined Mie-Grüneisen equation of state, that was developed based on the Hugoniot of TPX.

These simulations show that the average velocity of the shock wave through the ramp compressed material is consistently within 20% of the steady shock wave velocity generated by the impact of the liquid iron. This relative indifference to the conditions of the liquid-vapor mixture stagnation are again related to the insensitive nature of the $U_s - u_p$ relation to the specific properties of the shocked material Nellis (2006).

The impact velocity of the liquid is determined by the relative transit time between two gap thicknesses,

$$V_{imp,corr} = \frac{\Delta X_{gap}}{\Delta T_{ref} - \Delta T_{corr}} \tag{B.3}$$

where ΔX_{gap} is the difference in thickness between the two stagnation gaps, ΔT_{ref} is the time

difference between the shock wave becoming reflecting in the window at the large gap and in the window at the small gap distance, and ΔT_{corr} is the correction to the transit time to account for the relative time it takes for the shock to become reflecting in the window at the large gap and the small gap distance.

$$\Delta T_{corr} = \frac{X_{2,ref} - X_{1,ref}}{U_{s,avg.}} \tag{B.4}$$

$X_{2,ref}$ and $X_{1,ref}$ are the depths within the window that the shock wave becomes reflecting and $U_{s,avg.}$ is the average shock wave velocity through the ramp compression wave, in the laboratory reference frame. The contribution to the uncertainty in the impact velocity V_{imp} from the uncertainty in $U_{s,avg.}$ is relatively small as the difference in $X_{2,ref}$ and $X_{1,ref}$ are comparable to their respective uncertainties, see Table B.3. The average steady shock velocity in the window is used for $U_{s,avg.}$ and for the purposes of error propagation a conservative 20% uncertainty is assumed for $U_{s,avg.}$.

Table B.3: Stagnation Correction Data

Position	Window	X_{gap} [μm]	$U_{s,wnd}$ [km s^{-1}]	T_{ref} [ns]	X_{ref} [μm]
			Z2385		
N02	Quartz	213 ± 6	14.85 ± 0.03	17.30 ± 0.24	24.7 ± 5.9
N09	Quartz	402 ± 7	14.86 ± 0.02	31.44 ± 0.08	26.4 ± 6
N04	TPX	213 ± 6	15.90 ± 0.04	17.20 ± 0.12	25.6 ± 6.5
N07	TPX	401 ± 11	15.94 ± 0.04	31.19 ± 0.14	27.5 ± 7.8
			Z2455		
S02	Quartz	215 ± 11	13.93 ± 0.14	17.84 ± 0.31	46.0 ± 14.1
S09	Quartz	409 ± 16	13.93 ± 0.10	34.90 ± 0.64	52.5 ± 12.3
S04	TPX	226 ± 13	14.82 ± 0.12	18.44 ± 0.15	28.2 ± 15.9
S07	TPX	414 ± 16	14.71 ± 0.06	34.20 ± 0.29	33.5 ± 17.0
N02	Quartz	216 ± 8	13.38 ± 0.08	19.37 ± 0.17	19.2 ± 10.9
N09	Quartz	400 ± 7	13.28 ± 0.04	36.93 ± 0.25	23.4 ± 7.0
N04	TPX	221 ± 9	14.07 ± 0.09	20.16 ± 0.23	19.8 ± 9.8
N07	TPX	407 ± 6	14.13 ± 0.10	36.55 ± 0.09	26.9 ± 10.8

X_{gap} – Fe to window gap thickness; $U_{s,wnd}$ – Shock velocity in the window; T_{ref} – Time to reflecting shock in window; X_{ref} – Position of reflecting shock in window.

The uncorrected impact velocities, $V_{imp,uncorr}$, use the time that the shock becomes reflecting in the same composition window for two different gap thicknesses (without a correction for the slightly

different propagation distances for the shock to overtake the inital ramp wave). The uncorrected and corrected impact velocities are presented in Table B.1.

B.1.4 Shock Response of Porous Iron

The Hugoniot of porous iron has been measured with high accuracy over a wide range of initial densities and shock pressures by Brown et al. (2000); Trunin et al. (1989a,b, 1998). Kerley (1993) developed a multiphase equation of state for iron that accurately reproduces the Hugoniots of porous and nonporous iron at the level of a few percent residuals in shock velocity over the entirety of the measurements. However, the residuals are systematic, and the mean residual shifts systematically with initial density from -2% at 7 g cm^{-3} to nearly +2% at 6 g cm^{-3}, which suggests that there is a systematic overestimate of the Grüneisen parameter.

To minimize the model dependence in the data analysis, we developed a Mie-Grüneisen equation of state for iron over the density range from 9 to 12 g cm^{-3}. A temperature independent Grüneisen parameter was not sufficient to reproduce the high porosity Hugoniots and so we used a modified Al'tshuler form of the Grüneisen parameter,

$$\gamma = \gamma_\infty + (\gamma_0 - \gamma_\infty) \left(\frac{\rho_0}{\rho}\right)^q e^{-\phi E} \tag{B.5}$$

where γ_∞, γ_0, q, and ϕ are fitting parameters and ρ is the density and E is the internal energy. We use ρ_0=7.85 g cm^{-3}, γ_∞=0.7, γ_0=2.1, q=1.7, and ϕ=0.045 kg MJ^{-1}. The Hugoniot of non-porous iron was used as the reference curve and the model data comparison is presented in Figure B.5.

B.1.5 Shock Response of Liquid Iron

Based on our experimentally constrained Mie-Grüneisen equation of state for iron, we calculated the Hugoniot of fluid iron starting at the specific internal energy of the boiling point, 2.39 MJ kg^{-1},

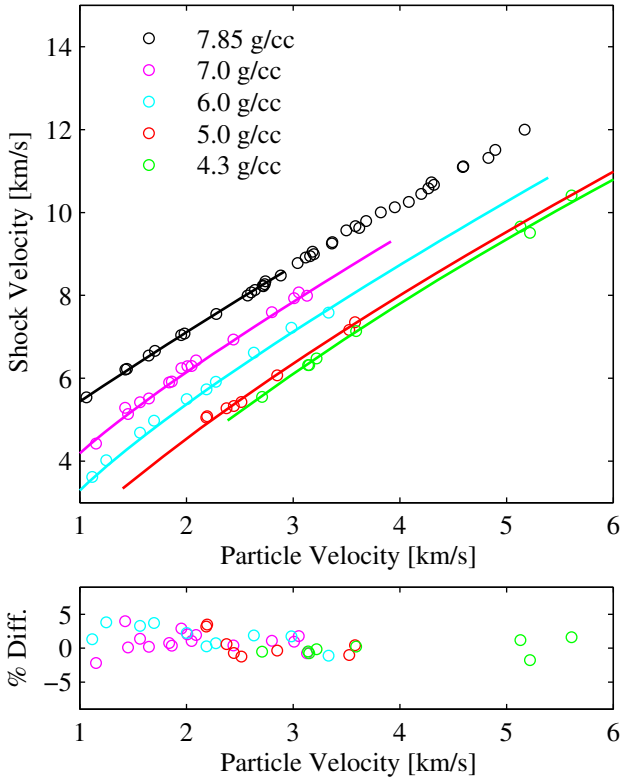

Figure B.5: Hugoniots of porous and non-porous iron Brown et al. (2000); Trunin et al. (1989a,b, 1998). Also shown are porous Hugoniots derived from our energy dependent Mie-Grüneisen equation of state (Section B.1.4).

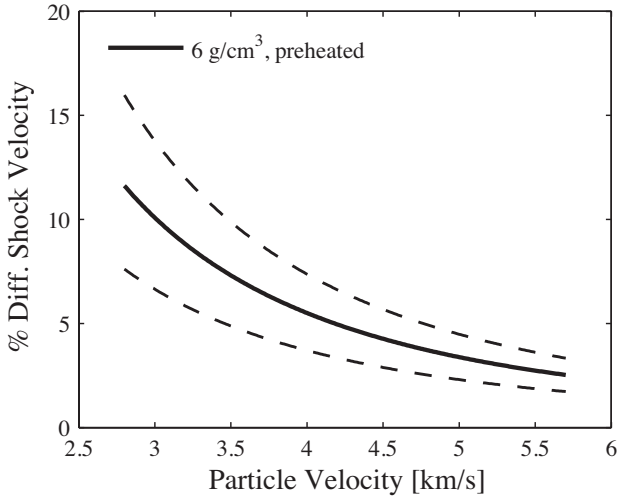

Figure B.6: Percent difference in shock velocity between fluid and porous iron at a density of 6 g cm^{-3}. The solid black line represents fluid iron at the specific internal energy at the boiling point, the dashed lines represent the specific internal energy state at the temperature of the boiling point ±1000 K.

and over a range of initial densities, 5 to 7 g cm^{-3}. The fluid iron Hugoniot is well parameterized by the form,

$$U_s = C_{00} + \alpha\rho_0 + (S_{00} + \beta\rho_0)\, u_p, \tag{B.6}$$

where C_{00}=0.79, α=0.50, S_{00}=1.19, and β=0.0307 for velocities in units of km s^{-1} and density in units of g cm^{-3}.

The residuals between the porous shock velocity data and the Mie-Grüneisen equation of state at the ambient temperature internal energy state suggest that the equation of state reproduces porous Hugoniots to within 4% (Figure B.5). Because the shock compression path in the fluid phase is path independent, measuring the shocked state of a porous material is equivalently valid at constraining the equation of state surface as measuring the shocked state of a material at an elevated internal energy state (e.g., initially liquid); consequently there is no systematic contribution to the uncertainty by using the Mie-Grüneisen equation of state to determine the Hugoniot of an initially high internal energy state.

As we are interested in states that are releasing near the 1-bar boiling point, we considered the effect of starting at the specific internal energy of liquid iron at the 1-bar boiling point, or 2.39 MJ kg^{-1} Chase (1998). For the purpose of error propagation, we assume a conservative 30% uncertainty in the initial specific internal energy of 0.75 MJ kg^{-1}, which for the heat capacity of liquid iron is equivalent to a ∼1000 K uncertainty in the temperature at the boiling point. The percent difference in shock velocity between the fluid and porous iron Hugoniot, for a starting density of 5, 6, and 7 g cm^{-3}, is presented in Figure B.6. It is important to note that the difference in shock velocity between the fluid and porous iron is insensitive to the value of the Grüneisen parameter: a 50% change in the value of the reference Grüneisen parameter only yields an equivalent uncertainty to the percent shock velocity difference as the uncertainty in the initial specific internal energy of 0.75 MJ kg^{-1}. The effect of the uncertainty in the initial internal energy state is to add an ∼2 to 4% contribution to the uncertainty in the shock velocity of the iron liquid.

B.1.6 Shock State in Iron Samples

The Hugoniot of non-porous iron is well constrained by Hugoniot measurements by Brown et al. (2000) up to 440 GPa and by Al'tshuler et al. (1996); Krupnikov et al. (1963); Trunin et al. (1993) at significantly higher pressures. The principal Hugoniot of iron is well defined in the particle velocity range of interest, 4 to 8 km s^{-1}, with a best fit

$$U_s = 3.41(14) + 1.84(6)u_p - 0.036(5)u_p^2. \tag{B.7}$$

To determine the shock state in the iron samples, we impedance matched the aluminum flyer to the iron samples, using the aluminum Hugoniot from Knudson et al. (2003). The impedance matched states for the experiments are presented in Table B.4.

The aluminum flyer plates are accelerated to the impact velocities over the distance of a few

Table B.4: Shock States in Fe Samples

Position	V_F [km s^{-1}]	X_{Fe} [μm]	$U_{s,imp}$ [km s^{-1}]	$U_{s,free-surface}$ [km s^{-1}]
		Shot Z2385		
N02	17.43 ± 0.10	217.6 ± 3.0	13.12 ± 0.06	13.23 ± 0.07
N04	17.44 ± 0.10	224.3 ± 1.8	13.13 ± 0.05	13.24 ± 0.06
N07	17.49 ± 0.10	218.0 ± 2.9	13.15 ± 0.05	13.26 ± 0.06
N09	17.52 ± 0.10	214.2 ± 3.5	13.17 ± 0.05	13.28 ± 0.06
		Shot Z2455		
N02	15.03 ± 0.07	214.1 ± 9.2	11.92 ± 0.04	11.94 ± 0.04
N04	15.05 ± 0.07	227.4 ± 5.3	11.93 ± 0.04	11.95 ± 0.04
N07	15.12 ± 0.07	205.4 ± 4.8	11.97 ± 0.04	11.99 ± 0.04
N09	15.17 ± 0.07	222.7 ± 1.6	12.00 ± 0.04	12.02 ± 0.04
S02	16.30 ± 0.12	205.7 ± 4.9	12.56 ± 0.06	12.58 ± 0.06
S04	16.32 ± 0.12	204.6 ± 5.8	12.57 ± 0.06	12.59 ± 0.06
S07	16.26 ± 0.25	200.7 ± 2.1	12.54 ± 0.13	12.56 ± 0.13
S09	16.10 ± 0.25	230.1 ± 7.6	12.46 ± 0.12	12.48 ± 0.12

V_F – Al flyer velocity; X_{Fe} – Fe sample thickness; $U_{s,imp}$ – Fe impedance match shock velocity; $U_{s,free-surface}$ – Fe shock velocity at free surface, corrected for Al flyer density gradient.

millimeters and consequently large stress gradients are needed to achieve the required acceleration. The stress histories are tuned so as not to drive a shock in the aluminum flyer Lemke et al. (2011); however, there is a slight density gradient within the flyer at the time of impact. The density gradient may cause the shock wave to accelerate through the sample, and upon breakout at the free surface, the wave has reached a shock pressure that is slightly greater than the impedance matched state. To experimentally assess the required correction to the impedance matched pressure, a thick fused silica window was placed on each target panel, through which the acceleration of the shock velocity could be observed directly using the VISAR diagnostic. However, because fused silica and iron have a significantly different shock impedance, there is not a one-to-one correlation between the shock acceleration in the iron and in the fused silica. To correct for the impedance difference, we used CTH to simulate the impact of an aluminum flyer with a fused silica window and an iron sample. The aluminum flyer was initialized with a simple linear density gradient. The slope of the density gradient was modified until the simulated acceleration of the shock velocity in the fused silica matches the acceleration of the shock wave in the fused silica measured in the experiment,

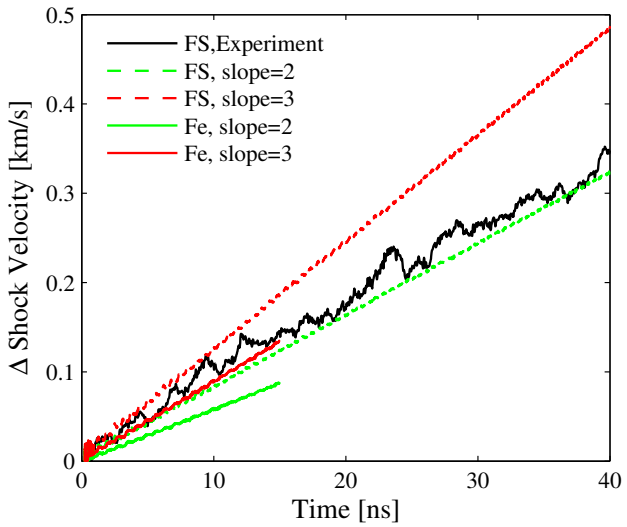

Figure B.7: Acceleration of the shock wave through the fused silica and iron targets, relative to the shock velocity at the time of impact. The measured shock acceleration through the fused silica is shown in black and the simulated shock acceleration through a fused silica window is shown in dashed green and red lines, representing density gradients through the flyer of 2 and 3 g cm^{-3} cm^{-1}, respectively. The solid green and red lines represent the shock acceleration through an iron sample for the respective density gradients.

see Figure B.7. The corrections to the shock velocities through the iron are presented in Table B.4. The initial iron shock pressure, $P_{0,Fe}$, before the release corresponds to the shock velocity just before the free surface, $U_{s,free-surface}$. It is worth noting that the shock acceleration presented in Figure B.7 is less than 1% of the average shock velocity and the correction applied here is performed in an effort to avoid systematic errors, however small.

B.1.7 Density and Entropy of Liquid Iron at the Boiling Point

Quasi-static isobaric resistive heating techniques in Beutl et al. (1994); Hixson et al. (1990) were used to measure the density, temperature, and electrical resistivity of liquid iron as a function of enthalpy from ∼2000 to 4000 K. The temperature and entropy at the 1-bar boiling point of iron is 3133±70 K and 2240±60 J kg^{-1} K^{-1}, respectively Chase (1998). The boiling point calculation is based on a Gibbs free energy minimization using the best available thermodynamic data in the

liquid phase and a statistical mechanics calculation for the vapor phase. The uncertainty in the boiling point temperature is based on our best estimate of the uncertainty in the enthalpy and entropy of iron liquid and vapor.

The weighted average of the liquid density measurements by Beutl et al. (1994); Hixson et al. (1990) at 3133±70 K is 6.01±0.15 g cm^{-3}.

B.1.8 Releasing to the Boiling Point

The density of iron on the liquid branch of the liquid-vapor dome is presented as a function of the initial shock pressure in the iron samples, Table B.5. To determine the critical shock pressure required to release to the boiling point, the iron liquid density is fit to a linear function of the initial shock pressure in the iron samples. The critical shock pressure to release to the one atmosphere boiling point is then determined by the intersection of the iron liquid density fit with the density at the boiling point (Figure 1 in main text). This intersection occurs at 507^{+65}_{-85} GPa, where the uncertainties represent the overlapping confidence bounds. Due to the large uncertainties, we also determined the intersection of the iron liquid density and the density at the boiling point using a Monte-Carlo procedure, where the densities and shock pressures were populated in a normal distribution about their mean values. The probability density distribution is skewed, with the median critical pressure occurring at 533^{+83}_{-99} GPa, where the uncertainties here represent the 16% and 84% cumulative probability distribution values.

B.2 Supporting Calculations

B.2.1 Entropy on the Iron Hugoniot

As can be seen from Figure 2 in the main text, the SESAME 2150 model equation of state for iron Kerley (1993) is closest in entropy to our experimental measurement. We expect that the

Table B.5: Release Density Measurements

$P_{0,Fe}$ [GPa]	$\rho_{liq,Qtz}$ [g cm^{-3}]	$\rho_{liq,TPX}$ [g cm^{-3}]	$\rho_{liq,Avg}$ [g cm^{-3}]
632 ± 9	5.35 ± 0.87	4.92 ± 1.20	5.20 ± 0.71
552 ± 8	6.01 ± 1.79	5.47 ± 2.59	5.83 ± 1.47
487 ± 5	6.19 ± 1.10	5.84 ± 1.67	6.08 ± 0.92

$P_{0,Fe}$ – Initial shock in Fe; $\rho_{liq,Qtz}$ – Density of Fe liquid by impedance matching to Qtz window; $\rho_{liq,TPX}$ – Density of Fe liquid by impedance matching to TPX window; $\rho_{liq,Avg}$ – Weighted average density of Fe liquid;

SESAME 2150 equation of state is most accurate because it uses the INFERNO model of Liberman (1979) to treat the thermal electronic contribution to the free energy. Because of this more realistic treatment of the electronic equation of state, we use the SESAME 2150 equation of state to estimate the entropy change along the Hugoniot, fixed to the experimental reference point we have defined in this work (by subtracting 171.7 J kg^{-1} K^{-1} from the SESAME 2150 Hugoniot entropy). Our polynomial fit to the entropy along the principal Hugoniot from ∼300 GPa to 10 TPa, where the entropy is in units of J kg^{-1} K^{-1} and pressure is in GPa, is

$$S = -1.984 \times 10^4 \times P^{-1/2} + 39.9 \times P^{1/2} - 0.1047 \times P + 2279. \tag{B.8}$$

For the purpose of determining the degree of vaporization, we assume an illustrative uncertainty in the entropy change along the iron principal Hugoniot of 10%, which is the relative difference in entropy at 500 GPa between our data point and the equations of state of Kerley (1993) and Thompson and Lausen (1972). The polynomial fits to the upper and lower confidence bounds of the entropy along the principal Hugoniot, respectively, are given by:

$$S_U = -1.845 \times 10^4 \times P^{-1/2} + 45.7 \times P^{1/2} - 0.1193 \times P + 2270, \tag{B.9}$$

$$S_L = -2.631 \times 10^4 \times P^{-1/2} + 22.33 \times P^{1/2} - 0.007689 \times P + 2804. \quad \text{(B.10)}$$

The core temperatures of planetesimals will be elevated for long timescales due to the energy of accretion and the decay of short-lived isotopes. The higher starting entropy state will lead to a higher entropy state in the fluid for a given shock pressure, effectively decreasing the critical pressure for vaporization upon release. To treat the higher initial temperature, we use the model SESAME 2150 Hugoniot of iron at an initial pressure of 1 GPa and 1500 K, and again subtracted 171.7 J kg^{-1} K^{-1} to account for the higher model entropy in the SESAME 2150 equation of state at ∼500 GPa. A polynomial fit to the entropy along the iron Hugoniot, with a 1 GPa and 1500 K initial state, is

$$S = -1.257 \times 10^4 \times P^{-1/2} + 45.24 \times P^{1/2} - 0.1321 \times P + 2038, \quad \text{(B.11)}$$

where the critical pressure for incipient vaporization upon release to 1 bar has decreased to ∼390 GPa.

B.2.2 Impact Velocity to Vaporize Iron

To determine the percentage of iron core vaporized as a function of impact velocity, Figure 3 in the main text, we used the planar impact approximation of a differentiated planetesimal impacting the mantle of the proto-Earth. We assumed the mantles to be composed of enstatite. The Hugoniot for enstatite was obtained from Spaulding et al. (2012),

$$U_s = 5.1(1.1) + 1.15(9)u_p, \quad \text{(B.12)}$$

which is the best fit over a particle velocity range of 8 to 14 km s^{-1}.

The shock state in the iron was then obtained by impedance matching the initial shock state in the enstatite mantle to the iron Hugoniot presented in Section B.1.6. For a given shock pressure in the iron, the entropy at that pressure was obtained using Equation B.8. The vapor fraction upon decompression to 1 bar was then determined using the lever rule and reference liquid and vapor entropies of 2240 and 4238 J kg^{-1} K^{-1}, respectively Chase (1998).

B.2.3 Iron Penetration and Vapor Expansion Velocities

If the planetesimal or embryo core penetrates through the mantle, then metal-silicate equilibration will be limited. Penetration depth is a function of size and velocity and may be estimated by crater formation scaling laws O'Keefe and Ahrens (1993) as long as the planetesimal is much smaller than the proto-Earth. Considering head-on impacts with a penetration depth of the present mantle thickness, we calculate a nominal limit to the size planetesimal that may be deposited within the mantle assuming approximately equal densities for the planetesimal and mantle, shown below Figure 3B in the main text. Impactors with diameters smaller than the size limit for each impact velocity will form transient craters in the mantle lined by impactor material. If the iron core (or silicate matrix of an undifferentiated body) achieves vaporization, impactor core (or bulk impactor) will expand out of the transient crater and be dispersed widely, enabling a greater degree of chemical equilibration with the mantle.

Upon vaporization, we estimate the particle velocities achieved upon adiabatic expansion of iron from a state on the liquid-vapor dome to a final pressure of 1 Pa using the SESAME 4272 equation of state Lyon and Johnson (1992), shown in Figure B.8. On Earth, the vaporized iron would be widely dispersed but remain gravitationally bound. Thus we define a range of impact parameters, bounded approximately by impact velocities >15 km s^{-1} and diameters smaller than ∼1000 km,

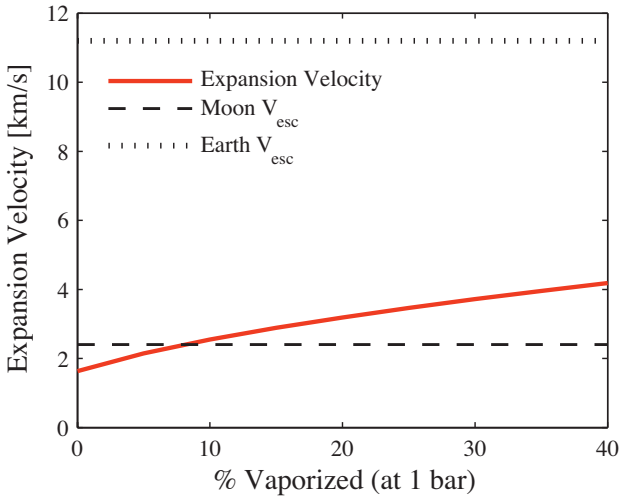

Figure B.8: Velocity change upon isentropic expansion from a state on the liquid vapor dome to a reference pressure of 1 Pa. The model liquid-vapor dome is from the SESAME 4272 equation of state model Lyon and Johnson (1992). The abscissa is defined by the isentrope that would reach the defined percentage of vapor at 1 bar.

where metal-silicate chemical equilibration would be enhanced by shock-induced vaporization of iron during the period of terrestrial core formation.

The estimated iron vapor expansion velocities are sufficient to escape the Moon. Material loss by adiabatic expansion is a bulk ejection process that would not fractionate iron isotopes. During late accretion, a large fraction of planetesimals impact fast enough to vaporize iron cores (Figure 3B in main text). Iron and highly siderophile elements (HSEs) would be preferentially lost from the Moon but retained on the Earth, contributing to the lower than expected concentration of HSEs in the Moon.

Acknowledgments: Sandia National Laboratories is a multi-program laboratory managed and operated by Sandia Corporation, a wholly owned subsidiary of Lockheed Martin Corporation, for the U.S. Department of Energy's National Nuclear Security Administration under Contract No. DE-AC04-94AL85000.

Disclaimer: This report was prepared as an account of work sponsored by an agency of the United States Government. Neither the United States Government nor any agency thereof, nor any of their employees, makes any warranty, express or implied, or assumes any legal liability or responsibility for the accuracy, completeness, or usefulness of any information, apparatus, product, or process disclosed, or represents that its use would not infringe privately owned rights. Reference herein to any specific commercial product, process, or service by trade name, trademark, manufacturer, or otherwise does not necessarily constitute or imply its endorsement, recommendation, or favoring by the United States Government or any agency thereof. The views and opinions of authors expressed herein do not necessarily state or reflect those of the United States Government or any agency thereof.

Appendix C

Additional calculations for Chapter 5

The following appendix contains:

1. Table C.1 provides shock wave equation of state parameters used in impedence match solution to determine peak pressure in shocked mixture.
2. Figure C.4 showing visible and near-infrared radiance data and fits from 7.9 GPa experiment.
3. Figure C.1 showing visible and near-infrared radiance data and fits from 12.9 GPa experiment.
4. Figure C.2 showing visible and near-infrared radiance data and fits from 16.2 GPa experiment.
5. Figure C.3 showing post-shock radiance data and fits from 18.5 GPa experiment.
6. Figure C.5 showing solution to one-dimensional thermal diffusion equation for H_2O-SiO_2 interface.
7. Figure C.6 showing idealized one-dimensional diagram of radiating mixture used to derive the emissivity and area fraction of H_2O
8. Text C.1 derives the one-dimensional radiation absorption analysis used in multi-component hotspot fit.
9. Text C.2 provides experimental details.

Table C.1: Hugoniot equation of state ($U_s = C_0 + su_p$) used in impedence match solution for peak shock pressure in mixture. The release isentrope of the driver is assumed to be the reflected Hugoniot.

Material	ρ_0 [g/cm^3]	C_0 [km/s]	s	Reference
304 Stainless Steel (flyer)	7.896	4.569	1.49	Steinberg (1991)
Al-2024 (driver)	2.785	5.23	1.32	Steinberg (1991)

C.1 Radiative Transfer Model for the Mixture

From Kirchoff's law we know that the emissivity is related to the coefficient of absorption 'a' by Equation (C.1), where d is the thickness of the radiating material.

$$\epsilon = 1 - e^{-ad} \tag{C.1}$$

Now consider the one-dimensional geometry of alternating plates of H_2O and SiO_2, as shown in Figure C.6; the H_2O and SiO_2 have absorption coefficients of a_H and a_S, respectively. Heat the plates so they begin emitting thermal radiation. The emitted radiation from the free surface of the mixture will be the superposition of light emitted from the individual layers, $\epsilon_H L_H$ and $\epsilon_S L_S$ respectively, minus the light absorbed by the layers in the path of the radiation. Neglecting internal reflections, the radiance emitted from such a surface, L_ϵ, is described by Equation (C.2), where $\epsilon_i = \left(1 - e^{-a_i d_i}\right)$, and d_i is the thickness of plate type 'i'.

$$\begin{aligned} L_\epsilon = {} & L_S\epsilon_S + L_H\epsilon_H e^{-a_S d_S} + L_S\epsilon_S e^{-a_H d_H} e^{-a_S d_S} \\ & + L_H\epsilon_H e^{-2a_S d_S} e^{-a_H d_H} + L_S\epsilon_S e^{-2a_H d_H} e^{-2a_S d_S} + \ldots \end{aligned} \tag{C.2}$$

Assuming there are '$2N$' plates, one can separate the sum over the radiation emitted from the

separate types of plates, shown in Equation (C.3).

$$L_\epsilon = L_S \epsilon_S \sum_{n=0}^{N-1} e^{-na_H d_H} e^{-na_S d_S} + L_H \epsilon_H e^{-a_S d_S} \sum_{n=0}^{N-1} e^{-na_H d_H} e^{-na_S d_S} \tag{C.3}$$

However, this sum is simply a finite geometric series of the form $\sum_0^{N-1} Ra^n$, which can be simplified to the form shown in Equation (C.4).

$$L_\epsilon \approx L_S \epsilon_S \frac{\left(1 - e^{-Na_H d_H} e^{-Na_S d_S}\right)}{\left(1 - e^{-a_H d_H} e^{-a_S d_S}\right)} + L_H \epsilon_H e^{-a_S d_S} \frac{\left(1 - e^{-Na_H d_H} e^{-Na_S d_S}\right)}{\left(1 - e^{-a_H d_H} e^{-a_S d_S}\right)} \tag{C.4}$$

This expression is not sufficient to describe emission from a mixture that is heterogeneous in three dimensions as there is an asymmetric term related to whichever plate is at the free surface, this term being $e^{-a_s d_s}$ in Equation (C.4) derived for the geometry shown in Figure C.6. To fully describe emission from an isothermal mixture of H_2O and SiO_2 one could envision the case where columns of alternating plates are stacked adjacent to each other in such a way that the physical area fractions of H_2O and SiO_2 at the free surface, α_H^P and α_S^P, match what would be measured experimentally if the real samples of H_2O and SiO_2 were sectioned and analyzed to determine relative area fractions. As we can measure the relative volume fractions of H_2O and SiO_2, V_H and V_S, for the samples used in the experiments, we can determine their relative area fractions using Equation (C.5) and the fact that the area fractions must add up to one.

$$\frac{\alpha_H^P}{\alpha_S^P} = \left(\frac{V_H}{V_S}\right)^{\frac{2}{3}} \tag{C.5}$$

By combining Equations (C.4) and (C.5), we can fully describe emission from a heterogeneous isothermal mixture of H_2O and SiO_2, shown in the follow equation.

$$L_\epsilon = \alpha_S^P \left[L_S \epsilon_S \frac{\left(1 - e^{-Na_H d_H} e^{-Na_S d_S}\right)}{\left(1 - e^{-a_H d_H} e^{-a_S d_S}\right)} + L_H \epsilon_H e^{-a_S d_S} \frac{\left(1 - e^{-Na_H d_H} e^{-Na_S d_S}\right)}{\left(1 - e^{-a_H d_H} e^{-a_S d_S}\right)} \right] + \alpha_H^P \left[L_S \epsilon_S e^{-a_H d_H} \frac{\left(1 - e^{-Na_H d_H} e^{-Na_S d_S}\right)}{\left(1 - e^{-a_H d_H} e^{-a_S d_S}\right)} + L_H \epsilon_H \frac{\left(1 - e^{-Na_H d_H} e^{-Na_S d_S}\right)}{\left(1 - e^{-a_H d_H} e^{-a_S d_S}\right)} \right] \quad \text{(C.6)}$$

With regards to a shock wave experiment, we have discussed in the paper how the radiation emitted from the SiO_2 grains is insignificant with respect to the radiation emitted from the H_2O because of the much lower temperature in the SiO_2. This reasonable assumption of neglecting the radiation emitted from the SiO_2 significantly reduces the complexity of L_ϵ.

$$L_\epsilon = \left(\alpha_H^P + \alpha_S^P e^{-a_S d_S}\right) L_H \epsilon_H \frac{\left(1 - e^{-Na_H d_H} e^{-Na_S d_S}\right)}{\left(1 - e^{-a_H d_H} e^{-a_S d_S}\right)}. \quad \text{(C.7)}$$

From Equation (C.7) we can define the effective area fraction of H_2O, Eqn. (C.8), which we denote as the radiative area fraction, α_H^R, in the paper. The dependence of the radiative area fraction of H_2O on the absorption coefficient of SiO_2 can be understood by looking at the end-member cases. If the SiO_2 has a very low absorption, the radiative area fraction of the ice will be approximately 1 as radiation from the H_2O directly behind the SiO_2 grains will also emit radiation from the shock front. If the SiO_2 has an extremely high absorption coefficient, then the radiative area fraction will equal the physical area fraction, $\alpha_{H_2O}^P$, as the SiO_2 particles will absorb all the radiation from the H_2O directly behind.

$$\alpha_H^R = \left(\alpha_H^P + \alpha_S^P e^{-a_S d_S}\right) \quad \text{(C.8)}$$

We can also define the effective emissivity for H_2O, ϵ_H^*, seen in Equation (C.9). Here we have used the substituted the total thickness of the radiating H_2O and SiO_2 components, D_H and D_S, for

$N \times d_H$ and $N \times d_S$, respectively.

$$\epsilon_H^* = \left(1 - e^{-a_H D_H} e^{-a_S D_S}\right) \frac{\epsilon_H}{\left(1 - e^{-a_H d_H} e^{-a_S d_S}\right)} \tag{C.9}$$

C.2 Experimental Details

An off-axis Al-coated parabolic mirror collects and collimates radiance emitted from the downrange face of the sample through a CaF_2 window in the sample vacuum chamber. The mirror also focuses the incident and collects the reflected laser light for the velocity inteferometer (VISAR). The window through the target tank is Al_2O_3 protected by CaF_2. The collimated light is split with two dichroic beamsplitters between the Los Alamos near-infrared (NIR) pyrometer, the Ktech Model VMBV-04 velocity interferometer, and the Thorlabs Model PDA10A amplified Si diode visible detectors. The infrared pyrometer is sensitive to radiance temperatures as low as 300 K with a time resolution of 17 ns. The silicon diodes have a time resolution of 3 ns, and the visible filters were centered at 650 and 810 nm with full width half maximum of 100 and 30 nm, respectively. Emitted light is spatially filtered with a 17 mm diameter aperture so as to only collect light from the shocked sample. The optical path is enclosed in light-tight tubing to shield from the impact flash and propellant gases during the experiment. The system is calibrated with a Mikron M360 black body source (for the NIR) and an Optronic Laboratories OL-550 tungsten ribbon lamp (for the Si diode detectors), which are observed with the same optics and fibers as used in the experiments. The typical error in radiance is 2% at each wavelength. The NIR pyrometer data are recorded on 12-bit digitizers (e.g., Acqiris DC 440). The driver plate is lapped plane parallel and polished to an optical ($\sim$ 100 nm) finish to minimize thermal emission upon shock (Seifter et al., 2006). In two experiments (7.9 and 22.7 GPa), the ice-quartz mixtures were cold pressed directly onto the driver plate to reduce the gap between the driver and sample. The sample is affixed mechanically to the driver plate,

which is cooled to ~ 100 K by circulating liquid nitrogen. Initial temperatures of the samples were determined by a thermocouple on the driver plate. When the temperature of both the sample and driver are measured, the temperature deviation is typically less than 5 K. The sample vacuum chamber CaF_2 window is heated to prevent frosting. The velocity per fringe of the VISAR was 1896 m s^{-1}; two dropped fringes were added to the 22.7 GPa experiment presented in Figure 7. The VISAR spot size was large enough to average over ~ 8 grains.

In the 18.5 GPa experiment, the SiO_2 was compacted and saturated with water, and then frozen in a manner similar to the preparation of polycrystalline columnar ice, as in Stewart et al. (2008). This preparation method produced a 40:60 H_2O to SiO_2 volumetric ratio with higher porosity than the evacuated cold press technique described in the main text. In this case, emission from trapped air prevented derivation of the shock temperature.

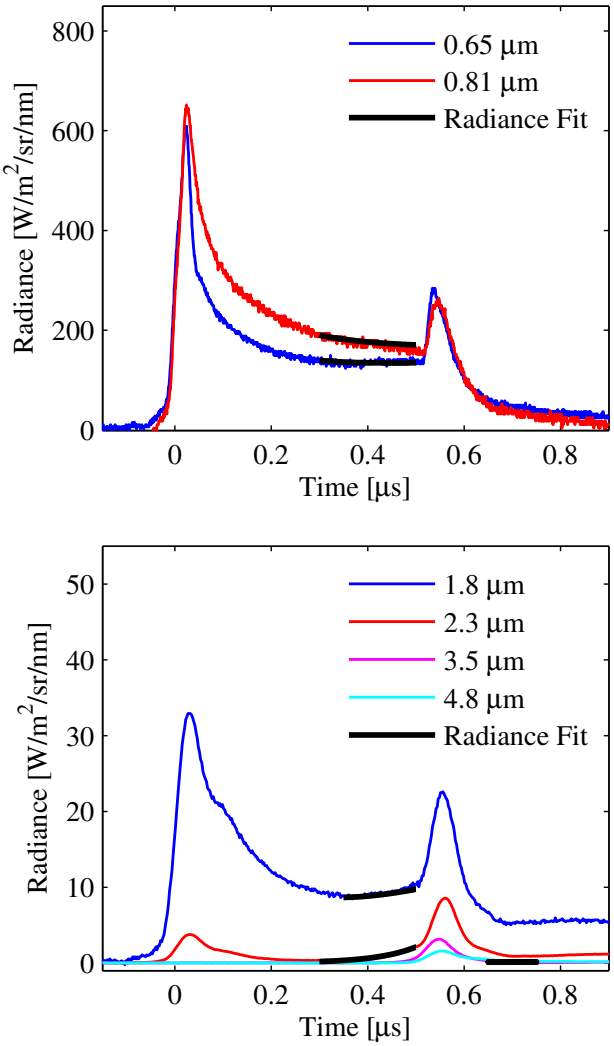

Figure C.1: Thermal radiation emitted from a mixture of H_2O and SiO_2 subjected to a 12.9 GPa planar shock wave. For 0.65, 0.81, 1.8, and 2.3 μm, black lines are fits using equation 2. For 3.5 and 4.8 μm, black lines denote time interval used to determine post-shock temperatures.

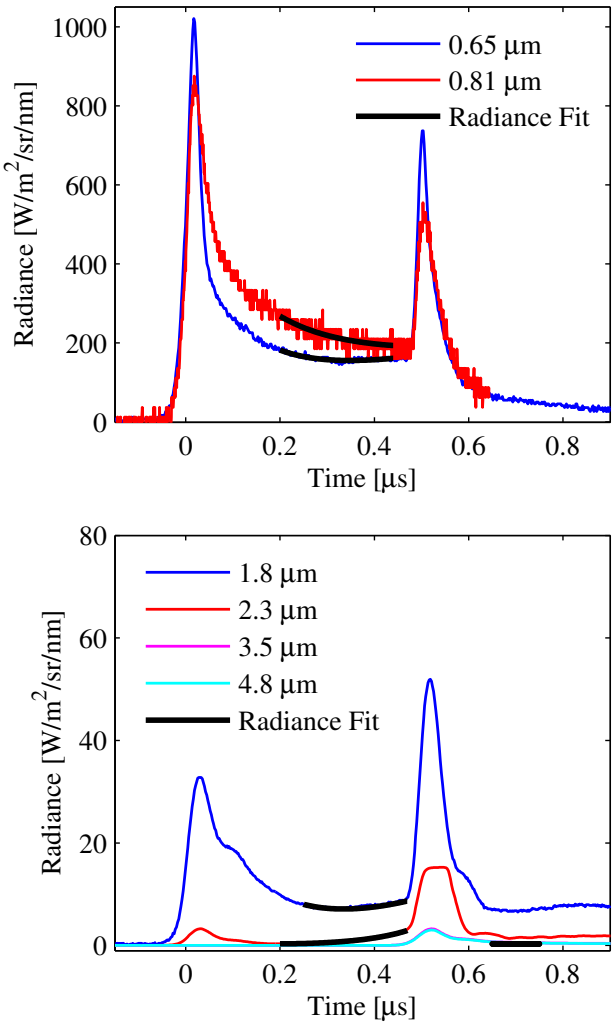

Figure C.2: Thermal radiation emitted from a mixture of H_2O and SiO_2 subjected to a 16.2 GPa planar shock wave. For 0.65, 0.81, 1.8, and 2.3 μm, black lines are fits using equation 2. For 3.5 and 4.8 μm, black lines denote time interval used to determine post-shock temperatures.

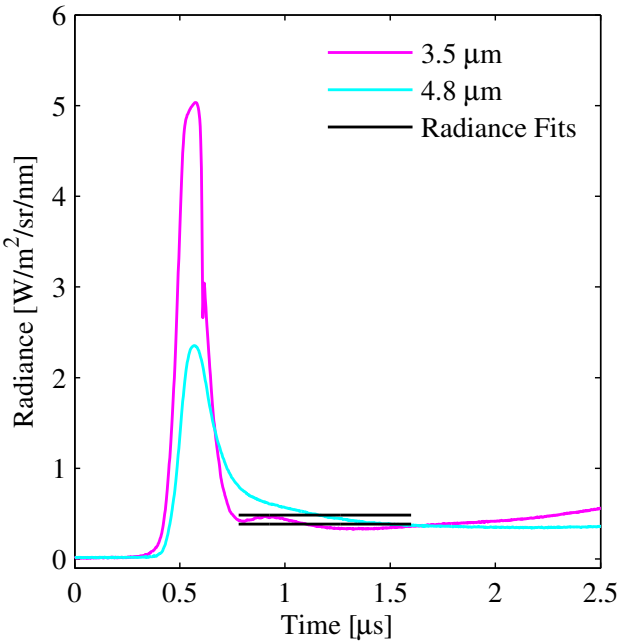

Figure C.3: Post-shock thermal radiation emitted from a 40:60 volumetric mixture of H_2O and SiO_2 subjected to a 18.5 GPa planar shock wave. For 3.5 and 4.8 μm, black lines denote time interval used to determine post-shock temperatures. Detectors were saturated at shorter wavelength channels and consequently a shock temperature could not be obtained.

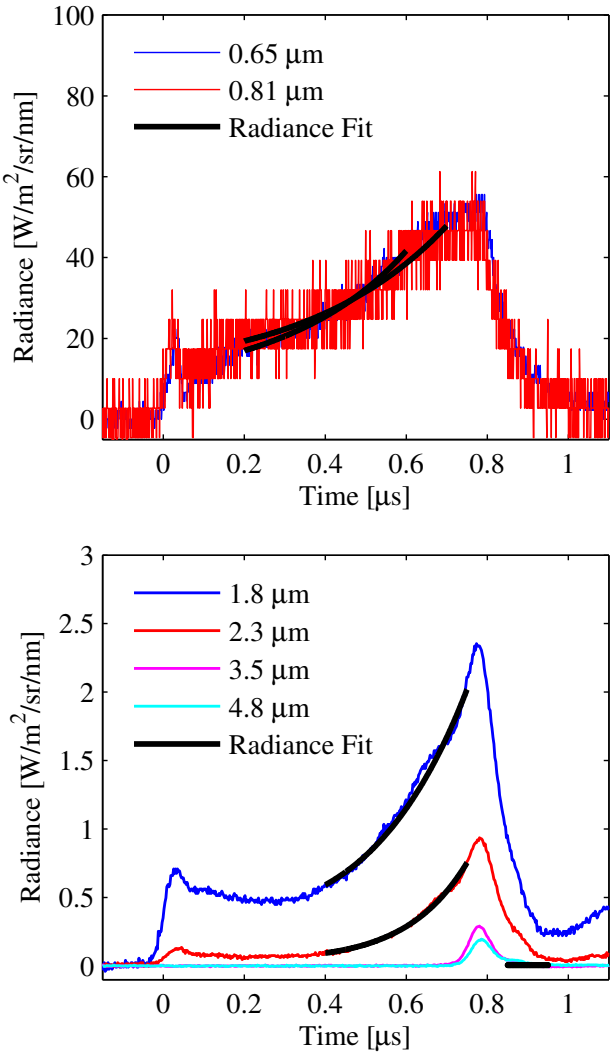

Figure C.4: Thermal radiation emitted from a mixture of H_2O and SiO_2 subjected to a 7.9 GPa planar shock wave. For 0.65, 0.81, 1.8, and 2.3 μm, black lines are fits using equation 2. For 3.5 and 4.8 μm, black lines denote time interval used to determine post-shock temperatures.

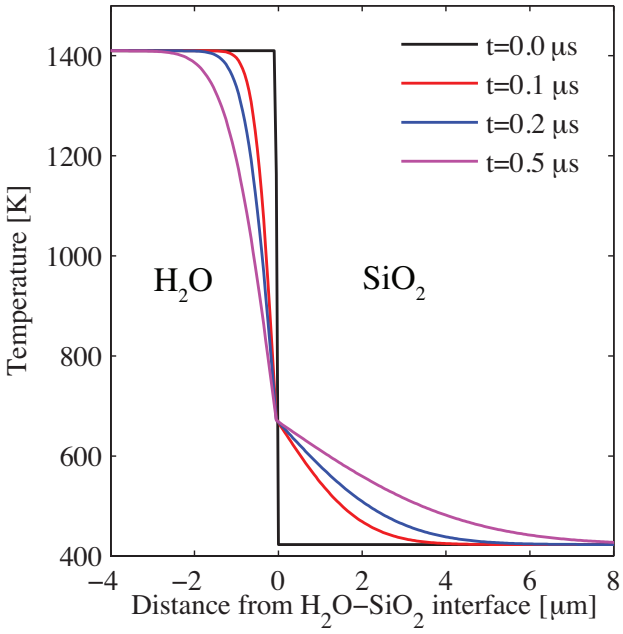

Figure C.5: Numerical solution to the thermal diffusion equation across an interface between H_2O and SiO_2, accounting for their different thermal transport properties. Initial conditions were 22.7 GPa and the shock temperature on the principal Hugoniot of each component. The shock temperature in the H_2O was determined from the 5-phase equation of state model for H_2O (Senft and Stewart, 2008), and the shock temperature in the SiO_2 was taken from calculations by Wackerle (1962). The temperature at the interface was solved exactly using the method described in Carslaw and Jaeger (1946), and the temperatures within the H_2O and SiO_2 were determined by integrating the thermal diffusion equation by a first-order accurate finite difference technique. Note that the conclusion that thermal diffusion is negligible during the experiment is robust to a wide variations in material parameters.

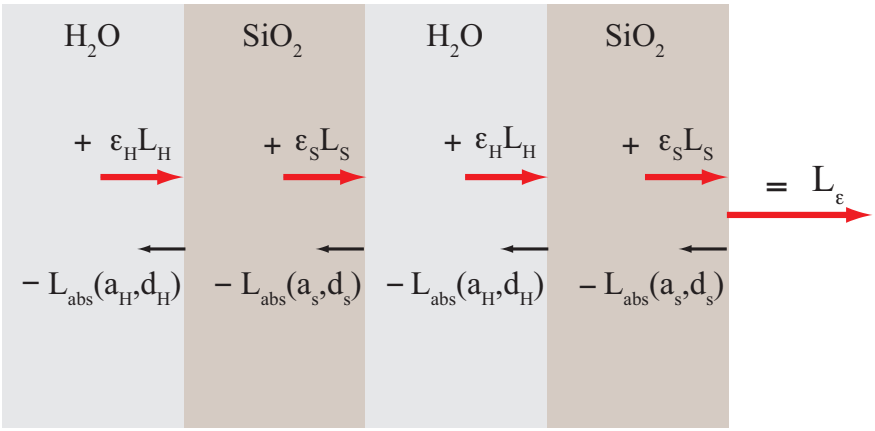

Figure C.6: Schematic of one-dimensional radiation absorption (black arrows pointing to the left) and radiance emitted (red arrows pointing to the right) in a mixture of H_2O and SiO_2. The radiance from the free surface, L_ϵ, is the sum of the radiation emitted from each cell of H_2O and SiO_2, $\epsilon_H L_H$ and $\epsilon_S L_S$, minus the radiation absorbed by each cell of H_2O and SiO_2, $L_{abs}(a_H, d_H)$ and $L_{abs}(a_S, d_S)$ respectively. Here a_H and a_S are the wavelength dependent optical absorption coefficients in H_2O and SiO_2, respectively, and d_H and d_S are the average thicknesses of the cells of H_2O and SiO_2, respectively.

Bibliography

Abramson, E., Brown, J., Slutsky, L., 2001. The thermal diffusivity of water at high pressures and temperatures. J. Chem. Phys 115 (22), 1046110463, doi:10.1063/1.1418244.

Ageev, V. G., Bushman, A. V., Kulish, M. I., Lebedev, M. E., Leontev, A. A., Ternovoi, V. Y., Filimonov, A. S., Fortov, V. E., 1988. Thermodynamics of a dense lead plasma near the high-temperature boiling curve. JETP Letters 48 (11), 659–663.

Agnor, C. B., Canup, R. M., Levison, H. F., 1999. On the character and consequences of large impacts in the late stage of terrestrial planet formation. Icarus 142, 219–237, doi:10.1006/icar.1999.6201.

Ahrens, T., 1993. Impact erosion of terrestrial planetary atmospheres. Annu. Rev. Earth Planet. Sci. 21, 525–555, doi:10.1146/annurev.ea.21.050193.002521.

Ahrens, T., O'Keefe, J., 1977. Equations of state and impact-induced shock-wave attenuations on the Moon. In: Roddy, D., Pepin, R., Merrill, R. (Eds.), Impact and Explosion Cratering. Pergamon, Oxford, pp. 639–656.

Ahrens, T., O'Keefe, J., 1985. Shock vaporization and the accretion of the icy satellites of Jupiter and Saturn. In: Klinger, J. (Ed.), Ices in the Solar System. D. Reidel Publishing Co., Dordrecht, pp. 631–654.

Ahrens, T., O'Keefe, J., 1987. Impact on the Earth, ocean, and atmosphere. Int. J. Impact Engng. 5, 13–32.

Ahrens, T. J., 1987. Shock wave techniques for geophysics and planetary physics. In: Sammis, C. G., Henyey, T. L. (Eds.), Methods of Experimental Physics, vol 24, part A. Academic Press, New York, pp. 185–235.

Ahrens, T. J., Johnson, M. L., 1995a. Shock wave data for minerals. In: Ahrens, T. J. (Ed.), Mineral Physics and Crystallography, A Handbook of Physical Constants, Vol. 2. American Geophysical Union, Washington, D. C., pp. 143–184.

Ahrens, T. J., Johnson, M. L., 1995b. Shock wave data for rocks. In: Ahrens, T. J. (Ed.), Rock Physics and Phase Relations, A Handbook of Physical Constants, Vol. 3. American Geophysical Union, Washington, D. C., pp. 35–44.

Ahrens, T. J., O'Keefe, J. D., 1972. Shock melting and vaporization of lunar rocks and minerals. The Moon 4 (1-2), 214–249, DOI:10.1007/BF00562927.

Akaogi, M., Yusa, H., Shiraishi, K., Suzuki, T., 1995. Thermodynamic properties of α-quartz, coesite, and stishovite and equilibrium phase relations at high pressures and high temperatures. Journal of Geophysical Research 100 (B11), 22337–22347, doi:10.1029/95JB02395.

Akins, J. A., Ahrens, T. J., 2002a. Dynamic compression of SiO_2: A new interpretation. Geophysical Research Letters 29 (10), 31, doi:10.1029/2002GL014806.

Akins, J. A., Ahrens, T. J., 2002b. Dynamic compression of SiO_2: A new interpretation. Geophys. Res. Lett. 29 (10), 1394, doi:10.1029/2002GL014806.

Alexander, C. S., Vogler, T. J., Thornhill, T. F., Reinhart, W. D., 2010. Expansion of a tungsten carbide-epoxy composite following hypervelocity impact. In: Proceedings of the 11^{th} Hypervelocity Impact Symposium. Fraunhofer Verlag, Freiburg, Germany, pp. 96–110.

Al'tshuler, L., Trunin, R. F., Krupnikov, K., Panov, N. V., 1996. Explosive laboratory devices for shock wave compression studies. Physics-Uspekhi 39, 539–544.

Al'tshuler, L. V., Pavlovskii, M. N., 1971. Response of clay and clay shale to heavy dynamic loading. Journal of Applied Mechanics and Technical Physics 1, 161–165.

Anderson, J., Schultz, P., Heineck, J., 2004. Experimental ejection angles for oblique impacts: Implications for subsurface flow-field. Meteoritics & Planetary Science 39 (2), 303–320.

Anderson, O. L., 1995. Equations of state of solids for geophysics and ceramic science. Oxford University Press, New York.

Anderson, W. W., 1997. Properties of shocked aerogel. In: Proc. Lunar Planet. Sci. Conf. Abs. 1833.

Anzellini, S., Dewaele, A., Mezouar, M., Loubeyre, P., Morard, G., 2013. Melting of iron at earths inner core boundary based on fast x-ray diffraction. Science 340 (6131), 464–466, DOI:10.1126/science.1233514.

Artemieva, N., Lunine, J., 2003. Cratering on Titan: impact melt, ejecta, and the fate of surface organics. Icarus 164 (2), 471–480, doi:10.1016/S0019-1035(03)00148-9.

Artemieva, N., Lunine, J. I., 2005. Impact cratering on Titan II. global melt, escaping ejecta, and aqueous alteration of surface organics. Icarus 175 (2), 522–533.

Artemieva, N. A., Shuvalov, V. V., 2008. Numerical simulation of high-velocity impact ejecta following falls of comets and asteroids onto the moon. Solar System Research 42 (4), 329–334, DOI:10.1134/S0038094608040059.

Asay, J., Shahinpoor, M., 1993. High-Pressure Shock Compression of Solids. Springer-Verlag, New York.

Asay, J. R., Trucano, T. G., 1990. Studies of density distributions in one-dimensional shock-induced debris clouds. International Journal of Impact Engineering 10 (1-4), 35–50, doi:10.1016/0734-743X(90)90047-Y.

Bakanova, A., Dudoladov, I. P., Zhernokletov, M. V., Zubarev, V. N., Simakov, G. V., 1983. Vaporization of shock-compressed metals on expansion. Journal of Applied Mechanics and Technical Physics 24 (2), 204–209, doi:10.1007/BF00910688 (Translated from Zhurnal Prikladnoi Mekhaniki i Tekhnicheskoi Fiziki 2, 76-81, 1983.).

Bakanova, A., Zubarev, V., Sutulov, Y., Trunin, R., 1975. Thermodynamic properties of water at high pressures and temperatures. Soviet Physics JETP 41 (3), 544–548.

Balluffi, R. W., Allen, S. M., Carter, W. C., Kemper, R. A., 2005. Kinetics of Materials. John Wiley and Sons, Hoboken, NJ.

Barker, L. M., 1971. A model for stress wave propagation in composite materials. J. Composite Materials 5, 140–162.

Barker, L. M., Hollenbach, R. E., 1972. Laser interferometer for measuring high velocities of any reflecting surface. Journal of Applied Physics 43, 4669–4675, DOI:10.1063/1.1660986.

Barr, A., Citron, R., 2011. Scaling of melt production in hypervelocity impacts from high-resolution numerical simulations. ICARUS 211, 913–916, doi:10.1016/j.icarus.2010.10.022.

Barr, A. C., Canup, R. M., 2010. Origin of the Ganymede-Callisto dichotomy by impacts during the late heavy bombardment. Nat. Geosci 3 (3), 164–167.

Benlow, A., Meadows, A., 1977. The formation of the atmospheres of the terrestrial planets by impact. Astrophys. Space Sci. 46, 293–300, doi:10.1007/BF00644376.

Benz, W., Anic, A., Horner, J., Whitby, J. A., 2007. The Origin of Mercury. Solar System Reviews 132, 189–202, doi:10.1007/s11214-007-9284-1.

Benz, W., Cameron, A., 1989. The origin of the moon and the single-impact hypothesis III. Icarus 81, 113–131.

Benz, W., Slattery, W. L., Cameron, A. G. W., 1986. The origin of the moon and the single-impact hypothesis .1. Icarus 66 (3), 515–535.

Benz, W., Slattery, W. L., Cameron, A. G. W., 1988. Collisional stripping of Mercury's mantle. Icarus 74 (3), 516–528, doi:10.1016/0019-1035(88)90118-2.

Beutl, M., Pottlacher, G., Jager, H., 1994. Thermophysical properties of liquid iron. International Journal of Thermophysics 15 (6), 1323–1331, DOI:10.1007/BF01458840.

Bibring, J.-P., Langevin, Y., Mustard, J. F., Poulet, F., Arvidson, R., Gendrin, A., Gondet, B., Mangold, N., Pinet, P., Forget, F., the OMEGA team, Berth, M., Bibring, J.-P., Gendrin, A., Gomez, C., Gondet, B., Jouglet, D., Poulet, F., Soufflot, A., Vincendon, M., Combes, M., Drossart, P., Encrenaz, T., Fouchet, T., Merchiorri, R., Belluci, G., Altieri, F., Formisano, V., Capaccioni, F., Cerroni, P., Coradini, A., Fonti, S., Korablev, O., Kottsov, V., Ignatiev, N., Moroz, V., Titov, D., Zasova, L., Loiseau, D., Mangold, N., Pinet, P., Dout, S., Schmitt, B., Sotin, C., Hauber, E., Hoffmann, H., Jaumann, R., Keller, U., Arvidson, R., Mustard, J. F., Duxbury, T., Forget, F., Neukum, G., 2006. Global mineralogical and aqueous Mars history derived from OMEGA/Mars express data. Science 312 (5772), 400–404, doi:10.1126/science.1122659.

Birch, F., 1952. Elasticity and constitution of the earth's interior. Journal of Geophysical Research 57 (2), 227–286, doi:10.1029/JZ057i002p00227.

Bjorkman, M., Holsapple, K., 1987. Velocity scaling impact melt volume. Int. J. Impact Engng. 5, 155–163.

Blochl, P. E., 1994. Projector augmented-wave method. Physical Review B 54, 17953–17979, doi:10.1103/PhysRevB.50.17953.

Boboridis, K., Seifter, A., Obst, A. W., 2003. High-speed infrared pyrometry for surface temperature measurements on shocked solids. VDI-Bericht 1784, 119–126.

Boca, M., Kucharik, M., Vasiljev, R., Danek, V., 2003. Surface tension of melts of the system KF-K_2MoO_4-SiO_2. Chemical Papers-Chemicke Zvesti 57 (2).

Boslough, M. B., 1985. A model for time dependence in shock-induced thermal radiation of light. J. Appl. Phys. 58 (9), 3394–3399, doi:10.1063/1.335756.

Boslough, M. B., 1988. Postshock temperatures in silica. Journal of Geophysical Research 93 (B6), 6477–6484, doi:10.1029/JB093iB06p06477.

Boslough, M. B., Venturini, E. L., Morosin, B., Graham, R. A., Williamson, D. L., 1986. Physical-properties of shocked and thermally altered nontronite - implications for the martian surface. Journal of Geophysical Research 91 (B13), E207–E217.

Boslough, M. B., Weldon, R. J., Ahrens, T. J., 1980. Impact-induced water loss from serpentine, nontronite and kernite. In: Proceedings of the 11th Lunar and Planetary Science Conference. pp. 2145–2158.

Bottke, W. F., Walker, R. J., Day, J. M. D., Nesvorny, D., Elkins-Tanton, L., 2010. Stochastic late accretion to earth, the moon, and mars. Science 330 (6010), 1527–1530, DOI:10.1126/science.1196874.

Bourne, N. K., Gray III, G. T., 2005. Computational design of recovery experiments for ductile metals. Proceedings of the Royal Society A-Mathematical Physical and Engineering Sciences 461 (2062), 3297–3312.

Bowden, E., Kondo, K., Ogura, T., Jones, A. P., Price, G. D., DeCarli, P. S., 2000. Loading path effects on the shock metamorphism of porous quartz. In: Lunar and Planetary Science Conference. Vol. 31. p. Abs. 1582.

Brown, J. M., Fritz, J. N., Hixson, R. S., 2000. Hugoniot data for iron. J. Appl. Phys. 88 (9), 5496–5498, DOI:10.1063/1.1319320.

Brygoo, S., Henry, E., Loubeyre, P., Eggert, J., Koenig, M., Loupias, B., Benuzzi-Mounaix, A., Le Gloahec, M. R., 2007. Laser-shock compression of diamond and evidence of a negative-slope melting curve. Nature Materials 6 (4), 274–277, doi:10.1038/nmat1863.

Canup, R. M., 2004. Simulations of a late lunar-forming impact. Icarus 168, 433–456, DOI:10.1016/j.icarus.2003.09.028.

Canup, R. M., 2005. A giant impact origin of Pluto-Charon. Science 307, 546–550, doi:10.1126/science.1106818.

Canup, R. M., Asphaug, E., 2001. Origin of the moon in a giant impact near the end of the earth's formation. Nature 412 (6848), 708–712, doi:10.1038/35089010.

Carr, M. H., Crumpler, L. S., Cutts, J. A., Greeley, R., Guest, J. E., Masursky, H., 1977. Martian impact craters and emplacement of the ejecta by surface flow. J. Geophys. Res. 82 (28), 4055–4065, doi:10.1029/JS082i028p04055.

Carslaw, H. S., Jaeger, J. C., 1946. Conduction of Heat in Solids. Oxford University Press, USA, New York, NY.

Celliers, P., Ng, A., 1993. Optical probing of hot expanded states produced by shock release. Physical Review E 47 (5), 3547–3565, doi:10.1103/PhysRevE.47.3547.

Celliers, P. M., Collins, G. W., Da Silva, L. B., Gold, D. M., Cauble, R., 1998. Accurate measurement of laser-driven shock trajectories with velocity interferometry. Applied Physics Letters 73 (10), 1320–1322, doi:10.1063/1.121882.

Celliers, P. M., Collins, G. W., Hicks, D. G., Koenig, M., Henry, E., Benuzzi-Mounaix, A., Batani, D., Bradley, D. K., Da Silva, L. B., Wallace, R. J., Moon, S. J., Eggert, J. H., Lee, K. K. M., Benedetti, L. R., Jeanloz, R., Masclet, I., Dague, N., Marchet, B., Le Gloahec, M. R., Reverdin, C., Pasley, J., Willi, O., Neely, D., Danson, C., 2004. Electronic conduction in shock-compressed water. Physics of Plasmas 11 (8), L41–L44, doi:10.1063/1.1758944.

Celliers, P. M., Loubeyre, P., Eggert, J. H., Brygoo, S., McWilliams, R. S., Hicks, D. G., Boehly, T. R., Jeanloz, R., Collins, G. W., 2010. Insulator-to-conducting transition in dense fluid helium. Physical Review Letters 104 (18), 184503, doi:10.1103/PhysRevLett.104.184503.

Chapman, C., McKinnon, W., 1986. Cratering of planetary satellites. In: Burns, J., Matthews, M. (Eds.), Satellites. University of Arizona Press, Tucson, pp. 492–580.

Chase, M. W., 1998. NIST-JANAF thermochemical tables. Monograph No. 9. American Institute of Physics, Washington, DC.

Chhabildas, L. C., Reinhart, W. D., Thornhill, T. F., Brown, J. L., 2006. Shock-induced vaporization in metals. International Journal of Impact Engineering 33 (1-12), 158–168, doi:10.1016/j.ijimpeng.2006.09.014.

Clérouin, J., Laudernet, Y., Recoules, V., Mazevet, S., 2005. Ab initio study of the optical properties of shocked LiF. Physical Review B 72, 155122, doi:10.1103/PhysRevB.72.155122.

Cockell, C. S., Bland, P. A., 2005. The evolutionary and ecological benefits of asteroid and comet impacts. Trends Ecol. Evol. 20 (4), 175–179.

Collins, G. S., Melosh, H. J., Ivanov, B. A., 2004. Modeling damage and deformation in impact simulations. Meteoritics & Planetary Science 39 (2), 217–231.

Croft, S., 1985. The scaling of complex craters. In: Ryder, G., Schubert, G. (Eds.), Proc. Lunar Planet. Sci. Conf. Vol. 15. p. 828.

Croft, S. K., 1980. Cratering flow fields - Implications for the excavation and transient expansion stages of crater formation. In: Bedini, S. (Ed.), Proc. Lunar Planet. Sci. Conf. Vol. 11. pp. 2347–2378.

Croft, S. K., 1982. A first-order estimate of shock heating and vaporization in oceanic impacts. In: Silver, L. T., Schultz, P. H. (Eds.), Geological implications of impacts of large asteroids and comets on the Earth. Vol. 190 of Geological Society Special Paper. pp. 143–152.

Croft, S. K., 1983. A proposed origin for palimpsests and anomalous pit craters on ganymede and callisto. In: Proc. Lunar Planet. Sci. Conf. Vol. 14. pp. 71–89.

Cuk, M., Stewart, S. T., 2012. Making the moon from a fast-spinning earth: A giant impact followed by resonant despinning. Science 338 (6110), 1047–1052, DOI:10.1126/science.1225542.

Dahl, T. W., Stevenson, D. J., 2010. Turbulent mixing of metal and silicate during planet accretion and interpretation of the Hf–W chronometer. Earth and Planetary Science Letters 295 (1), 177–186, DOI:10.1016/j.epsl.2010.03.038.

Dale, C. W., Burton, K. W., Greenwood, R. C., Gannoun, A., Wade, J., Wood, B. J., Pearson, D. G., 2012. Late accretion on the earliest planetesimals revealed by the highly siderophile elements. Science 336 (6077), 72–75, DOI:10.1126/science.1214967.

Davison, T., Collins, G., Ciesla, F., 2010. Numerical modelling of heating in porous planetesimal collisions. Icarus 208, 468–481.

de Koker, N., Stixrude, L., Karki, B. B., 2008. Thermodynamics, structure, dynamics, and freezing of Mg_2SiO_4 liquid at high pressure. Geochimica et Cosmochimica Acta 72, 1427–1441, doi:10.1016/j.gca.2007.12.01.

DeCarli, P. S., Bowden, E., Jones, A. P., Price, G. D., 2002. Laboratory impact experiments versus natural impact events. Geological Society of America Special Papers 356, 595–605, doi:10.1130/0-8137-2356-6.595.

Dolgoborodov, A. Y., Voskoboinkikov, I. M., Tolstov, I. K., Sudarikov, A. V., 1992. Anomalies of the propagation of shock waves in mixtures. Fizika Goreniya i Vzryva 28, 106–111.

Downing, H. D., Williams, D., 1975. Optical-constants of water in infrared. JGR 80 (12), 1656–1661, doi:10.1029/JC080i012p01656.

Dremin, A. N., Adadurov, G. A., 1964. The behavior of glass under dynamic loading. Soviet Physics-Solid State 6 (6), 1379–1384.

Dremin, A. N., Shvedov, K. K., 1964. Estimation of Chapman-Jouget pressure and time of reaction in detonation waves of powerful explosives. J. Appl. Mech. Tech. Phys. 2, 154–159.

Drummond, D., 1936. The infra-red absorption spectra of quartz and fused silica from 1 to 7.5 μm . II. experimental results. Proc. R. Soc. London, Ser. A 153 (879), 328–339.

Duffy, T. S., Ahrens, T. J., 1997. Dynamic compression of an Fe-Cr-Ni alloy to 80 GPa. Journal of Applied Physics 82, 4259–4269.

Dunaeva, A. N., Antsyshkin, D. V., 2010. Phase diagram of H_2O: Thermodynamic functions of the phase transitions of high-pressure ices. Solar System Research 44 (3), 202–222.

Duvall, G., Taylor, S.M., J., 1971. Shock parameters in a two component mixture. J. Composite Materials 5 (2), 130–139.

Ehlmann, B. L., Berger, G., Mangold, N., Michalski, J. R., Catling, D. C., Ruff, S. W., Chassefière, E., Niles, P. B., Chevrier, V., Poulet, F., 2013. Geochemical consequences of widespread clay mineral formation in Mars ancient crust. Space Science Reviews 174 (1-4), 329–364.

Friedlander, L. R., Glotch, T., Michalski, J. R., Sharp, T. G., Dyar, M. D., Bish, D. L., 2012. Spectroscopic studies of nontronite after impacts at 3 pressures. In: Lunar and Planetary Science Conference. Vol. 43. p. Abs. 2520.

Frost, R. L., Kloprogge, J. T., Ding, Z., 2002. The Garfield and Uley nontronites–An infrared spectroscopic comparison. Spectrochimica Acta Part A: Molecular and Biomolecular Spectroscopy 58 (9), 1881–1894, doi:10.1016/S1386-1425(01)00638-2.

Furukawa, Y., Sekine, T., Oba, M., Kakegawa, T., Nakazawa, H., 2009. Biomolecule formation by oceanic impacts on early earth. Nat. Geosc. 2 (1), 62–66.

Gathers, G. R., Shaner, J. W., Brier, R. L., 1976. Improved apparatus for thermophysical measurements on liquid metals up to 8000 K. Review of Scientific Instruments 47 (4), 471–479, doi:10.1063/1.1134657.

Gavin, P., Chevrier, V., 2010. Thermal alteration of nontronite and montmorillonite: Implications for the martian surface. Icarus 208, 721–734.

Gavin, P., Chevrier, V., Ninagawa, K., Gucsik, A., Hasegawa, S., 2013. Experimental investigation into the effects of meteoritic impacts on the spectral properties of phyllosilicates on Mars. Journal of Geophysical Research: Planets 118 (1), 65–80, doi:10.1029/2012JE004185.

Gillet, P., Lecleach, A., Madon, M., 1990. High-temperature Raman-spectroscopy of SiO_2 and GeO_2 polymorphs: Anharmonicity and thermodynamic properties at high-temperatures. Journal of Geophysical Research 95 (B13), 21635–21655, doi:10.1029/JB095iB13p21635.

Grady, D. E., 1988. The spall strength of condensed matter. Journal of the Mechanics and Physics of Solids 36, 353–384, doi:10.1016/0022-5096(88)90015-4.

Hartmann, W., Davis, D. R., 1975. Satellite-sized planetesimals and lunar origin. Icarus 24, 504–515.

Herrmann, W., 1969. Constitutive equation for the dynamic compaction of ductile porous materials. J. Appl. Phys. 40 (6), 2490–2499.

Hicks, D. G., Boehly, T. R., Celliers, P. M., Eggert, J. H., Vianello, E., Meyerhofer, D. D., Collins, G. W., 2005. Shock compression of quartz in the high-pressure fluid regime. Physics of Plasmas 12 (8), 082702, doi:10.1063/1.2009528.

Hicks, D. G., Boehly, T. R., Eggert, J. H., Miller, J. E., Celliers, P. M., Collins, G. W., 2006. Dissociation of liquid silica at high pressures and temperatures. Physical Review Letters 97 (2), 025502, doi:10.1103/PhysRevLett.97.025502.

Hicks, D. G., Celliers, P. M., Collins, G. W., Eggert, J. H., Moon, S. J., 2003. Shock-induced transformation of Al_2O_3 and LiF into semiconducting liquids. Physical Review Letters 91 (3), 035502, doi:10.1103/PhysRevLett.91.035502.

Hixson, R. S., Winkler, M. A., Hodgdon, M. L., 1990. Sound speed and thermophysical properties of liquid iron and nickel. Physical Review B 42 (10), 6485–6491, DOI:10.1103/PhysRevB.42.6485.

Hohenberg, P., Kohn, W., 1964. Inhomogeneous electron gas. Physical Review B 136 (3B), B864, doi:10.1103/PhysRev.136.B864.

Holmes, B., Tsou, F., 1972. Steady shock waves in composite materials. J. Appl. Phys. 43, 957–961.

Holsapple, K. A., 1993. The scaling of impact processes in planetary sciences. Annu. Rev. Earth Planet. Sci. 21, 333–373.

Holsapple, K. A., Schmidt, R. M., 1982. On the scaling of crater dimensions II-Impact processes. J. Geophys. Res. 87 (NB3), 1849–1870.

Holst, B., Redmer, R., Desjarlais, M. P., 2008. Thermophysical properties of warm dense hydrogen using quantum molecular dynamics simulations. Physical Review B 77 (18), doi:10.1103/PhysRevB.77.184201.

Hudon, P., Jung, I. H., Baker, D. R., 2002. Melting of beta-quartz up to 2.0 Gpa and thermodynamic optimization of the silica liquidus up to 6.0 Gpa. Physics of the Earth and Planetary Interiors 130 (3-4), 159–174, doi:10.1016/S0031-9201(02)00005-5.

Ioffe, A. F., Regel, A. R., 1960. In: Gibson, A. F., Kroger, F. A., Burgess, R. E. (Eds.), Progress in Semiconductors. Vol. 4. John Wiley and Sons, New York, p. 237.

Ivanov, B., Pierazzo, E., 2011. Impact cratering in H_2O bearing targets on Mars: Thermal field under craters as starting conditions for hydrothermal activity. Meteoritics & Planetary Science 46 (4), 601–619.

Ivanov, B. A., Langenhorst, F., Deutsch, A., Hornemann, U., 2002. How strong was impact-induced CO_2 degassing in the cretaceous-tertiary event? Numerical modeling of shock recovery experiments. In: Koeberl, C., MacLeod, K. (Eds.), Catastrophic Events and Mass Extinctions: Impacts and Beyond. Geological Society of America Special Paper 356, Boulder, CO, pp. 587–594.

Karki, B. B., Bhattarai, D., Stixrude, L., 2007. First-principles simulations of liquid silica: Structural and dynamical behavior at high pressure. Physical Review B 76 (10), doi:10.1103/PhysRevB.76.104205.

Kerley, G. I., 1993. Multiphase equation of state for iron. Tech. Rep. SAND93-0027, Sandia National Laboratories, Albuquerque, NM.

Kieffer, S., Getting, I., Kennedy, G., 1976. Experimental determination of the pressure dependence of the thermal diffusivity of teflon, sodium chloride, quartz, and silica. J. Geophys. Res. 81 (B17), 3018–3024, doi:10.1029/JB081i017p03018.

Kieffer, S. W., 1979. Thermodynamics and lattice-vibrations of minerals: 3. Lattice-dynamics and an approximation for minerals with application to simple substances and framework silicates. Reviews of Geophysics 17 (1), 35–59, doi:10.1029/RG017i001p00035.

Kieffer, S. W., 1980. Thermodynamics and lattice-vibrations of minerals: 4. Application to chain and sheet silicates and orthosilicates. Reviews of Geophysics 18 (4), 862–886.

Kieffer, S. W., 1982. Thermodynamics and lattice-vibrations of minerals: 5. Applications to phase-equilibria, isotopic fractionation, and high-pressure thermodynamic properties. Reviews of Geophysics 20 (4), 827–849, doi:10.1029/RG020i004p00827.

Kieffer, S. W., Delany, J. M., 1979. Isentropic decompression of fluids from crustal and mantle pressures. Journal of Geophysical Research 84 (B4), 1611–1620, doi:10.1029/JB084iB04p01611.

Kittel, C., Kroemer, H., 1980. Thermal Physics. W. H. Freeman and Company, New York.

Kleeman, J., Ahrens, T., 1973. Shock induced transition of quartz to stishovite. JGR 78, 5954–5960, doi:10.1029/JB078i026p05954.

Kleine, T., Touboul, M., Bourdon, B., Nimmo, F., Mezger, K., Palme, H., Jacobsen, S. B., Yin, Q. Z., Halliday, A. N., 2009. Hf-w chronology of the accretion and early evolution of asteroids and terrestrial planets. Geochimica Et Cosmochimica Acta 73 (17), 5150–5188, DOI:10.1016/j.gca.2008.11.047.

Knudson, M., Desjarlais, M., 2009. Shock compression of quartz to 1.6 TPa: Redefining a pressure standard. Phys. Rev. Lett. 103, 225501, DOI:10.1103/PhysRevLett.103.225501.

Knudson, M. D., Lemke, R. W., Hayes, D. B., A., H. C., Deeney, C., Asay, J. R., 2003. Near-absolute hugoniot measurements in aluminum to 500 gpa using a magnetically accelerated flyer plate technique. Journal of Applied Physics 94 (7), 4420–4431, DOI:10.1063/1.1604967.

Kondo, K., Ahrens, T. J., 1983. Heterogeneous shock-induced thermal-radiation in minerals. Phys. Chem. Miner. 9 (3-4), 173–181.

Kraus, R., Senft, L. E., Stewart, S. T., 2011. Impacts onto H_2O ice: Scaling laws for melting, vaporization, excavation, and final crater size. Icarus 214, 724–738, doi:10.1016/j.icarus.2011.05.016.

Kraus, R. G., Stewart, S. T., 2010. Impact induced melting and vaporization on icy planetary bodies. In: Lunar Planet. Sci. Conf. XLI. No. 2693.

Kraus, R. G., Stewart, S. T., Seifter, A., Obst, A. W., 2010. Shock and post-shock temperatures in an ice-quartz mixture: implications for melting during planetary impact events. Earth Planet. Sci. Lett. 289 (1-2), 162–170, DOI:10.1016/j.epsl.2009.11.002.

Kraus, R. G., Stewart, S. T., Swift, D. C., Bolme, C. A., Smith, R., Hamel, S., Hammel, B., Spaulding, D. K., Hicks, D. G., Eggert, J. H., Collins, G. W., 2012a. Shock vaporization of silica and the thermodynamics of planetary impact events. J. Geophys. Res. - Planets 117, E09009, DOI:10.1029/2012JE004082.

Kraus, R. G., Swift, D. C., Hicks, D. G., Stewart, S. T., 2012b. High accuracy equations of state for planetary collision modeling. In: Proc. Lunar Planet. Sci. Conf. Abs. 2649.

Kresse, G., Hafner, J., 1993. AB-initio molecular-dynamics for liquid-metals. Physical Review B 47 (1), 558–561, doi:10.1103/PhysRevB.47.558.

Krueger, B. R., Vreeland, T., 1991. A Hugoniot theory for solid and powder mixtures. J. Appl. Phys. 69 (2), 710–716.

Krupnikov, K., Bakanova, A. A., Brazhnik, M., Trunin, R. F., 1963. An investigation of the shock compressibility of titanium, molybdenum, tantalum, and iron. Sov. Phys. Doklady 8, 205–208.

Kurosawa, K., Kadono, T., Sugita, S., Shigemori, K., Hironaka, Y., Sano, T., Sakaiya, T., Ozaki, N., Shiroshita, A., Ohno, S., Cho, Y., Hamura, T., Fujioka, S., Tachibana, S., Vinci, T., Kodama, R., Matsui, T., 2012. Time-resolved spectroscopic observations of shock-induced silicate ionization. In: Butler, W., Elert, M., Furnish, M. (Eds.), Shock Compression of Condensed Matter - 2011. American Institute of Physics, Melville, New York, p. 855.

Kurosawa, K., Kadono, T., Sugita, S., Shigemori, K., Sakaiya, T., Hironaka, Y., Ozaki, N., Shiroshita, A., Cho, Y., Tachibana, S., Vinci, T., Ohno, S., Kodama, R., Matsui, T., 2012. Shock-induced silicate vaporization: The role of electrons. JJournal of Geophysical Researc–Planets 117, E04007, DOI10.1029/2011JE004031.

Kurosawa, K., Sugita, S., Kadono, T., Shigemori, K., Hironaka, Y., Otani, K., Sano, T., Shiroshita, A., Ozaki, N., Miyanishi, K., Sakaiya, T., Sekine, Y., Tachibana, S., Nakamura, K., Fukuzaki, S., Ohno, S., Kodama, R., Matsui, T., 2010. In-situ spectroscopic observations of silicate vaporization due to $>$ 10 km/s impacts using laser driven projectiles. Geophysical Research Letters 37, L23203, doi:10.1029/2010GL045330.

Kvitov, S. V., Bushman, A. V., Kulish, M. I., Lomonosov, I. V., Polishchuk, A. Y., Semenov, A. Y., Ternovoi, V. Y., Filimonov, A. S., Fortov, V. E., 1991. Measurements of the optical-emission of a dense bismuth plasma during its adiabatic expansion. JETP Letters 53 (7), 353–357.

Lamorgese, A. G., Mauri, R., 2009. Diffuse-interface modeling of liquid-vapor phase separation in a Van der Waals fluid. Physics of Fluids 21 (4), 044107, doi:10.1063/1.3103826.

Lange, M. A., Ahrens, T. J., 1982. The evolution of an impact-generated atmosphere. Icarus 51 (1), 96–120.

Larsen, J. T., Lane, S. M., 2002. Hyades–a plasma hydrodynamics code for dense plasma studies. Journal of Quantitative Spectroscopy and Radiative Transfer 51 (1-2), 179–186, doi:10.1016/0022-4073(94)90078-7.

Larson, D. B., Bearson, G. D., Taylor, J. R., 1973. Shock-wave studies of ice and two frozen soils. In: Permafrost: The North American Contribution to the Second International Conference. National Academy of Sciences, Washington, D.C., pp. 318–325.

Laudernet, Y., Clérouin, J., Mazevet, S., 2004. Ab initio simulations of the electrical and optical properties of shock-compressed SiO_2. Physical Review B 72, 155122, doi:10.1103/PhysRevB.70.165108.

Laughlin, R. B., 1980. Optical absorption edge of SiO_2. Physical Review B 22 (6), 3021–3029, doi:10.1103/PhysRevB.22.3021.

Le Feuvre, M., Wieczorek, M. A., 2011. Nonuniform cratering of the Moon and a revised crater chronology of the inner Solar System. Icarus 214 (1), 1–20, doi:10.1016/j.icarus.2011.03.010.

Leinhardt, Z. M., Marcus, R. A., Stewart, S. T., 2010. The formation of the collisional family around the dwarf planet Haumea. Astrophysical Journal 714, 1789–1799, doi:10.1088/0004-637X/714/2/1789.

Lemke, R. W., Knudson, M. D., Davis, J.-P., 2011. Magnetically driven hyper-velocity launch capability at the Sandia Z accelerator. International Journal of Impact Engineering 38, 480–485, DOI:10.1063/1.2084316.

Liberman, D. A., 1979. Self-consistent field model for condensed matter. Physical Review B 20, 4981–4989, DOI:10.1103/PhysRevB.20.4981.

Lisse, C. M., Chen, C. H., Wyatt, M. C., Morlok, A., Song, I., Bryden, G., Sheehan, P., 2009. Abundant circumstellar silica dust and sio gas created by a giant hypervelocity collision in the similar to 12 myr hd172555 system. Astrophysical Journal 701 (2), 2019–2032.

Louzada, K. L., Stewart, S. T., Weiss, B. P., 2007. Effect of shock on the magnetic properties of pyrrhotite, the martian crust, and meteorites. Geophysical Research Letters 34, L05204.

Luo, S. N., Ahrens, T. J., 2004. Shock-induced superheating and melting curves of geophysically important minerals. Physics of the Earth and Planetary Interiors 143-144, 369–386, doi:10.1016/j.pepi.2003.04.001.

Luo, S. N., Ahrens, T. J., Asimow, P. D., 2003a. Polymorphism, superheating, and amorphization of silica upon shock wave loading and release. JGR 108 (B9), 13, doi:10.1029/2002JB002317.

Luo, S. N., Ahrens, T. J., Asimow, P. D., 2003b. Polymorphism, superheating, and amorphization of silica upon shock wave loading and release. Journal of Geophysical Research 108 (B9), 2421, doi:10.1029/2002JB002317.

Luo, S. N., Ahrens, T. J., Cagin, T., Strachan, A., Goddard, W. A., Swift, D. C., 2003c. Maximum superheating and undercooling: Systematics, molecular dynamics simulations, and dynamic experiments. Physical Review B 68, 134206, doi:10.1103/PhysRevB.68.134206.

Luo, S. N., Akins, J. A., Ahrens, T. J., Asimow, P. D., 2004. Shock-compressed $MgSiO_3$ glass, enstatite, olivine, and quartz: Optical emission, temperatures, and melting. Journal of Geophysical Research 109 (B5), B05205, doi:10.1029/2003JB002860.

Luo, S. N., Mosenfelder, J. L., Asimow, P. D., Ahrens, T. J., 2002. Direct shock wave loading of stishovite to 235 GPa: Implications for perovskite stability relative to an oxide assemblage at lower mantle conditions. Geophysical Research Letters 29 (14), 1691, doi:10.1029/2003JB002860.

Lyon, S. P., Johnson, J. D., 1992. SESAME: The Los Alamos National Laboratory Equation of State Database. Tech. Rep. LA-UR-92-3407, Los Alamos National Laboratory, Los Alamos, NM.

Lyzenga, G. A., Ahrens, T. J., 1979. A multiwavelength pyrometer for shock compression experiments. Reviews of Scientific Instruments 50, 1421–1424, doi:10.1063/1.1135731.

Lyzenga, G. A., Ahrens, T. J., 1980. Shock temperature measurements in Mg_2SiO_4 and SiO_2 at high pressures. Geophysical Research Letters 7 (2), 141–144, doi:10.1029/GL007i002p00141.

Lyzenga, G. A., Ahrens, T. J., Mitchell, A. C., 1983. Shock temperatures of SiO_2 and their geophysical implications. J. Geophys. Res. 88 (B3), 2431–2444, doi:10.1029/JB088iB03p02431.

M. E. Savage *et al.*, 2007. An overview of pulse compression and power flow in the upgraded z pulsed power driver. In: 2007 IEEE Pulsed Power Conference. Vol. 1-4. p. 979.

Mao, H., Sundman, B., Wang, Z. W., Saxena, S. K., 2001. Volumetric properties and phase relations of silica - thermodynamic assessment. Journal of Alloys and Compounds 327 (1-2), 253–262, doi:10.1016/S0925-8388(01)01465-7.

Marsh, S. P., 1980. LASL Shock Hugoniot Data. University of California Press, Berkeley, California.

Mattsson, T. R., Desjarlais, M. P., 2006. Phase diagram and electrical conductivity of high energy-density water from density functional theory. Physical Review Letters 97 (1), doi:10.1103/PhysRevLett.97.017801.

Matzen, M., 1997. Z pinches as intense x-ray sources for high-energy density physics applications. Physics of Plasmas 4 (5), 1519–1527, DOI:10.1063/1.872323.

Maxwell, D., 1977. Simple Z model of cratering, ejection, and the overturned flap. In: Roddy, D., Pepin, R., Merrill, R. (Eds.), Impact and Explosion Cratering. Pergamon Press, New York, pp. 1003–1008.

McGlaun, J. M., Thompson, S. L., Elrick, M. G., 1990. CTH: A three-dimensional shock wave physics code. International Journal of Impact Engineering 10 (1-4), 351–360, DOI:10.1016/0734-743X(90)90071-3.

McKinnon, W., Parmentier, E., 1986. Ganymede and Callisto. In: Burns, J., Matthews, M. (Eds.), Satellites. University of Arizona Press, Tucson, pp. 718–763.

McQueen, R. G., 1992. The velocity of sound behind strong shocks in SiO_2. In: Schmidt, S., Dick, R. D., Forbes, J., Tasker, D. G. (Eds.), Shock Compression of Condensed Matter - 1991. Elsevier Science Publishers, Amsterdam, pp. 75–78.

Melosh, H. J., 1979. Acoustic fluidization - A new geologic process. Journal of Geophysical Research 84 (NB13), 7513–7520.

Melosh, H. J., 1989. Impact Cratering, A Geologic Process. Oxford University Press, New York.

Melosh, H. J., 2003. Shock viscosity and rise time of explosion waves in geologic media. J. Appl. Phys. 94 (7), 4320–4325.

Melosh, H. J., 2007. A hydrocode equation of state for SiO_2. Meteoritics & Planetary Science 42 (12), 2079–2098, doi:10.1111/j.1945-5100.2007.tb01009.x.

Melosh, H. J., Ivanov, B. A., 1999. Impact crater collapse. Annu. Rev. Earth Planet. Sci. 27, 385–415.

Melosh, H. J., Vickery, A. M., 1989. Impact erosion of the primordial atmosphere of Mars. Nature 338, 487–489.

Meyers, M. A., 1994. Dynamic Behavior of Materials. John Wiley and Sons, Inc., New York.

Miller, J. E., Boehly, T. R., Melchior, A., Meyerhofer, D. D., Celliers, P. M., Eggert, J. H., Hicks, D. G., Sorce, C. M., Oertel, J. A., Emmel, P. M., 2007. Streaked optical pyrometer system for laser-driven shock-wave experiments on OMEGA. Review of Scientific Instruments 78 (3), 034903, doi:10.1063/1.2712189.

Millett, J. C. F., Bourne, N. K., 2006. Shock and release of polycarbonate under one-dimensional strain. Journal of Material Science 41, 1683–1690.

Monteux, J., Ricard, Y., Coltice, N., Dubuffet, F., Ulvrova, M., 2009. A model of metal-silicate separation on growing planets. Earth Planet. Sci. Lett. 287 (3-4), 353–362.

Munson, D., Schuler, K., 1971. Steady wave analysis of wave propagation in laminates and mechanical mixtures. J. Composite Materials 5 (3), 286–304.

Mysen, B. O., Kushiro, I., 1988. Condensation, evaporation, melting, and crystallization in the primitive solar nebula: Experimental data in the system MgO-SiO_2-H_2 to 1.0×10^{-9} bar and 1870 C with variable oxygen fugacity. American Mineralogist 73 (1-2), 1–19.

Navrotsky, A., 1995. Energetics of silicate melts. Reviews in Mineralogy 32, 121–143.

Nellis, W. J., 2006. Sensitivity and accuracy of hugoniot measurements at ultrahigh pressures. In: Furnish, M., Elert, M., Russell, T., White, C. (Eds.), Shock Compression of Condensed Matter - 2005. American Institute of Physics, Melville, NY, pp. 115–118.

O'Brien, D. P., Lorenz, R. D., Lunine, J. I., 2005. Numerical calculations of the longevity of impact oases on Titan. Icarus 173, 243–253.

O'Brien, D. P., Morbidelli, A., Levison, H. F., 2006. Terrestrial planet formation with strong dynamical friction. Icarus 184 (1), 39–58, DOI:10.1016/j.icarus.2006.04.005.

Ogilvie, K. M., Duvall, G. E., 1983. Shock induced changes in the electronic-spectra of liquid CS_2. J. Chem. Phys. 78 (3), 1077–1087.

O'Keefe, J., Ahrens, T., 1977. Impact-induced energy partitioning, melting, and vaporization on terrestrial planets. In: R.B. Merril (Ed.), Proc. Lunar Planet. Sci. Conf. Vol. 8. pp. 3357–3374.

O'Keefe, J. D., Ahrens, T. J., 1993. Planetary cratering mechanics. J. Geophys. Res. 98, 17011–17028, DOI:10.1029/93JE01330.

Ottonello, G., Zuccolini, M. V., Belmonte, D., 2010. The vibrational behavior of silica clusters at the glass transition: Ab initio calculations and thermodynamic implications. Journal of Chemical Physics 133 (10), 104508, doi:10.1063/1.3483195.

Panero, W. R., Benedetti, L. R., Jeanloz, R., 2003. Equation of state of stishovite and interpretation of SiO_2 shock-compression data. Journal of Geophysical Research 108 (B1), 2015, doi:10.1063/1.2712189.

Perdew, J. P., Burke, K., Ernzerhof, M., 1996. Generalized gradient approximation made simple. Physical Review Letters 77 (18), 3865–3868, doi:10.1103/PhysRevLett.77.3865.

Petersen, C. F., Murri, W. J., Cowperthwaite, M., 1970. Hugoniot and release-adiabat measurements for selected geologic materials. Journal of Geophysical Research 75 (11), 2063–2072.

Petrenko, V., Whitworth, E., 1999. Physics of Ice. Oxford University Press, Oxford.

Pierazzo, E., Artemieva, N. A., Ivanov, B. A., 2005. Starting conditions for hydrothermal systems underneath martian craters: Hydrocode modeling. In: Kenkmann, T., Hörz, F., Deutsch, A. (Eds.), Large Meteorite Impacts III, Special Paper 384. The Geological Society of America, Boulder, CO, pp. 443–457.

Pierazzo, E., Melosh, H. J., 2000. Melt production in oblique impacts. Icarus 145, 252–261.

Pierazzo, E., Vickery, A., Melosh, H. J., 1997. A reevaluation of impact melt production. Icarus 127, 408–423, DOI:10.1006/icar.1997.5713.

Povarnitsyn, M. E., Khishchenko, K. V., Levashov, P. R., 2008. Simulation of shock-induced fragmentation and vaporization in metals. International Journal of Impact Engineering 35 (12), 1723–1727, doi:10.1016/j.ijimpeng.2008.07.011.

Prescher, C., Langenhorst, F., Hornemann, U., Deutsch, A., 2011. Shock experiments on anhydrite and new constraints on the impact-induced SO_x release at the K-Pg boundary. Meteoritics & Planetary Science 46 (11), 1619–1629.

Presnall, D. C., 1995. Phase diagrams of Earth-forming minerals. In: Ahrens, T. J. (Ed.), Mineral Physics and Crystallography, A Handbook of Physical Constants, Vol. 2. American Geophysical Union, Washington, D. C., pp. 248–268.

Pyalling, A. A., Gryaznov, V. K., Kvitov, S. V., Nikolaev, D. N., Ternovoi, V. Y., Filimonov, A. S., Fortov, V. E., Hoffmann, D., Stockl, C., Dornik, M., 1998. Time-resolved optical spectroscopy of lead at near critical-point states. International Journal of Thermophysics 19 (3), 993–1001, doi:10.1023/A:1022671813209.

Raikes, S. A., Ahrens, T. J., 1979a. Measurements of post-shock temperatures in aluminum and stainless steel. In: Timmerhaus, K. D., Barber, M. S. (Eds.), High Pressure Science and Technology. Vol. 2. pp. 889–894.

Raikes, S. A., Ahrens, T. J., 1979b. Post-shock temperature in minerals. Geophys. J. R. Astr. Soc. 58, 717–747.

Raymond, S. N., O'Brien, D. P., Morbidelli, A., Kaib, N. A., 2009. Building the terrestrial planets: Constrained accretion in the inner solar system. Icarus 203 (2), 644–662, DOI:10.1016/j.icarus.2009.05.016.

Reinhart, W. D., Thornhill, T. F., Chhabildas, L. C., Breiland, W. G., Brown, J. L., 2008. Temperature measurements of expansion products from shock compressed materials using high-speed spectroscopy. International Journal of Impact Engineering 35 (12), 1745–1755, doi:10.1016/j.ijimpeng.2008.07.062.

Rice, M. H., McQueen, R. G., Walsh, J. M., 1958a. Compression of solids by strong shock waves. In: Solid State Physics, Advances in Research and Applications. Vol. 6. Academic Press, Inc, New York, pp. 1–63.

Rice, M. H., McQueen, R. G., Walsh, J. M., 1958b. Compression of solids by strong shock waves. Solid State Physics 6, 1–63.

Richet, P., Bottinga, Y., 1986. Thermochemical properties of silicate glasses and liquids: A review. Reviews of Geophysics 24 (1), 1–25, doi:10.1029/RG024i001p00001.

Richet, P., Bottinga, Y., Denielou, L., Petitet, J., 1982. Thermodynamic properties of quartz, cristobalite and amorphous SiO_2: drop calorimetry measurements between 1000 and 1800 K and a review from 0 to 2000 K. Geochemica et Cosmochimica Acta 46, 2639–2658, doi:10.1016/0016-7037(82)90383-0.

Robie, R. A., Hemingway, B. S., Fisher, J. R., 1978. Thermodynamic Properties of Minerals and Related Substances at 298.15 K and 1 Bar (10^5 Pascals) Pressure and at Higher Temperatures. U.S. Geological Survey Bulletin 1452. U.S. Government Printing Office, Washington, DC.

Robie, R. A., Waldbaum, D. R., 1968. Thermodynamic properties of minerals and related substances at 298.15 K (25.0 C) and one atmosphere (1.013 Bars) pressure and at higher temperatures. U.S. Geological Survey Bulletin 1259. U.S. Government Printing Office, Washington, DC.

Root, S., Asay, J. R., 2010. Loading path dependence of inelastic behavior: x-cut quartz. In: Elert, M. L., Buttler, W. T., Furnish, M. D., Anderson, W. W., Proud, W. G. (Eds.), Shock Compression of Condensed Matter – 2009. American Institute of Physics, pp. 999–1002.

Rubie, D. C., Melosh, H. J., Reid, J. E., Liebske, C., Righter, K., 2003. Mechanisms of metal–silicate equilibration in the terrestrial magma ocean. Earth and Planetary Science Letters 205 (3), 239–255, DOI:10.1016/S0012-821X(02)01044-0.

Rubie, D. C., Nimmo, F., Melosh, H. J., 2007. Formation of earth's core. In: Treatise on Geophysics Volume 9. Elsevier, New York, pp. 51–90.

Saxena, S., Chatterjee, Y., Fei, Y., Shen, G., 1993. Thermodynamic Data on Oxides and Silicates. Springer Verlag, New York.

Saxena, S. K., 1996. Earth mineralogical model: Gibbs free energy minimization computation in the system MgO-FeO-SiO_2. Geochimica et Cosmochimica Acta 60 (13), 2379–2395, doi:10.1016/0016-7037(96)00096-8.

Schenk, P. M., 1991. Ganymede and callisto: Complex crater formation and planetary crusts. J. Geophys. Res. 96 (E1), 15635–15664.

Schenk, P. M., 2002. Thickness constraints on the icy shells of the Galilean satellites from a comparison of crater shapes. Nature 417 (6887), 419–421.

Schenk, P. M., Turtle, E. P., 2009. Europa's impact craters: Probes of the icy shell. In: Pappalardo, R. T., McKinnon, W. B., Khurana, K. (Eds.), Europa. pp. 181–198.

Schick, H. L., 1960. A thermodynamic analysis of the high-temperature vaporization properties of silica. Chemical Reviews 60 (4), 331–362, doi:10.1021/cr60206a002.

Schlichting, H. E., Warren, P. H., Yin, Q. Z., 2012. The last stages of terrestrial planet formation: Dynamical friction and the late veneer. Astrophysical Journal 752 (1), DOI:10.1088/0004-637x/752/1/8.

Schmitt, D. R., Ahrens, T. J., 1989. Shock temperatures in silica glass - implications for modes of shock-induced deformation, phase-transformation, and melting with pressure. JGR 94 (B5), 5851–5871, doi:10.1029/JB094iB05p05851.

Sedoi, V. S., Valevich, V. V., Chemezova, L. I., 1998. Journal of Aerosols 4e, 41.

Segura, T. L., Toon, O. B., Colaprete, A., 2008. Modeling the environmental effects of moderate-sized impacts on Mars. J. Geophys. Res. 113 (E11), doi:10.1029/2008JE003147.

Segura, T. L., Toon, O. B., Colaprete, A., Zahnle, K., 2002. Environmental effects of large impacts on Mars. Science 298, 1977–1980.

Seifter, A., Obst, A. W., 2007. About the proper wavelength for pyrometry on shock physics experiments. Int. J. Thermophys 28 (3), 934–946, doi:10.1007/s10765-007-0191-1.

Seifter, A., Stewart, S. T., Furlanetto, M. R., Kennedy, G. B., Payton, J. R., Obst, A. W., 2006. Post-shock temperature measurements of aluminum. In: Furnish, M. D., Elert, M., Russell, T. P., White, C. T. (Eds.), Shock Compression of Condensed Matter – 2005. American Institute of Physics, pp. 139–142.

Seifter, A., Swift, D. C., 2008. Pyrometric measurement of the temperature of shocked molybdenum. Phys. Rev. B 77 (13), 134104, doi:10.1103/PhysRevB.77.134104.

Senft, L. E., Stewart, S. T., 2008. Impact crater formation in icy layered terrains on Mars. Meteoritics & Planetary Science 43 (12), 1993–2013.

Senft, L. E., Stewart, S. T., 2011. Modeling the morphological diversity of impact craters on icy satellites. Icarus, in pressDoi:10.1016/j.icarus.2011.04.015.

Sharp, T. G., Michalski, J. R., Dyar, M. D., Bish, D. L., Friedlander, L. R., Glotch, T., 2012. Effects of shock metamorphism on phyllosilicate structures and spectroscopy. In: Lunar and Planetary Science Conference. Vol. 43. p. Abs. 2806.

Sheffield, S., Gustavsen, R., Alcon, R., 2006. In-situ magnetic gauging technique used at LANL-method and shock information obtained. In: Furnish, M., Chhabildas, L., Hixson, R. (Eds.), Shock Compression of Condensed Matter - 2000. American Institute of Physics, Melville, NY, pp. 1207–1210.

Shoemaker, E. M., 1962. Interpretation of lunar craters. In: Kopal, Z. (Ed.), Physics and Astronomy of the Moon. Academic Press, New York, pp. 283–359.

Shuvalov, V., 2009. Atmospheric erosion induced by oblique impacts. Meteoritics & Planetary Science 44 (8), 1095–1105.

Skala, R., Ederova, J., Matejka, P., Horz, F., 2002. Mineralogical investigations of experimentally shocked dolomite: Implications for the outgassing of carbonates. In: Koeberl, C., MacLeod, K. G. (Eds.), Catastrophic Events and Mass Extinctions: Impacts and Beyond. Geological Society of America Special Paper 356, Boulder, CO, pp. 571–585.

Spaulding, D. K., 2010. Laser driven shock compression studies of planetary composition. PhD thesis, University of California, Berkeley.

Spaulding, D. K., Hicks, D. G., Smith, R. F., Eggert, J. H., McWilliams, R. S., Collins, G. W., Jeanloz, R., 2007. New optical diagnostics for equation-of-state experiments on the Janus laser. In: Elert, M., Furnish, M., Chau, R., Holmes, N., Nguyen, J. (Eds.), Shock Compression of Condensed Matter - 2007. American Institute of Physics, Melville, New York, pp. 295–298.

Spaulding, D. K., McWilliams, R. S., Jeanloz, R., Eggert, J. H., Celliers, P. M., Hicks, D. G., Collins, G. W., Smith, R. F., 2012. Evidence for a phase transition in silicate melt at extreme pressure and temperature conditions. Physical Review Letters 108, 065701, DOI:10.1103/PhysRevLett.108.065701.

Steinberg, D., 1991. Equation of state and strength properties of selected materials. Tech. Rep. UCRL-MA-106439, Lawrence Livermore National Laboratory.

Stewart, S. T., Mar. 2004. The Shock Compression Laboratory at Harvard: A New Facility for Planetary Impact Processes. In: Mackwell, S., Stansbery, E. (Eds.), Lunar and Planetary Institute Science Conference Abstracts. Vol. 35. p. 1290.

Stewart, S. T., Ahrens, T. J., 2004. A new H_2O ice Hugoniot: implications for planetary impact events. In: Furnish, M., Gupta, Y., Forbes, J. (Eds.), Shock Compression of Condensed Matter - 2003. American Institute of Physics, Melville, NY.

Stewart, S. T., Ahrens, T. J., 2005. Shock properties of H_2O ice. J. Geophys. Res. 110, E03005, doi:10.1029/2004JE002305.

Stewart, S. T., Ahrens, T. J., O'Keefe, J. D., 2004a. Impact processing and redistribution of near-surface water on Mars. In: Furnish, M., Gupta, Y., Forbes, J. (Eds.), Shock Compression of Condensed Matter - 2003. American Institute of Physics, Melville, NY.

Stewart, S. T., Leinhardt, Z. M., 2012a. Collisions between gravity-dominated bodies: 2. the diversity of impact outcomes during the end stage of planet formation. Astrophysical Journal, in revision.

Stewart, S. T., Leinhardt, Z. M., 2012b. Collisions between gravity-dominated bodies. ii. the diversity of impact outcomes during the end stage of planet formation. The Astrophysical Journal 751 (1), 32, DOI:10.1088/0004-637X/751/1/32.

Stewart, S. T., O'Keefe, J. D., Ahrens, T. J., 2004b. Impact processing and redistribution of near-surface water on Mars. In: Furnish, M. D., Gupta, Y. M., Forbes, J. W. (Eds.), Shock Compression of Condensed Matter – 2003. American Institute of Physics, Melville, NY, pp. 1484–1487.

Stewart, S. T., Seifter, A., Obst, A. W., 2008. Shocked H_2O ice: Thermal emission measurments and the criteria for phase changes during impact events. Geophys. Res. Lett. 35, L23203, doi:10.1029/2008GL035947.

Stewart, S. T., Valiant, G. J., 2006. Martian subsurface properties and crater formation processes inferred from fresh impact crater geometries. Meteoritics & Planetary Science 41 (10), 1509–1537.

Stixrude, L., Karki, B., 2005. Structure and freezing of $MgSiO_3$ liquid in earth's lower mantle. Science 310, 297–299, doi:10.1126/science.1116952.

Swift, D. C., Tierney, IV, T. E., Kopp, R. A., Gammel, J. T., 2004. Shock pressures induced in condensed matter by laser ablation. Physical Review E 69 (3), 036406, doi:10.1103/PhysRevE.69.036406.

Tarasov, V. D., Chekhovskoi, V. Y., Puchkova, G. A., 1973. Enthalpy of several grades of quartz glass within the 1300-2450 °K temperature range. Journal of Engineering Physics and Thermophysics 25 (2), 1054–1056, doi:10.1007/BF00829860 (Translated from Inzhenerno-Fizicheskii Zhurnal 25 (2), 341-344, 1973.).

Taylor, G., 1950. Similarity solutions to the problems involving gas flow and shock waves. Proceedings of the Royals Society of London, Series A, Mathematical and Physical Sciences 204 (1076), 8–9.

Ternovoi, V. Y., Filimonov, A. S., Fortov, V. E., Lomonosov, I. V., Nikolaev, D. N., Pyalling, A. A., 1998. Investigation of tin thermodynamics in near critical point region. In: Schmidt, S., Dandekar, D., Forbes, J. (Eds.), Shock Compression of Condensed Matter - 1997. American Institute of Physics, Woodbury, New York, pp. 87–90.

Thompson, S. L., Lausen, H. S., 1972. Improvements in the CHARTD radiation-hydrodynamic code III: Revised analytic equation of state. Tech. Rep. SC-RR-710714, Sandia National Laboratories, Albuquerque, NM.

Thompson, W. R., Sagan, C., 1992. Organic chemistry on Titan: Surface interactions. In: Proc. of the Symposium on Titan. ESA Special Paper Volume 338. pp. 167–176.

Tkachenko, S. I., Vorob'ev, V. S., Malyshenko, S. P., 2004. The nucleation mechanism of wire explosion. Journal of Physics D 37 (3), 495–500, doi:10.1088/0022-3727/37/3/030.

Tonks, W. B., Melosh, H. J., 1992. Core formation by giant impacts. Icarus 100 (2), 326–346.

Tonks, W. B., Melosh, H. J., 1993. Magma ocean formation due to giant impacts. J. Geophys. Res. 98 (E3), 5319–5333.

Tonks, W. B., Pierazzo, E., Melosh, H. J., 1993. Impact-induced differentiation in icy bodies. unpublished manuscript.

Trunin, R., Medvedev, A. B., Funtikov, A. I., Podurets, M. A., Simakov, G., Sevast'yanov, A. G., 1989a. Shock compression of porous iron, copper, and tungsten, and their equation of state in the terapascal range. Zh. Eksp. Teor. Fiz. 95, 631–641.

Trunin, R., Simakov, G., Sutulov, Y. N., Medvedev, A. B., Rogozkin, B. D., 1989b. Compressibility of porous metals in shock waves. Zh. Eksp. Teor. Fiz. 96, 1024–1038.

Trunin, R., Simakov, G., Zhernokletov, M., Dorokhin, V., 1999. Shock compression of snow. High Temperature 37 (5), 702–707.

Trunin, R., Zhernokletov, M. V., Simakov, G., Gudarenko, L. F., Gushchina, O. N., 1998. Shock compression of highly porous samples of copper, iron, nickel, and their equation of state. In: Schmidt, S., Dandekar, D., Forbes, J. (Eds.), Shock Compression of Condensed Matter - 1997. American Institute of Physics, Woodbury, New York, pp. 83–86.

Trunin, R. F., 1994. Shock compressibility of condensed materials in strong shock waves generated by underground nuclear explosions. Physics-Uspekhi 37 (11), 1123–1145, doi:10.1070/PU1994v037n11ABEH000055.

Trunin, R. F., 1998. Shock Compression of Condensed Materials. Cambridge University Press, Cambridge.

Trunin, R. F., Gudarenko, L. F., Zhernokletov, M. V., Simakov, G. V., 2001. Experimental Data on Shock Compression and Adiabatic Expansion of Condensed Matter. Russian Federal Nuclear Center-VNIEF, Sarov.

Trunin, R. F., Podurets, M. A., Popov, L. V., Moiseev, B. N., Simakov, G. V., Sevast'yanov, A. G., 1993. Determination of the shock compressibility of iron at pressures up to 10 tpa (100 mbar). Zh. Eksp. Teor. Fiz. 103, 2189–2195.

Turtle, E., Pierazzo, E., 2001. Thickness of a Europan ice shell from impact crater simulations. Nature 294, 1326–1328, dOI:10.1126/science.1062492.

Tyburczy, J. A., Krishnamurthy, R. V., Epstein, S., Ahrens, T. J., 1990. Impact-induced devolatilization and hydrogen isotopic fractionation of serpentine: Implications for planetary accretion. Earth and Planetary Science Letters 98 (2), 245–260.

Vladimirova, N., Malagoli, A., Mauri, R., 1998. Diffusion-driven phase separation of deeply quenched mixtures. Physical Review E 58 (6), 7691–7699, 10.1103/PhysRevE.58.7691.

Vocadlo, L., Poirer, J. P., Price, G. D., 2000. Grüneisen parameters and isothermal equations of state. American Mineralogist 85, 390–395.

Wackerle, J., 1962. Shock-wave compression of quartz. J. Appl. Phys. 33, 922.

Wagner, W., Pruss, A., 2002. The IAPWS formulation 1995 for the thermodynamic properties of ordinary water substance for general and scientific use. J. Phys. Chem. Ref. Data 31 (2), 387–535.

Walker, R. J., 2009. Highly siderophile elements in the earth, moon and mars: Update and implications for planetary accretion and differentiation. Chemie der Erde-Geochemistry 69 (2), 101–125, DOI:10.1016/j.chemer.2008.10.001.

Wallace, D. C., 2002. Statistical Physics of Crystals and Liquids. World Scientific, Singapore.

Warren, S., 1984. Optical constants of ice from the ultraviolet to the microwave. Appl. Opt. 23, 1026–1225.

Watanabe, H., 1982. Thermochemical properties of synthetic high pressure compounds relevant to geophysics. In: Akimoto, S., Manghnani, M. H. (Eds.), High-Pressure Research in Geophysics. Center for Academic Publications, Tokyo, Japan, pp. 441–464.

Weidner, D. J., Bass, J. D., Ringwood, A. E., Sinclair, W., 1982. The single-crystal elastic moduli of stishovite. Journal of Geophysical Research 87 (B6), 4740–4746, doi:10.1029/JB087iB06p04740.

Weldon, R. J., Thomas, W. M., Boslough, M. B., Ahrens, T. J., 1982. Shock-induced color changes in nontronite - implications for the martian fines. Journal of Geophysical Research 87 (NB12), 102–114.

Wietzel, R., 1921. Die stabilitätsverhältnisse der glas- und kristallphase des siliziumdioxydes. Zeitschrift für anorganische und allgemeine Chemie 116 (1), 71–95, doi:10.1002/zaac.19211160108.

Wünnemann, K., Collins, G. S., Osinski, G. R., 2008. Numerical modelling of impact melt production in porous rocks. Earth and Planetary Science Letters 269, 530–539, doi:10.1016/j.epsl.2008.03.007.

Zahnle, K., Schenk, P., Levison, H., Dones, L., 2003. Cratering rates in the outer solar system. Icarus 163 (2), 263–289.

Zel'dovich, Y. B., Raizer, Y. P., 1966. Physics of Shock Waves and High-Temperature Hydrodynamic Phenomena. Dover Publications, Mineola, New York.

Zhang, F. P., Sekine, T., 2007. Impact-shock behavior of Mg- and Ca-sulfates and their hydrates. Geochimica et Cosmochimica Acta 71 (16), 4125–4133.

Zhuang, S. M., Ravichandran, G., Grady, D. E. W., 2003. An experimental investigation of shock wave propagation in periodically layered composites. J. Mech. Phys. Solids 51 (2), 245–265.

Zhugin, Y. N., Krupnikov, K. K., 1987. Structural peculiarities of plastic front in quartz in the mixed phase region. In: Kedrinskii, V. K. (Ed.), Proceedings of IUPAP, IUTAM Symposium on Nonlinear Acoustics. pp. 196–200.